



ASTM INTERNATIONAL  
Selected Technical Papers

# Application of Automation Technology in Fatigue and Fracture Testing and Analysis 6<sup>th</sup> Volume

STP 1571  
Editors:  
Peter McKeighan  
Arthur Braun



**SELECTED TECHNICAL PAPERS**  
**STP1571**

---

Editors: Peter C. McKeighan, Arthur A. Braun

# Application of Automation Technology in Fatigue and Fracture Testing and Analysis

---

ASTM Stock #STP1571

### **Library of Congress Cataloging-in-Publication Data**

Application of automation technology in fatigue and fracture testing and analysis / Peter C. McKeighan, Arthur A. Braun, editors.

pages cm. -- (STP ; 1571)

Includes bibliographical references.

ISBN 978-0-8031-7587-7

1. Fatigue testing machines. 2. Materials--Fatigue--Testing. 3. Strains and stresses--Testing. 4. Fracture mechanics. I. McKeighan, P. C. (Peter C.) II. Braun, Arthur A., 1953-

TA413.A67 2014

620.1'1260287--dc23

2014041031

**ISSN:** 1537-7407

Copyright © 2014 ASTM INTERNATIONAL, West Conshohocken, PA. All rights reserved. This material may not be reproduced or copied, in whole or in part, in any printed, mechanical, electronic, film, or other distribution and storage media, without the written consent of the publisher.

### **Photocopy Rights**

Authorization to photocopy items for internal, personal, or educational classroom use, or the internal, personal, or educational classroom use of specific clients, is granted by ASTM International provided that the appropriate fee is paid to the Copyright Clearance Center, 222 Rosewood Drive, Danvers, MA 01923, Tel: (978) 646-2600; <http://www.copyright.com/>

The Society is not responsible, as a body, for the statements and opinions expressed in this publication. ASTM International does not endorse any products represented in this publication.

### **Peer Review Policy**

Each paper published in this volume was evaluated by two peer reviewers and at least one editor. The authors addressed all of the reviewers' comments to the satisfaction of both the technical editor(s) and the ASTM International Committee on Publications.

The quality of the papers in this publication reflects not only the obvious efforts of the authors and the technical editor(s), but also the work of the peer reviewers. In keeping with long-standing publication practices, ASTM International maintains the anonymity of the peer reviewers. The ASTM International Committee on Publications acknowledges with appreciation their dedication and contribution of time and effort on behalf of ASTM International.

### **Citation of Papers**

When citing papers from this publication, the appropriate citation includes the paper authors, "paper title", STP title, STP number, book editor(s), page range, Paper doi, ASTM International, West Conshohocken, PA, year listed in the footnote of the paper. A citation is provided on page one of each paper.

Printed in Bay Shore, NY  
November, 2014

## Foreword

This compilation of *Selected Technical Papers*, STP1571, *Application of Automation Technology in Fatigue and Fracture Testing and Analysis*, contains eleven peer-reviewed papers that were presented at a symposium held May 23, 2013 in Indianapolis, IN, USA. The symposium was sponsored by the ASTM International Committee E08 on Fatigue and Fracture and Subcommittee E08.03 on Advanced Apparatus and Techniques.

The Symposium Chairmen and STP Editors are Peter C. McKeighan, Exponent®-Failure Analysis Associates, Warrenville, IL, USA and Arthur A. Braun, Chapel Wood Engineering LLC, Columbia, MO, USA.



# Contents

<b>Overview</b>	vii
<b>Constant-Amplitude Versus K-Control in Fatigue Crack Growth Rate Testing</b> M. A. Adler	1
<b>Automated Real Time Correction of Motion Induced Dynamic Load Errors in the Force Readout of a Test Apparatus</b> D. Dingmann, A. White, and T. Nickel	18
<b>Application of Automation Methods for Nonlinear Fracture Test Analysis</b> P. A. Allen and D. N. Wells	31
<b>A Novel Shear Test Procedure for Determination of Constitutive Behavior of Automotive Aluminum Alloy Sheets</b> J. Kang and G. Shen	50
<b>In-Plane Biaxial Fatigue Testing Machine Powered by Linear Iron-Core Motors</b> M. Freitas, L. Reis, B. Li, I. Guelho, V. Antunes, J. Maia, and R. A. Cláudio	63
<b>Automation in Strain and Temperature Control on VHCF with an Ultrasonic Testing Facility</b> Y. Lage, A. M. R. Ribeiro, D. Montalvão, L. Reis, and M. Freitas	80
<b>Evaluation of Fracture Toughness Test Methods for Linepipe Steels</b> J. Kang, G. Shen, J. Liang, K. Brophy, A. Mendonca, and J. Gianetto	101
<b>Analysis Round Robin Results on the Linearity of Fracture Toughness Test Data</b> P. C. McKeighan and M. A. James	116
<b>Uncertainty in Ductile Fracture Initiation Toughness (<math>J_{ic}</math>) Resulting From Compliance Measurement</b> S. M. Graham	134

---

<b>Combining Visual and Numeric Data to Enhance Understanding of Fatigue and Fracture Properties and Mechanisms</b>	153
E. A. Schwarzkopf	

---

<b>Software Tools for a Materials Testing Curriculum</b>	163
C. Leser, F. Kelso, A. P. Gordon, and S. Ohnsted	

## Overview

Automation in the testing laboratory has resulted in exciting new capabilities in the general areas of test control, data acquisition, data analysis and interpretation, modeling, and the integration of testing into mechanical design. As automated computer-based technology has become entrenched in the laboratory, our ability to record more meaningful and precise data has increased dramatically. The ever increasing capability of computers integrated into materials testing has allowed us to investigate some of the more unique and difficult problems in the materials testing world.

This Symposium is the fifth in a series of symposia concerned with documenting and advancing the state of the art in automated fatigue and fracture testing. This series of symposia was initiated in 1989 with STP 1092 held in Kansas City, Missouri. Over the nearly 25 years since that time, the tools in the laboratory, including both sensors and computers, have evolved markedly. The evolution of automation systems was well described in Keith Donald's keynote paper presented at this most recent symposium. A key graphic from this invited presentation, reproduced below in Figure 1, describes the capability increase and cost decrease over three generations of the Fracture Technology Associates automation systems.

The challenge facing the test engineer today differs from the initial phase of computer involvement in the test laboratory when computer processing technology limited the capabilities of our automation tools. The challenges today are at the opposite end of the spectrum: managing the enormous amount of data that can now be generated and stored by the newest and most robust computer systems. In a sense, the issues today are developing the appropriate smart algorithms and tools that can distill vast amounts of information in a rapid and meaningful manner. Our computer automation systems are becoming increasingly more sophisticated for interpreting different material behavior and effects.

This symposium, and the eleven papers contained in it, emphasizes refined experimental methods, new methods and techniques, data analysis, and software development. The enhanced processing capabilities available with our test lab computers are highlighted in the first two papers contained herein. More specifically, Adler discusses an automated K-control method for fatigue crack growth testing that is only available given the processing speed and capability of our current data acquisition tools in the laboratory. Dynamic issues associated with high cyclic rate testing are addressed in the next paper by Dingmann, White, and Nickel; where a novel method is implemented and used to correct for force readout error in the testing system due to moving mass.

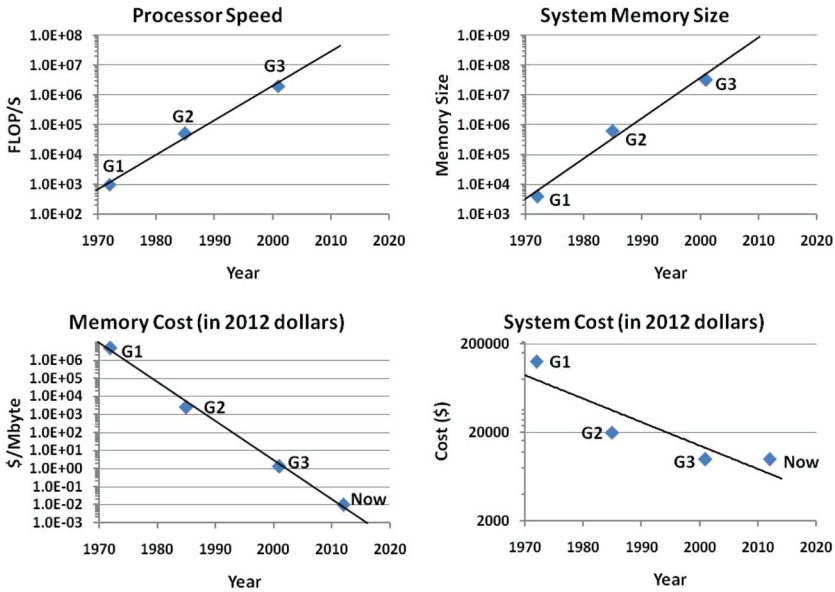


Figure 1. Evolution in automation system capability and cost over time (from J. K. Donald's keynote presentation "A Personal Perspective on 40 years of Automated Fatigue Crack Growth Testing").

The next five papers address new methods and techniques developed to investigate a variety of technical issues. Allen and Wells introduce an analysis method, developed from extensive experimental results and full-scale test simulation analyses, where a database is developed to assist in the interpretation of surface crack fracture testing in the elastic-plastic regime. The enhanced processing capabilities of test laboratory computers are emphasized in the next four papers, addressing unusual and non-traditional experimental setups. A new shear specimen geometry and test is proposed in the next paper by Kang and Shen that uses full-field digital image correlation methods to interpret the shear behavior of automotive aluminum alloy sheets. Another unique experimental setup is then discussed and described in detail by de Freitas et al. concerning an in-plane biaxial fatigue testing machine powered by linear iron core motors. Lage et al. discuss the automation of strain and temperature measurements and control in a high cycle, ultrasonic fatigue testing application. A final paper by Kang et al. in this section examines automation of J- and CTOD-based fracture test methods as applied to linepipe steel.

The remaining four papers in the symposium address data analysis and software developments. McKeighan and James present results from a fracture toughness inter-laboratory study with nine participants analyzing fracture toughness results and highlighting the importance of a consistent and systematic linearity assessment when interpreting linear elastic fracture toughness test results. The subsequent paper continues along the same general theme of test uncertainty where Graham examines

how compliance measurements can affect the measurement of ductile fracture initiation toughness  $J_{Ic}$ . The next paper in this section by Schwarzkopf addresses the issue of how automation software can effectively represent information (in visual graphic or numeric form) and provide an efficient interface between the actual test and the technician in the laboratory. Finally, Leser et al. address the practical challenges associated with integrating mechanical testing into a teaching curriculum using both physical test methods and virtual test simulation environments.

The common theme evident with all the papers in this symposium is the increasing role of computer automation while actually performing a test and then interpreting the results once testing is complete. Without question, test automation remains a critical area for developing the tools and techniques required to understand the more difficult problems that face the materials engineer and designer today. It is the intent of Automation Task Group within ASTM E08.03 to revisit the automation research every five years to report and track how testing methods, techniques, and tools evolve. This is a developmental area that continues to flourish in the fatigue and fracture testing world. Recent efforts within the Task Group on algorithm development promise to provide useful tools to the analyst for interpreting material behavior and coping with the vast amount of data that is typically recorded in the laboratory today.

In closing, the editors would like to express their sincere appreciation to all of the authors and co-authors responsible for the papers included in this STP and the presentations made during the symposium. This STP would not have been possible without your fine technical work and contributions. We also appreciate the tireless efforts provided by the numerous reviewers who assisted in the technical vetting and provided a high degree of professionalism and a timely response to ensure the quality of this publication. Finally, the editors would also like to express their sincere gratitude to the ASTM planning and editorial staff for their assistance in making this symposium a great success.

Peter C. McKeighan  
Arthur A. Braun



---

STP 1571, 2014 / available online at [www.astm.org](http://www.astm.org) / doi:10.1520/STP157120130115

Matthew A. Adler<sup>1</sup>

# Constant-Amplitude Versus K-Control in Fatigue Crack Growth Rate Testing

## Reference

Adler, Matthew A., "Constant-Amplitude Versus K-Control in Fatigue Crack Growth Rate Testing," *Application of Automation Technology in Fatigue and Fracture Testing and Analysis*, STP 1571, Peter C. McKeighan and Arthur A. Braun, Eds., pp. 1-17, doi:10.1520/STP157120130115, ASTM International, West Conshohocken, PA 2014.<sup>2</sup>

## ABSTRACT

This study compared  $K$ -control to constant-amplitude fatigue crack growth rate testing to determine under what conditions  $K$ -control testing should be used for  $K$ -increasing tests. The results showed that there is no significant difference between the data generated from constant-amplitude and  $K$ -control testing for compact-tension specimens when the normalized  $K$ -gradient ranged from 1.65 to 5.00 (1/in.) and test time was improved by as much as 70 % for the  $K$ -control tests. In most cases, and especially for small test specimens,  $K$ -Control  $K$ -increasing tests are recommended as a more efficient alternative to constant-amplitude testing.

## Keywords

$K$ -control, constant-amplitude, fatigue crack growth, crack propagation,  $K$  gradient, efficiency

## Introduction

Separate tests are typically required to determine the crack growth rate behavior of an alloy over the full range of crack driving force, i.e., a  $K$ -decreasing test and a

---

Manuscript received July 7, 2013; accepted for publication August 19, 2014; published online September 17, 2014.

<sup>1</sup>Director of Advanced Fracture Mechanics, Westmoreland Mechanical Testing & Research, Inc., 221 Westmoreland Drive, Youngstown, PA 15696.

<sup>2</sup>ASTM Sixth Symposium on *Application of Automation Technology in Fatigue and Fracture Testing and Analysis*, on May 23, 2013 in Indianapolis, IN.

$K$ -increasing test, where  $K$  is the stress-intensity factor and  $\Delta K$  is the driving force for fatigue crack growth. The  $K$ -decreasing test is a test in which  $K$  continually decreases during the test with a negative normalized  $K$  gradient and results in the measure of threshold crack growth rate data, usually below  $4E-7$  in/cycle. The opposite is the  $K$ -increasing test in which  $K$  continually increases with increasing crack length, usually for measuring Region II or III crack growth rate data. The scope of this investigation was limited to the latter case.

$K$ -control crack growth tests offer numerous advantages over constant-amplitude testing for generating upper-end  $da/dN$  versus  $\Delta K$  data including reduced test time, avoidance of steep  $K$ -gradients, and improved potential difference crack length accuracy [1]. Given these advantages, however, the percentage of customers that request  $K$ -control  $K$ -increasing tests is relatively low.

ASTM E647-13 [2] specifies that either constant force amplitude or a positive, normalized  $K$ -gradient can be used for the  $K$ -increasing test. Experience by the author indicates that almost all customers of crack growth rate data request constant-amplitude and not  $K$ -control tests when a  $K$ -increasing test is desired. The percentage of customers requesting  $K$ -control tests is so vanishingly small, in fact, that either these customers are collectively not aware of the advantages of  $K$ -control testing or, since these customers are making their decisions independently, it was considered that  $K$ -control testing was possibly a bad method. It was this contradictory situation that motivated this study.

One complicating issue, however, is the concept of similitude. Similitude states that in the absence of mitigating factors such as crack closure or residual stress that crack growth is a function of  $\Delta K$  and it is the equivalency in  $\Delta K$  that produces a given crack growth rate. This is so regardless of whether that  $\Delta K$  is measured in a lab specimen or in an actual structure or whether that  $\Delta K$  is produced by constant-amplitude or  $K$ -control. If similitude was not valid, then we could not apply crack growth data from small test specimens such as compact-tension specimens to actual structures unless our structures looked like compact-tension specimens, which of course they do not. Therefore, a test lab should utilize the test method that produces valid data in the quickest time.

## Background

The normalized  $K$ -gradient  $C$  is defined:

$$(1) \quad C = \frac{1}{K} \frac{dK}{da}$$

where  $K$  is modified according to:

$$(2) \quad K = K_0 e^{C(a-a_0)}$$

where:

$K_0$  and  $a_0$  are the initial  $K$  and crack length, respectively, at the start of the  $K$ -control process, and  $C$  is the normalized  $K$ -gradient.

A special feature of this expression is the feature of producing an equal number of  $da/dN - \Delta K$  data points per decade when the  $da/dN$  versus  $\Delta K$  data is plotted in log-log space and data is acquired in set  $\Delta a$  intervals.

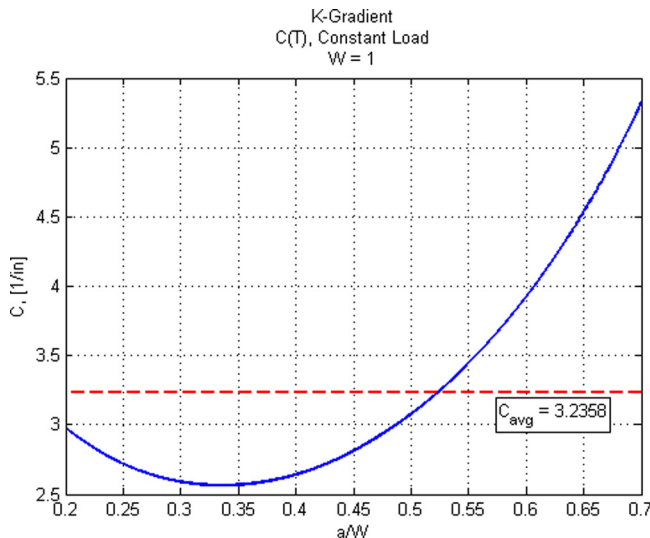
The normalized  $K$  gradient  $C$  specifies the rate of change of  $K$  with respect to crack length relative to the instantaneous value of  $K$ , and therefore is not a true normalized (unitless) number. The units of  $C$  are [L] and are typically (1/in.) in English units when  $K$  is expressed in  $\text{ksi}\sqrt{\text{in}}$  and the crack length in inches.

## Analytical Study

To understand how  $C$  changes during constant-amplitude loading,  $C$  was calculated for numerous compact-tension C(T) and middle-tension M(T) specimens by substituting the appropriate stress-intensity factor solution into Eq 1 and using central finite difference to numerically differentiate to determine  $dK/da$ . This study included C(T) and M(T) specimens as they are by a wide majority the most common specimen types for fatigue crack growth testing. This problem neatly presented itself for numerical investigation because ensuring identical test specimen and crack length dimensions could not be achieved through physical experimentation.

**Figure 1** depicts  $C$  as a function of  $a/W$  for a  $W = 1$  in. compact-tension specimen, where  $W$  is the specimen finite width and  $a/W$  is the normalized crack length. The title of the figure indicates constant load boundary conditions, which is

**FIG. 1** Normalized K-gradient for a  $W = 1$  in. C(T) specimen as a function of normalized crack length. The dashed horizontal line represents the average K-gradient over the simulation.



synonomous with constant-amplitude. The horizontal dashed line represents the average  $K$ -gradient over the range of the simulation. One of the important takeaways (and often a misnomer regarding constant-amplitude testing) is that the normalized  $K$ -gradient is not constant during constant-amplitude testing as we can see in Fig. 1. Observe that  $C$  decreases, reaches a minimum, and then increases, which is the typical shape for  $C$  in C(T) and M(T) specimens. Also note that  $C$  is a function of  $W$  and  $a/W$  only. The model was analyzed over a range  $0.2 \leq a/W \leq 0.7$ , as a typical test range for the C(T) specimen. The final  $K$ -gradient at the end of the test was  $C = 5.33 \text{ in.}^{-1}$ . Had the test progressed to  $a/W = 0.8$  and  $0.9$ , the final normalized  $K$ -gradients would have been  $C = 7.95$  (1/in.) and  $15.42$  (1/in.), respectively. Clearly, it would be difficult to accurately control target loads and acquire adequate data at such high rates of change of  $K$ . The obvious problem is that as the  $da/dN$  rate is increasing asymptotically towards a vertical line at the limit as the fracture toughness is approached, the constant-amplitude test methodology is requiring that we increase  $K$  at a faster and faster rate. Because the  $K$ -gradient is increasing with increasing crack growth rate it is made more difficult to acquire data at the extreme high end of the curve because small changes in  $\Delta K$  result in very large changes in  $da/dN$ . As a result, data may not be captured in time before the specimen breaks unless the test frequency is reduced before Region III crack growth, which should be avoided for test efficiency purposes.

The impact of increasing the finite width is a decrease in the average  $K$ -gradient and an increase in the overall test duration. Figure 2 represents the same model as above, except that the finite width is increased from 1 to 6 in.

This sample size range is representative of the most common sample sizes. Notice that the average  $C$  has decreased exactly by the ratio of the finite widths and the average  $C$  is a recursion function of  $W$  for constant-amplitude loading:

$$(3) \quad C_{avg}(W_2) = C_1 \frac{W_1}{W_2}$$

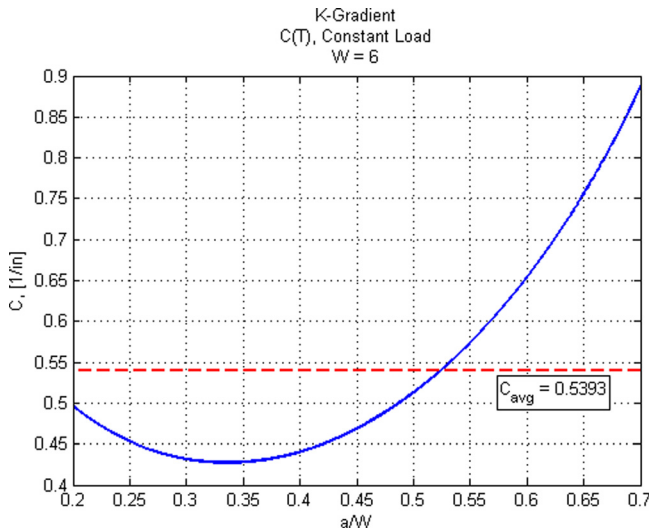
and for the case at hand:

$$(4) \quad C_{avg}(6) = 3.2358 \frac{1}{6} \text{in.}^{-1} = 0.5393 \text{in.}^{-1}$$

Equation 3 can be deduced from the  $K$  expression for a C(T) specimen by observing that as crack length increases that the  $K$  increases by a factor of  $\sqrt{W_1/W_2}$  and  $dK/da$  increases by a factor of  $\sqrt{W_1/W_2} \times W_1/W_2$  when the finite width of the sample changes from  $W_1$  to  $W_2$  at a given  $a/W$  [2].

It is seen that the larger the test specimen, the lower the average normalized  $K$ -gradient occurring during the test. Therefore, not only will tests on larger test specimens take longer than on smaller test specimens simply because of the additional test ligament that must be tested, but they will also take considerably longer because the  $K$ -gradient is reduced at any given crack length. This means that all things being equal for a given specimen type and initial crack size when data is taken based on fixed  $\Delta a$  intervals and not  $\Delta a/W$ , the test on the larger sample will generate a finer

**FIG. 2** Normalized K-gradient for a  $W = 6$  in. C(T) specimen as a function of normalized crack length.



distribution of data at the onset of the test than for the same region on the  $da/dN - \Delta K$  curve for a smaller specimen. In other words, for larger specimens,  $K$  will increase more slowly over a given crack growth interval than for smaller specimens such that there will be many data points close together in  $da/dN - \Delta K$  space. This means that the marginal information produced by each data point is less for larger test specimens. From an efficiency standpoint, this situation should be avoided.

Equation 3 also holds for the M(T) specimen as inferred by Figs. 3 and 4. The relationship described by Eq 3. Is apparent when rearranging Eq 2 to show that the normalized  $K$  gradient is proportional to the inverse change in crack length:

$$(5) \quad C = \frac{\ln\left(\frac{K}{K_0}\right)}{\Delta a}$$

but we keep in mind from the stress-intensity factor solutions that the normalized  $K$  is proportional to normalized  $a$ , not  $a$ . The result is then a quantity proportional to  $a/W$  divided by a quantity proportional to  $a$ , which results in the  $1/W$  proportionality.

The comparison between the average  $K$ -gradient occurring in an M(T) versus a C(T) specimen is shown in Fig. 5 over the range  $0.1 < a/W < 0.7$  and  $0.1 < 2a/W < 0.7$ , respectively. The  $K$ -gradient for an M(T) specimen is less than the  $K$ -gradient for a C(T) at a given  $a/W$  which is counterintuitive; however, this is an outcome of the  $K$ -gradient being defined in terms of  $da/dN$  and not  $2 da/dN$ . Notice

**FIG. 3** Normalized K-gradient for a  $W = 1$  in. M(T) specimen as a function of normalized crack length.

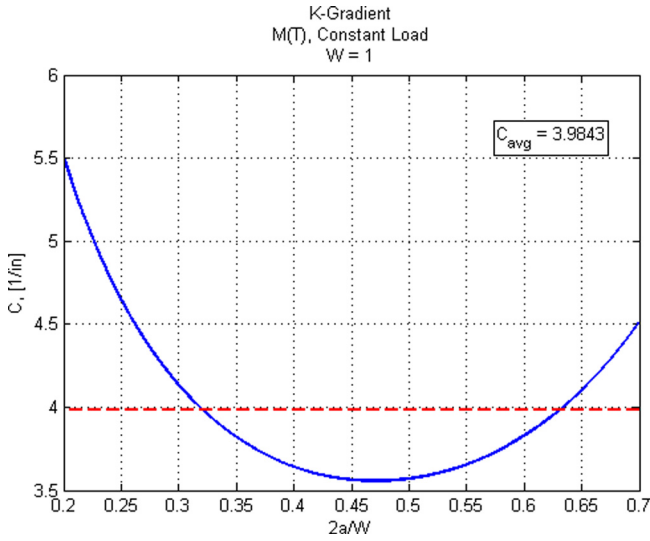


**FIG. 4** Normalized K-gradient for a  $W = 6$  in. M(T) specimen as a function of normalized crack length.

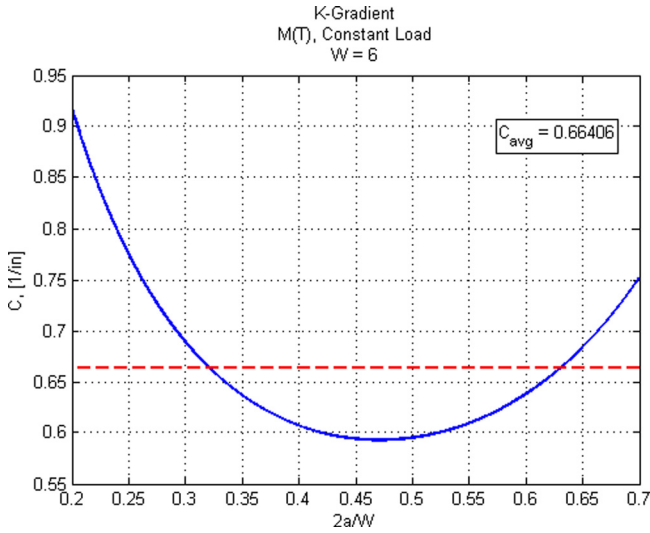
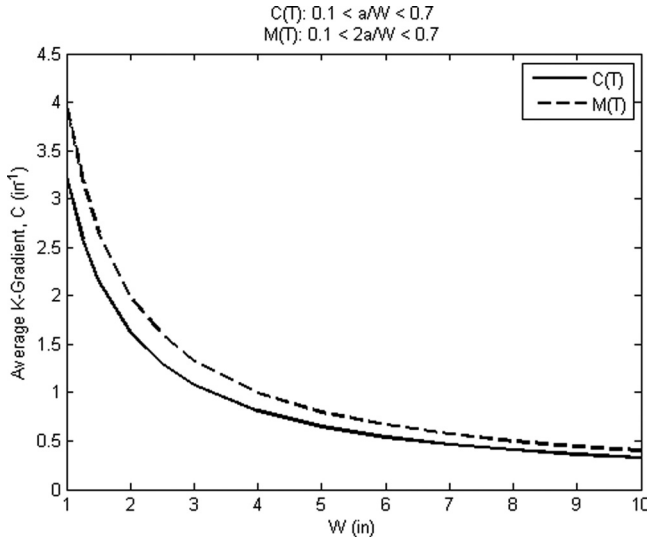


**FIG. 5** Comparison of the average  $K$ -gradient occurring in a  $C(T)$  and  $M(T)$  specimen as a function of specimen size. The average  $K$ -gradients converge at large sample sizes indicating diminishing geometry effects as sample size increases.



that the average  $K$ -gradients converge for increasing specimen size. In other words, there are no geometry effects on the  $K$ -solutions for infinite panels, or conversely, that the biggest difference between the  $K$ -gradients for  $M(T)$  and  $C(T)$  specimens occurs the smaller the specimen.

To compare the two methods, a crack growth rate test was numerically simulated in both constant-amplitude and  $K$ -control mode in WESGRO, a custom-written fatigue crack growth simulation program. The specimen for simulation was an  $M(T)$  specimen with  $W = 5$  in., initial  $2a/W = 0.1$ , and thickness of 0.25 in. Since it is the most well-established fatigue crack growth program available, NASGRO [3] v6.2 was used for evaluating the in-house WESGRO program. The  $da/dN - \Delta K$  data was the designated NASGRO Material ID M7HB11AB01A2 at  $R = 0.1$  for Al 7075-T651. The data was provided as a lookup table into NASGRO such that the model would be as loyal as possible to the original input data so to avoid any interpolation issues that have been associated with NASGRO [4]. The model was run one cycle at a time in WESGRO in constant-amplitude starting at  $\Delta K = 3$  ksi $\sqrt{\text{in}}$  to failure resulting in  $N_f = 1\,252\,250$  cycles. This stress-intensity factor range was chosen because it produces a rate of approximately  $4E-7$  in./cycle, which is the typical starting point for an increasing  $da/dN$  test. Crack length and  $K$  were updated on a cycle-by-cycle basis. This result was compared to a simulation in NASGRO with the same model and loading parameters to confirm the result, with NASGRO reporting 1 253 845 cycles, a difference of only 0.13 %. Additional verification

models were performed to cover a wider range of test cases and are summarized in [Table 1](#).

In NASGRO, the input data was limited to 45 ( $\Delta K$ ,  $da/dN$ ) points with linear interpolation performed at intermediate values because NASGRO is limited to 45 points for the lookup-table option. Differences in the results are likely caused by the different integration algorithms: NASGRO integrates on the basis of  $\Delta a$  where WESGRO integrated on a cycle-by-cycle basis. This difference was considered acceptably small for purposes of the validation of the in-house code. Because NASGRO is not capable of loading a specimen at a constant  $K$ -rate, this part was then performed in the in-house code.

To simulate a  $K$ -control test, after each load cycle, the crack length was incremented by the instantaneous crack growth rate associated with the current  $\Delta K$ . The necessary load was then determined from Eq 2 such that  $K$  would increase according to Eq 1 with  $C = 2 \text{ in.}^{-1}$ . The difference in the number of cycles to failure from each model was converted into a time basis assuming a nominal test frequency of 20 Hz. For the  $W = 5 \text{ in.}$  M(T) specimen, time saved was 6.57 h and 473 140 cycles or 38 % of the test time. Thus a  $K$ -control test at these conditions would have saved 38 % of the test time.

The in-house code was then modified to increase  $K$  in fixed  $\Delta a$  intervals instead of continuously. This was more realistic scenario that takes into account the fact that there is a finite  $\Delta a$  that must occur before growth can be accurately measured and provided as feedback into the control loop so that the load is modified only after set intervals in crack length. The saved cycles to failure was then 445 624 cycles when assuming a minimum  $\Delta a = 0.010 \text{ in.}$  such that the time saved was slightly decreased. This decrease is slight because while the changes in applied load occurred less frequently this was compensated by the larger magnitudes of the load changes.

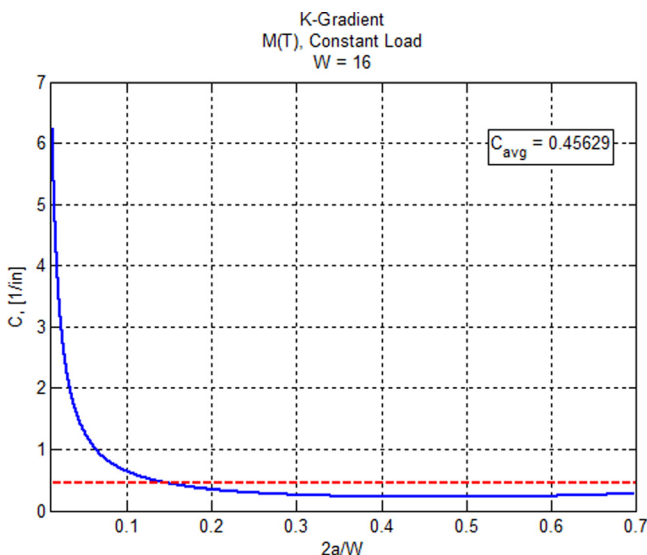
In light of the fact that the M(T) panel with  $W = 5 \text{ in.}$ , initial  $2a/W = 0.1$  was shown to save 38 % of the test time in  $K$ -control versus constant-amplitude it was expected that a  $K$ -control test on a  $W = 16 \text{ in.}$ , initial  $2a/W = 0.01$  would save even more substantial time given the much larger test specimen and initial uncracked ligament. The simulations did not bear this out. A constant-amplitude simulation on this geometry with an initial  $\Delta K$  of  $3 \text{ ksi}\sqrt{\text{in}}$  resulted in 599 420 cycles to failure but the  $K$ -control simulation with these same initial conditions and  $C = 2 \text{ in.}^{-1}$  resulted in 779 110 cycles to failure, an additional 179 110 cycles or 30 % additional time to failure. This surprising result led to further investigation.

**TABLE 1** WESGRO crack growth code validation comparing crack growth rate simulations in WESGRO to NASGRO for NASGRO material ID M7HB11AB01A2 for AI 7075-T651 at  $R = 0.1$ .

W	$2a_0$	$DK_0$	$N_f$ (WESGRO)	$N_f$ (NASGRO)	% Error
5	0.5	3	1 252 250	1 253 845	0.13 %
4	0.8	5	285 777	286 154	0.13 %
10	2	6	403 858	404 113	0.06 %

A plot of the  $K$ -gradient occurring for this constant-amplitude test is shown in Fig. 6 and clarifies the situation. Clearly, the figure shows what is happening; the  $K$ -gradient for the very small starting normalized crack length is very high for the constant-amplitude test, and then decays rapidly with increasing crack length with an average  $C$  of only 0.46. Thus we have a competition between a higher initial  $K$ -gradient for the constant-amplitude test and a higher average  $K$ -gradient for the  $K$ -control test. In this particular case, because the  $K$ -gradient is large at the onset of the constant-amplitude test the test rapidly climbs out of the threshold portion of the crack growth data and even though the  $K$ -control test is at larger crack lengths increasing  $K$  at a faster rate than for the constant-amplitude test, the  $K$ -control test can never catch up. Thus, as  $C$  is held constant as the starting crack length for a test decreases, then the likelihood that the constant-amplitude test is faster than a  $K$ -control test increases, or in other words, higher  $K$ -gradients may be required for a  $K$ -control test to be faster than a constant-amplitude test as the starting crack size decreases. This is due to the fact that large  $K$ -gradients occur at small crack lengths under constant-amplitude testing. Of course, in a situation of a rapidly changing  $\Delta K$  one does have to be cautious in regards to being able to accurately calculate  $\Delta K$  during data processing such that even if constant-amplitude testing is faster than  $K$ -control testing under a given scenario it may not be preferable because it may lead to inaccurate  $\Delta K$  calculations since  $\Delta K$  is changing rapidly over very small crack length intervals.

**FIG. 6** Normalized  $K$ -gradient as a function of normalized crack length for a  $W = 16$  in.  $M(T)$  specimen starting at  $2a/W = 0.01$  in constant-amplitude.



Given this information, we can easily create maps for a given specimen geometry, sample size, starting crack length, and material, to determine at what  $K$ -gradient a  $K$ -control test would be faster than a constant-amplitude test at the same initial conditions. Such maps are presented in Figs. 7–9 for C(T) and M(T) samples. With a goal of producing a valid test as fast as possible, such maps are considered useful to any test lab with limited resources. Note that in order for a  $K$ -control test to be faster than a constant-amplitude test, the  $C$  that is required decreases as the finite width increases. Although the curves appear asymptotic, in the limit as the sample size becomes infinite, then the  $C$  required such that the  $K$ -control test takes an equal amount of time as a constant-amplitude test approaches zero since the stress-intensity factor would never change in an infinite panel and  $C = 0$  would produce constant  $\Delta K$  conditions. Whether  $K$ -control testing would be faster at a given  $K$ -gradient is a strong function of the starting crack length. Figure 8 shows that for a test starting at  $2a/W = 0.2$  in a  $W = 6$  in. M(T) panel when  $C$  is greater than approximately 0.72. Then the  $K$ -control test will be faster, but  $C$  must be greater than approximately 6.93 for  $K$ -control testing to be a faster test when  $2a/W$  is 0.01, as shown in Fig. 9.

For a given specimen geometry and initial  $a/W$ , the number of cycles and total change in crack length is constant for tests conducted at a given normalized  $K$ -gradient. This means that for a given specimen geometry, initial  $a/W$ , and  $K$ -gradient, the amount of untested ligament increases for increasing specimen widths. If there

**FIG. 7** Domain map showing domains of test space in which  $K$ -control or constant-amplitude (CA) testing is faster for the C(T) specimen with an initial normalized crack length  $a/W = 0.2$ .

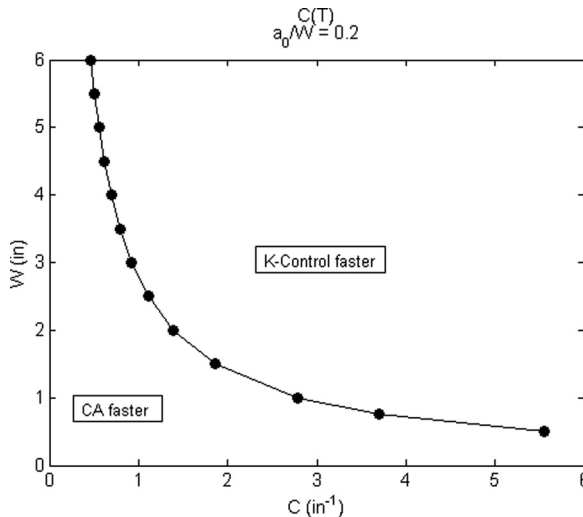


**FIG. 8** Domain map showing domains of test space in which K-control or constant-amplitude (CA) testing is faster for the M(T) specimen with an initial normalized crack length  $2a_0/W = 0.2$ .

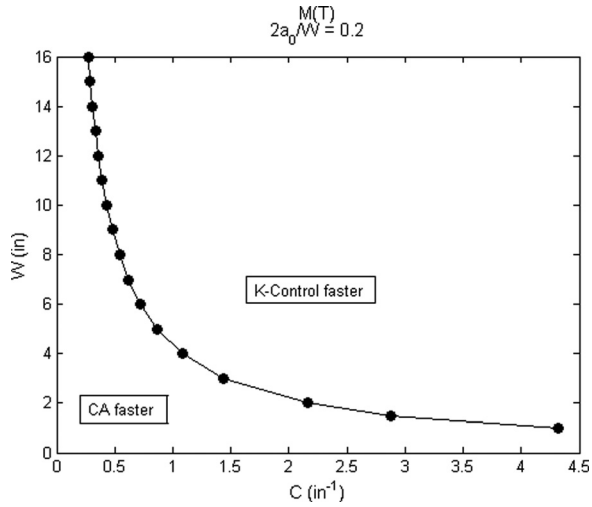
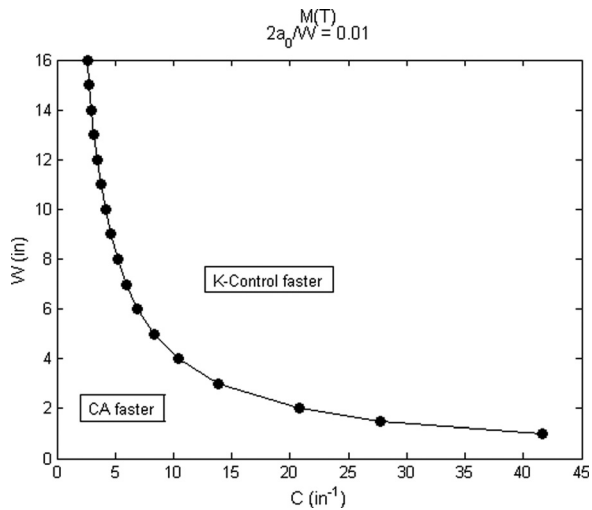


**FIG. 9** Domain map showing domains of test space in which K-control or constant-amplitude (CA) testing is faster for the M(T) specimen with an initial normalized crack length  $2a_0/W = 0.01$ .



is no physical reason why the data must be measured over a larger specimen such as the specimen being a subscale test article with inherent residual stresses representative of the actual structure, then this suggests that test specimens can be reduced in size, or that the initial notch lengths in larger test specimens can be increased. Increasing the notch length in a specimen has a number of advantages including reducing the load necessary to produce a given  $K$ , and increasing the measurability, repeatability, and accuracy of crack lengths predicted with potential difference. For  $M(T)$  panels tested in constant-amplitude, it is not uncommon for initial notch lengths to be on the order of  $a/W = 0.01$ . The prevailing wisdom from those who desire to test specimens of this geometry is that it is to one's advantage to produce a specimen with the greatest amount of possible crack ligament. This is reasonable from a constant-amplitude viewpoint, because the  $\Delta K$  range that can be measured in a single test is directly proportional to the amount of initial uncracked ligament. However, the initial notch lengths do not have to be so small in  $K$ -control tests because the parameters can be chosen so that the test covers a wider range in  $\Delta K$  by simply increasing the magnitude of the normalized  $K$  gradient. The initial notch length can often be significantly increased for a slight increase in  $C$ . This is especially significant for the  $M(T)$  specimen in which the size of the initial notch is on the order of the scale of the diameter of the drilled starter hole. In this situation, the starter hole degrades the quality of the predicted crack length with potential difference because the analytical calibration equation used to determine crack length, Johnson's Eq. [5], is a solution assuming a perfectly thin mathematical potential boundary condition at the notch. The presence of the hole modifies the current and potential fields in the vicinity of the notch and results in error when using Johnson's equation. It is not until the crack grows some multiples of the hole diameter away from the starter hole that the physical situation approaches the correct boundary conditions for Johnson's equation to be accurate. Within a paradigm of  $K$ -control, an initial crack length of  $a/W < 0.1$  is hardly ever justified, regardless of the size of the test specimen and issues of any inaccuracies caused by small starter notches are avoided. At a minimum, the normalized  $K$ -gradient should be allowed to be no less than the initial value that occurs at the start of the constant-amplitude test. If we have a  $W = 16$  in.  $M(T)$  panel with an initial crack length  $2a/W = 0.01$  with a total active probe gage length of 0.6 in., then the voltage will increase by a factor of 23 from  $2a/W = 0.01$  to 0.7. This presents a conundrum for accurate crack length measurement over the full range of the test because if the initial voltage associated with the  $2a/W = 0.01$  notch is too large then by the time the crack is at  $2a/W = 0.7$  (with a voltage 23 times the initial value) then it is likely that this voltage has then exceeded the full-scale voltage, usually 10 V, of the monitoring equipment. This means that the test operator must accept an undesirable tradeoff of accepting poor crack length measurements at the onset of the test in exchange for being able to measure the crack at all by the end of the test.

Performing a constant-amplitude test with the full use of all crack growth rate data measured over the full test duration implicitly assumes that there is no issue

with any of the normalized  $K$ -gradients that occur during that test. There is no qualifying calculation required to determine whether constant-amplitude data is valid based upon a check against a maximum allowable normalized  $K$ -gradient criterion; it is assumed that any  $C$  that occurred during the test is fully valid and results in valid data. Why then, if we accept that this maximum value of  $C$  results in valid data, is a test operator not allowed to perform the entire test at a constant value of  $C$  equal to this max value? For example, a common sample tested in the nuclear industry is a  $W = 0.75$  in., initial  $a/W = 0.2$ , C(T) sample in which case by the time the test reaches  $a/W = 0.7$  in constant-amplitude then the  $K$ -gradient is  $C = 7.11$  (1/in.). There is no requirement to report this  $K$ -gradient for a constant-amplitude test nor any consideration made for evaluating its impact on the test results. The argument must be that there should be no difference between constant-amplitude and  $K$ -control testing when the  $K$ -control test is performed at a  $K$ -gradient no greater than the maximum  $K$ -gradient that occurs naturally during constant-amplitude testing.

This argument is supported in part by the allowable  $K$ -gradients permitted for  $K$ -decreasing tests—currently a minimum of  $C = -2$  (1/in.) without any extraordinary qualification. Of course, it should be noted that the  $C = -2$  (1/in.)  $K$ -gradient came not out of any physical argument but merely from the limitation of the state of the art in fatigue crack growth automation methods at the time that it was adopted. Even so, that  $C = -2$  is permitted per ASTM E647-13 should permit us to at a minimum use the same magnitude on the  $K$ -increasing side.

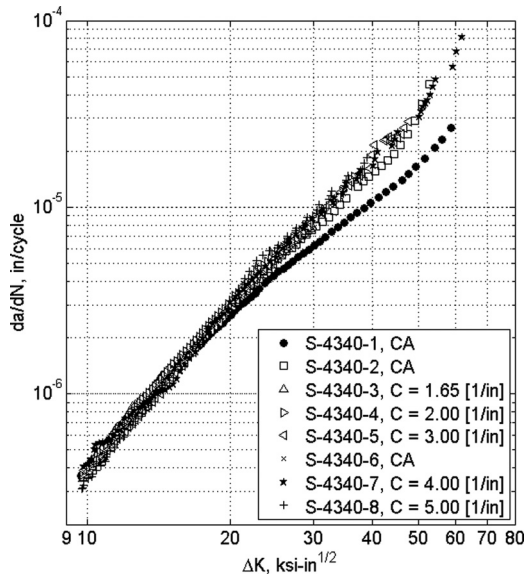
Of course,  $K$ -decreasing tests are physically distinct from  $K$ -increasing tests because the crack closure that occurs when the minimum load decreases below the crack opening load during a  $K$ -decreasing test is not expected to occur during a  $K$ -increasing test [6]. When the magnitude of the negative  $K$ -gradient is too small in  $K$ -decreasing tests, the crack may stall and result in a threshold stress-intensity factor that is artificially high relative to an effective  $\Delta K$  that is determined between  $K_{max}$  and  $K_{opening}$ .  $K$ -increasing tests, conversely, are presumed to be negligibly affected by crack closure because  $K$  always increases and the load typically increases with crack length. Assuming that the test specimen does not contain some structural feature such as a weld, a change in specimen dimensions, a known change in residual stress, or inhomogeneous material, once the load is above crack closure, there is no physical argument to oppose very steep  $K$ -gradients for increasing  $K$  testing, supposing that the data acquisition can be still maintained as adequate. In fact, remember that one principal advantage of  $K$ -control tests is that smaller test ligaments may be needed compared to constant-amplitude testing.

Smaller crack growth quantities would almost always be preferred because it stochastically avoids issues with crack deflection or bifurcation [7] as is common in alloys such as aluminum-lithium alloys or Ti-6Al-4V. When crack deflections and bifurcation occurs they at best obfuscate and at worst invalidate the test since  $K$  or  $a$  cannot as accurately be determined in those cases. Therefore, why would one want to risk a test potentially not being usable because of needlessly growing the crack over a larger length than was needed in order to generate a valid test?

## Experimental Study

The next phase of the study involved direct experimentation. Eight compact-tension C(T) 4340 steel specimens with  $W = 2.50$  in., 0.25 in. thickness  $B$ , in the L-T orientation were machined and tested at 20 Hz at  $R = 0.1$ . The material type, size, crack length dimensions, and initial crack lengths were conveniently chosen as typical and well-representative of a standard production test, but the selections were arbitrary and do not in any way affect any conclusions to be drawn from the study. The samples were removed such that the constant-amplitude and  $K$ -control test specimens were each as uniformly distributed about the parent material as possible to avoid any potential local material issues. A total of 3 constant-amplitude tests and 5  $K$ -control tests were performed. The  $K$ -control tests were performed with a constant, positive value of the normalized  $K$ -gradient with a separate test at each value of  $C = (1.65, 2.00, 3.00, 4.00, 5.00)$  (1/in.). The  $K$ -gradient of  $C = 1.65$  (1/in.) was chosen as the initial value since this was the average  $K$ -gradient that occurred during the constant-amplitude tests. This choice allowed the comparison of the two methods as directly as possible with the assumption that the data produced would be equivalent when the  $K$ -gradient used in the  $K$ -control test is equal to the average that naturally occurs

**FIG. 10** Experimental comparison of constant-amplitude to  $K$ -control testing for  $C = 1.65$  to  $5.00$  in<sup>-1</sup> in 4340 steel. Each test is shown as a separate test series. Sample S-4340-1 appears to be out of family with the rest of the data, but is the only test that could not be post-test corrected.



during the constant-amplitude test. Crack length was measured using DCPD and fatigue crack growth rates were determined by means of the secant method against the raw crack length versus time data. The test results are shown in Fig. 10. Except for sample S-4340-1, all of the data is extremely consistent and there is no observable difference between the constant-amplitude and the  $K$ -control data over the range tested. Sample S-4340-1 could not be post-test corrected for the actual final test crack length relative to the DCPD predicted crack length because the sample failed during testing before a marker band could be grown in the specimen. Given the consistency of the remaining data when a post-test correction was able to be performed on the data, this suggests that a post-test correction of the crack length is a critical step in fatigue crack growth rate testing. In the subsequent Fig. 11, sample S-4340-1 is removed from the comparison based on engineering decision that the data for S-4340-1 was not reliable as it could not be post-test corrected. Determining a best-fit linear line through the  $da/dN - \Delta K$  data for both constant-amplitude and  $K$ -control data for the 2 remaining constant-amplitude and the 5 remaining  $K$ -control samples produced  $n = 2.68$  and 2.78 from  $da/dN = C\Delta K^n$ , respectively. A zoomed-in region of the crack growth rate is shown between  $\Delta K = 10$  to 30 ksi $\sqrt{\text{in}}$  in Fig. 12, which clearly demonstrates the consistency of the constant-amplitude and  $K$ -control data. Moreover, the  $K$ -control

**FIG. 11** Experimental comparison of constant-amplitude to  $K$ -control testing for  $C = 1.65$  to  $5.00 \text{ in}^{-1}$  in 4340 steel. The constant-amplitude (2 tests) and  $K$ -control testing (5 tests) are grouped independently into a single series each to directly contrast the data for the difference in control mode.

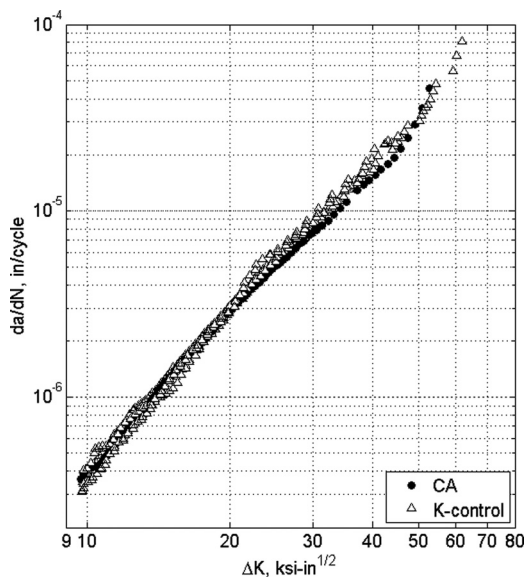
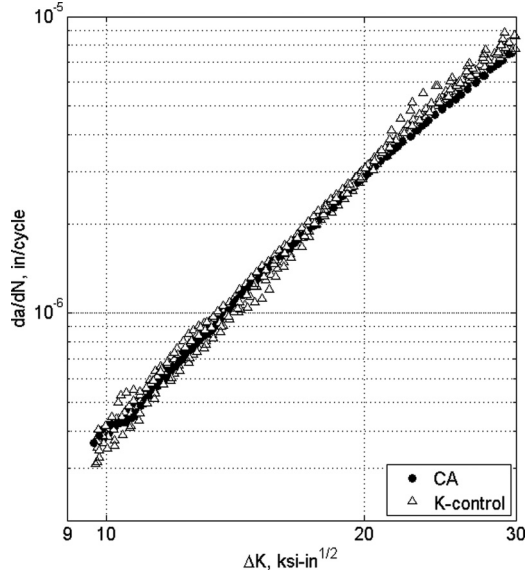


**FIG. 12** Figure 5: Experimental comparison of constant-amplitude to K-control testing for  $C = 1.65$  to  $5.00 \text{ in.}^{-1}$  in 4340 steel. The constant-amplitude (2 tests) and K-control testing (5 tests) are grouped independently into a single series each to directly contrast the control mode. The graph is zoomed into the range of  $\Delta K$  from 9 to  $30 \text{ ksi}\sqrt{\text{in}}$  in order to better highlight the similarity in the two datasets.



test at  $C = 5.00 \text{ in.}^{-1}$  saved a substantial 70 % of the test time by taking only 241 475 cycles versus 795 547 cycles for the average of the constant-amplitude tests.

These results are not surprising. Differences in the data produced from *K*-control and constant-amplitude testing would not be expected to occur based on considering fracture mechanics from first principles:  $\Delta K$  is related to the strain energy release rate in the material, which is itself related to the energy density per unit volume available for crack growth, i.e., the stress-strain hysteresis that develops during fatigue cycling. While this is so, there is one major caveat, namely, that for certain kinds of unusual cracks, there is a higher probability that *K*-control will produce erroneous results. For example, if a test specimen experiences crack growth that is not symmetrical, then the real-time crack length measurements and stress-intensity-factor calculations will be inaccurate. In such cases, the resultant loads that are calculated and targeted by the test machine during *K*-control testing would be inaccurate. While not generally done in practice or unequivocally allowed by ASTM E647-13, should such crack growth anomalies occur during constant-amplitude testing, then the raw crack length measurements could be reinterpreted in the context of the known crack path to salvage that test data. This would not generally be possible with *K*-control tests under ordinary circumstances.

## Conclusion

A methodology was developed for determining under what conditions a  $K$ -control test would be expected to be more efficient than a constant-amplitude test for C(T) and M(T) specimens. The normalized  $K$ -gradient  $C$  was shown to not be a constant during constant-amplitude tests in these specimen geometries. In many situations, assuming that the crack follows the symmetry plane and does not bifurcate, etc., then  $K$ -control appears to be preferable over constant-amplitude testing because test time is reduced, smaller specimens are needed, steep  $K$ -gradients may be avoided, and the initial crack length measurement may be improved in M(T) samples. Experimental results confirmed that there is no statistically significant difference in crack growth rate data measured in  $K$ -control or constant-amplitude testing when tests were performed on 4340 steel C(T) specimens with the normalized  $K$ -gradient  $C$  ranging over a typical range from 1.65 to 5.00  $\text{in}^{-1}$ . While this study included a limited experimental program and further research is required to make general conclusions regarding other materials, the experimentalist would often be well-served by recognizing that  $K$ -control may often be advantageous, especially when testing smaller specimens.

## References

- [1] Donald, J. K. and Schmidt, D. W., "Computer-Controlled Stress Intensity Gradient Technique for High-Rate Fatigue Crack Growth Testing," *J. Test. Eval.*, Vol. 8, No. 1, 1980, pp. 19–24.
- [2] ASTM E647-13: Standard Test Method for Measurement of Fatigue Crack Growth Rates, *Annual Book of ASTM Standards*, ASTM International, West Conshohocken, PA, 2013.
- [3] NASGRO v6.2. (2011). Southwest Research Institute, San Antonio, TX.
- [4] Adler, M. A., *NASFLA Interpolation User Experience*, Southwest Research Institute, San Antonio, TX, 2009.
- [5] Johnson, H. H., "Calibrating the Electrical Potential Method for Studying Slow Crack Growth," *Mater. Res. Stand.*, Vol. 5, No. 9, 1965, pp. 442–445.
- [6] Elber, W., "The Significance of Fatigue Crack Closure, Damage Tolerance of Aircraft Structures," *ASTM STP-486*, ASTM International, Philadelphia, PA, 1971, pp. 230–242.
- [7] McKeighan, P. C., Tabrett, C. P., and Smith, D. J., "The Influence of Crack Deflection and Bifurcation on DC Potential Drop Calibration, Special Applications and Advanced Techniques for Crack Size Determination," *ASTM-STP 1251*, J. J. Ruschau and J. K. Donald, Eds., ASTM International, Philadelphia, PA, 1995, pp. 51–66.

---

STP 1571, 2014 / available online at [www.astm.org](http://www.astm.org) / doi: 10.1520/STP157120130080

D. Dingmann,<sup>1</sup> A. White,<sup>1</sup> and T. Nickel<sup>1</sup>

# Automated Real Time Correction of Motion Induced Dynamic Load Errors in the Force Readout of a Test Apparatus

## Reference

Dingmann, D., White, A., and Nickel, T., "Automated Real Time Correction of Motion Induced Dynamic Load Errors in the Force Readout of a Test Apparatus," *Application of Automation Technology in Fatigue and Fracture Testing and Analysis*, STP 1571, Peter C. McKeighan and Arthur A. Braun, Eds., pp. 18–30, doi:10.1520/STP157120130080, ASTM International, West Conshohocken, PA 2014.<sup>2</sup>

## ABSTRACT

In mechanical testing, it is often important to understand the dynamic characteristics of the test system to assess if there could be any error in the indicated force readout induced by the motions of the system. That these errors exist is readily apparent for load sensors which are mounted on the actuator; the actuator is expected to move during the course of the test. What may be less obvious is that these errors also exist in load measurements taken on the "grounded" side of a sample. Methods have been developed (such as ASTM E467-08e1) for the assessment and correction of these errors; however, these methods can be time consuming to implement. In some cases, they may not be practical or even possible (e.g., placing strain gauges on a biological sample). Existing methods using accelerometers to predict acceleration induced load have been used for some time. What is presented are a set of approaches to increase the simplicity and reliability of using acceleration sensors to address dynamic load errors. Using various modes of stimulation of the system, software algorithms are used to assess the correct compensation factors to use for both magnitude and phase of the acceleration signal, as a function of frequency. This has the additional benefit of allowing the use of load and acceleration sensors

---

Manuscript received May 21, 2013; accepted for publication June 27, 2014; published online August 29, 2014.

<sup>1</sup>Bose ElectroForce Systems Group, Bose Corporation, Eden Prairie, MN, 55344.

<sup>2</sup>ASTM Sixth Symposium on *Application of Automation Technology in Fatigue and Fracture Testing and Analysis* on May 23, 2013 in Indianapolis, IN.

which may not be ideally phase matched. These methods also allow stimulation of both motor mounted load sensors as well as frame mounted sensors.

## Nomenclature

$b_c$  = damping coefficient of the load sensor

$b_f$  = damping coefficient of the frame

$b_g$  = damping coefficient of the frame support structure

$b_s$  = damping coefficient of the sample

$F_a$  = system applied force (actuator)

$F_c$  = forces on the load sensor

$F_e$  = force measurement error (dynamic)

$F_s$  = forces on the sample

$k_c$  = stiffness coefficient of the load sensor

$k_f$  = stiffness coefficient of the frame

$k_g$  = stiffness coefficient of the frame support structure

$k_s$  = stiffness coefficient of the sample

$m_e$  = the mass which induces the dynamic load error (effective mass supported by the load sensor)

$m_f$  = the mass of the fixture attaching the sample to the load sensor

$m_s$  = the mass of the sample

$x_c$  = displacement of the load sensor

$x_f$  = displacement within the test system frame

$x_g$  = displacement of the test system frame with respect to ground

$x_s$  = displacement of the sample

$\phi$  = the phase offset of the acceleration signal from the load signal

## Introduction

When making load measurements on a dynamic material testing machine, one of the primary sources of error is acceleration induced forces. These forces are the load sensor's response to the real forces induced by motion of the load sensor. Obviously, motion is induced in load sensors that are attached to the output shaft of the testing system; however, any grounded sensor is also subject to motion, albeit of a smaller magnitude. This is due to vibrations within the frame and its supporting structure. These vibrations can be due to the operation of the testing machine or may be induced in the system from its environment.

While these forces are real, they exist within the load sensing system and are not loads on the sample; they are simply the forces involved in accelerating the mass attached to the load-sensing element. As these loads are measured, but do not reflect actual load supported across the sample, they can be a significant source of error in the measurement of dynamic loads.

## Basic Theory and Mitigation

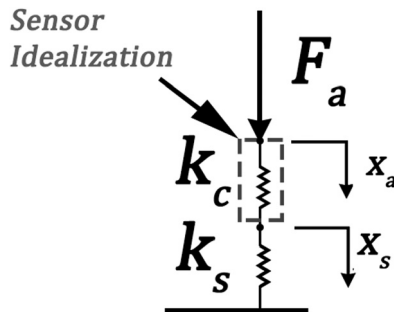
The issue of dynamic load errors is typically best illustrated for test cases where the load sensor is attached to the actuator of the test system, as the test intentionally induces motion of the load sensor. **Figure 1** shows an idealized diagram for this case. In this ideal (i.e., zero-mass) case, the forces acting on the sensor (represented as the dashed box) are the actuator force on one side,  $F_a$ , and the reaction force from the sample on the other side,  $F_s$  (Eq 1). This results in a (typically very small) relative deflection,  $x_c$  (Eq 2); for an ideal sensor this deflection is proportional to the applied force (Eq 3—note: this term applies to the measured load; the sign of this equation was chosen to define tension as positive). In a similar fashion, the force on an ideal elastic sample is proportional to the deflection of the sample (Eq 4).

$$\begin{aligned}
 (1) \quad \sum_c^F &= F_s + F_a \\
 (2) \quad x_c &= x_s - x_a \\
 (3) \quad F_c &= x_c k_c \\
 (4) \quad F_s &= -x_s k_s
 \end{aligned}$$

For any real test, there are masses associated with the load sensor, sample, and fixtures. As all of these elements are moving during a dynamic test, there is an associated force term based on the acceleration of the moving masses [1]. The force term,  $F_e$ , experienced by the load sensor can be estimated from Newton's second law, applied to the effective mass ( $m_e$ ) acting on the load sensor. The measured load error is due to the acceleration of the mass attached to the active element of the load sensor. This corresponds to the point where the active element of the sensor attaches to the sample, which is here defined as  $x_s$  (Eq 5).

From the point of view of measuring forces on the sample then, these forces are an error term ( $F_e$ ) that must be identified and minimized (Eq 6).

**FIG. 1** Idealization of a frame mounted load sensor and sample.



$$(5) \quad F_e = m_e \ddot{x}_s$$

$$(6) \quad \sum_c^F = F_s + F_a + F_e = -x_s k_s + F_a + m_e \ddot{x}_s$$

Methods and practices already exist for mitigating, assessing, and correcting these errors using various methods:

1. Mitigation (reduce motion of the sensor)
  - (a) Selection of sensor location (i.e., grounded, rather than mounted to the system actuator)
  - (b) System design (appropriately stiff and massive frame and supporting structure)
2. Error assessment and correction
  - (a) Test a strain gauged sample to provide a reference load signal to compare with the load measurement from the system sensor [2].
  - (b) Taking an acceleration measurement of the load sensor and using this to compute the load error based on Newton's Second Law of Motion.

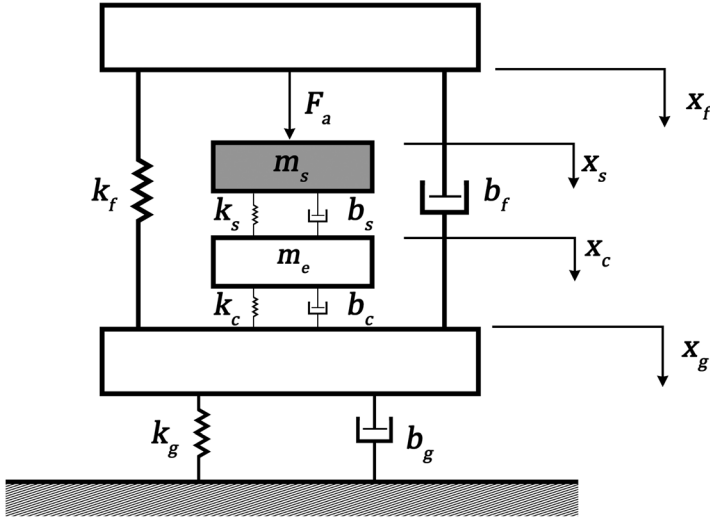
Clearly, sound system design is critically important, but it cannot eliminate all vibration of the load sensor. In addition, cases exist where a load sensor must be mounted on the actuator for reasons of practicality. In these cases, dynamic errors cannot be significantly minimized mechanically, and so assessment and correction becomes critical. Finally, since some samples are not appropriate for strain gauging (e.g., biologic samples), the best remaining option is to use acceleration measurements to estimate and correct these errors. It is for these cases that the methods discussed in this paper are focused.

## Dynamic Load Errors—Examples

There are two general locations for mounting a load sensor within a dynamic test system: either mounted to the actuator as shown above, or grounded to the frame. As already mentioned, the reason behind dynamic load errors for an actuator-mounted sensor is fairly easy to understand. For the grounded sensor case, the causes are less obvious and the errors are typically lower in magnitude; however, they can still be significant.

**Figure 2** shows a spring-mass-damper model for a frame mounted load sensor. Looking at this case, the equations need to be written slightly differently. Here, the output of the load sensor is defined as in Eq 7 (tension is defined as positive), again assuming a sensor whose output is proportional to its deflection; the dynamic load error,  $F_e$ , would be defined as the effective mass,  $m_e$ , subject to the motion of the active sensor element,  $x_c$  (Eq 8). When viewed in this form, one can see that vibration in any of these elements can and will result in some level of dynamic load error. The severity of this will depend on the relative stiffness and mass of the supporting elements (e.g., the load frame and the supporting structure).

FIG. 2 Frame mounted load sensors.



$$(7) \quad F_c = (x_g - x_c)k_c$$

$$(8) \quad F_e = m_e \ddot{x}_c$$

For the case of an actuator mounted load sensor, Eqs 9 and 10 show the theoretical acceleration [10] for a sinusoidal displacement [9].

$$(9) \quad x = A \sin(2\pi ft + \Phi)$$

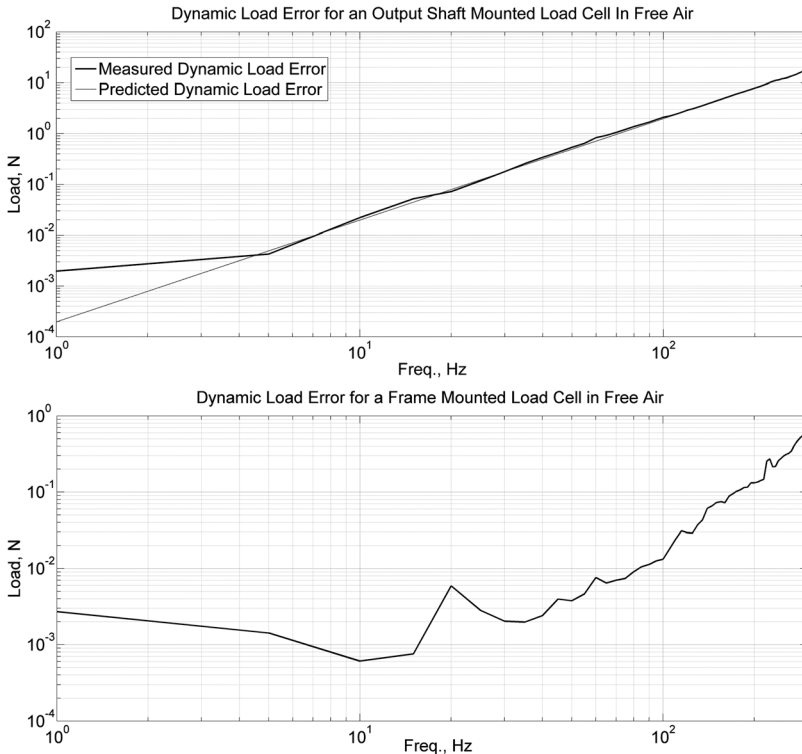
$$(10) \quad \ddot{x} = A(2\pi f)^2 \sin(2\pi ft + \Phi)$$

The top plot of Fig. 3 shows the measured load for a series of tests run with an output shaft mounted load sensor, with no sample in place. The waveform was a 40  $\mu\text{m}$  amplitude sine wave run for a series of frequencies between 1 and 300 Hz with a 125 g fixture attached to the load sensor. Without a sample in place, the measured load was assumed to be dominated by dynamic load error; as the maximum deviation from the theoretical values was on the order of 3 %, this was considered a reasonable assumption.

The bottom plot of Fig. 3 shows the measured load for a frame mounted load sensor for the same set of test conditions. Here it can be seen that the load error function would not be particularly well fitted by a 2nd order function of frequency because the frame and its supporting table have a non-uniform frequency response in the range of test frequencies.

As an example, it would not be unreasonable for a test using the defined waveform to be performed on a sample with a stiffness of 40 N/mm. As this would result

**FIG. 3** Top: output shaft mounted load sensor: amplitude of dynamic load errors as a function of frequency for a constant displacement amplitude sinusoidal input. Bottom: frame mounted load sensor: amplitude of dynamic load errors as a function of frequency for a constant displacement amplitude sinusoidal input.



in expected peak sample forces on the order of 1.6 N, the predicted load errors shown are significant. In the output shaft mounted sensor case, the error could be nearly an order of magnitude larger than the load to be measured. Even for the case of the frame-mounted sensor, the dynamic error could be between 6 and 38 % of the load to be measured.

## Acceleration Measurement From a Displacement Sensor

From the data shown, dynamic load errors for load sensors mounted on the output shaft of a dynamic test system are primarily due to the prescribed motion of the output shaft. Accelerometers have long been used to provide a source for an acceleration signal to estimate and compensate dynamic load errors in real time. However, as can be seen from Eqs 9 and 10, theoretically if one can measure

displacement as a function of time, then acceleration can be computed for an output shaft mounted load sensor. A note should be made that, while this is theoretically true, it may not prove to be so in practice. This is for the same reasons that dynamic load error for a grounded load cell will not be zero: the entire frame of reference of the displacement sensor (i.e., the frame) may move relative to ground. The displacement sensor can only measure displacement relative to the frame, and so can only compute accelerations relative to the frame; if the entire frame moves there will still be a dynamic load induced on the sensor, but a displacement based acceleration signal will not be able to detect or correct for it. In most cases, the actuator induced motion will be much more significant than frame motion in inducing dynamic errors.

When it is possible to do so, there are several reasons to pursue this approach:

1. It uses an existing sensor which simplifies the system, reducing the number of potential points of failure, e.g., cable fatigue of moving accelerometers.
2. No additional sensor needs to be placed in the load path, which had several advantages:
  - (a) An additional sensor and its supporting fixture can negatively affect the stiffness and, therefore, the dynamic response of the system.
  - (b) Adding sensor and fixture mass can lower the resonant frequency of the load measuring system due to increased mass on the load sensor spring element. This can increase dynamic load errors and reduce the frequency bandwidth of the measurement system.

In addition, adding hardware to the load path will decrease the available test space of the system.

To make this possible requires taking a numerical derivative of the displacement signal. While doing this is a relatively simple procedure, it can be problematic in practice. Estimation of the derivative of a real signal will accentuate any noise present, and this will only be compounded when producing a 2nd derivative estimation. While this can be improved by using digital filters that attenuate high frequency noise to produce the acceleration signal, it still requires a very low noise input signal. [Figure 4](#) shows the basic block diagram of the signal processing steps to produce the acceleration signal. In the example, two separate filter steps are shown;

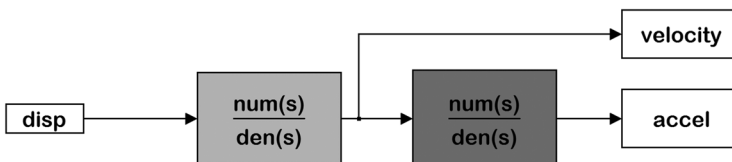


**FIG. 4** Block diagram of numerical derivative filter.

this allows velocity to be computed separately, if that is desired. If only acceleration is required, a single filter stage can be designed to produce the acceleration signal.

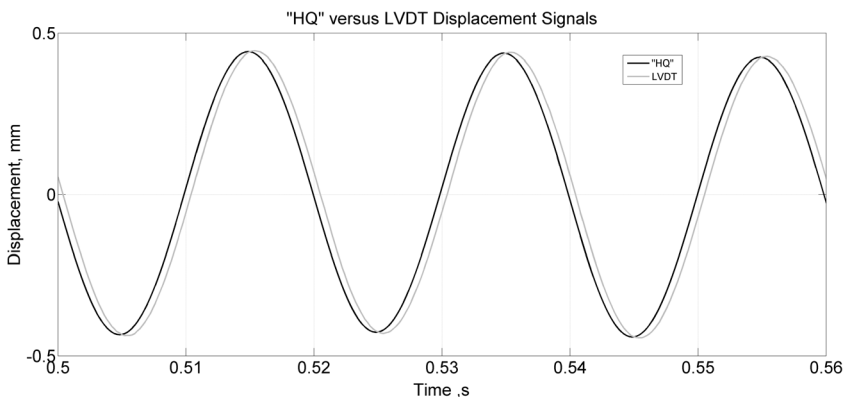
However, even given well designed signal processing, any noise present in the original displacement signal will be amplified. In order to produce a useful acceleration signal, there are three requirements:

1. High resolution (digital): due to the stepwise nature of digital signals, insufficient resolution in the signal will have the effect of increasing the minimum noise floor of the differential signal
2. Low noise: to minimize the amount of noise amplification due to the signal differentiation so that the output signal is of useful quality.
3. Low latency: the differentiation filter adds some latency; use of a low latency input signal makes it possible to filter the signal and still phase match it with the load sensor, while still producing a real-time signal.

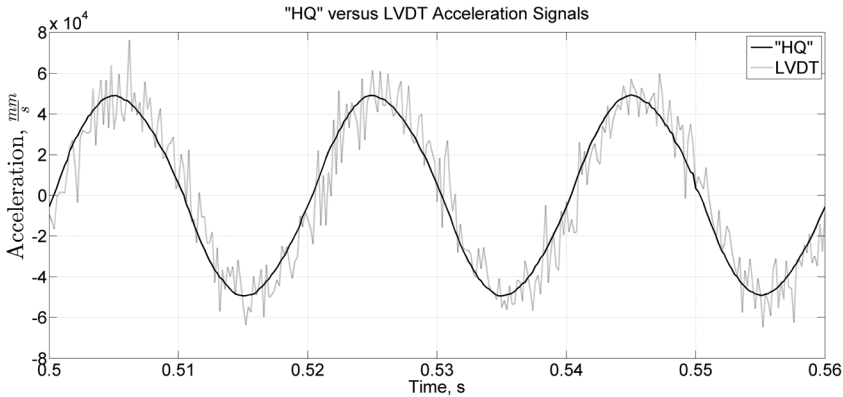
Figures 5 and 6 show the results from a sensor with suitable signal qualities, labeled the "HQ" (High Quality) sensor; it is compared with an instrument grade linear variable differential transformer (LVDT) signal. For both these examples, the acceleration signal was produced via a double differentiation filter that begins to roll off above 1000 Hz. The difference in the quality of the acceleration signals produced is pronounced. Due to the improved signal qualities, the THD+N of the acceleration signal computed from the HQ sensor only increased by about 13 % compared to the displacement signal. This is in contrast to an increase of approximately 1000 % for the LVDT based acceleration signal.

Table 1 shows the level of dynamic load error reduction that can be realized with this method, compared to the results for a standard accelerometer. The load error reduction is on par with the accelerometer method, but with the advantages listed above. In this case, the accelerometer used was a variable capacitance sensor design. The test waveform was a 1 mm amplitude sine wave at 60 Hz; attached mass was 110 g.

FIG. 5 High resolution, low noise sensor versus LVDT displacement signals.



**FIG. 6** High resolution, low noise sensor-based versus LVDT-based acceleration signals.



**TABLE 1** Comparison of Accelerometer and Computed Acceleration compensation.

Test Case	Measured Load Amplitude (Error)	% Reduction
Raw signal	16.6 N	—
Accelerometer Based Compensation	0.6 N	96.4 %
HQ Based Compensation	0.4 N	97.6 %

## Equipment Used

For the above section of the paper, the “HQ” sensor used was a HADS (High Accuracy Displacement Sensor) on a Bose ElectroForce Systems Group 3230 Test System.

## Automation of Acceleration Compensation

Whether the acceleration signal comes from a traditional acceleration sensor or is generated from the displacement sensor, the goals are the same: to both estimate the dynamic load error and then compensate it out. Again, based on Eq 5, the remaining term that needs to be determined to estimate dynamic load error is the mass term ( $m_e$ ).

Theoretically, this term is defined as the effective mass supported by the load sensor, and can be approximated as:

$$(11) \quad m_e \cong \frac{m_s}{2} + m_f$$

The mass of the sample and the supporting fixtures can be measured and can be used directly. However, for real systems, the sensor response typically has a

dependence on frequency that will introduce errors. In addition, any difference in the phasing of the acceleration and load signals will also bound the lower limit for the error term  $F_e$ ; this can be quite significant (see Fig. 7).

The goal of the method described is to simplify the process of assessing and correcting these sources of error, automating as much of the process as possible. In addition, the desire is for a solution which works regardless of where the load sensor is located.

By assessing the dynamics of the load and acceleration responses of the actual system and sensors, filters can be created that estimate the effective mass as a computed gain term. In extreme cases where the response of either the load or acceleration signals is not constant with frequency, this gain term could be computed as a function of frequency.

In practice, this assessment is made by stimulating the system with the system actuator, without an intact sample in place. All fixtures are installed and a mass representing  $1/2$  a sample is mounted to the load sensor. For this system, the load supported by the sample is known to be zero as the sample is not intact, so it is reasonable to approximate any measured load to be due to dynamic load errors. The method can be used with either an output shaft or frame mounted load sensor. The stimulation can be a series of individual displacement sine waves of one or more frequencies, or it could be done with a broadband noise signal.

In either case, the transfer function of load error to acceleration is computed where load error is assumed to be equal to the load signal. In the ideal case, this transfer function would be a constant equal to  $m_e$  (effective mass on the load cell), in practice both the magnitude and phase of this transfer function is a function of frequency. Based on this transfer function, a best-fit gain term is computed, as is

**FIG. 7** Theoretical residual dynamic load error due purely to 0.5 ms time delay between load and acceleration signals (2.5 mm amplitude sine wave, 0.11 kg attached load).

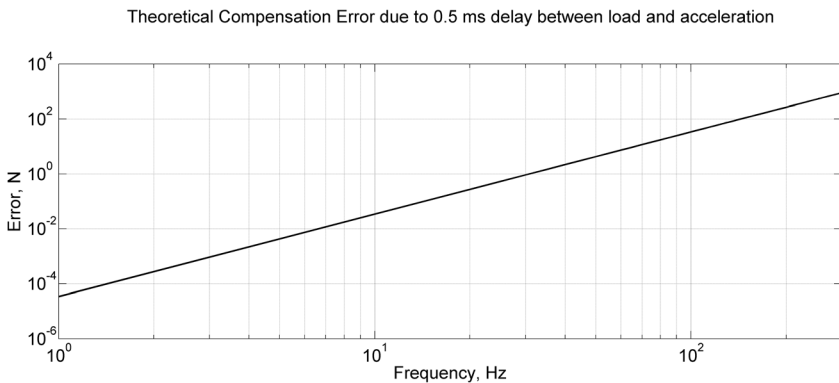
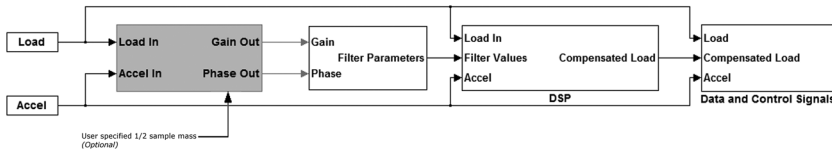


**FIG. 8** Block diagram of the automated compensation scheme. Section in dashed box is run during test set up, without an intact sample in place, to assess the gain and phase relationship between load and acceleration signals.



the appropriate phase delay to match the phase between the load and acceleration signals (note: this phase delay can be applied to either the load or acceleration signal, depending on which is the lagging signal). This gain and phase information is used to create a digital filter to be applied to the acceleration signal. Once this filter is created, the sum of the new filtered acceleration signal and the load channel are reported as the compensated load.

For cases where it is not practical to mount half a sample to the grips, a measured sample mass can be input into the computation by the user. Some examples where this could be required are biologic samples, or purely compression tests where it might be challenging to cut a sample in half and then find a way to bond it to a platen.

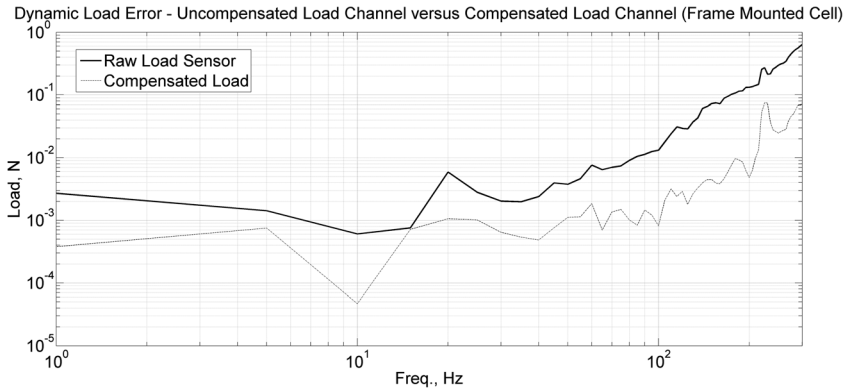
As these filters are being created, the terms of the filter can be calculated so as to match the phase between the acceleration and the load sensors. Figure 8 shows the basic system steps for this method. The result is improved dynamic load error estimation and compensation (Table 2).

This method allows for error estimation and compensation for load sensor that is straightforward for any user to implement, as the entire process is automated. This automated process can be used for output shaft mounted load sensors, as well as frame mounted sensors. For frame mounted sensors, an accelerometer must be

**TABLE 2** Comparison of non-compensated signal, a non-phase matched signal and the compensated sample load, from simulation; 10 N/mm sample, 2.5 mm amplitude sine wave, 100 Hz, 2° Phase offset.

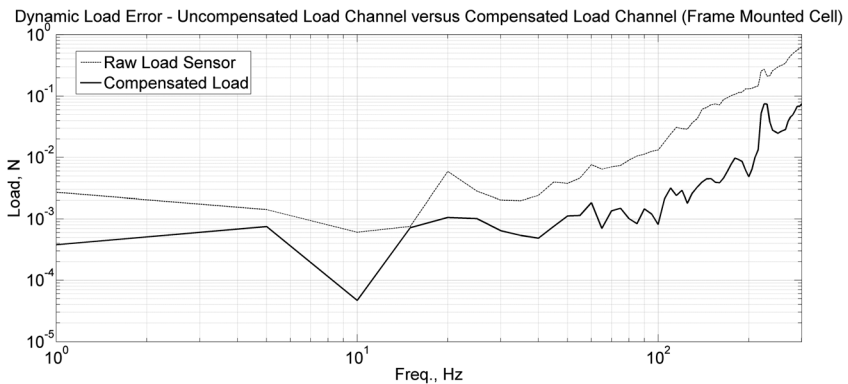
Test Case	Measured Load Amplitude (Error)	Error, % of Measurement
Uncompensated Load	98.18 N	293.51 %
Non-Phased Matched Compensation	25.29 N	1.36 %
HQ Based Compensation	24.95 N	—

**FIG. 9** Peak load error as a function of frequency, for compensated and uncompensated signals. Test conditions: output shaft mounted load sensor, 110 g mass on the load sensor (includes grip and  $1/2$  sample), 0.040 mm amplitude sine wave run at each frequency. Sample was not intact; any measured load amplitude was estimated to be due to dynamic error.



used, but for output shaft mounted sensors, the displacement derived acceleration can be used. For critical use cases, this prepares the investigator for full implementation of ASTM E467 [2]; for others, the user will have greatly minimized the dynamic load error and can better estimate the level of error present in their test

**FIG. 10** Peak load error as a function of frequency, for compensated and uncompensated signals. Test conditions: frame mounted load sensor, 110 g mass on the load sensor (includes grip and  $1/2$  sample), 0.040 mm amplitude sine wave run at each frequency. Sample was not intact; any measured load amplitude was estimated to be due to dynamic error.



results. [Figures 9](#) and [10](#) show the magnitude of reduction in load errors that have been realized using this automated routine for both output shaft and frame mounted load sensors.

## Conclusion

For dynamic testing systems, load errors due to the motion of the load sensor can easily be significant in magnitude, and not just for load sensors mounted to the output shaft of the system actuator. It is important to be able to both estimate this error and minimize it. While this can be done using current methods, it can be challenging in some applications. By using the methods described here, a user can simplify the process of estimating load errors, and viewing compensated data in real-time, during a test. While these methods will not fully satisfy all aspects of ASTM [E467 \[2\]](#), in and of themselves, they should simplify the process of doing so. For load sensors mounted to the output shaft of the actuator, this can be done without requiring an additional sensor. For frame mounted sensors, load errors due to vibration of the frame can be reduced, which can be important for low force applications. In all cases, the compensation parameters can be set automatically by the test system based on data from a quick and simple pre-test characterization.

## References

- [1] Ogata, K., *Systems Dynamics*, 2nd ed., Prentice Hall, Englewood Cliffs, NJ, 1992.
- [2] ASTM [E467-08e1](#): Standard Practice for Verification of Constant Amplitude Dynamic Forces in an Axial Fatigue Testing System, *Annual Book of ASTM Standards*, ASTM International, West Conshohocken, PA, 2008.

---

STP 1571, 2014 / available online at [www.astm.org](http://www.astm.org) / doi: 10.1520/STP157120130062

Phillip A. Allen<sup>1</sup> and Douglas N. Wells<sup>2</sup>

# Application of Automation Methods for Nonlinear Fracture Test Analysis

## Reference

Allen Phillip A., and Wells, Douglas N., "Application of Automation Methods for Nonlinear Fracture Test Analysis," *Application of Automation Technology in Fatigue and Fracture Testing and Analysis*, STP 1571, Peter C. McKeighan and Arthur A. Braun, Eds., pp. 31-49, doi:10.1520/STP157120130062, ASTM International, West Conshohocken, PA 2014.<sup>3</sup>

## Abstract

As fracture mechanics material testing evolves, the governing test standards continue to be refined to better reflect the latest understanding of the physics of the fracture processes involved. The traditional format of ASTM fracture testing standards, utilizing equations expressed directly in the text of the standard to assess the experimental result, is self-limiting in the complexity that can be reasonably captured. The use of automated analysis techniques to draw upon a rich, detailed solution database for assessing fracture mechanics tests provides a foundation for a new approach to testing standards that enables routine users to obtain highly reliable assessments of tests involving complex, non-linear fracture behavior. Herein, the case for automating the analysis of tests of surface cracks in tension in the elastic-plastic regime is utilized as an example of how such a database can be generated and implemented for use in the ASTM standards framework. The presented approach forms a bridge between the equation-based fracture testing standards of today and the next generation of standards solving complex problems through analysis automation.

---

Manuscript received April 29, 2013; accepted for publication November 25, 2013; published online April 30, 2014.

<sup>1</sup>Materials and Process Laboratory, NASA Marshall Space Flight Center, MSFC AL, 35812, United States of America (Corresponding author).

<sup>2</sup>Materials and Process Laboratory, NASA Marshall Space Flight Center, MSFC AL, 35812, United States of America.

<sup>3</sup>ASTM Sixth Symposium on *Application of Automation Technology in Fatigue and Fracture Testing and Analysis* on May 23, 2013 in Indianapolis, IN.

### Keywords

nonlinear analysis, analysis automation, elastic-plastic, surface crack,  $J$ -integral, nonlinear fracture, test standard

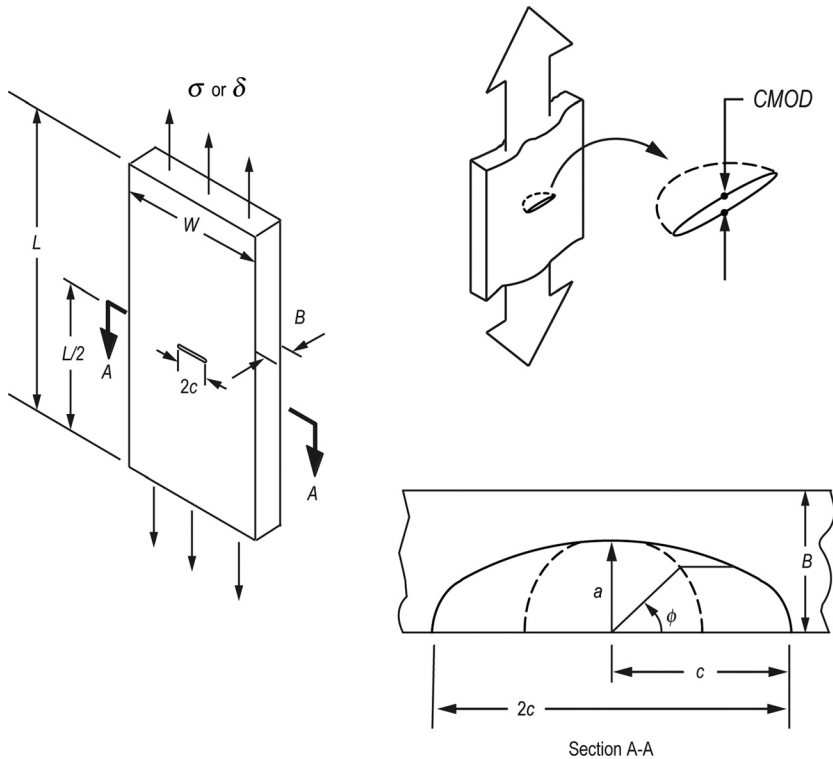
## Introduction

Mechanical test standards are intended to enable users to test materials in a controlled and consistent manner to evaluate a material property repeatably from one laboratory to another. In the realm of fracture toughness test standards, the test methods take a complicated physical process, the fracture of materials, and distill it through fracture mechanics principles to single material property—the fracture toughness. This is not a trivial task due to the complex nature of the fracture process and the wide range of applicable material types with their various associated fracture mechanisms. As the fracture mechanics community develops further understanding of the detailed mechanics of fracture processes, the authors of fracture mechanics testing standards struggle with two, sometimes opposing, goals: (1) creating test standards that accurately reflect the physics of the problem and consistently produce the “most correct” answers, and (2) creating test standards that are not overly complex and burdensome for the user. Ideally both of these goals would be achieved: fracture mechanics test standards could capture and explain the physics of the problem, while not being arduous to use or require particularly unique expertise to execute reliably.

All of the current ASTM fracture (3D) testing standards such as E399 [1] and E1820 [2] take the three-dimensional reality of the fracture test and, through the use of various assumptions, simplify the problem to a two-dimensional planar form to report an average fracture toughness representing the entire crack front. In general, the simplifications required to reduce all the relations needed to evaluate the fracture mechanics test into a tractable form for conveyance in print limits the ability to accommodate heightened complexity, such as multiple forms of non-linearity. For example, E1820 addresses material plasticity through the use of  $\eta_{pl}$  factors to calculate the plastic portion of the  $J$ -integral, but does not address the through-thickness nonlinear variation of the crack front  $J$ -integral values. These simplifying assumptions are not inappropriate; in fact, they allow standards to provide manageable equations for the calculation of toughness values that are reasonable engineering approximations of the actual 3D problem. However, the current framework of test standards requiring this level of distillation of the solution clearly limits the scope of test complexity that can be accommodated.

As more complicated fracture toughness tests are considered for standardization, it may not be practical or desirable to reduce the fracture toughness test analysis down to a simple equation form. Consider the difficulties that arise in assessing laboratory fracture toughness tests with surface cracks (see Fig. 1). In these tests, due to practical specimen size limitations, the material fracture toughness is commonly

**FIG. 1** Illustration of a semi-elliptical surface crack in a flat plate.



not reached until well beyond the linear-elastic fracture mechanics (LEFM) limit. In addition, the surface crack toughness test is highly three-dimensional with a crack driving force that varies nonlinearly along the crack perimeter. The advance of surface crack fracture testing is hindered significantly by the lack of a readily available set of solutions to correlate the applied force and observed crack mouth opening displacement (*CMOD*) in a surface crack experiment to an evaluation of the elastic-plastic *J*-integral or deformation state of a test specimen at fracture. Currently, the only practical way to fully analyze such a test is through the use of elastic-plastic finite element analysis (FEA). A convenient and practical set of elastic-plastic surface crack solutions could help mitigate many of these obstacles; however, to date, it has proven impractical to reduce the 3D elastic-plastic surface crack solution to a set of equations suitable for inclusion in a testing standard. Herein, the authors utilize the surface crack example to illustrate the use of analysis automation to offer a solution to this dilemma and argue for a new generation of test standards based on more advanced, automated methods of test analysis.

In the years prior to the advent of routine finite element based fracture mechanics analysis, many researchers provided alternative and robust engineering solutions to the elastic-plastic surface crack problem, though subject to many practical limitations. An excellent summary of the development of elastic-plastic  $J$ -integral solutions up to the year 1999 is given by McClung et al. [3]. Apart from FEA, the commonly used methods for calculating elastic-plastic  $J$ -integral solutions usually follow one of two basic techniques [4]: the Electric Power Research Institute (EPRI) approach [5–7] or the reference stress method (RSM) [8]. The EPRI and RSM techniques have found wide application in analysis of structures, but have limited application in the detailed assessment of surface crack laboratory tests. Understanding the crack tip conditions at the point the fracture toughness is reached in an experimental surface crack test requires knowledge of the specimen geometry, the applied force,  $P$ , the resulting  $CMOD$  response, the elastic-plastic flow properties of the material, and a corresponding solution for the  $J$ -integral versus  $\phi$  relationship as it evolves with increasing specimen deformation. The current RSM and EPRI solutions for surface cracks do not provide the user with the full  $P$  versus  $CMOD$  trace which serves as the most fundamental connection between experiment and analysis. The measured  $CMOD$  value provides the most robust predictor of the  $J$ -integral values at the crack tip [4,9]. In addition, most of the current RSM and EPRI solutions only provide results at a limited number of crack perimeter  $\phi$  locations and have  $J$  versus  $\phi$  relationships that are based on either linear-elastic solutions (RSM) or fully plastic solutions (EPRI), neither of which capture the changes in the  $J$  versus  $\phi$  distribution and maximum  $J$ -integral location as elastic-plastic deformation increases.

Working within an ASTM task group, the authors have developed a new surface crack testing standard, E2899-13 [10]. E2899 provides mandatory equations (Newman–Raju Equations [11,12]) for solutions within the linear-elastic regime, but requires the use of an independent FEA for test evaluations in the elastic-plastic regime. E2899 is the first ASTM fracture mechanics testing standard allowing a test result to be obtained from a method other than standardized equations codified in print. Although both flexible and enabling in scope, this method for evaluating an elastic-plastic surface crack test result requires a unique and time-consuming FEA for each test. While elastic-plastic fracture mechanics (EPFM) assessment of surface cracks has become significantly more accessible through improved finite element interfaces such as FEACrack [13] or ABAQUS CAE [14], the cost of such assessments in analysis time, code licensing, and requisite user expertise remain, unfortunately, a significant impediment to common use.

With the advent of today's computing power and inexpensive data storage, an alternative method for providing a solution to a complex mechanics problem is to pre-solve the solution space and provide a method for interpolating to the correct solution through automated analytical methods. A fracture mechanics test, even a complicated one such as the elastic-plastic surface crack test, is a bounded problem based on the practical limitations of specimen geometries, engineering material

properties, and defined loading conditions. In addition, an automated method for interpolating between pre-solved solutions eliminates the need for the user to interpret and program the equations from the standard and, thereby, should result in a more reliably “standard” answer for the test. The methodology of pre-solving the problem and interpolating to an answer allows the common user to get a high fidelity solution that captures the latest understanding in the physics of the problem without the restrictions and distillations associated with equations. This methodology directly utilizes the 3D FEA solutions, avoiding the need to fit numerous nonlinear equations to the solution space and the loss of fidelity that usually accompanies such multi-dimensional fits. This approach forms a bridge between the equation-based ASTM fracture testing standards of today and the next generation of standards for complex problems.

As an example of a pre-solved solution methodology, this paper briefly describes a simple and robust method developed by the authors for analyzing surface crack tension tests based on an array of 600, 3D nonlinear finite element models for surface cracks in flat plates under tension loading. The solution space covers a wide range of crack geometric parameters and material properties. The solution of this large array of nonlinear models was made practical by computer routines that automate the process of building the finite element models, running the nonlinear analyses, post-processing model results, and compiling and organizing the solution results into multi-dimensional arrays. The authors have developed a methodology for interpolating between the geometric and material property variables that allows the user to estimate the  $J$ -integral solution around the surface crack perimeter ( $\phi$ ) as a function of loading condition from the linear-elastic regime continuously through the fully elastic-plastic regime. In addition to the  $J$ -integral solution, the complete force versus  $CMOD$  record is estimated to provide a direct anchor to the experimental result. The user of this interpolated solution space need only know the crack and plate geometry and the basic material flow properties to reliably evaluate the full surface crack  $J$ -integral and force versus  $CMOD$  solution; thus, a solution can be obtained very rapidly by users without elastic-plastic fracture mechanics finite element modeling experience. The solution method has been incorporated into a computer program, Tool for Analysis of Surface Cracks (TASC), with a graphical user interface (GUI), to allow easy access to the solution space.

### **SURFACE CRACK SOLUTION PROCEDURES**

The process of building the new space of surface crack solutions was logistically intense. Though computationally each part of the process followed mostly well established paths, combining those parts effectively into a functional whole required planning at every level. This section provides a brief summary of the solution space and methods. Details of the computational procedures and solution verifications are given in NASA/TP-2013-217480 [15]. The logistics of building, executing, and then assembling the solution space was made practical only through automation.

### Solution Space

The solution space for this array of models is four-dimensional. Two dimensions are used to describe surface crack geometric variation, and two dimensions are used to describe material property variation. The material and geometric spaces were carefully crafted to provide sufficient coverage for most common engineering problems without becoming so large as to be intractable. The following sections summarize the choices and reasoning for the material and geometric dimensions of the solution space.

*Material Space.* Using a linear then power law (LPPL) representation of the stress-strain response defined by

$$\frac{\varepsilon}{\varepsilon_{ys}} = \frac{\sigma}{\sigma_{ys}} \quad \varepsilon \leq \varepsilon_{ys}; \quad \frac{\varepsilon}{\varepsilon_{ys}} = \left( \frac{\sigma}{\sigma_{ys}} \right)^n \quad \varepsilon > \varepsilon_{ys} \quad (1)$$

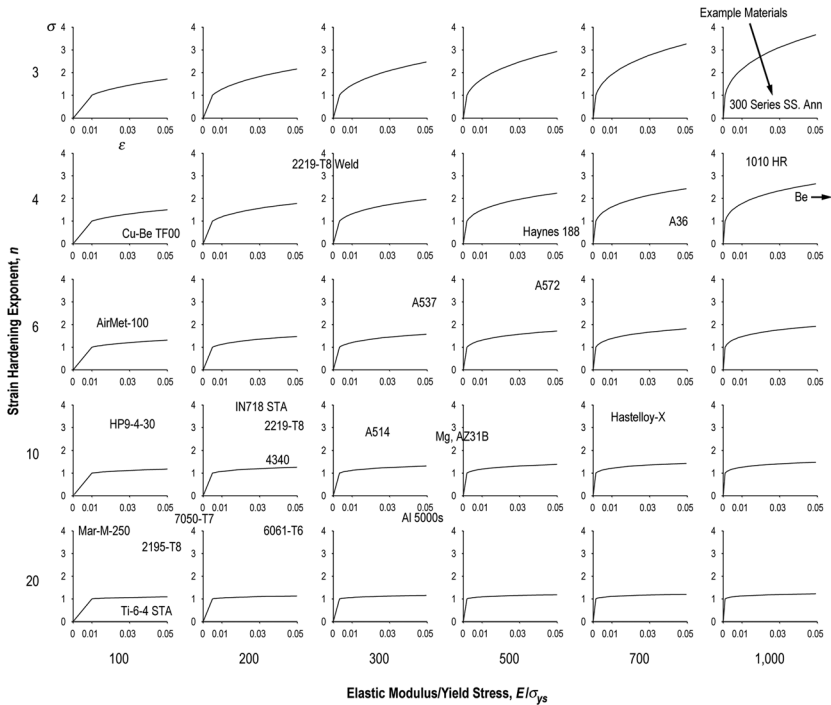
the material response can be fully defined by just 3 parameters:  $\sigma_{ys}$ ,  $\varepsilon_{ys}$  (or  $E$ ), and  $n$ , where  $\sigma_{ys}$  is a representative a yield stress, and  $\varepsilon_{ys}$  a corresponding yield strain defined by  $\varepsilon_{ys} = \sigma_{ys} / E$ , with the elastic modulus,  $E$ , and  $n$  is the strain hardening exponent. If the yield strength is normalized to unity for all materials ( $\sigma_{ys} = 1$ ), then only  $\varepsilon_{ys}$  and  $n$  are required to define the shape of the stress-strain curve throughout the space. For convenience of eliminating small fractional numbers, the reciprocal of the yield strain is commonly used,  $E/\sigma_{ys}$ .

**Figure 2** illustrates the material space for the study described in terms of the six  $E/\sigma_{ys}$  and five  $n$  values resulting in thirty different material combinations. In all cases,  $\sigma_{ys} = 1$  and Poisson's ratio,  $\nu = 0.30$ . The names of several common engineering materials are overlaid on the material matrix in **Fig. 2** to illustrate how some common materials are represented in the material matrix. The low  $E/\sigma_{ys}$  values of 100 to 200 are materials capable of high values of elastic strain; thus they have low elastic modulus and relatively high yield strength, such as many high performance titanium and aluminum alloys. The opposite end of the  $E/\sigma_{ys}$  space with values of  $E/\sigma_{ys} = 1000$  have very little elastic strain capability due to high elastic modulus and low yield strength. Austenitic stainless steels are a common example of this material class.

The other dimension of the material space is the strain hardening exponent,  $n$ . The values of  $n$  range from 3 to 20, spanning the hardening characteristics of most all structural metals from very high strain hardening ( $n=3$ ) to almost elastic-perfectly plastic behavior ( $n=20$ ). The specific values of  $n$  for this study were chosen to uniformly divide the strain hardening response in the stress versus plastic strain space.

*Geometric Space.* **Figure 3** illustrates the geometric solution space for this study as sketches of cross-sections through the crack plane arranged in terms of crack depth-to-thickness ratio ( $a/B$ ) and crack depth-to-half-length ratio ( $a/c$ ) with  $0.2 \leq a/c \leq 1.0$  and  $0.2 \leq a/B \leq 0.8$  for a total of 20 different geometries. For each  $a/B$

FIG. 2 Illustration of the material space.

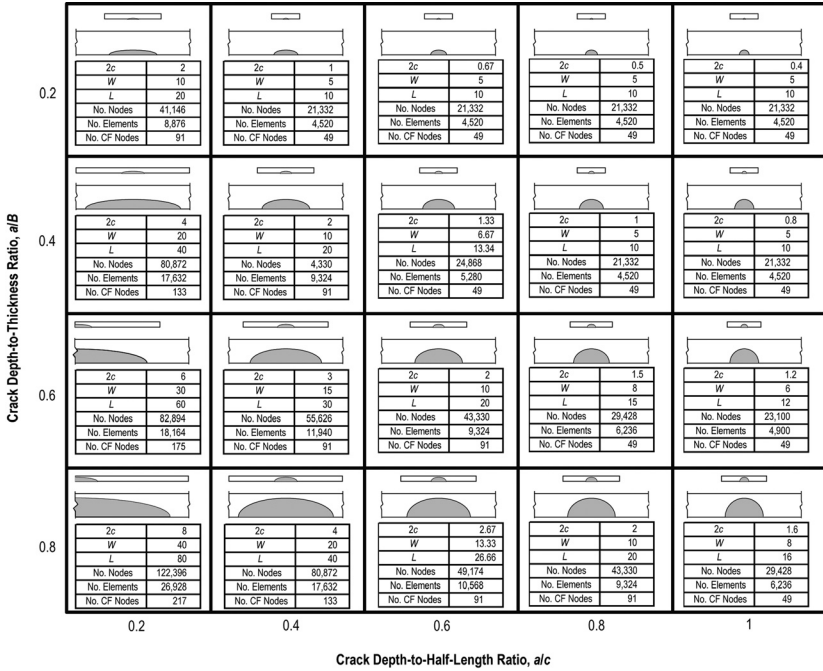


and  $a/c$  combination in Fig. 3, the smaller, upper illustration is a sketch of the crack plane cross-section drawn in proportion to the other geometries (the illustrations for  $a/c=0.2$ ,  $a/B=0.6$ , and  $a/c=0.2$ ,  $a/B=0.8$  are half-symmetry drawings to allow space for the proportional sketches). These sketches allow the reader to visualize the difference in overall cross-section size for each geometry. For each  $a/B$  and  $a/c$  combination in Fig. 3, the lower illustration is a close up view of the crack plane cross-section with the thickness held constant for all geometries. The close-up sketches better illustrate the semi-elliptical crack shape in relation to the specimen thickness. For all geometries,  $B=1$  and  $L/W=2$ . Figure 3 lists the  $2c$ ,  $W$ , and  $L$  values for all the geometries. The plate widths were set equal to the greater of  $W=5*2c$  or  $W=5*B$  to minimize width effects on the  $J$ -integral solutions and to ensure that the plates maintained a “plate like” width-to-thickness aspect ratio for small cracks. Utilizing these minimum width criteria precludes the need to include the  $W/2c$  ratio as a third variable in the geometric space [15].

### Finite Element Models

A total of 600 nonlinear finite element analyses were required to perform the analysis of the 30 material and 20 geometric combinations. All of the finite element

FIG. 3 Illustration of the geometric space.



models (FEMs) were created using the commercial finite element mesh creation and post-processing tool FEACrack [13], and the finite element analyses were performed using the freely available research code WARP3D version 16.3.1 [16]. All of the surface cracked plates were modeled with 3D quarter-symmetric FEMs using 20-node reduced integration isoparametric elements (element type *q3disop* in WARP3D). For each model geometry, Fig. 3 lists the total number of nodes and elements as well as the number of nodes in the  $\phi$  direction along the crack perimeter. Uniform axial displacements were applied to all of the nodes on the top surface of the plate to apply tension, and the FEMs were loaded with 20 to 30 even load steps with an average of 2–5 Newton iterations for convergence within each step to a tight tolerance on residual nodal forces.

**Computational Automation Methods**

Handling this large array of nonlinear models was made practical by computer routines that automate the process of building the finite element models, running the nonlinear analyses, post-processing model results, and organizing the solution results into multi-dimensional arrays. Computer routines were written in Matlab [17] to create the file storage directory structure and serve as the overall controller for the model building, execution, and post-processing procedure.

The FEMs were built using FEACrack in batch control mode on a Windows XP computer with Matlab scripts automating FEACrack runs to produce fully defined WARP3D models throughout the defined solution space. For efficient parallel processing analysis, the WARP3D models were solved using a Linux-based server. Once the finite element analyses were complete, a compact set of WARP3D packet result files were returned to the Windows XP computer for post-processing in batch mode with FEACrack, resulting in a set of 600 text-based result files containing all the pertinent model result data. A set of Matlab scripts then consolidated the full data set into arrays of  $J$ -integral versus  $\phi$  values, far field stresses, and  $CMOD$  values in an easily indexed data structure.

### Interpolation Methodology

*Normalization Scheme.* To derive useful results from the solution space, interpolation within the geometry and material dimensions is necessary, but scaling of the solutions with respect to geometry and material is also required. The solution space was normalized to a dimensionless state to simplify scaling. There are three primary results in the solution set that need to be normalized:  $J$ ,  $CMOD$ , and far-field stress,  $\sigma$ . By dimensional analysis it is clear that the  $J$ -integral is conveniently normalized by a product of stress and length; therefore the normalized  $J$ -integral value,  $J_n$ , can be written as

$$J_n = \frac{J}{\sigma_{ys}B} \quad (2)$$

The yield stress and plate thickness are particularly convenient normalizing factors because, as discussed previously, both  $\sigma_{ys}$  and  $B$  were defined to have unit value in the model space. Thus, the  $J$ -integral result from the analysis does not change when normalized. The same follows for the  $CMOD$  and far-field stress results where

$$CMOD_n = \frac{CMOD}{B} \quad (3)$$

and the normalized far field stress,  $\sigma_n$ , is

$$\sigma_n = \frac{\sigma}{\sigma_{ys}}. \quad (4)$$

*Solution Space Interpolation.* Interpolation within the space provides an estimated solution at any crack shape and depth within the geometric space and at any modulus of elasticity and strain hardening exponent within the material space. The solution of interest is the  $J_n$  value as a function of  $\phi$  around the crack perimeter,  $J_n(\phi)$ . For each of the 600 models in the space,  $J_n(\phi)$  is calculated as a function of increasing deformation increment. The state of the deformation increment can be described by either the models' far field stress,  $\sigma_n$ , or displacement at the crack mouth,  $CMOD_n$ . Though  $\sigma_n$  (or force) is an intuitive descriptor of the load

increment, for elastic-plastic analysis, the *CMOD* is a more reliable predictor of *J* (*J* is nearly a linear function of *CMOD* in the plastic regime) [4,9,18]; as such, the authors chose to use *CMOD* as the characteristic loading condition in the interpolation methodology. Figure 4 shows a plot of  $J_n(\phi)$  versus  $CMOD_n$  for a solution with 30 load increments. Open symbols are placed at the  $\phi = 30^\circ$  location to help visualize the  $J_n$  versus  $CMOD$  trajectory for a given  $\phi$  location. In the solution space, the  $\sigma_n$  versus  $CMOD_n$  values are also recorded; thus by multiplying  $\sigma_n$  by the final dimensioned area, a prediction of the *P* versus *CMOD* trace is available. This trace is particularly useful for comparison with experimental surface crack test results.

The solution space consists of 600 result data sets, each containing  $J_n(\phi)$  versus  $CMOD_n$  and  $\sigma_n$  versus  $CMOD_n$  data. The space is structured in a four dimensional array that is most easily visualized by considering a 4 by 5 geometry matrix with four rows of *a/B* ratios and five columns of *a/c* ratios. Within each of the 20 geometric combinations, there exist 30 material solutions described by a 5 by 6 matrix of material solutions, five values of *n* and six values of  $E/\sigma_{ys}$ . The solution space is readily indexed by these four dimensions. For a given model result, *R*, the solution is given by the notation:  $R(a/B, a/c, n, E/\sigma_{ys})$ . Figure 5 shows a conceptual illustration of the  $R(a/B, a/c, n, E/\sigma_{ys})$  solution space with the geometric space at the highest level and the entire material space existing at the next level repeated within each geometric combination followed by the  $J_n(\phi)$  versus  $CMOD_n$  and  $\sigma_n$  versus  $CMOD_n$  data for each of the 600 models at the lowest level.

In general, the actual surface crack geometry and material of interest will not fall directly on an existing solution and interpolation is necessary. To interpolate to

FIG. 4 Example illustration of the  $J(\phi)$  versus *CMOD* space.

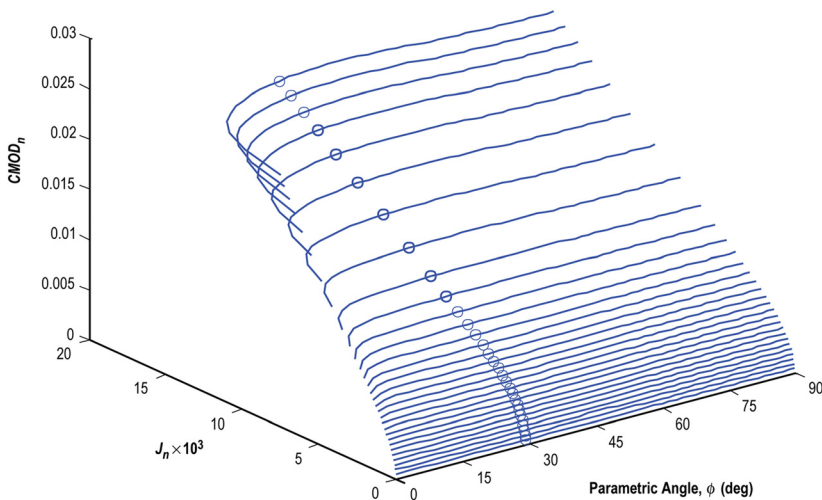
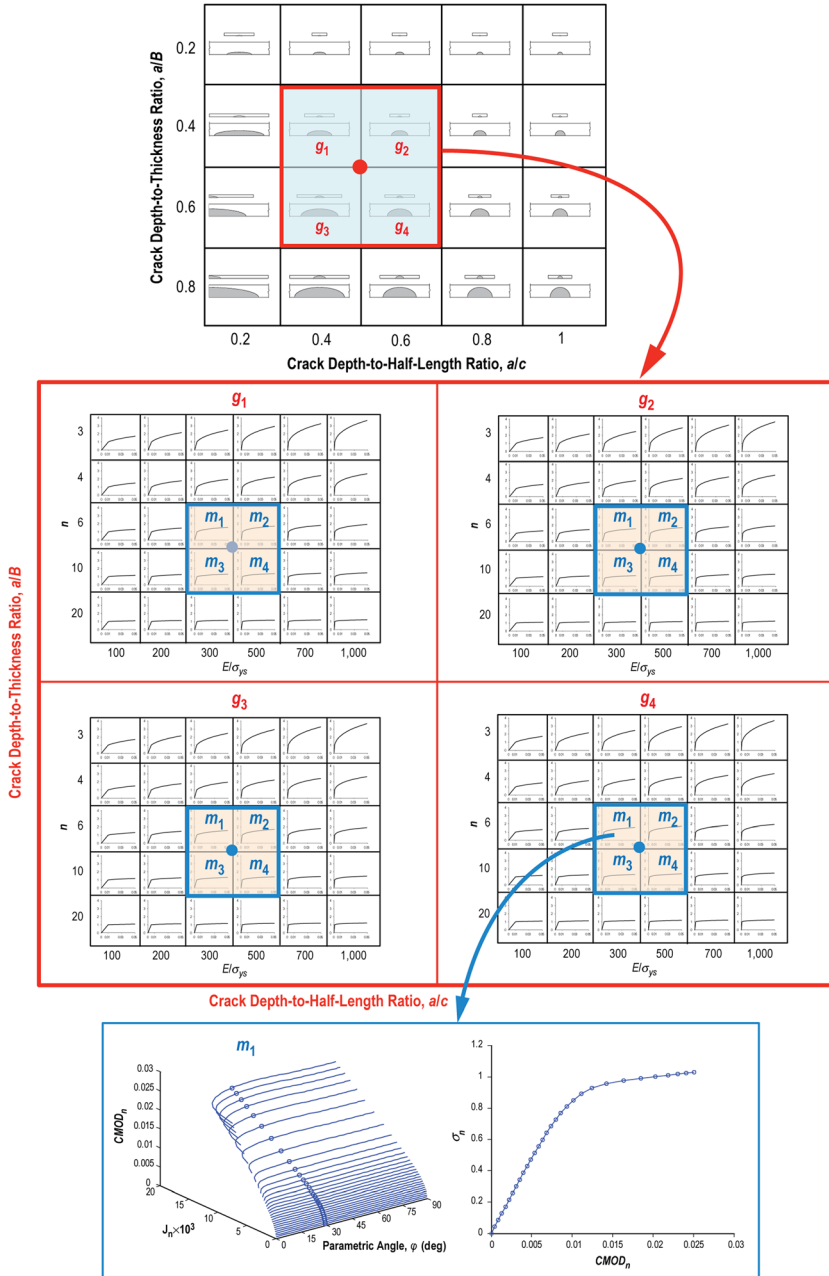


FIG. 5 Conceptual illustration of the interpolation space.



a new solution,  $\bar{R}(a/B, a/c, n, E/\sigma_{ys})$ , the first step is to identify the subset of the 600 model space that will be active in the interpolation process by determining the location of  $\bar{R}$  in the geometry and material matrices. For illustration, consider a choice of  $\bar{R}(a/B = 0.5, a/c = 0.5, n = 8, E/\sigma_{ys} = 400)$  that is located between the cells labeled  $g_1$  through  $g_4$  in the geometry matrix of Fig. 5. The four “nearest-neighbor” subset solutions are the geometry combinations designated as  $g_1$ – $g_4$ . For each of the  $g_1$ – $g_4$  geometries, a point for  $\bar{R}$  can be placed in the material matrix resulting in materials  $m_1$  through  $m_4$ . Identifying the sets  $g_1$ – $g_4$  and their associated  $m_1$ – $m_4$  sets provides the 16 nearest-neighbor data sets for use in the interpolation of the  $\bar{R}$  solution. Linear interpolation is performed across the four-dimensional solution space to estimate the  $\bar{R}$  solution, details of which are given in NASA/TP-2013-217480 [15].

### Solution Verification

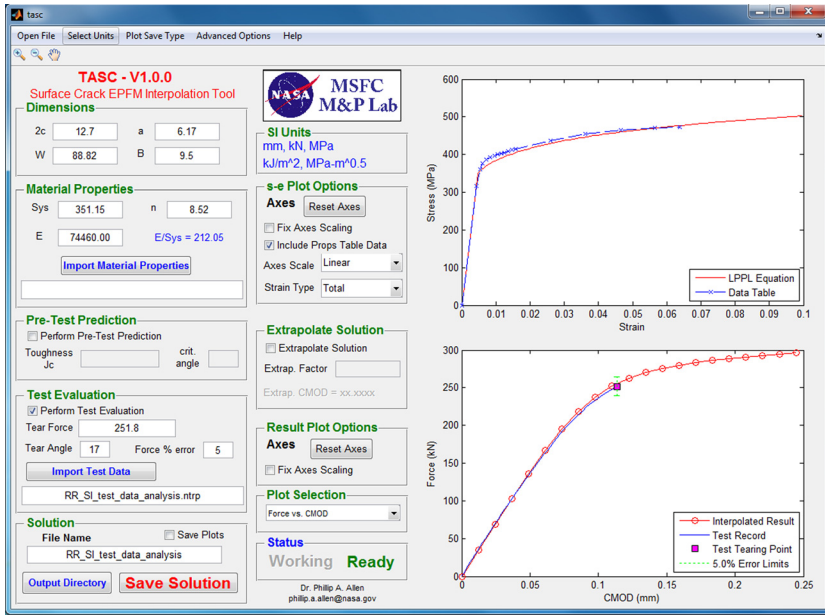
The surface crack solutions and the interpolation method were verified through several techniques, summarized as follows. The linear-elastic  $J$ -integral solutions were shown to be in proper agreement with the Newman–Raju [11,12] solutions. Domain convergence for the elastic-plastic  $J$ -integral values at the final load step was demonstrated for the complete set of solutions at all crack perimeter nodal locations. Twenty-five benchmark FEMs were created purposefully exploiting gaps in the geometry and material solution matrices to test the effectiveness of the interpolation method. The interpolated solutions were able to predict the benchmark  $J$ -integral and reaction force solutions for a given  $CMOD$  value to within a few percent. Significant effort was expended to ensure the reliability of this new tool, and the details of the verification methods are discussed in detail in NASA/TP-2013-217480 [15].

### GRAPHICAL USER INTERFACE TOOL

After the verification was complete, the solution space and interpolation methods were incorporated into a Matlab tool, TASC, as shown in Fig. 6. For a set of solutions of this magnitude, a convenient and easy-to-use computer program must be created to enable ready access to the solutions. TASC provides an interface for a non-expert to quickly interpolate to a fully elastic-plastic solution for a surface crack in tension. The only required inputs are the surface crack dimensions ( $2c$  and  $a$ ), plate cross-section dimensions ( $W$  and  $B$ ), and LPPL material properties ( $E$ ,  $\sigma_{ys}$ , and  $n$ ). With the geometry and material parameters entered, the tool interpolates to the appropriate  $J(\phi)$  versus  $CMOD$  and  $\sigma$  versus  $CMOD$  solution, providing the full solution as  $CMOD$  ranges from zero out to the  $CMOD$  limit of the solution space at the given input parameters. With surface crack test design and analysis in mind, TASC also has several other useful features such as:

1. material property import capability with automated material constant fitting,
2. pre-test prediction capabilities based on a critical  $J$ -integral value and critical  $\phi$  location,

FIG. 6 Computer program TASC for automated elastic plastic surface crack analysis.



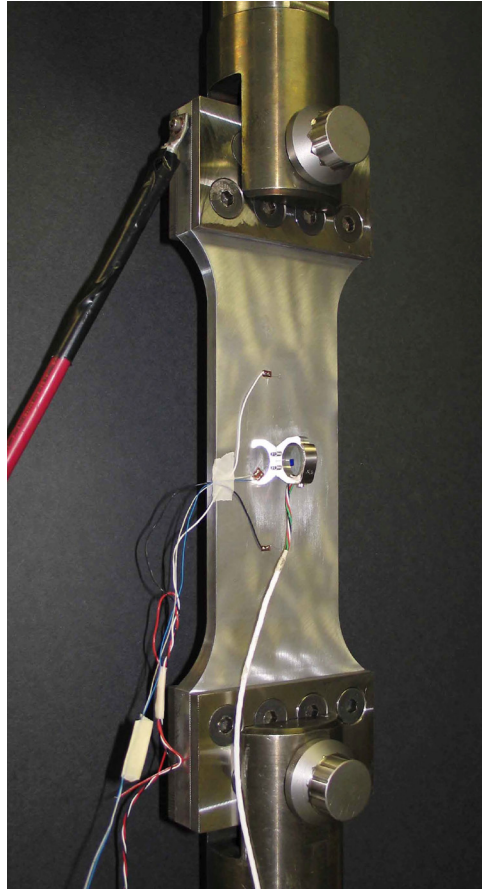
3. test record  $P$  versus  $CMOD$  evaluation and comparison with analysis,
4. the ability to review result plots such as  $J(\phi)$ ,  $J$  versus  $CMOD$ , and deformation limit comparisons, and,
5. the ability to save the solution and plot files.

Consolidation of these new elastic-plastic surface crack solutions and the corresponding interpolation methodology into an easily accessible program represents a significant bridge for the practicing engineer toward commonplace elastic-plastic assessment of surface crack tests.

### INTERPOLATED SOLUTION OF THE ROUND ROBIN SURFACE CRACK TEST

TASC was used to create an interpolated solution to compare with the author-led inter-laboratory round robin (RR) concerning the elastic-plastic analysis of surface cracked plates as documented in NASA/TM-2012-217456 [9]. A surface crack tension test was performed to serve as the basis for the RR work. The experiment existed of a 2219-T8 aluminum specimen with  $W = 88.82$  mm,  $B = 9.50$  mm,  $L = 177.8$  mm (uniform cross-section length),  $a = 6.17$  mm, and  $2c = 12.70$  mm as shown in Fig. 7. The specimen was loaded under displacement control in tension until ductile tearing was detected. The tearing force was 252 kN corresponding to a tearing  $CMOD$  of 0.114 mm, and the location of maximum tearing along the crack front was at  $\phi = 17^\circ$ . The round robin participants were requested to blindly

**FIG. 7** Round robin specimen configured for testing.



predict the force versus  $CMOD$  trace and to provide  $J$  versus  $\phi$  at forces of 200, 252, and 289 kN.

The interpolated solution is compared to the FE analyses of the other fourteen RR participants. In the following section the authors' original FE analysis performed for the RR is labeled "FEA," and the other participants' results are labeled "Labs 2–15." A LPPL approximation of the material's stress-strain curve is required to estimate an interpolated solution to the problem. The interpolated solutions assume the same elastic properties provided to the RR participants ( $E = 74.46$  GPa and  $\nu = 0.33$ ) with the exception that  $\nu$  is a fixed value of 0.30 in all the interpolated solutions. The authors conducted a study on the sensitivity of the interpolated solution to the choice of  $\sigma_{ys}$  and  $n$ , and determined that the interpolated solution is fairly insensitive to reasonable choices of flow properties [15]. Values of

$\sigma_{ys} = 365.4$  MPa and  $n = 9.5$  were chosen as representative of an “average” choice for material flow properties and were used to solve for the interpolated result shown here.

**Figure 8** shows the comparison of the  $P$  versus  $CMOD$  test data with the authors original FEA, the interpolated solution, and the analysis results of other RR participants, labs 2-15. The interpolated solution falls directly within the family of the RR results. Note that the interpolated solution is provided out to the limit of the chosen solution space, so the final  $CMOD$  of the interpolated solution is not part of the prediction; rather, it is the  $P$  versus  $CMOD$  trace up through any specified  $CMOD$  value of interest. **Figure 9** compares the  $J$ -integral values at  $\phi = 17^\circ$  versus the  $CMOD$  results for the interpolated solution and all of the lab solutions. Again the interpolated solution is in excellent agreement with the family of solutions represented in the round robin. It is clear from the trace of the interpolated solution that

**FIG. 8** Interpolation, FEM, and RR participant results compared to experimental force versus  $CMOD$  response.

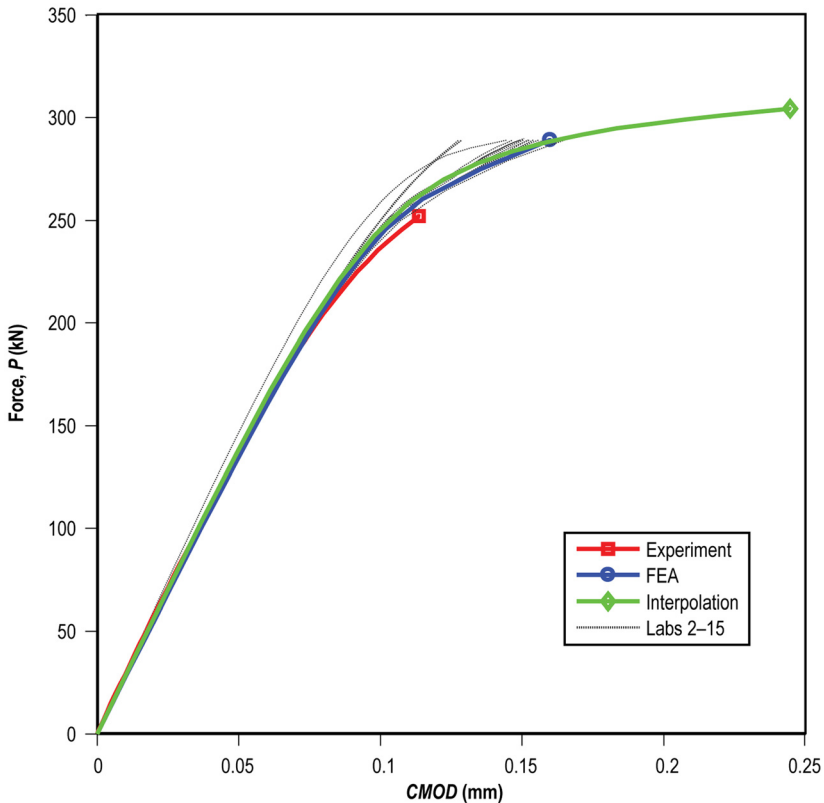
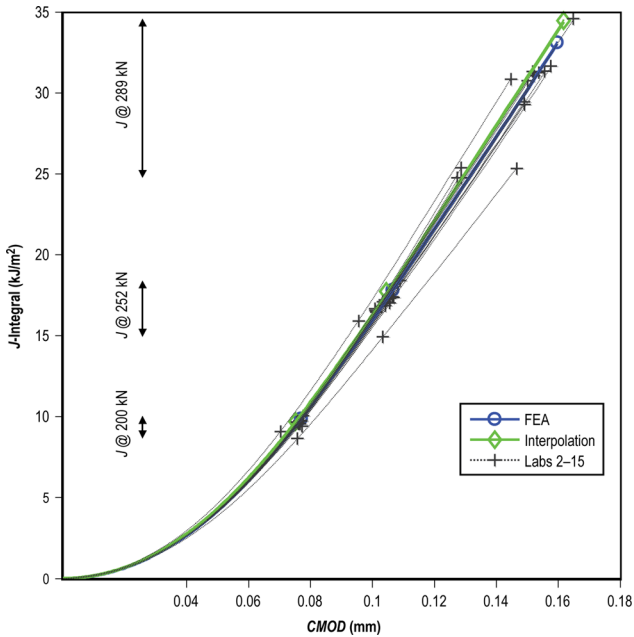


**FIG. 9** Comparison of interpolation, FEM, and RR participant results for  $J(\phi = 17^\circ)$  versus CMOD.



it passes cleanly through the family of RR results and provides an answer of equivalent quality as may be expected from a custom finite element assessment of the test.

## Conclusions

This paper presents a case for moving beyond equation-based test standards for certain classes of complicated fracture mechanics tests. Using automated and standardized computer tools to calculate the pertinent test result values has several advantages such as:

1. allowing high-fidelity solutions to complex nonlinear phenomena that would be impractical to express in written equation form,
2. eliminating errors associated with the interpretation and programming of analysis procedures from the text of test standards,
3. lessening the need for expertise in the areas of solid mechanics, fracture mechanics, numerical methods, and/or finite element modeling, to achieve sound results,
4. and providing one computer tool and/or one set of solutions for all users for a more “standardized” answer.

In summary, this approach allows a non-expert with rudimentary training to get the best practical solution based on the latest understanding with minimum difficulty.

As a practical example, the authors presented an automated method to determine the elastic-plastic solution for a surface crack plate in tension using interpolation methodologies. This new set of elastic-plastic surface crack solutions, the interpolation methodology, and the simple GUI implementation through TASC represent a significant step toward commonplace assessment of surface cracks by the  $J$ -integral. This is particularly true for the case of standardized experimental evaluation of surface crack fracture toughness. Unfortunately, the use of elastic-plastic experimental methods in the evaluation of fracture toughness of materials continues to lag significantly behind linear-elastic methods, even for common two-dimensional geometries such as the compact tension specimen, despite the advantages in flexibility and breadth of information elastic-plastic methods reveal. Surface crack toughness testing can provide the most direct measure of material performance in structurally representative configurations; yet, the detailed working knowledge of finite element modeling currently required to properly assess a surface crack test in the elastic-plastic regime (as most are) has kept surface crack toughness testing reserved mainly as a domain for the specialist. The costs in modeling time and software infrastructure are largely prohibitive for most experimental labs. The interpolation methodology and solution space described herein represents a new evolutionary step in tools for the analyst and experimentalist alike.

A strong case can be made for developing automated analysis tools for certain classes of complicated fracture testing standards and for providing standard computer tools as a companion with the ASTM standards. This is a novel concept in the ASTM fracture testing arena, but standard computer programs are already being used with other ASTM standards that cover complicated physical phenomena or processes such as: ASTM C1340/C1340M-10—Standard Practice for Estimation of Heat Gain or Loss Through Ceilings Under Attics Containing Radiant Barriers by Use of a Computer Program, ASTM F2815-10—Standard Practice for Chemical Permeation through Protective Clothing Materials: Testing Data Analysis by Use of a Computer Program, and ASTM E2807-11—Standard Specification for 3D Imaging Data Exchange, Version 1.0 [19–21]. The verification, validation, and round-robin processes required of a computer tool closely parallel the methods that are used to ensure the solution validity for equations included in test standards. In many ways, an automated solution method using a computer program can be thought of as a complicated equation that cannot be simply written down on a page; instead the answer has to be obtained through the use of automated numerical methods. For the surface crack example presented here, the automated interpolation method has the advantage of being a bounded problem with verified solutions that populate the space.

Of course providing a standard computer tool with an ASTM standard requires consideration of some technical details. As with any analytical method, users have to input appropriate analysis values to get reasonable solutions. Most gross input errors can be mitigated or detected by analysis comparison back to the actual test data such as the force versus  $CMOD$  data for the surface crack test. For any test standard incorporating automated analysis tools, the governing task group has to

be willing to create the solutions and build the analytical tools to make the solutions useable and accessible. Computer tools also require consideration of details concerning configuration control, tool publishing, platform releases, and file sharing. None of these obstacles are insurmountable, and the advantages of automated analysis tools easily outweigh any difficulties.

As more complicated fracture toughness tests are considered for standardization, automated analysis tools provide a viable option for obtaining test results. The use of automated analysis tools allows the creation and practical implementation of advanced fracture mechanics test standards that capture the physics of a nonlinear fracture mechanics problem without adding undue burden or expense to the user. Providing ASTM fracture testing standards with companion computer tools has many advantages and has already been implemented by other ASTM committees. The authors especially hope the automated analysis methods presented here will provide a useful method for advanced surface crack test analysis.

## References

- [1] ASTM E399-09: Standard Test Method for Linear-Elastic Plane-Strain Fracture Toughness  $K_{IC}$  of Metallic Materials, *Annual Book of ASTM Standards*, ASTM International, West Conshohocken, PA, 2012.
- [2] ASTM E1820-11: Standard Test Method for Measurement of Fracture Toughness, *Annual Book of ASTM Standards*, ASTM International, West Conshohocken, PA, 2012.
- [3] McClung, R. C., Chell, G. G., Lee, Y. D., Russell, D. A., and Orient, G. E., "Development of a Practical Methodology for Elastic-Plastic and Fully Plastic Fatigue Crack Growth," *NASA/CR-1999-209428*, NASA, Washington, DC, 1999.
- [4] Anderson, T. L., *Fracture Mechanics: Fundamentals and Applications*, 3rd ed., CRC Press, Boca Raton, FL, 2005.
- [5] Kumar, V., German, M. D., and Shih, C. F., "An Engineering Approach for Elastic-Plastic Fracture Analysis," *Report NP-1931*, Electric Power Research Institute, Palo Alto, CA, 1981.
- [6] Kumar, V., German, M. D., Wilkening, W. W., Andrews, W. R., deLorenzi, H. G., and Mowbray, D. F., "Advances in Elastic-Plastic Fracture Analysis," *Report NP-3607*, Electric Power Research Institute, Palo Alto, CA, 1984.
- [7] Kumar, V. and German, M. D., "Elastic-Plastic Fracture Analysis of Through-Wall and Surface Flaws in Cylinders," *Report NP-5596*, Electric Power Research Institute, Palo Alto, CA, 1988.
- [8] Ainsworth, R. A., "The Assessment of Defects in Structures of Strain Hardening Material," *Eng. Fract. Mech.*, Vol. 19, 1984, pp. 633–642.
- [9] Wells, D. N. and Allen, P. A., "Analytical Round Robin for Elastic-Plastic Analysis of Surface Cracked Plates: Phase I Results: NASA MSFC," *NASA/TM-2012-217456*, NASA, Washington, DC, 2012.

- [10] ASTM E2899-13: Standard Test Method for Measurement of Initiation Toughness in Surface Cracks Under Tension and Bending, *Annual Book of ASTM Standards*, ASTM International, West Conshohocken, PA, 2013.
- [11] Newman, J. C. and Raju, I. S., "Stress-Intensity Factor Equations for Cracks in Three-Dimensional Finite Bodies Subjected to Tension and Bending Loads," *Comput. Methods Mech. Fract.*, Vol. 2, 1986, pp. 311-334.
- [12] Newman, J. C., Reuter, W. G., and Aveline, C. R. J., "Stress and Fracture Analyses of Semi-Elliptical Surface Cracks," *ASTM Special Technical Publication, STP1360*, pp. 403-423, ASTM International, West Conshohocken, PA, 2000.
- [13] Quest Integrity Group, 2012, "FEA-Crack," <http://www.questintegrity.com/products/feacrack-3D-crack-mesh-software/> (Last accessed 12 Dec 2012).
- [14] Dassault Systemes, 2013, "ABAQUS CAE," <http://www.3ds.com/products/simulia/portfolio/abaqus/abaqus-portfolio/abaquscae/> (Last accessed 16 Jan 2013).
- [15] Allen, P. A. and Wells, D. N., "Elastic-Plastic J-Integral Solutions for Surface Cracks in Tension Using an Interpolation Methodology," *NASA/TP-2013-217480*, NASA, Washington, DC, 2013.
- [16] University of Illinois at Urbana-Champaign, 2012, "WARP3D Dodds RH," <http://code.google.com/p/warp3d/> (Last accessed 12 Dec 2012).
- [17] Matlab, Mathworks, <http://www.mathworks.com/products/matlab/> (Last accessed 12 Dec 2012).
- [18] Brocks, W. and Scheider, I., "Reliable J-Values; Numerical Aspects of the Path-Dependence of the J-Integral in Incremental Plasticity," *MP Mater.*, Vol. 45, 2003, pp. 264-275.
- [19] ASTM C1340/C1340M-10: Standard Practice for Estimation of Heat Gain or Loss Through Ceilings Under Attics Containing Radiant Barriers by Use of a Computer Program, *ASTM Book of Standards, Annual Book of ASTM Standards*, ASTM International, West Conshohocken, PA, 2012.
- [20] ASTM F2815-10: Standard Practice for Chemical Permeation through Protective Clothing Materials: Testing Data Analysis by Use of a Computer Program, *ASTM Book of Standards, Annual Book of ASTM Standards*, ASTM International, West Conshohocken, PA, 2012.
- [21] ASTM E2807-11: Standard Specification for 3D Imaging Data Exchange, Version 1.0, *ASTM Book of Standards, Annual Book of ASTM Standards*, ASTM International, West Conshohocken, PA, 2012.

STP 1571, 2014 / available online at [www.astm.org](http://www.astm.org) / doi: 10.1520/STP157120130076

Jidong Kang<sup>1</sup> and Guowu Shen<sup>1</sup>

# A Novel Shear Test Procedure for Determination of Constitutive Behavior of Automotive Aluminum Alloy Sheets<sup>2</sup>

## Reference

Kang, Jidong and Shen, Guowu, "A Novel Shear Test Procedure for Determination of Constitutive Behavior of Automotive Aluminum Alloy Sheets," *Application of Automation Technology in Fatigue and Fracture Testing and Analysis*, STP 1571, Peter C. McKeighan and Arthur A. Braun, Eds., pp. 50–62, doi:10.1520/STP157120130076, ASTM International, West Conshohocken, PA 2014.<sup>3</sup>

## ABSTRACT

Various shear tests have been proposed over decades leading to the publication of the ASTM Standard B831-93 [ASTM B831-93: Standard Test Method for Shear Testing of Thin Aluminum Alloy Products, *Annual Book of ASTM Standards*, ASTM International, West Conshohocken, PA, 2011] and its latest revision B831-11 for shear test of aluminum alloy thin sheet materials. However, this standard only measures the shear strength of aluminum sheets. A new shear specimen design has been developed by Kang et al. [Kang, J., Wilkinson, D. S., Wu, P. D., Bruhis, M., Jain, M., Embury, J. D., and Mishra, R., "Constitutive Behavior of AA5754 Sheet Materials at Large Strains," *J. Eng. Mater. Technol.*, Vol. 130, No. 3, 2008, p. 031004]. We propose using digital image correlation for shear strain measurements, which is impractical for conventional extensometry techniques. A new shear test method is then used to measure both the shear strength and shear stress–shear strain curves up to large strains. 3D finite element analysis (FEA) was carried out for both the standard and new shear specimen designs.

---

Manuscript received May 17, 2013; accepted for publication May 2, 2014; published online August 29, 2014.

<sup>1</sup>CanmetMATERIALS, 183 Longwood Rd. South, Hamilton, Ontario L8P 0A5, Canada.

<sup>2</sup>This licence is granted on the condition that clear attribution is given to the author(s) and Natural Resources Canada and, when feasible, that the Crown copyright is acknowledged as follows: © Her Majesty the Queen in Right of Canada, as represented by the Minister of Natural Resources, 2014.

<sup>3</sup>ASTM Sixth Symposium on *Application of Automation Technology in Fatigue and Fracture Testing and Analysis* on May 23, 2013 in Indianapolis, IN.

The results show that simple shear state is reached within the shear zone. The results also reveal that the out-of-plane shear strain is significantly reduced to 5 % in new shear specimen design compared to that of over 12 % for the standard specimen design. The rotation of the end of the shear zone is, thus, prevented.

## Introduction

In response to the greater demand for fuel-efficient vehicles, coupled with more stringent environmental emissions regulations, automotive manufacturers are increasingly adopting aluminum alloys for lightweight structural components to reduce vehicle weight. Performance prediction of these components during the design process is critical to achieving optimal cost and weight solutions. Shear tests are therefore of interest because they avoid the early localization that is observed in uniaxial tensile tests. In the meantime, shear is also a major strain path in stamping operations, as well as a major failure mode in structures under complex loading conditions [1].

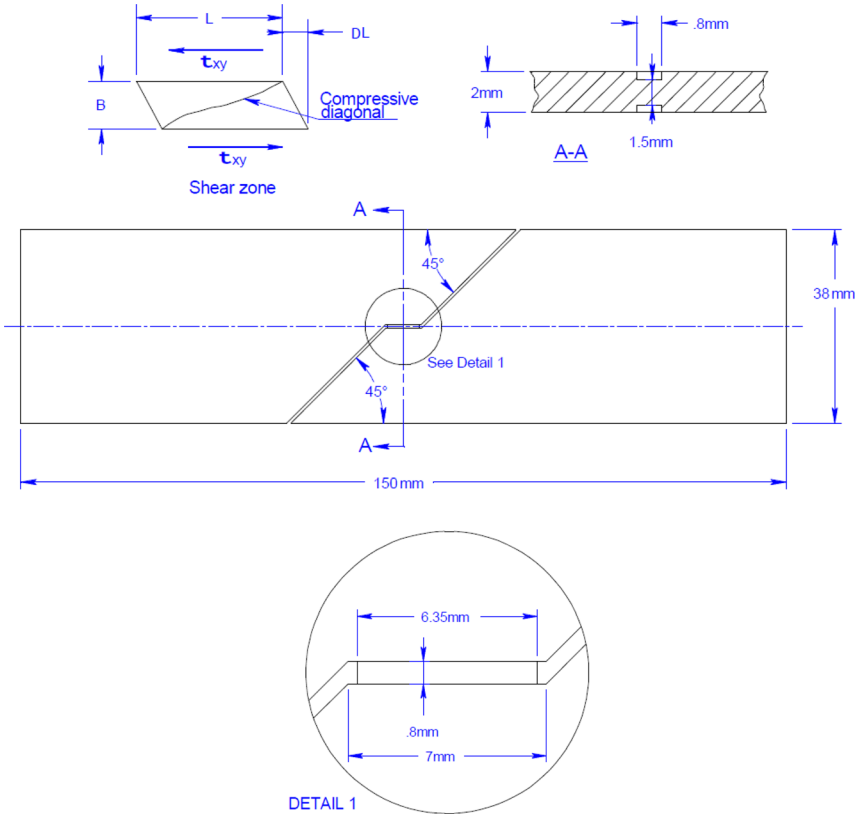
Numerous types of specimens have been proposed for shear testing of sheet materials in the literature [2–5], which leads to the publication of ASTM B831-93 [6] for shear testing of aluminum sheet materials. In ASTM B831-93, the tensile loaded shear specimen geometry is chosen in which the simple shear state could be reached over a smaller area called a “shear zone,” using a conventional tensile machine without any additional device. However, the current version of ASTM B831-93 only provides guidance to the measurement of shear strength measurements. In practice, shear strain measurement is difficult to realize using conventional extensometry techniques. Digital image correlation (DIC) [7] provides 2D or 3D full-field, non-contact strain mapping in which shear strain components can be easily measured. A new shear test method that coupled shear test with DIC measurement was developed to measure constitutive behavior of aluminum alloy sheets up to large strains [8]. The method has been further developed and applied to measure constitutive behavior of aluminum spot welds [9,10] and gas metal arc welds [11].

In this work, we will address several issues related to standardization of the new shear specimen and test procedures.

## Experimental

The material used in the present study is AA5754 sheets in 2 mm thickness in annealing temper. The chemical composition of the material can be found in Ref 8. The new shear specimen geometry used in the present study is shown in Fig. 1. Compared to the ASTM standard, two modifications were made: (1) A notch of 0.25 mm in the thickness direction on both sides of the sample was machined using sinker electrical discharge machining to ensure simple shear state in the shear zone; (2) as the thickness is reduced, the width of the shear zone is accordingly reduced from 1.6 mm as specified in the ASTM standard to 0.8 mm to prevent buckling of

**FIG. 1** A new shear test specimen geometry.

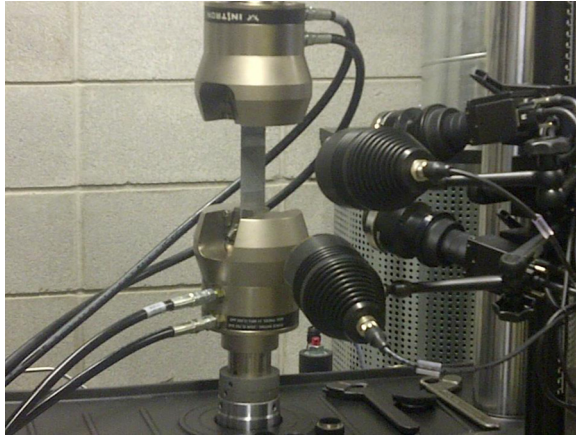


the sample. All the shear tests were carried out at room temperature at a cross-head speed of 0.9 mm/min using an Instron 5566 screw driven test frame or an MTS Landmark hydraulic testing frame (model 310) and TestWork software. A commercially available optical strain-measuring system based on digital image correlation, ARAMIS [12], was used to measure shear stain evolution within the shear zone. A random ink speckle pattern was applied to the shear zone prior to shear testing. A set of snapshots every 2 s were made during the shear testing. The captured images were further processed to obtain shear angle maps within the shear zone using the ARAMIS system. The DIC experimental setup is shown in Fig. 2.

The shear strains were measured through the shear angles in the ARAMIS system [12]. The shear angle is defined as the change of an angle of  $90^\circ$  in the undeformed state to a new angle in the deformed state (Fig. 3). Note in Fig. 3, the shear angle  $\theta = \theta_x + \theta_y$ .

The measured shear angles,  $\theta$ , were averaged over the entire shear zone and then converted to shear strain,  $\gamma$ , using  $\gamma = \tan(\theta)$  for each load step recorded.

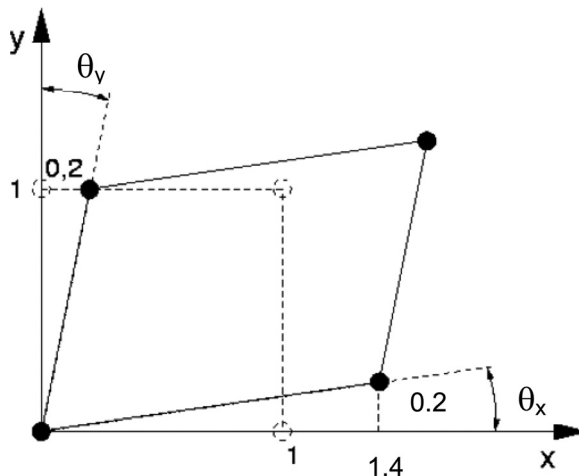
**FIG. 2** 2D digital image correlation setup for shear tests.



## Finite Element Simulation

It was demonstrated in the previous experimental study [8] that the new specimen design prevents the rotation of the end of the shear zone, thus, leading to large shear strain measurements.

**FIG. 3** Shear strain calculation using digital image correlation [12].

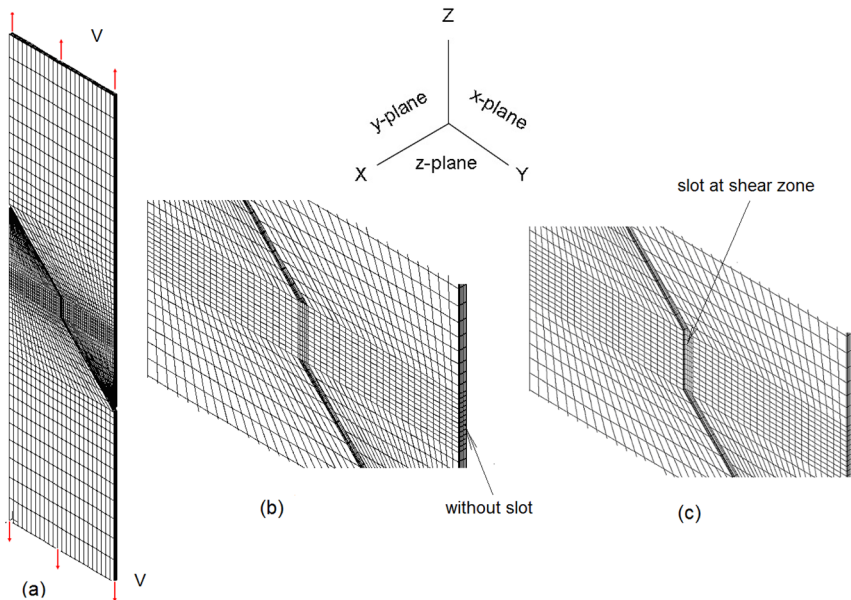


In the present study, we carry out elastic–plastic finite element (FE) simulations to further analyze the stress state of the shear zone in both the standard and new designs.

A commercially available FE code, ADINA [13], was used for the simulation. Three-dimensional 20-node brick elements were used in the simulations. Tests by varying element and node numbers were conducted to ensure that the elements were fine enough for convergence. The final FE meshes of the entire specimen are shown in Fig. 4 for both specimen designs. The minimum element size is 0.5 mm in length and width and 0.1 mm in thickness in the shear zone area. Uniform displacement increments were applied on the two ends of the samples until the shear stress at the shear zone reached its maximum value. The coordinate system used, shown in Fig. 4, has the  $x$  axis in the through-thickness direction,  $y$  axis in the transverse direction, and  $z$  axis along the loading direction.

To simplify the problem, isotropic hardening was assumed in the A5754 sheet and the following true stress–true strain curve was used for the material [8] in the FE analysis:

**FIG. 4** Finite element meshes of (a) shear specimen and details near the shear zone for the (b) standard design and (c) new design. Tensile loading direction is along the vertical direction as shown.



$$(1) \quad \sigma = \sigma_s \left\{ 1 - \left[ \left( 1 - \frac{\sigma_y}{\sigma_s} \right)^{1-\alpha} - (1-\alpha) \frac{h_0}{\sigma_s} \varepsilon \right]^{1/(1-\alpha)} \right\}$$

where:

$$\sigma_y = 94 \text{ MPa,}$$

$$\sigma_s = 316 \text{ MPa,}$$

$$h_0 = 400 \text{ MPa, and}$$

$$\alpha = 1.13.$$

## Results and Discussion

Shear strain (in terms of shear angles) maps at maximum loading are shown in Fig. 5 for both the standard and new design specimens. Clearly, the new design gives higher shear strain [8]. It is also seen in Fig. 5 that for the new design specimen the material does fail in simple shear mode, whereas in the standard design the failure is along the compressive diagonal.

Another important feature of the new design is that no shear banding was observed prior to the maximum load indicating that the deformation within the shear zone is macroscopically homogeneous during the entire deformation process [8]. This is evident when varying the facet and step size for shear strain calculation (Fig. 6) in the DIC analysis using ARAMIS.

**FIG. 5** Measured shear strain distribution at max load in AA5754 shear specimens (a) the standard design; (b) the new design [8].

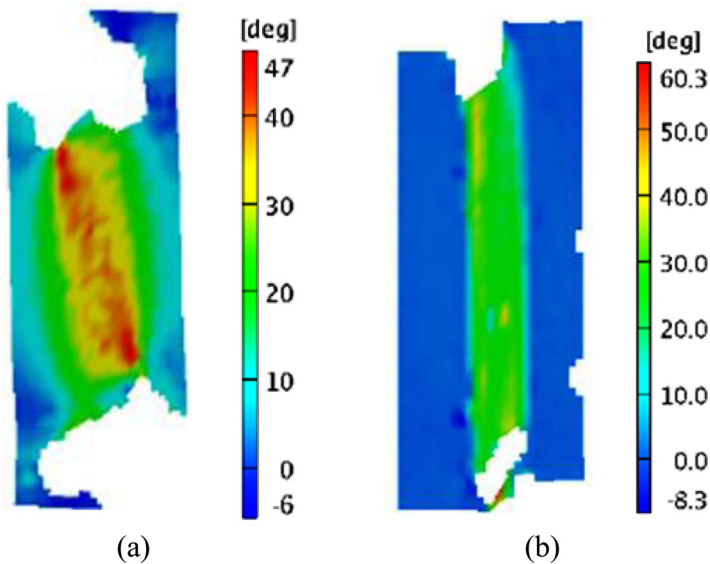


**FIG. 6** Effect of facet size and step size on shear strain measurements. The first and second numbers in the labels of 13 × 9, 26 × 9, and 26 × 15 represent facet size and step size, respectively.

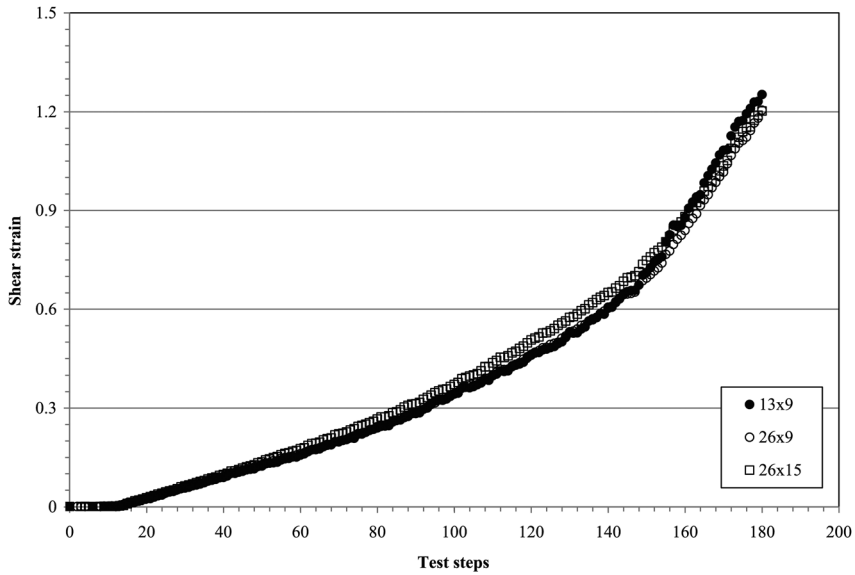
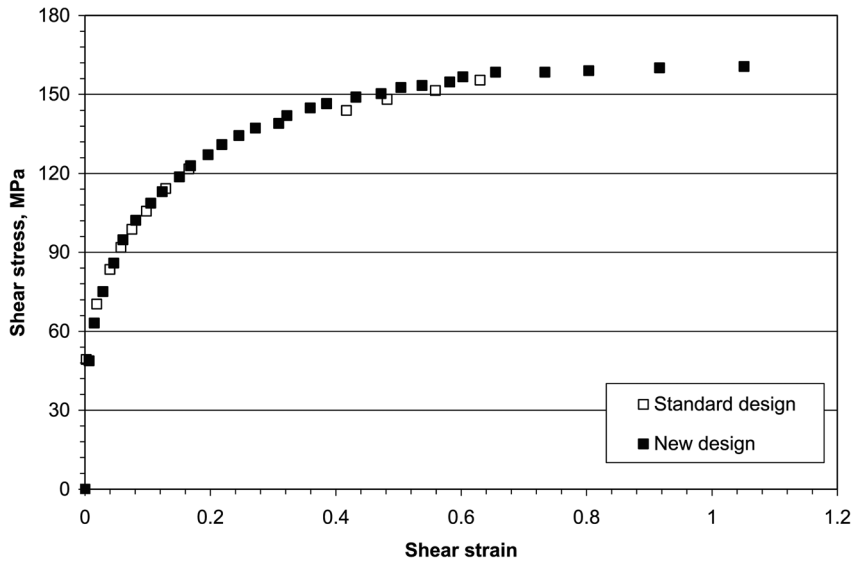


**FIG. 7** Comparison of measured shear stress–shear strain curves in the standard and new design specimens.



When plotting shear stress–shear strain curves for both the standard and new designs (Fig. 7), it is shown that the new specimen design reaches slightly higher shear stress at fracture compared to the standard specimen design.

The calculated shear stress ( $\tau$ , i.e.,  $\tau_{yz}$ , normalized by shear stress at the center point,  $\tau_{ct}$ ) distribution from FE analysis is shown in Fig. 8 at the middle plane along the shear zone for both the standard and the new design. In Fig. 8,  $h$  and  $z$  are the length of the shear zone and the coordinates along the shear zone that starts at the top of the shear zone, respectively. From Fig. 8, it is seen that the shear stress is generally uniform along the shear zone both for the standard and the new specimen design, except the ending points of the shear zone. It is also seen in Fig. 8 that the deviation of the shear stress at the ending points to the center part for the new design is smaller than that of the standard specimen. The shear stress distribution within the shear zone (Fig. 9) confirms these observations. It is seen in Fig. 9 that the shear stress is concentrated at the shear zone for the new specimen design, whereas in the standard specimen design the shear stress spreads to the adjacent area near the shear zone.

It is interesting to look at out-of-plane shear strain distribution within the shear zone (Fig. 10). In Fig. 10, the calculated out-of-plane shear strain ( $\gamma$ , i.e.,  $\gamma_{xy}$ )

**FIG. 8** Calculated distribution of shear stress along the shear zone for the standard and new designs.

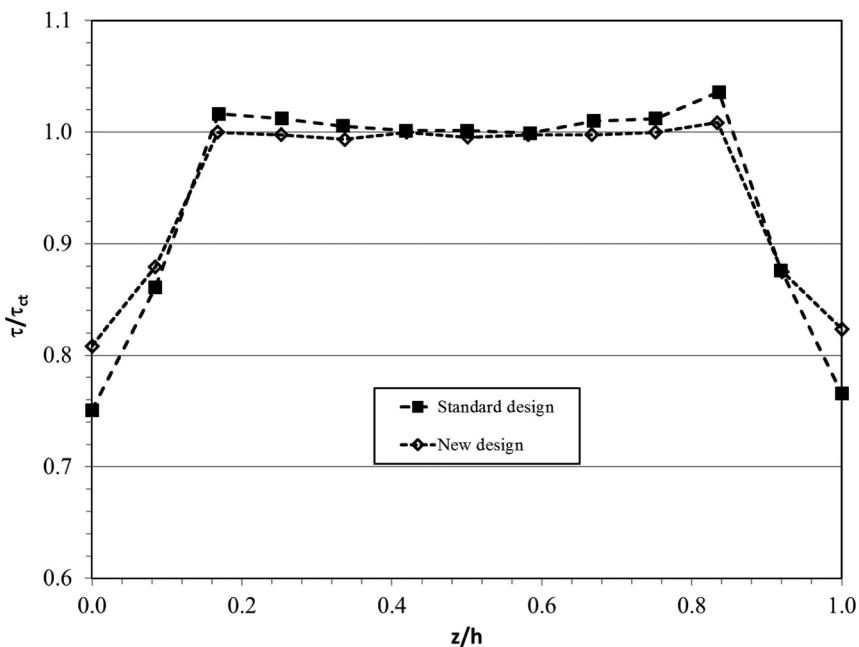
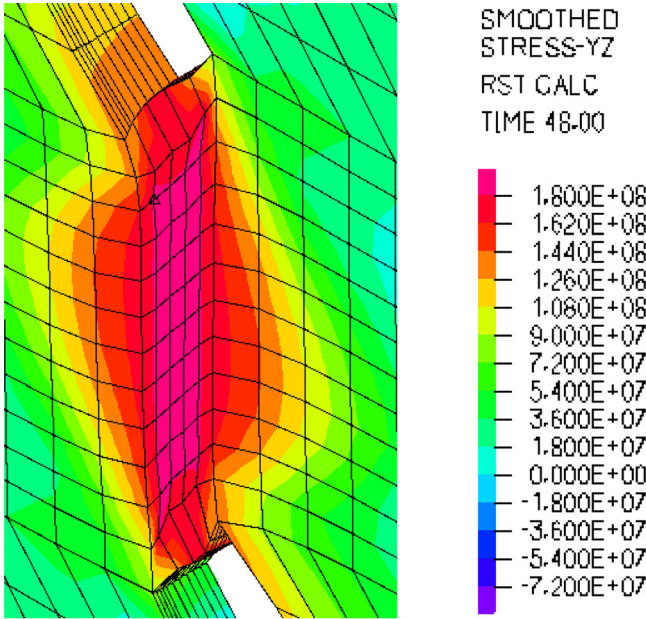
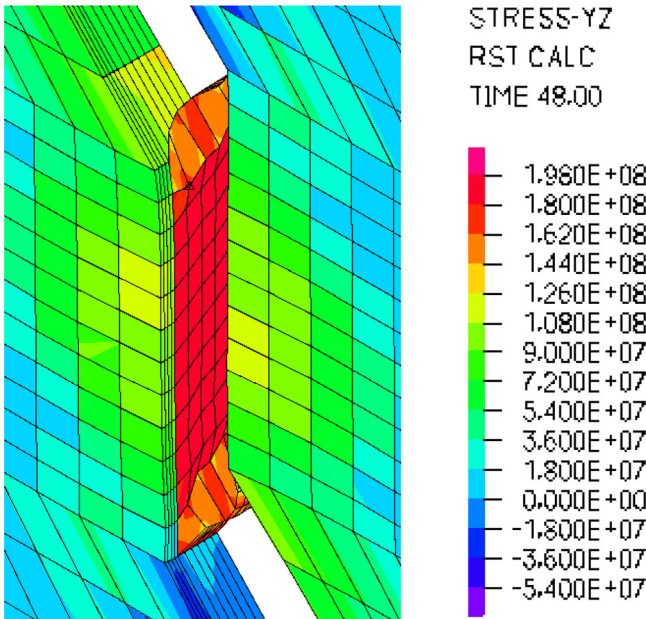


**FIG. 9** Calculated shear stress  $\tau_{yz}$  at the shear zone for (a) the standard; and (b) the new designs. The unit of the stresses shown is Pa.

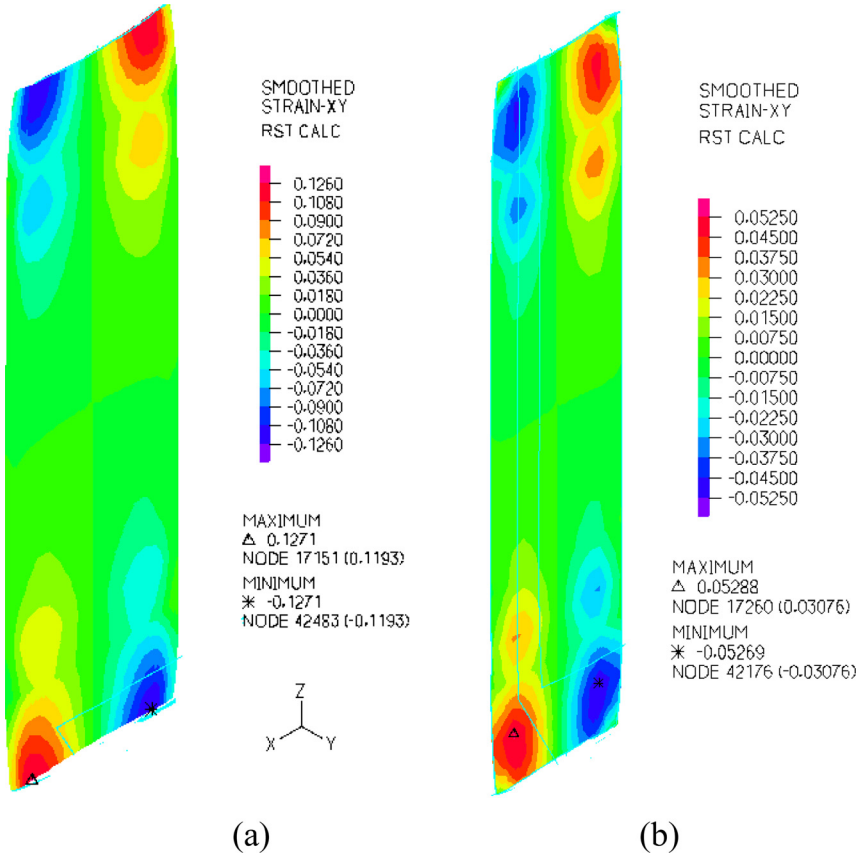


(a)



(b)

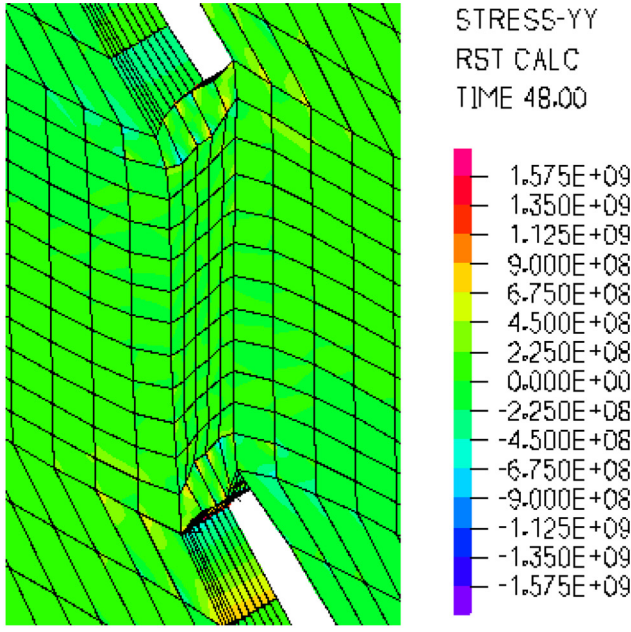
**FIG. 10** Calculated out-of-plane shear strain  $\gamma_{xy}$  for (a) the standard design; and (b) the new design.



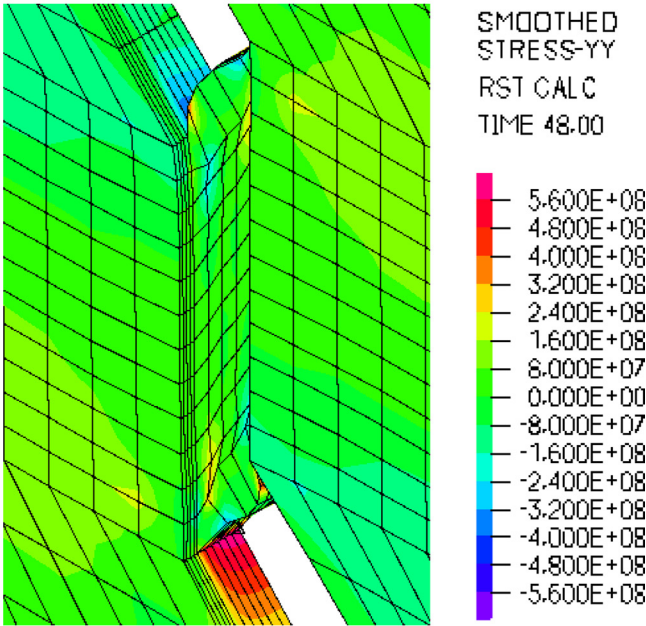
distributions from FE analysis are shown at the middle plane of the shear zone for both the standard and new design specimens at the same shear stress  $\tau_{yz} = 176$  MPa. From Fig. 10, it is seen that the shear strains  $\gamma_{xy}$  at the top and bottom of the middle plane of the shear zone are identical with opposite signs. This suggests that the out-of-plane rotation leads to the rotation of the end of the shear zone. Further, it is seen in Fig. 10 that the maximum out-of-plane shear strain of the standard specimen is 0.124, which is 2.5 times that of the new specimen design (0.05). In other words, the new specimen design minimizes out-of-plane shear strain that prevents the rotation of the end of the shear zone.

Another interesting question is how the normal stress distributes around the shear zone and its impact on the shear stress within the shear zone. G'Sell and Boni suggested that there are always "unwanted" normal stresses in the conventional

**FIG. 11** Calculated normal stress distribution in (a) the standard design; and (b) the new specimen design. The unit of the stresses shown is Pa.



(a)



(b)

shear test because of grip constraints [14]. However, the calculated normal stresses within the shear zone for both the standard and new specimen designs are very small from the FE analysis (Fig. 11). These results are consistent with the earlier ones in Ref. 5 on a similar geometry to the standard one in the present study. Again, these results suggest that the shear zone is indeed in simply shear state and the impact of the normal stress on shear stress calculation is negligible.

## Conclusions

A new shear test method has been successfully developed that coupled a new shear test specimens with digital image correlation to measure both the shear strength and shear stress–shear strain curves of AA5754 sheets up to large strains. The results show that simple shear state is reached within the shear zone. 3D finite element analysis (FEA) reveals that the out-of-plane shear strain is significantly reduced to 5 % in new shear specimen design compared to that of over 12 % for the standard specimen design. The rotation of the end of the shear zone is, thus, prevented.

## References

- [1] Wierzbicki, T., Bao, Y., Lee, Y.-W., and Bai, Y., “Calibration and Evaluation of Seven Fracture Models,” *Int. J. Mech. Sci.*, Vol. 47, Nos. 4–5, 2005, pp. 719–743.
- [2] Ramberg, W. and Miller, J. A., “Twisted Square Plate Method and Other Methods for Determining the Shear Stress–Strain Relation of Flat Sheet,” *J. Res. Natl. Bur. Stand.*, Vol. 50, No. 2, 1953, pp. 111–123.
- [3] Davis, H. E., Troxel, G. E., and Wiskocil, C. T., *Testing and Inspection of Engineering Materials*, McGraw-Hill, New York, 1949, p. 112.
- [4] Bradley, W. A., “Stress Distribution in Single-Shear Sheet Specimens,” ASTM STP No. 289, ASTM International, West Conshohocken, PA, 1960, pp. 21–24.
- [5] Chen, F.-K., “Deformation Analysis of Simple-Shear Sheet Specimens,” *J. Eng. Mater. Technol.*, Vol. 117, No. 3, 1995, pp. 269–276.
- [6] ASTM B831-93: Standard Test Method for Shear Testing of Thin Aluminum Alloy Products, Annual Book of ASTM Standards, ASTM International, West Conshohocken, PA, 2011.
- [7] Sutton, M. A., Orteu, J.-J., and Schreier, H. W., *Image Correlation for Shape, Motion and Deformation Measurements*, Springer, New York, 2009.
- [8] Kang, J., Wilkinson, D. S., Wu, P. D., Bruhis, M., Jain, M., Embury, J. D., and Mishra, R., “Constitutive Behavior of AA5754 Sheet Materials at Large Strains,” *J. Eng. Mater. Technol.*, Vol. 130, No. 3, 2008, p. 031004.
- [9] Kang, J., McDermid, J. R., and Bruhis, M., “Determination of the Constitutive Behavior of AA6022-T4 Aluminum Alloy Spot Welds at Large Strains,” *Mater. Sci. Eng. A*, Vol. 567, 2013, pp. 95–100.

- [10] Kang, J., McDermid, J. R., and Bruhis, M., "Measuring the Mechanical Properties of Aluminum Sheets and Their Resistance Spot Welds at Large Strains Using Digital Image Correlation Coupled with a Modified Shear Test," *Paper No. 2012-01-0181*, SAE Institute, New York, 2012.
- [11] Kang, J., Gong, K., Shen, G., Chen, J., and Liang, J., "Evaluation of Constitutive Behavior of Aluminum Extrusions and Their GMAW Welds," *Paper No. 2013-01-0384*, SAE Institute, New York, 2013.
- [12] GOM *mbH User's Manual; Version 6*, "Aramis-Deformation Measurement Using the Grating Method," Braunschweig, Germany, 2011.
- [13] ADINA, "Theory and Modeling Guide," Report ARD 01-7, Vol. 1, ADINA R&D, Watertown, MA, 2001.
- [14] G'Sell, C. and Boni, S., "Application of the Plane Simple Shear Test for Determination of the Plastic Behavior of Solid Polymers at Large Strains," *J. Mater. Sci.*, Vol. 18, No. 3, 1983, pp. 903-918.

---

STP 1571, 2014 / available online at [www.astm.org](http://www.astm.org) / doi: 10.1520/STP157120130078

M. Freitas,<sup>1</sup> L. Reis,<sup>1</sup> B. Li,<sup>1</sup> I. Guelho,<sup>1</sup> V. Antunes,<sup>2</sup> J. Maia,<sup>2</sup>  
and R. A. Cláudio<sup>3</sup>

## In-Plane Biaxial Fatigue Testing Machine Powered by Linear Iron-Core Motors

### Reference

Freitas, M., Reis, L., Li, B., Guelho, I., Antunes, V., Maia, J., and Cláudio, R. A., "In-Plane Biaxial Fatigue Testing Machine Powered by Linear Iron-Core Motors," *Application of Automation Technology in Fatigue and Fracture Testing and Analysis*, STP 1571, Peter C. McKeighan and Arthur A. Braun, Eds., pp. 63–79, doi:10.1520/STP157120130078, ASTM International, West Conshohocken, PA 2014.<sup>4</sup>

### ABSTRACT

This work presents a new in-plane biaxial fatigue-testing machine built with four iron-core linear motors, which are presently the most powerful on the market for industrial applications. The testing system includes a non-conventional guiding device, allowing an adjustable and precise linear movement without contact, with many advantages for fatigue testing and, in particular, for biaxial in-plane testing. These are assembled in a strong horizontal frame, allowing several configurations for uniaxial and biaxial testing. The control can be made in open loop (by controlling directly the current on the motor, which is almost proportional to the force) or closed loop through the  $\pm 5$ -kN dynamic force transducers or by the magnetic encoders with 1  $\mu$ m resolution. Details of the controller are also presented, which was specifically designed to keep the specimen stable and to ensure biaxial symmetry during the fatigue test. The dynamic force capacity under several biaxial force conditions is presented by

---

Manuscript received May 18, 2013; accepted for publication January 8, 2014; published online April 30, 2014.

<sup>1</sup>ICEMS, Instituto Superior Técnico, UTL, Av Rovisco Pais, 1049-001 Lisboa, Portugal.

<sup>2</sup>ESTSetúbal, Instituto Politécnico de Setúbal, Campus do IPS, Estefanilha, 2910-761 Setúbal, Portugal; and CIEEE, Instituto Superior Técnico, UTL, Av Rovisco Pais, 1049-001 Lisboa, Portugal.

<sup>3</sup>ICEMS, Instituto Superior Técnico, UTL, Av Rovisco Pais, 1049-001 Lisboa, Portugal; and ESTSetúbal, Instituto Politécnico de Setúbal, Campus do IPS, Estefanilha, 2910-761 Setúbal, Portugal.

<sup>4</sup>ASTM Sixth Symposium on *Application of Automation Technology in Fatigue and Fracture Testing and Analysis* on May 23, 2013 in Indianapolis, IN.

diagrams, showing that this machine is appropriated to test efficiently small samples of engineering materials.

### **Keywords**

in-plane biaxial fatigue, iron-core linear motors, fatigue-testing machine

## Introduction

Currently, many experimental fatigue tests are performed on servo-hydraulic-testing machines. The servo-hydraulic actuation provided over the last decades is a good solution for general test systems because of its versatility, fast response, and force capacity [1]. Examples of such machines can be found in the catalogue of the most important testing brands, such as Instron MTS, etc. The principle of these systems is based on servo valves that are able to deliver a precision-controlled amount of hydraulic power to an actuator, providing a fast and precise control to that actuator. With an appropriate feedback controller, accessing a variety of transducers, it is possible to control the actuator movement in either position, force, velocity, acceleration, sample strain, or any other coupled transducer, thereby allowing reproduction of any reference signal (waveforms, random spectrums, etc.) at frequencies that, in some cases, can exceed 200 Hz (generally, for most of the fatigue tests, the working frequency ranges from 5–20 Hz). For most of the cases, the hydraulic circuit operates as pressure source, keeping a constant oil pressure independent of the flow rate. This is essential for a fast and reliable answer from the machine controller. However, enormous power is lost in the form of heat with large consequences in running and maintenance costs.

In the last decade the most important manufacturers of fatigue-testing machines made available uniaxial testing machines with a new actuation technology, based on linear actuators and totally electrical. These types of machines can be found in the catalogue of some manufacturers such as Bose ElectroForce, Instron ElectroPuls, or MTS Acumen. This new technology is a viable alternative to the traditional hydraulic actuators, which is especially suitable for low-force capacity dynamic tests, being considered the state-of-the-art of non-hydraulic test systems. The commercial success of these actuators are due mainly to their much lower operating costs and many other advantages such as: no consumables needed, much less electrical consumption, less heat generation, less noise, high cleanliness, and essentially no wear or friction. The principal drawback is the limitation in force capacity, in which the most powerful machines can achieve 15 kN (with two linear motors in tandem), being much less than what is possible to achieve with hydraulics, but enough to test small samples of most engineering materials.

In many industries, such as aerospace, automotive, naval, and so on, critical components are generally subjected to complex multiaxial loading conditions. It is important to characterize and develop constitutive models to predict the mechanical behavior of structural materials under real service loading conditions. Biaxial loading is one particular case that can be found in many of the industries, being

necessary to quantify and clarify the yield criteria and constitutive equations of a particular material. For biaxial fatigue testing, there are currently two methods of producing biaxial stresses in material for different types of specimens [2]. The first method employs thin-walled cylindrical tube specimens subjected to combined axial-torsion loading, whereas the second method uses cruciform specimens subjected to the biaxial tension-tension loadings.

The combined axial-torsion test is a popular biaxial testing system used, for example, to simulate the stress states of power transmission shafts. This is, in most cases, an accessory that can be included in single axis servo-hydraulic test machines. However, only some stress states can be simulated with this test type [3]. This means that the biaxial tension stress state and the biaxial compression stress state cannot be simulated by the combined axial-torsion test system. Another disadvantage of the first method is that it requires the material be in the form of a circular tube, thus being difficult to apply to rolled sheet materials and most of the composite shapes.

For biaxial in-plane fatigue tests, at least four actuators are needed to ensure that the center of the specimen does not move during the test because of deformation and to ensure symmetry. The servo-hydraulic actuator type is almost the only option available on the market for biaxial in-plane fatigue tests. As can be found in the catalogues of some brands (Instron, MTS, etc.), these machines are huge and can exceed 500 kN in force capacity. The installation and maintenance costs are prohibitive for most laboratories, even if a lower force capacity is required. Bose ElectroForce has an alternative to servo-hydraulic actuators for in-plane biaxial fatigue tests; however, the biaxial testing machine presented in their catalogue has only a capacity of 200 N (peak force), which is appropriate to test materials on soft tissues but is too low to test engineering structural materials.

The purpose here is to present a novel, low-cost, and efficient in-plane, biaxial testing machine, based on the linear electrical motors and with an innovative guiding system different from the traditional solutions. This new test system was totally developed by the authors and is part of an extensive program to test several specimens under different combinations of in-plane biaxial forces. This system has been used to test several different materials to validate multiaxial fatigue damage models, including the minimum circumscribed ellipse (MCE) approach proposed by some authors [4].

## Machine Developed

### **HARDWARE USED**

Among the most important features for a fatigue test machine, based on electric motors, are the controller and the actuators. In the machine, developed, iron-core direct-drive linear motors were used with drivers from the Parker Hannifin Corporation. These iron-core motors offer the highest force available per unit volume having no mechanical devices to produce linear movement, resulting in a zero

backlash movement with a very fast response. The drawback of these motors is the high attractive force that is created between the coil and the magnet track, which is about 10 times the rated force of the motor that, in the solution presented, is used to pre-load several air bearings. Figure 1 shows one iron-core motor with the coil on the top and several rows of magnets on the bottom. In the assembly of the machine developed, the coil is fixed to the lower part and the magnets are installed in the moving part.

The technical characteristics of each motor with included hardware:

Motor (supplier parameters)

- force capacity: continuous: 2230 N, peak: 7433 N,
- attractive force (between coil and magnet): 21351 N,
- gap between coil and magnet: 0.9 mm,
- current (rms): continuous: 5.5 A, peak: 24.6 A,
- power: continuous: 1.06 kW, peak: 21.2 kW,
- force constant: 286.4 N/A,
- electrical time constant: 4.8 ms,
- length of the coil: 785.5 mm, and
- length of the magnets: 840 mm (four modular tracks).

Driver

- programming language: Codesys, and
- driver switching frequency: 8 kHz (can go up to 32 kHz with lower power).

Encoder

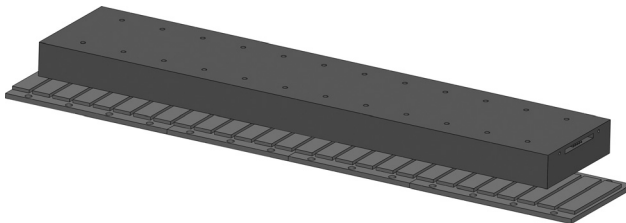
- type: magnetic encoder: RS422 digital output signal,
- encoder resolution: 1  $\mu\text{m}$ ,
- edge separation: 0.5  $\mu\text{s}$ ,
- maximum velocity: 1.04 ms,

Force transducer and conditioners

- stainless steel, low profile, pancake design,
- $\pm 5$  kN dynamic capacity,
- output: 1 mV/V (fatigue-rated version),

---

**FIG. 1** Linear motor (iron core and magnets).



- excitation voltage: 10 V (dc), and
- low-pass filter: 288 Hz.

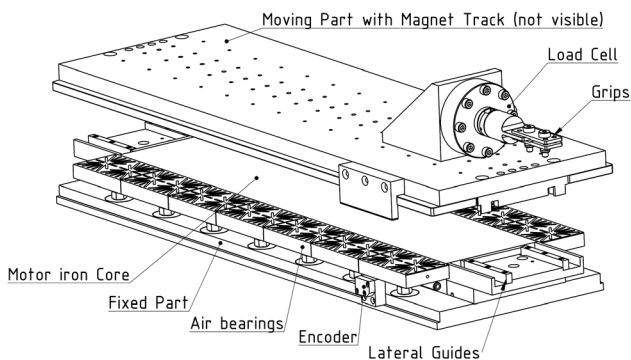
The peak values are for an actuation time less than 1 s. The force capacity given for continuous operation is for natural air cooling. As will be seen, the zone below the coil is water cooled, which guarantees that the motor can be operated above the nominal conditions.

These motors include a patented anti-cog technology from Parker Hannifin Corporation that reduces the cogging forces. In the installation developed, the cogging forces can reach 20 N on certain motor positions. To reduce this effect even more, the motor current necessary to move the motor can be mapped and used during subsequent motions to further reduce the cogging forces.

### DRIVING SYSTEM ASSEMBLY

The motor is assembled in an aluminum structure weighting  $\sim 80$  kg, including the transducers as shown in Fig. 2. The moving mass weighs 32 kg. An innovative guiding system without contact was developed to sustain the constant attractive forces that are created between the coil and magnet, which are 21 351 N excluding external forces. The guiding system was built with a combination of air bearing and lateral guides with rollers. The attractive magnetic force is used to pre-load two rows of air bearings (one in each side of the coil), allowing a planar movement of the moving part of the motor with almost no contact or friction supported by the air flow. In our installation, an air compressor with maximum power of 11 kW is used to supply air for the air bearings. Each air bearing has a fine adjustment to ensure that all the bearings are in the same plane and to reduce air gaps to  $\sim 5 \mu\text{m}$ . The lateral movement of the motor is limited by four lateral guides with rollers. As an option, the lateral movement can be adjusted easily for alignment purposes or to create a lateral gap in which the motor can move laterally without mechanical restrictions

**FIG. 2** Driving system assembly.



(patent pending). The encoders are attached to the side of the motors, being the maximum allowable lateral displacement of the motor compatible with the encoder. The force transducer is connected to the top of the motor (moving part), making it possible to adjust the distance from the force transducer to the specimen. Some care was taken to properly ground all parts of the motors and move the force transducer outside the magnetic fill to avoid problems with signal noise. The base of the coil is water cooled to increase the cooling capacity of the motor, allowing operating with higher forces without excess of heating. Note that the small air flow that is released from the air bearings to the gap between the coil and magnets also contributes to additionally cool the coil. To thermally protect the motors, the coil has a temperature switch and a thermal resistor.

The air bearings were designed and machined by the authors based on considerations that can be found in Ref 5. These particular air bearings do work properly; however, the air power consumption could be reduced if greater precision bearings were employed.

### **TESTING SYSTEM ASSEMBLY**

The machine is assembled on a steel table that weighs  $\sim 400$  kg and has  $2200 \times 2200$  mm size. The table was machined for flatness and marked to properly align the axes. Each motor weighs about 80 kg (including transducers) making the whole assembly weight more than 700 kg. As seen in Fig. 3(a), all the electronics, drives, and computers are in a closed rack, and are the most sensitive parts to noise inside the metal drawers. Figure 3(b) is an isometric view of the machine assembled in the biaxial configuration. The position of the four motors can be changed in the table providing different arrangements for other tests. This will allow, for example, the use of all the motors in a parallel position as a single axis version.

To monitor the fatigue test, a USB microscope can be attached to the machine as shown in Fig. 4. The control software can automatically take pictures of the specimen during the fatigue test and save these images to disk.

### **CONTROLLERS**

Three devices are being used to control the motors. The motor drivers, the control PC, and the interface PC with connections as shown in Fig. 5.

The motor drivers were programmed in Codesys language, operating at 1 kHz. These deliver the current to the motors (requested by the control PC) and safely stop the motors if they pass the second position or force limits or if one of the emergency stops is enabled. The control PC operates in a deterministic environment at 5 kHz. This computer has a data-acquisition board (DAQ) that is used to monitor all the transducers, encoders, and motor parameters and to generate a control (current) signal to the drivers. This computer implements the function generators and most of the control algorithms and a first step in the position or force limits.

The interface (Fig. 6) runs in another computer that communicates to the driver via USB and to the control PC via a TCP/IP network connection at 10 Hz

**FIG. 3** Biaxial fatigue testing system developed: (a) controller, and (b) biaxial configuration.

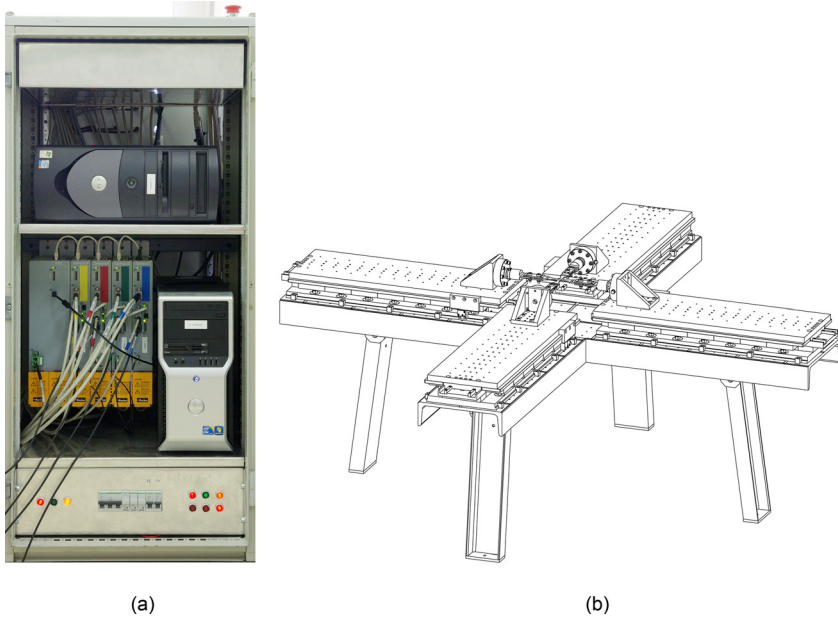


**FIG. 4** Biaxial grips, specimen, and camera.

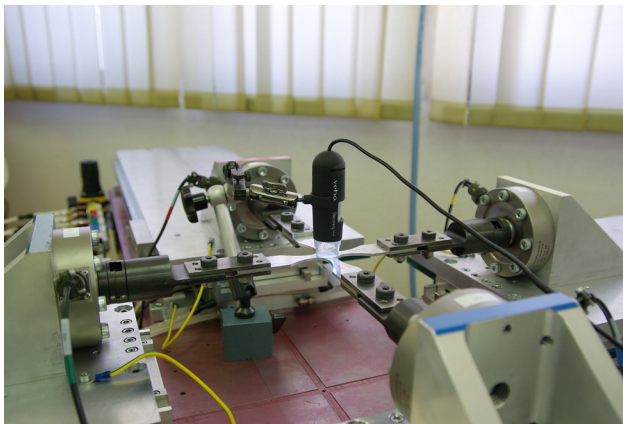
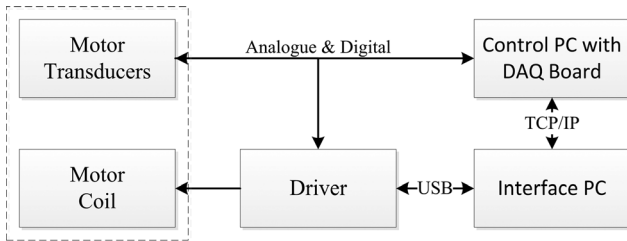


FIG. 5 Control hardware.

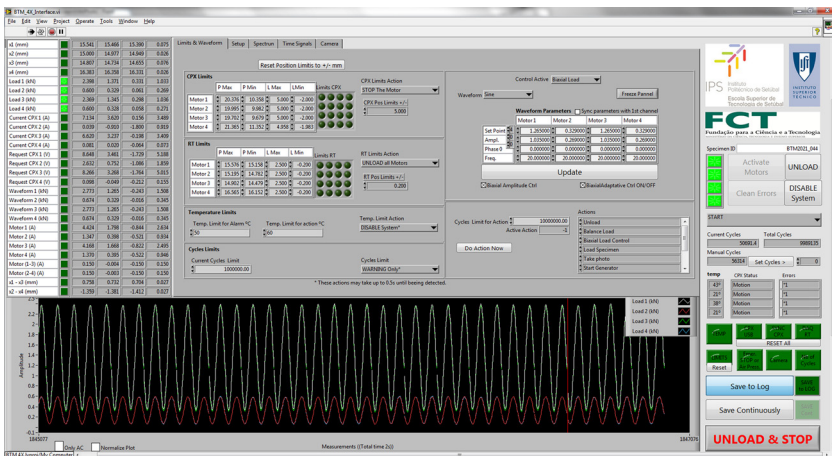


frequency. On this computer, the user can see in real time all the signals: forces, positions, current consumed by the motors, command signal, feedback errors, and temperatures. This includes maximum, mean, minimum, and amplitudes from the last cycles. A third step of low priority limits can be implemented on this computer with programmable actions (temperature, number of cycles, etc.). The actions can be, for example, to hold the generator at maximum force, take a photo with a USB microscope, and continue the generator.

Functions implemented in the interface computer:

- view all the channel with 1 kHz,
- monitor maximum, minimum, mean, and amplitude of each channel,
- change control [current (no feedback), position, force, and biaxial force control],
- change controller settings,
- change limits and actions,

FIG. 6 Interface screen.



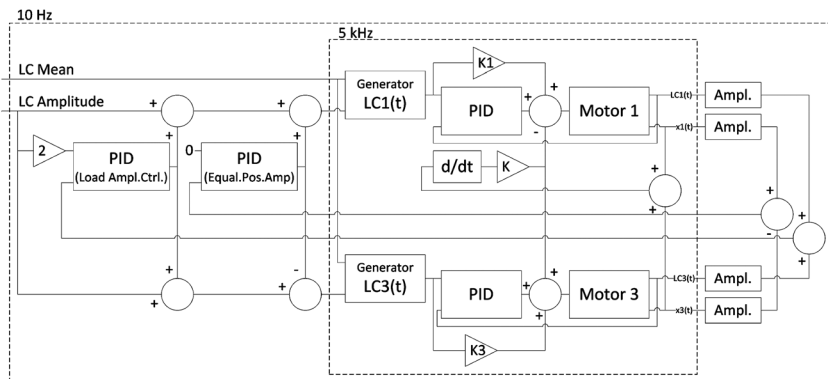
- capture specimen image,
- select waveform (can be drawn in Excel),
- change waveform parameters,
- start/stop and hold waveform generator,
- set peak control and/or biaxial adaptive control,
- system calibration,
- generate test reports, and
- check whole system status.

To monitor the machine operation, the maximum, mean, minimum, and amplitude of each channel can be saved to disk at a requested frequency up to 10 Hz. The signal from any transducer can be saved at 1 kHz. The interface software can also handle the USB microscope, saving the specimen image to disk at a specified frequency.

### BIAXIAL FORCE CONTROL ALGORITHM

For biaxial control, a simple traditional proportional integrative and derivative (PID) controller is not suitable because two motors are running against each other causing instability. Several modified PID controllers were implemented in cascade with references coming from both motors assembled on the same axis. The control algorithm is represented in Fig. 7, which are motor 1 and motor 3, the motors that are operating in opposite positions on the same axis. The algorithm that works at 5 kHz is implemented in the control PC with the DAQ board. The reference signal provided by the generator is multiplied by the motor constant “K1” or “K3” (relation between current and force), being the result of PID operation (that is added to the previous signal) used to do a slight adjustment to ensure that the motors give exactly the same as the reference requested. One other concern in biaxial testing is to stabilize the center of the specimen during a force cycle. Even if the parameters

FIG. 7 Control algorithm.



of the modified cascade PID controller are well adjusted for fatigue testing, the center of the specimen may shake because of continuous adjustment of each motor or even because of small measurement errors from force transducers that are being used for feedback control. This can be decreased slightly by reducing the controller dynamics but will have consequences in the waveform shape. During the first loading cycles, it is quite important to stabilize the machine because it is difficult to detect any problem in the loading without doing at least a few cycles. In the 5 kHz cycle, the specimen center is continuously calculated by adding the actual position of the motors that are operating in the same axis:  $(x1(t) + x3(t))$ . Note that  $x1(t)$  and  $x3(t)$  are positive if the motors are moving in the direction that creates positive forces. To stabilize the specimen center, a virtual damper was implemented by requesting a current signal to the motors that is proportional (“ $K$ ”) to the speed of the specimen center  $d(x1(t) + x3(t))/dt$ . If, for example, a positive speed is detected, it means the specimen is moving in the direction toward motor 1, subtracting an amount of current in motor 1 and adding that same amount in motor 3.

Two other slower PID controls are used in the 10 Hz cycle that is running in the interface computer. Both these controls change the force transducer [load cell (LC)] reference amplitude to ensure that the amplitude of the specimen center position  $(x1(t) - x3(t))$  is equal to zero and that the force amplitude of both motors  $(LC1(t) + LC3(t))$  is equal to the requested ( $2 \times LC$  amplitude) during a complete loading cycle.

This algorithm is quite effective in reducing specimen shake in biaxial force control at frequencies up to 20 Hz.

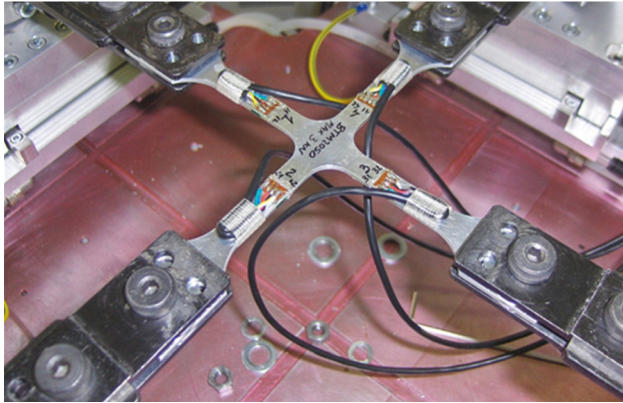
### POSITION CONTROL

When this paper was written, position control was not totally developed. Each motor runs almost without frictional forces making the PID control unstable if there is no specimen mounted. If a specimen is used, the control is easier but requires that the PID parameters must be well adjusted. The driver has a motion control for positioning but this is not appropriate for dynamic tests.

## Biaxial Machine Alignment

Problematic situations were found in controlling the machine under biaxial conditions during the initial tests. During most of these tests, only two arms of the biaxial specimen had displacement. It was also noticed that the center of the biaxial specimen had significant movement. Apart from the controller parameters, these were a consequence of machine misalignment and transducer calibrations. A slight difference between calibrations of two force transducers is enough to compromise biaxial symmetry. Geometrical alignment with traditional measuring equipment is quite difficult and not effective. The solution found to align the machine was to equip a specimen with strain gauges in the arms as shown in Fig. 8. The alignment specimen has eight strain gauges (two in each arm), connected in a 1/4 Wheatstone

**FIG. 8** Specimen for machine alignment.



bridge that is used to measure the normal force and bending in each arm of the alignment specimen. With this procedure, it was possible to align geometrically the machine and to correct force transducer calibrations in opposite arms.

## Machine Performance

### SPECIFICATIONS

The machine was tested using nominal conditions for air cooling provided by the motors supplier. The peak current was set to 200 % of the nominal conditions but the  $I^2t$  temperature protection was kept at nominal conditions. With water cooling, it is possible to extend these limits. However, it is difficult to know the limits of the motors without taking the risk of damaging a coil by excessive heat.

According to the hardware, software, and design project, the machine specifications are the following:

- independent control of the four motors in: position, force, strain, or by an external transducer,
- maximum force (long-term static)<sup>4</sup>:  $\pm 2.2$  kN,
- maximum force (dynamic)<sup>4</sup>:  $\pm 3.5$  kN,
- maximum test frequency: 100 Hz (excellent stability under biaxial loading up to 20 Hz),
- moving mass: 32 kg,
- force transducers:  $\pm 5$  kN,
- encoder resolutions:  $1 \mu\text{m}$ ,
- maximum specimen length: 2000 mm,
- maximum displacement of each motor: 85 mm,

<sup>4</sup> Peak current set to 200 % nominal conditions and  $I^2t$  in nominal conditions.

- maximum speed: 1.04 ms,
- maximum theoretically acceleration: 232 ms<sup>2</sup>,
- total weight: approximately 700 kg,
- horizontal specimen mounting,
- table dimensions: 2200 × 2200 × 1100 mm<sup>3</sup>,
- water cooling: typical flow at maximum power 5l/min,
- air flow and pressure for air bearings: 17 l/s at 5.5 bar,
- power supply: three phase,
- power consumption of the motors: 3.05 kWh (maximum force = 3.5 kN, R = 0), and
- power consumption of the air compressor: 10.3 kWh.

### RESPONSE TO A CURRENT PULSE

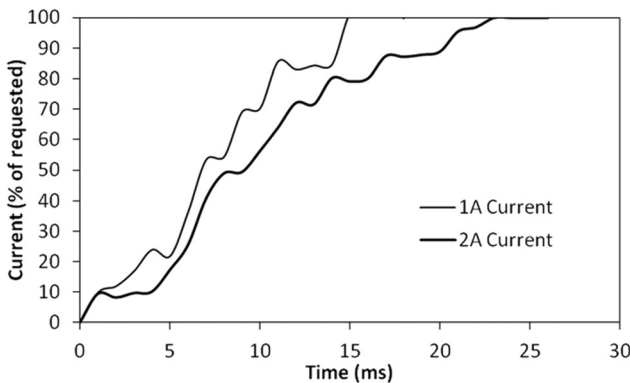
To measure the motors time constant a current pulse of 1 A and 2 A was generated in the controller and the time to reach 80 % of the requested current was measured (Fig. 9).

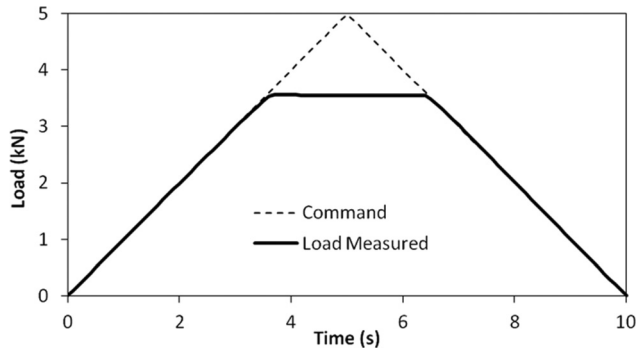
The time to reach 80 % of requested current is about 10 ms for 1 A and 14 ms for 2 A, that is above the specification given by the motor supplier as 4.8 ms.

### STATIC FORCE CAPACITY

The static force capacity was measured with a stiff specimen in force control at a loading rate of 1 kN/s up to 5 kN. As shown in Fig. 10, the machine follows the command exactly but when the motor reaches 200 % of the nominal current, the driver maintains this current, limiting the maximum force at 3.56 kN. For long periods of time, the maximum force allowed by the controller is 2.2 kN to avoid motors overheating.

FIG. 9 Response to a current pulse.



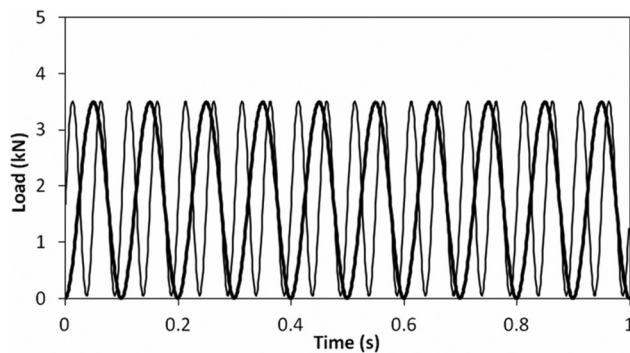
**FIG. 10** Static force capacity.

### BIAXIAL DYNAMIC BEHAVIOR

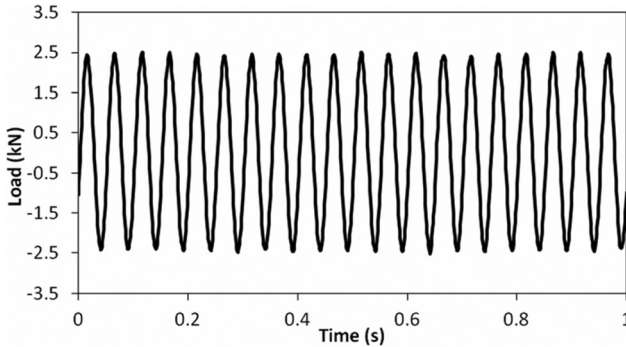
The dynamic force capacity was measured using an in-plane biaxial specimen with an optimized shape for crack initiation [6]. All the figures had the same controller parameters, at least 10 s after the generator was started.

Figure 11 presents the results of the two sine waveforms with 10 and 20 Hz between 0 and 3.5 kN (close to maximum capacity). Above 3.56 kN, the controller cuts the waveform to avoid coil overheating. Both waveforms are well defined. Above 20 Hz, the center of the specimen is no longer stable because the driver is not fast enough to apply the virtual damper.

For a force ratio with  $R = -1$  (Fig. 12), a very small secondary frequency with about 2.5 Hz can be noticed because of amplitude control corrections. This can be reduced by changing the PID parameters of the amplitude controller; however, the correction may take longer to become effective.

**FIG. 11** Sine waveform at 10 Hz and 20 Hz,  $R = 0$ , maximum force 3.5 kN.

**FIG. 12** Sine waveform at 20 Hz,  $R = -1$ , maximum force 2.5 kN.



The triangular waveforms are well-defined at low frequencies, as shown in Fig. 13. When the frequency increases (not shown) the shape becomes more like a sine wave. For the square waveforms, there appears to be a clear undershoot but increasing the PID dynamics can reduce that. The controller is almost supported by the motors constants (“K1” and “K3” in Fig. 7). The PID has a limited effect on this waveform to ensure that the center of the specimen remains stable (Fig. 14).

During several fatigue tests that were done on the optimized in-plane biaxial specimens for force amplitudes ranging from 0.5 kN up to 3.5 kN at frequencies up to 20 Hz,  $R = -1$  or  $R = 0.1$  and for several phase shifts between axes, the maximum deviations measured by the machine transducers are the indicated in Table 1.

**FIG. 13** Triangular waveform at 1 Hz and 5 Hz,  $R = 0$ , maximum force 3.5 kN.

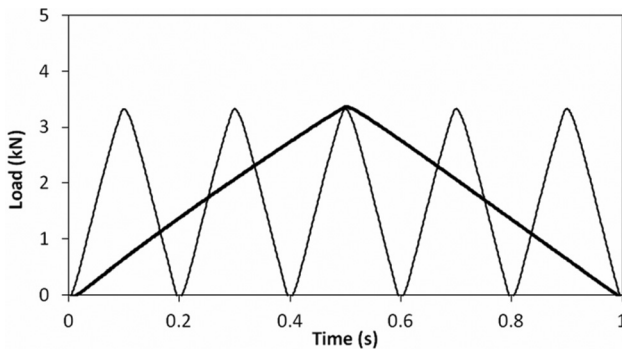
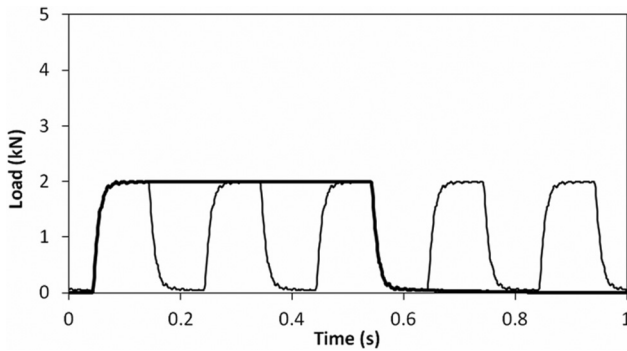


**FIG. 14** Square waveform at 1 Hz and 5 Hz,  $R = 0$ , maximum force 2.0 kN.



The first two rows of Table 1 indicates the condition when the motor is switched on but without current; that basically represents the transducers noise. Note that the force conditioners have a 288 Hz LPF, and the encoders have no filter. When the machine is running with the peak control and biaxial adaptive control active, the maximum force deviation between the four channels is always  $<71$  N, representing  $<2.0$  % relative to the maximum biaxial force capacity of the machine. The specimen center movement, which is obtained by subtracting the actual motors positions running in opposite positions, is  $<70$   $\mu\text{m}$ . Typically, this movement is  $<40$   $\mu\text{m}$ , and part of this is because of the PID controller that causes this movement, even if the machine is in “hold” mode. This can be reduced with a subsequent decrease in control dynamic by changing the PID limits.

### POWER CONSUMPTION

The power measured to run all the computers and drivers with the motors at zero currently is  $\sim 450$  W. Each motor has a nominal power of 1060 W; however, the peak power can increase to 21 195 W according to the motor specifications. At greater rms values of current (or force), there is greater power consumption by the

**TABLE 1** Typical and maximum machine deviations.

	Typical	Maximum
Force in N measured with zero current	1	2
Position in $\mu\text{m}$ measured with zero current	2	4
Force difference in N between channels	8	71
Specimen center movement in $\mu\text{m}$ with the machine in “hold” mode ( $x1(t) - x3(t)$ )	30	35
Specimen center movement in $\mu\text{m}$ with the machine in “running” mode ( $x1(t) - x3(t)$ )	40	70

machine. To have an indicator of the maximum machine power consumption during a regular fatigue test, the power was measured for a force cycle with  $R=0$ , 20 Hz and a maximum force of 3.5 kN (force cycle represented in Fig. 11). The power consumption measured of all motors, computers, electro-valves and motor drivers was 3.05 kWh. It is also necessary to include the air compressor that is essential to maintain the pressure in the air bearings, consuming 10.3 kWh.

The total consumption of the testing system during fatigue tests is then  $\sim 13.35$  kWh. This is much below the power necessary to run an equivalent servo-hydraulic test system, but even that this is quite high considering that the machine has only a 3.5 kN dynamic force capacity. Note that most of this power is being consumed by the air bearings.

## Machine Cost

This machine was built exclusively with the support from “Fundação para a Ciência e Tecnologia” FCT, Portugal (project ref. PTDC/EME-PME/102860/2008), “Deformation and fatigue life evaluation by a new biaxial testing system,” with a total funding of 130 000 euro. This includes 2 years of grants for graduated students and several publications; however, it does not include most of the engineering and development costs.

### FUTURE DEVELOPMENTS

This prototype is working well at conditions for which it was intended and designed. However, some improvements could give additional potential to this machine. This includes:

- determine maximum operating conditions with water cooling,
- track crack propagation with image recognition from the USB digital microscope,
- implement an effective position control that can work with and without specimen,
- improve air bearings to reduce air power consumption, and
- implement a remote control to enable this machine becoming part of a remote lab.

## Conclusions

A prototype of a biaxial in-plane fatigue test machine was built with iron-core linear motors, alternatively to the traditional servo-hydraulic systems. The motors are guided with a patented pending design, based on air bearings, that provides a smooth movement without contact, being appropriated for fatigue testing.

The advantages of these electromagnetic actuators for fatigue testing are many: low installation costs, low maintenance, do not need consumables, the electrical consumption is much less, and almost no noise, wear, or friction. The maximum dynamic force capacity is about 3.5 kN, which is lower when compared with traditional hydraulic based machines but enough to test small specimens of engineering

materials. The authors believe that with forced water cooling, the dynamic force capacity can go up to 5 kN.

The fast dynamic capacity of these actuators and the biaxial force control algorithm developed provide a stable and accurate control during biaxial fatigue tests under force control up to 20 Hz.

The power consumption of the system is much less than the traditional servo-hydraulic systems. Most of the energy consumed is with the air compressor for the bearings. If greater precision air bearings were used, the power consumption could be further reduced.

At the time this paper was written, the machine had completed more than  $30 \times 10^6$  cycles without any failure or evidence of damage, being a good indicator of its reliability in performing fatigue tests.

With future developments, in addition to some improvements, we expect to implement an ancillary lab for this in-plane biaxial test machine so it may be accessed remotely by potential partners from the scientific community.

#### ACKNOWLEDGMENTS

The project is supported by FCT - Portugal, project ref. PTDC/EME-PME/102860/2008, "Deformation and fatigue life evaluation by a new biaxial system."

## References

- [1] Skawki, G. S. A., "A Review of Fatigue Testing Machines," *Eng. J. Qatar Univ.*, Vol. 3, 1990, pp. 55-69.
- [2] Hannon, A. and Tiernan, P., "A Review of Planar Biaxial Tensile Test Systems for Sheet Metal," *J. Mater. Proc. Tech.*, Vol. 198, 2008, pp. 1-13.
- [3] Geiger, M., Hubnatter, W., and Merklein, M., "Specimen for a Novel Concept of the Biaxial Tension Test," *J. Mater. Proc. Tech.*, Vol. 167, 2005, pp. 177-183.
- [4] Freitas, M., Li, B., and Santos, J. L. T., "A Numerical Approach for High-Cycle Fatigue Life Prediction with Multiaxial Loading," *Multiaxial Fatigue and Deformation: Testing and Prediction*, ASTM STP 1387, S. Kalluri and P. J. Bonacuse, Eds., ASTM International, West Conshohocken, PA, 2000, pp. 139-156.
- [5] Van Beek, A., *Advanced Engineering Design, Lifetime Performance and Reliability*, TU Delft, The Netherlands, 2009.
- [6] Guelho, I., Reis, L., Freitas, M., Li, B., Madeira, J. F. A., and Cláudio, R. A., "Optimization of Cruciform Specimen for a Low Capacity Biaxial Testing Machine," *ICMFF10*, Kyoto, Japan, 2013.

---

STP 1571, 2014 / available online at [www.astm.org](http://www.astm.org) / doi: 10.1520/STP157120130079

Y. Lage,<sup>1</sup> A. M. R. Ribeiro,<sup>1</sup> D. Montalvão,<sup>2</sup> L. Reis,<sup>1</sup>  
and M. Freitas<sup>3</sup>

## Automation in Strain and Temperature Control on VHCF with an Ultrasonic Testing Facility

### Reference

Lage, Y., Ribeiro, A. M. R., Montalvão, D., Reis, L., and Freitas, M., "Automation in Strain and Temperature Control on VHCF with an Ultrasonic Testing Facility," *Application of Automation Technology in Fatigue and Fracture Testing and Analysis*, STP 1571, Peter C. McKeighan and Arthur A. Braun, Eds., pp. 80–100, doi:10.1520/STP157120130079, ASTM International, West Conshohocken, PA 2014.<sup>4</sup>

### ABSTRACT

Increased safety and reliability in mechanical components has become a subject of prime importance in recent years. Therefore, a proper understanding of damage and fracture mechanics in materials and components designed to withstand very high cycle fatigue (VHCF) loadings is extremely important nowadays. However, the use of conventional machines for fatigue testing is very time consuming and costly for VHCF tests. Ultrasonic machines have been introduced as a way to increase the number of cycles in fatigue testing up to  $1E^8$  to  $1E^{10}$  cycles within a considerably reduced amount of time. Nevertheless, the accurate measurement of the parameters that influence fatigue life at ultrasonic frequencies (e.g., stress, displacement, strain rate, temperature, and frequency) is still a matter of concern and ongoing development. Because of the high frequencies involved in VHCF testing, a huge amount of heat is generated over the specimen, which greatly affects the variables determining the fatigue behavior. This paper describes the

---

Manuscript received May 18, 2013; accepted for publication March 21, 2014; published online August 29, 2014.

<sup>1</sup>Dept. of Mechanical Engineering, Instituto Superior Técnico, Universidade de Lisboa, Av. Rovisco Pais, 1049-001 Lisbon, Portugal.

<sup>2</sup>School of Engineering and Technology, Univ. of Hertfordshire, College Ln. Campus, Hatfield, AL10 9AB, UK.

<sup>3</sup>Dept. of Mechanical Engineering, Instituto Superior Técnico, Universidade de Lisboa, Av. Rovisco Pais, 1049-001 Lisbon, Portugal (Corresponding author), e-mail: [manuel.freitas@ist.utl.pt](mailto:manuel.freitas@ist.utl.pt)

<sup>4</sup>ASTM Sixth Symposium on *Application of Automation Technology in Fatigue and Fracture Testing and Analysis* on May 23, 2013 in Indianapolis, IN.

design and instrumentation of an ultrasonic fatigue testing machine that operates at a working frequency of 20 kHz. Among other features, it incorporates automated strain and temperature control. In order to run automated tests, a closed-loop monitoring and control system was developed based on the measured temperature and displacement amplitudes. Temperature readings are made with a pyrometer and thermography camera, and displacement is monitored at the free end of the specimen with a high-resolution laser. The machine's power output is continuously adjusted from the displacement readings, so that the stress variations within the specimen are as flat as possible. When the temperature increases above a certain set value, a cooling function is triggered and the test is interrupted until the specimen is cooled down. Data are acquired, managed, and processed with a data acquisition device working at a 400 kHz sampling frequency. The advantages and limitations of metal fatigue testing at very high frequencies are discussed in this paper, with special emphasis on strain and temperature-control issues. Comparisons are made of tests carried out with and without both displacement and temperature control on two metallic alloys, copper 99 % and carbon steel, with the determination of strength-life (S-N) curves.

### Keywords

very high cycle fatigue (VHCF), ultrasonic fatigue testing, amplitude control, temperature control, experimental tests

## Introduction

The increasing need for faster measurements in fatigue combined with improvements in piezoelectric technology made ultrasonic testing an attractive technique for establishing strength-life (S-N) curves in very high cycle fatigue (VHCF). The piezoelectric technique was originated by Hopkinson in the beginning of the 20th century. Fifty years later, Mason presented the first ultrasonic fatigue testing machine working at 20 kHz. These were the early days of VHCF, and other machines operating at higher frequencies followed, but the difficulty of correlating results constituted a hindrance that slowed down the development of this technique.

Recent advances in sensor technology, new computational methods, and faster control systems have made it possible to tackle some of the problems related to VHCF. However, the accuracy of the determination of applied stresses and issues related to temperature control of the specimens when tested at very high frequencies still constitute a challenge.

The latest developments in the ultrasonic technique have been presented by Bathias and colleagues [1–5]. An extensive review of the fundamentals on VHCF using ultrasonic methods, including considerations of the machine development, its performance, and its applications, can be found in these works. It has been observed that specimens are subjected to very large temperature increases in ultrasonic fatigue testing as a result of internal friction. Temperature has been pointed out as the most significant variable affecting results in VHCF testing [6]. To gain control over the temperature, the specimen can be cooled down with cooling fluids.

However, some fluids may lead to changes in the mechanical properties of the specimen's surface, and thus condition results.

In the more recent works presented by Stanzl-Tschegg and colleagues [7,8], the principles and testing procedures of VHCF tests are overviewed. Findings in the areas of crack formation, nonpropagation of small cracks, long crack propagation and thresholds, effects due to frequency, and superimposed and variable amplitude loading are reported and discussed as well.

Many other publications can be found on the concept of ultrasonic waves in fatigue. In work by Mayer and colleagues [9,10], cyclic torsion and cyclic tensile-compression fatigue experiments were performed on aluminum alloy 2024-T351. These tests were conducted in both high cycle fatigue and VHCF regimens with either constant or variable amplitudes. Müller and Sander [11] quantified the effect of variable amplitude loadings and monitored crack growth. Sohar et al. [12] describe investigations on surface crack nucleation and propagation on AISI D2 cold work tool steel in the gigacycle regimen. Zimmermann et al. [13] studied the effects of particle strengthening and high temperature on the VHCF behavior of hardened nickel-base alloy Nimonic 80A. Many other authors have published in the area of ultrasonic fatigue as well [14–17].

The VHCF regimen is now an established technology in what concerns the layout of ultrasonic fatigue machines. Nevertheless, the accurate measurement of the variables that influence fatigue life (stress, displacement, temperature, etc.) at ultrasonic frequencies is still a matter of concern and under continuous development by the scientific community.

## Ultrasonic Fatigue Concept

An ultrasonic fatigue test differs from conventional fatigue tests in the nature of the vibration used. An ultrasonic test seeks to reproduce free vibration, with the specimen vibrating at its own fundamental frequency. In conventional testing the working frequency is set away from the fundamental frequencies (often below the fundamental frequency) and the specimen is subjected to forced vibration. In order to perform ultrasonic tests, it is necessary to design a specimen with a fundamental frequency that is tuned to match the machine's working frequency.

An ultrasonic fatigue machine is based on the concept of free vibration. Elastic wave theory can be used to explain this concept, in particular the theory of longitudinal waves that propagate through a solid material. Longitudinal waves are propagated throughout the specimen, and the displacement of its particles is parallel to the direction of the wave propagation. The speed of these waves is dependent on the material's properties and path geometry.

### **LONGITUDINAL ELASTIC WAVES—FORMULATION FOR THE SPECIMEN'S DESIGN**

The specimen is designed in such a way that, under longitudinal resonance [1], its response satisfies the differential equation of motion (Eq 1).

$$(1) \quad \frac{\partial^2 u(x, t)}{\partial x^2} + P(x) \frac{\partial u(x, t)}{\partial x} = \frac{1}{C^2} \frac{\partial^2 u(x, t)}{\partial t^2}$$

where:

$C = \sqrt{E_d/\rho}$  = wave propagation velocity,

$P(x) = S'(x)/S(x)$  = cross-sectional area ratio,

$E_d$  = dynamic Young's modulus, and

$\rho$  = mass density.

The solution of the differential equation of motion takes the form

$$(2) \quad u(x, t) = U(x) \sin(\omega t)$$

where  $\omega$  is the resonant frequency in radians per second. The amplitude of vibration  $U(x)$  along the specimen can be determined at each point from

$$(3) \quad U''(x) + P(x)U'(x) = -\frac{\omega^2}{C^2} U(x)$$

The specimen's geometry can be described as being composed of two well-determined parts (see Fig. 1): a cylindrical one and another with a variable cross-section obtained from the revolution of a hyperbolic cosine about the middle axis. These are expressed by the following functions:

$$(4) \quad \begin{aligned} y(x) &= R_2, & L_2 < |x| < L \\ y(x) &= R_1 \cosh(\alpha x), & |x| \leq L_2 \end{aligned}$$

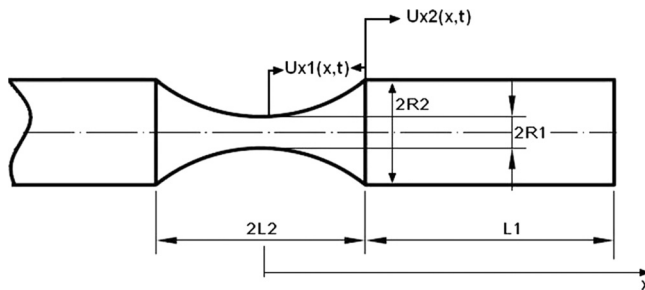
where:

$L = L_1 + L_2$ , and

$\alpha = (1/L_2) \text{arc cosh}(R_2/R_1)$ .

Once the appropriate boundary conditions and resonant frequency are determined, the solutions for the longitudinal displacements along the specimen are obtained.

FIG. 1 Standard specimen test geometry.



$$(5) \quad u_1(x, t) = A_0 \frac{\cos(kL_1) \cosh(\alpha L_2) \sinh(\beta x)}{\sinh(\beta L_2) \cosh(\alpha x)} \sin(\omega t), \quad x < L_2$$

$$(6) \quad u_2(x, t) = A_0 \cos[k(L - x)] \sin(\omega t), \quad L_2 < x \leq L$$

with

$$(7) \quad k = \sqrt{\frac{\omega^2}{C^2}}$$

$$(8) \quad \beta = \sqrt{\alpha^2 - k^2}$$

where  $A_0$  is the displacement amplitude at the free end of the specimen.

Equations 5 and 6 are used to obtain the stress  $\sigma$  and strain  $\varepsilon$  at any location  $x$ .

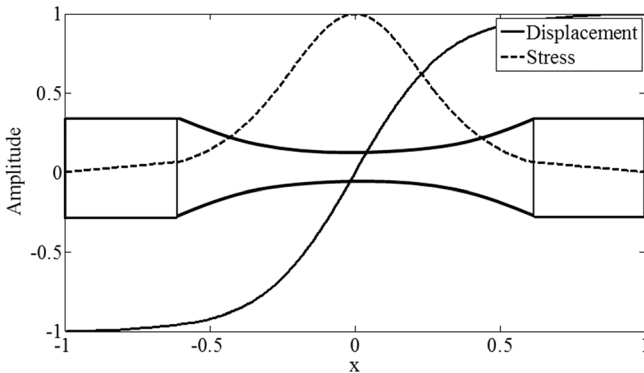
$$(9) \quad \varepsilon(x, t) = \frac{\partial u(x, t)}{\partial x}$$

$$(10) \quad \sigma(x, t) = E_d \varepsilon(x, t)$$

This analytical solution is used to determine the specimen's dimensions, so that the first longitudinal vibration mode is tuned with the exciting frequency. Note that in deducing the exact equations, a hyperbolic cosine was used to define the variable cross-section, but in practice a circular profile is used. This is because of the manufacturing advantages related to the milling process of the specimens. Nevertheless, it is possible to demonstrate that this is a good approximation, in which the error does not exceed 1.8 % [1].

Figure 2 shows the evolution of displacement and stress along the typical specimen geometry when calculated by the analytical Eqs 5, 6, and 10.

FIG. 2 Distribution of displacement and stress in the specimen.



# Ultrasonic Fatigue Testing Machine

In an ultrasonic fatigue testing machine, the displacement imposed by the piezoelectric actuator must be transmitted along a series of resonant elements connected together. The specimen is at the end of this series of elements, and the displacement is measured at its free end. The stress level is determined as a function of the displacement. Because of the very specific geometrical properties of the elements, the amplitude of vibration changes from the actuator to the specimen's free end, which translates into different levels of axial stresses being developed along the elements.

When designing an ultrasonic fatigue testing machine, the primary concern is that the whole system's longitudinal mode frequency must be the same as the working frequency of the exciter. Next comes monitoring and control. The ultrasonic fatigue testing machine must be able to monitor and control parameters such as temperature, stress level, frequency, and power output.

The first version of the ultrasonic fatigue testing machine being discussed in this paper is presented in Refs 18 and 19.

## GENERAL MACHINE SETUP

The setup of the ultrasonic fatigue testing machine presented here is identical to some other existing ones. Differences emerge regarding the types of sensors used and the monitoring and control features. The machine integrates four main systems, which are illustrated in Fig. 3:

- resonant system,
- cooling system,
- measurement system, and
- data acquisition, processing, and control system.

These four systems work together to carry out fatigue tests within the ranges initially set for temperature, stress level, etc.

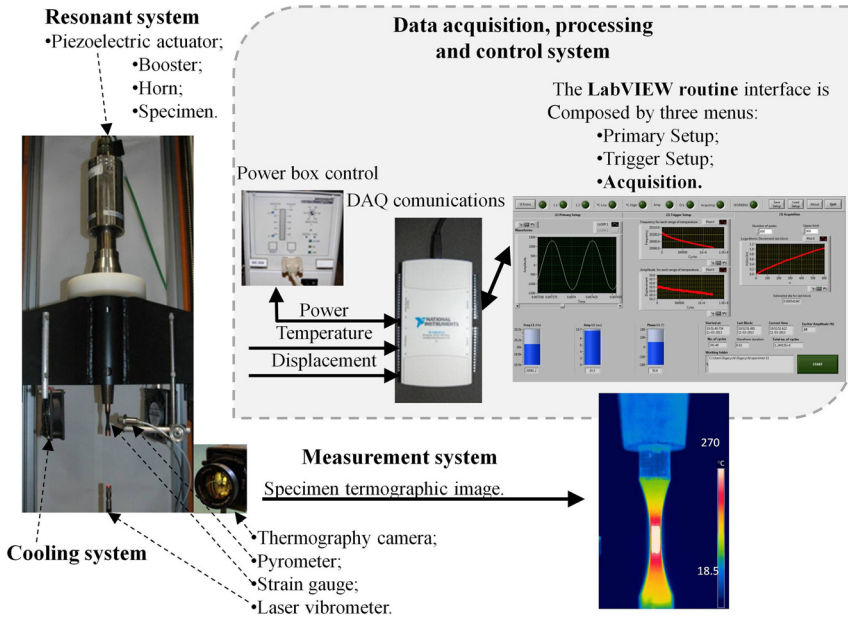
The resonant system incorporates an ultrasonic piezoelectric exciter that is used to excite the system to its first longitudinal vibration mode. It works in the range of 19.5 to 20.5 kHz. A power setting may be changed so that the displacement at the free end of the specimen can be adjusted.

The cooling system is composed of two fans that help to cool the resonant system and specimen during the different test phases.

The measurement system is composed of several sensors. A high-resolution laser Doppler vibrometer and an optional strain gauge are used for acquiring, respectively, the displacement at the free end of the specimen and the strain at its center. Two analog input channels are used to acquire these signals with a sampling frequency up to 200 kHz, or 400 kHz if only one channel is used. A pyrometer is used for monitoring the temperature at the narrow center section of the specimen, and a thermography camera is used to plot the temperature distribution and gradients along the specimen.

The data acquisition, processing, and control system deals with all the monitoring and control inputs and outputs. It controls the resonant system with a

**FIG. 3** Main parts of the ultrasonic fatigue machine setup.



closed-loop feedback system that continuously monitors the stress level and working frequency. A computer program was developed under LabVIEW to serve as the interface with the user.

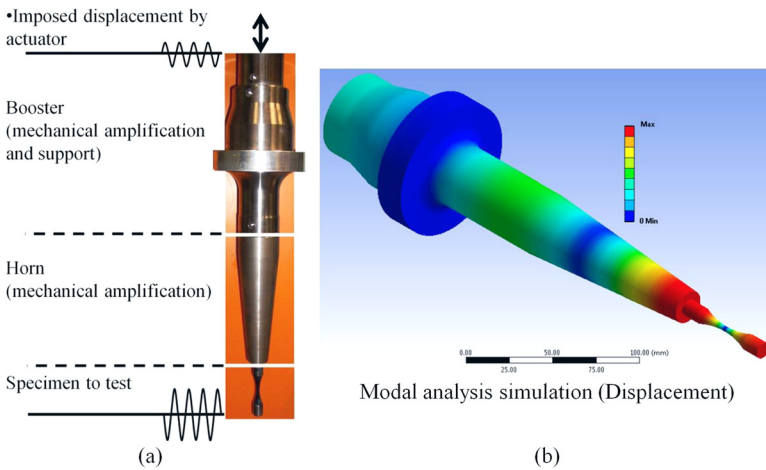
## RESONANT SYSTEM

The resonant system is composed of a piezoelectric actuator, a booster, a horn, and a specimen. These are assembled together in a sequence by screw connections. These four parts form the resonant system of the testing machine and are shown in Fig. 4(a). The mechanical vibration generated by the piezoelectric exciter is meant to reproduce a pure sine wave with a frequency of approximately 20 kHz. This wave is transmitted from element to element down to the end of the specimen. The principle of operation of the vibration system is based on free vibration resulting in a minimum of contact force between the elements in the system.

Each element in the resonant system is manufactured to have the same first longitudinal vibration mode and vibrate in phase opposition, as depicted in Fig. 4(b). Thus, tight tolerances have to be used and manufacturing needs to be very precise. If a single element in the system does not have the same first longitudinal vibration mode—within a tolerance of 2.5 %—the actuator is not able to operate and the system is shut down.

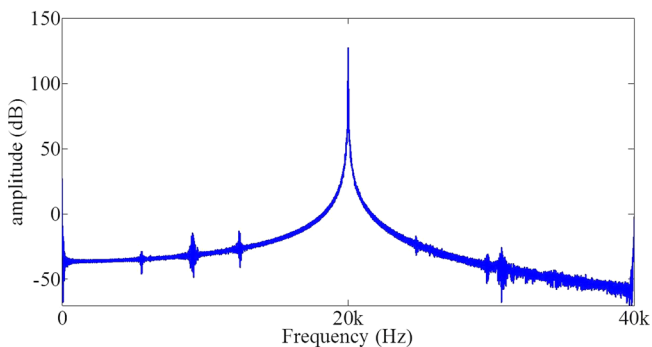
To verify that the system is working as intended, the dynamic response can be measured at the bottom of the specimen. The time signal must be as close as

**FIG. 4** (a) Resonant system components. (b) Modal analysis simulation for the first longitudinal vibration mode at 20 kHz.



possible to a pure sine wave, which is represented by a single peak in the Fourier spectrum. **Figure 5** shows that only residual spectral components exist, with peak amplitudes less than 0.1 % of the fundamental peak frequency at 20 kHz. To evaluate the quality of the time signal, a total harmonic distortion of the fundamental harmonic was computed using a standard LabVIEW routine, resulting in a 1.594 % harmonic distortion. The routine was set up to include up to the tenth harmonic at 200 kHz.

**FIG. 5** Fourier spectrum of signal measured at the bottom of the copper specimen, first longitudinal vibration mode at 20 013 Hz.



Power delivered to the piezoelectric actuator is controlled by a signal generator. A closed-loop feedback algorithm is used to keep the displacement amplitude constant by adjusting the power setting.

### COOLING SYSTEM

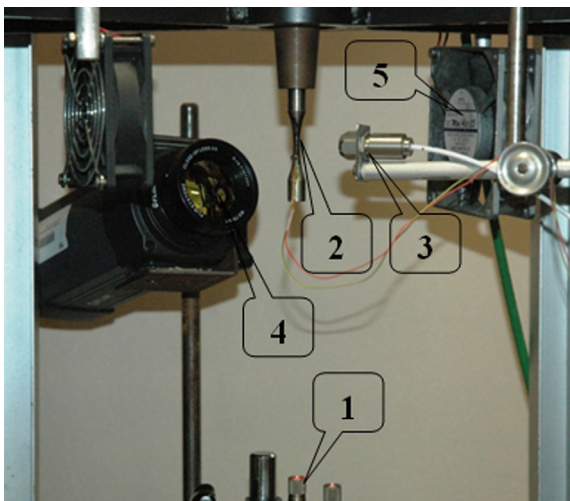
Vibrational energy delivered by the piezoelectric actuator is dissipated along the resonant elements by damping phenomena. Significant heat is generated, and cooler fans are used to speed up the process of bringing the temperature back to normal. The configuration of the cooling system is shown in Fig. 6, with balloon 5 pointing to one of the two existing fans.

### MEASUREMENT SYSTEM

The measurement system integrates the sensors needed to measure the dynamic parameters of the specimen. Their locations are illustrated in Fig. 6, and they include the following:

- a high-resolution laser vibrometer (1) to measure the dynamic response at the bottom of the specimen,
- a strain gauge (2) to measure the dynamic strain at the middle section of the specimen,
- a pyrometer (3) to monitor the temperature at the middle section of the specimen, and
- a thermography camera (4) to map the distribution of the temperature on the surface of the specimen.

**FIG. 6** Configuration of the measurement system.



The stress at the center of the specimen (nodal point) can be determined from the laser measurement at its end (Eq 11). If the strain gauge is used, the stress level can be determined directly from Eq 12. However, the strain gauge has limitations, as its own fatigue life is quite short relative to the whole test duration.

$$(11) \quad \sigma_{\text{laser}} = E_d \left. \frac{\partial u}{\partial x} \right|_{x=0}$$

$$(12) \quad \sigma_{\text{strain gauge}} = E_d \varepsilon$$

### DATA ACQUISITION, PROCESSING, AND CONTROL SYSTEM

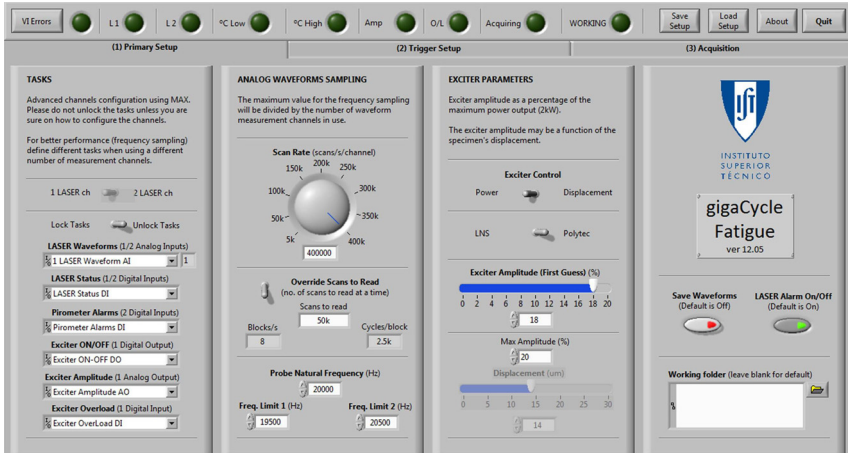
An in-house custom-made package was developed under LabVIEW from National Instruments (NI) for online monitoring and control of the VHCF machine. Communication between the peripherals and the software was accomplished using a multifunction data acquisition (DAQ) device from NI (NI USB-6216). The NI USB-6216 is a multiplexed 16-bit DAQ device with a maximum analog input sampling frequency of 400 kS/s. It can measure up to 16 analog signals at a time and has 32 digital transistor-transistor logic (TTL) inputs and outputs.

This computer software is the main interface with the user. It allows one to set up the initial testing frequency and initial power delivered to the piezoelectric actuator, based on a predetermined value for the axial stress. It also indicates and logs the specimen's temperature, displacement, frequency, power delivered to the piezoelectric exciter, and number of cycles until fracture. Furthermore, it includes an algorithm to estimate and monitor the damping ratio evolution during the whole test. When the fatigue test is finished, a summary of the monitoring history is shown on the computer screen and stored as a spreadsheet file.

This package includes three main displays:

- (1) Primary setup menu (Fig. 7). The measurement channels and acquisition settings (namely, the sampling frequency and the time duration of an acquisition block) are set up in this menu. These settings are related to the nature of the continuous acquisition process in LabVIEW. One run is composed of a finite number of time signal blocks. Each block is then "averaged" to extract the amplitude and frequency. Long blocks may produce inaccurate results because of the rapid change in both temperature and frequency, whereas short blocks may produce instability because of the need for faster processing capabilities. The primary setup also offers the possibility of setting the displacement value at the tip of the specimen. During measurement, a closed-loop feedback system adjusts the exciter's power so that the average displacement per block is constant.
- (2) Trigger setup menu (Fig. 8). The trigger setup offers the possibility to test the performance of the configuration set on the primary setup. This interface is also used to determine delays in the exciter that are very hard to predict otherwise. Once the primary settings are set and the triggers have been determined, there is no need to run the trigger setup again.

FIG. 7 LabVIEW software’s primary setup.



(3) Acquisition display (Fig. 9). The acquisition display shows the current time signal block and the history for a single run. It plots the frequency evolution per block, the average displacement per block, and the logarithmic decrement in the last block. The last block is a transient response time signal of the resonant system at free vibration, giving information on the damping factor.

FIG. 8 LabVIEW software’s trigger setup.

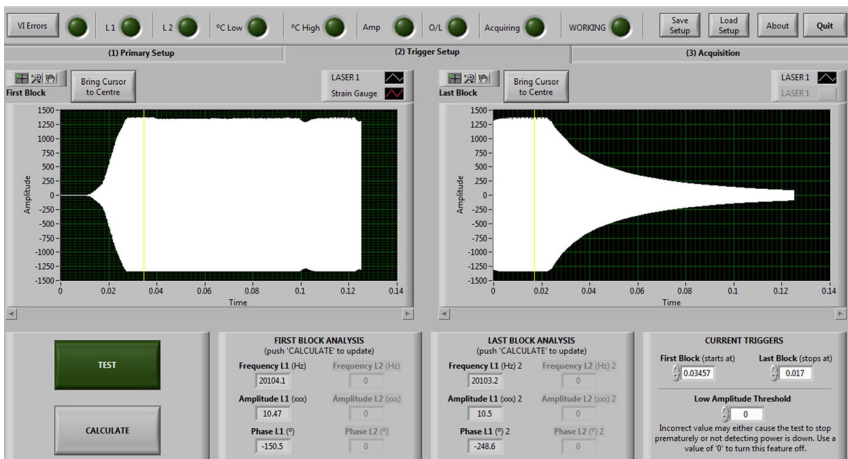
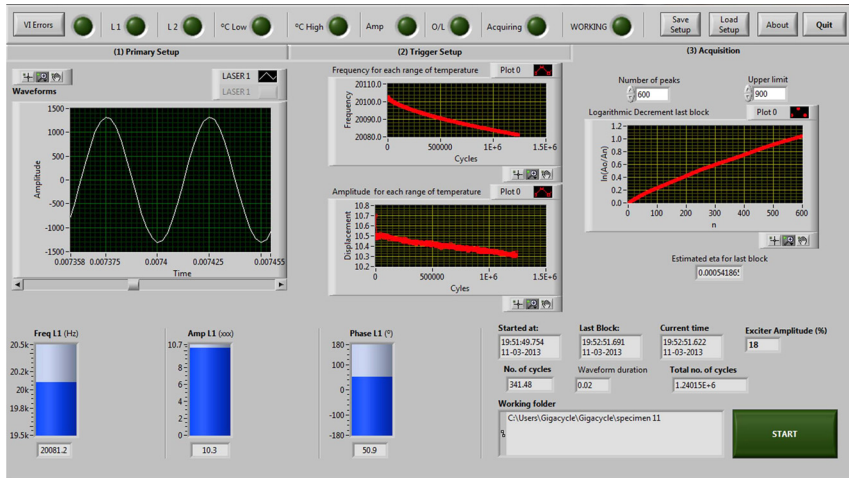


FIG. 9 LabVIEW software's acquisition display.



### Hysteretic Damping Estimation Method

One feature that the discussed machine offers is the ability to provide an estimation of the energy dissipated by the material during the test. For a hysterically damped single-degree-of-freedom system harmonically excited and at steady state, the energy  $\Delta E$  dissipated per cycle of oscillation may be defined as [20]

$$(13) \quad \Delta E = \int_0^{2\pi/\omega} f(u) du = \pi U^2 d \quad \text{with} \quad d = \eta k$$

where:

- $f(u)$  = dynamic force,
- $U$  = displacement peak amplitude per cycle,
- $d$  = hysteretic damping coefficient,
- $k$  = stiffness, and
- $\eta$  = hysteretic damping loss factor.

When plotted on a force-versus-displacement graph, the energy dissipated per cycle of oscillation takes the form of an ellipse.

Equation 13 is used for steady-state conditions, when the applied force is known. Assuming low damping in the system at resonance, the hysteretic damping model can be assumed to be equivalent to the viscous damping model, which can be estimated from the logarithm decrement [21]. The hysteretic damping loss factor may be estimated via Eq 14.

$$(14) \quad \eta = 2\xi \quad \text{with} \quad \delta = \frac{1}{n} \ln \left( \frac{U_i}{U_{i+n}} \right) = \frac{2\pi\xi}{\sqrt{1-\xi^2}} \quad \text{or} \quad \delta = 2\pi\xi \quad (\text{assuming } \xi \ll 1)$$

where:

- $\delta$  = logarithmic decrement ratio,
  - $\xi$  = viscous damping loss factor, and
  - $n$  = number of cycles between peak amplitudes  $U_i$  and  $U_{i+n}$ .
- In the LabVIEW routine, Eq 14 is used as follows:

$$(15) \quad n_j \delta_j = \ln \left( \frac{U_i}{U_{i+n_j}} \right) \quad \text{with } j = 1, \dots, n$$

For example, if a signal with an exponential decay envelope is considered as in Fig. 10(a), Eq 15 yields the results shown in Fig. 10(b), in which the slope is the logarithmic decrement.

Although the hysteretic damping loss factor can be estimated, a discussion of its performance and correlation with fatigue is left to future reports. However, as an example of the possible outcomes, Fig. 11 shows the hysteretic damping factor ( $\eta$ ) for an ultrasonic fatigue test carried out with a temperature between 40°C and 60°C and a middle-section stress of 372 MPa ( $R = -1$ ) for low-carbon steel.

### Parameter Control

When an ultrasonic fatigue test is performed without any type of feedback control, the piezoelectric system delivers a constant power output continuously. Temperatures may increase to very high levels, and in some materials values greater than 300°C have been registered. The increase in temperature has a strong effect on the displacement amplitude and, thus, on the stress amplitudes being generated. In order to keep the displacement and stress as steady as possible, two control

**FIG. 10** Algorithm implemented in LabVIEW to determine the logarithmic decrement and the hysteretic damping loss factor.

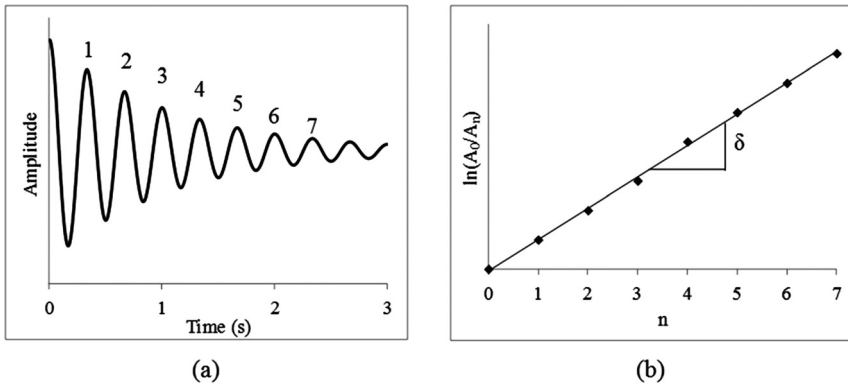
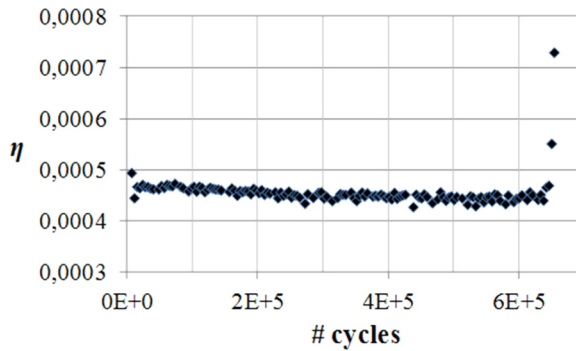


**FIG. 11** Typical hysteretic damping behavior in ultrasonic test for low-carbon steel (not discussed in this paper).



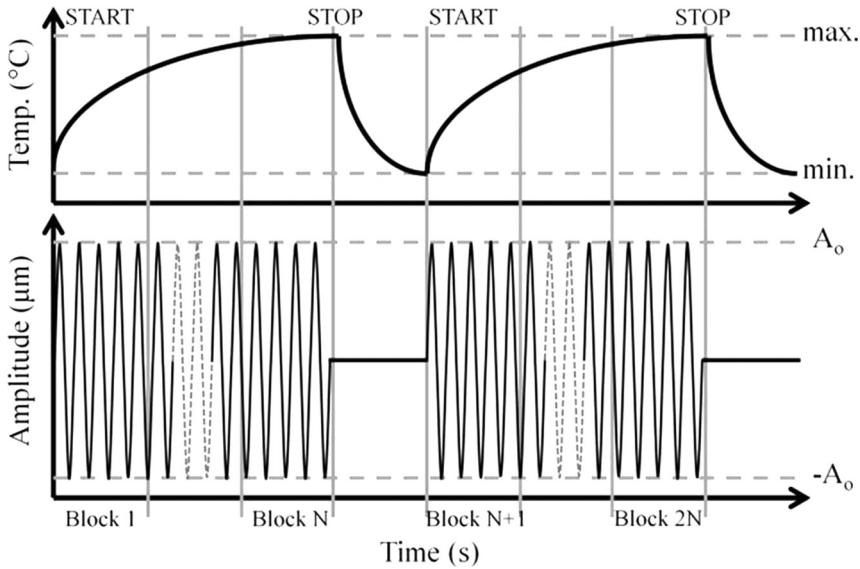
algorithms based on the measured test parameters were implemented. These algorithms are integrated in the LabVIEW package and are based on temperature control and amplitude control. These controls can operate together or independently. The current control functions are updated versions since the first attempt described in Refs 22 and 23.

In the basic test setup, the power provided to the piezoelectric actuator is set and there is no feedback-loop control. The fatigue test starts and runs continuously, without interruption, at 20 000 cycles per second. The signals from the laser and pyrometer are acquired and stored in order to monitor the specimen. The displacement amplitude per measurement period of time (block) is the average of the values measured at steady state. Because the test runs continuously, the temperature will eventually rise to a value outside an acceptable range.

In temperature control the fatigue test runs as long as the temperature is kept within a preset interval  $\Delta T$ . The temperature is continuously monitored while the test is in progress, and at the same time the amplitude, frequency, and power are measured and stored. When the temperature reaches the upper limit, the test is interrupted. The specimen cools down until the temperature reaches the lower preset value, at which point the test is restarted. This process is illustrated in the “saw tooth” plot in Fig. 12. Temperature control contributes to the stability of the vibration amplitude during the test, but it does not eliminate it completely.

With amplitude control activated, the displacement is monitored at the free end of the specimen during each period of time (block). The piezoelectric actuator’s power is continuously readjusted between blocks to keep the vibration amplitude at a constant pre-established value.

**FIG. 12** Illustration of recorded signal with amplitude/temperature control.



## Experimental Procedure in Very High Cycle Fatigue Tests

### TESTING MATERIALS

Two different types of materials, copper (99 %) and carbon steel like the one used in railway wheels, were tested.

The material properties are described in [Table 1](#), where  $E_d$ ,  $\rho$ , YS, and UTS represent, respectively, the dynamic Young’s modulus, the material’s density, the yield stress, and the ultimate tensile strength.

The specimen dimensions for each of the materials tested are presented in [Figs. 13](#) and [14](#).

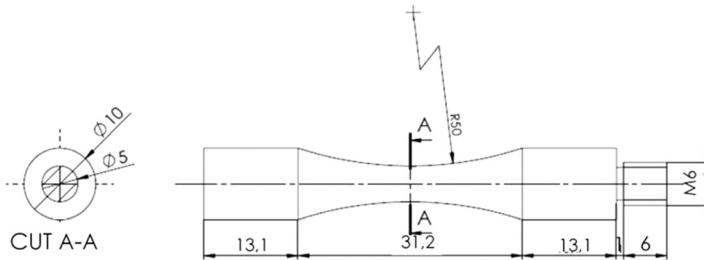
### PARAMETER CONFIGURATION

The specimens’ dimensions shown in “Testing Materials” were determined according to the formulation described in “Longitudinal Elastic Waves—Formulation for

**TABLE 1** Material properties.

	$E_d$ , GPa	$\rho$ , kg/m <sup>3</sup>	YS, MPa	UTS, MPa
Copper	106	9019	272	285
Steel	196	7850	455	800

**FIG. 13** Dimensions of the copper specimen.



the Specimen's Design," so that after manufacturing the first longitudinal mode frequency was approximately 20 kHz (the actuator's power box can only operate in the frequency range of 19.5 kHz to 20.5 kHz).

In the present experimental examples, the sampling frequency was set at 400 kHz and the duration of an acquisition block was set at 0.125 s. Thus, the feedback loop update occurred every 2500 cycles.

After several specimens of each material had been tested with amplitude control, temperature control, or both, S-N curves were plotted. [Table 2](#) presents a summary of the amplitude and temperature test specifications for each of the specimens considered.

## Results and Discussion

VHCF tests were performed at 20 kHz for different stress amplitudes under fully reversed cyclic loading ( $R = -1$ ). Also, as mentioned before, different types of control (amplitude control, temperature control, and both) were considered. Because the objectives of the present work were related to the study of VHCF only, S-N curves were plotted for  $1E^6$  up to  $1E^9$  cycles only.

**FIG. 14** Dimensions of the carbon steel specimen.

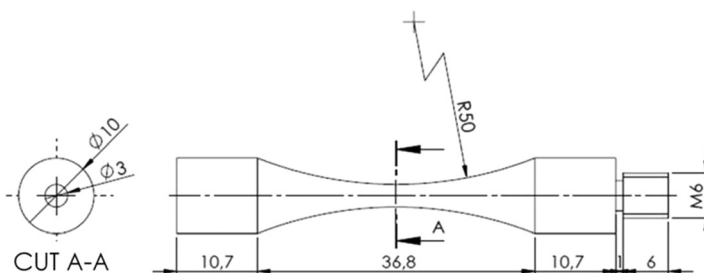


**TABLE 2** Amplitude and temperature test specifications.

Copper	With and without amplitude control	All with temperature control (45°C to 50°C)
Carbon steel	All without amplitude control	With temperature control (40°C to 60°C) and without

**S-N CURVES**

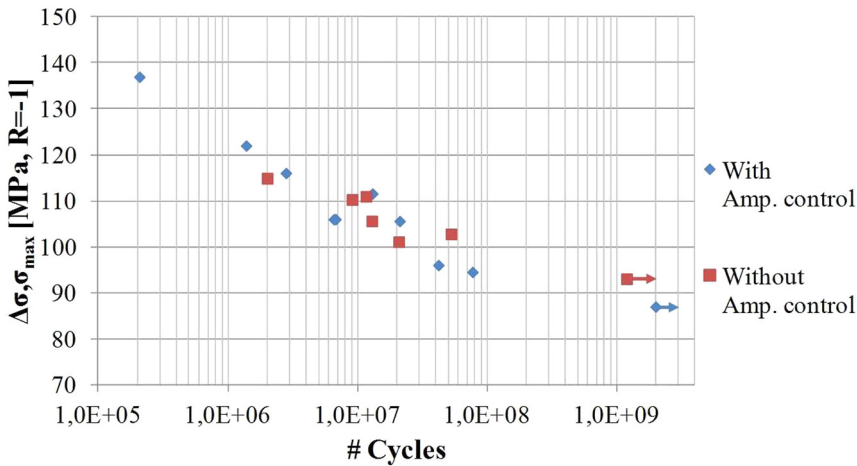
S-N results obtained for tests on copper are presented in Fig. 15. It is clear that the S-N data show a typical behavior for this type of material. Also, stress amplitudes were within the expected levels.

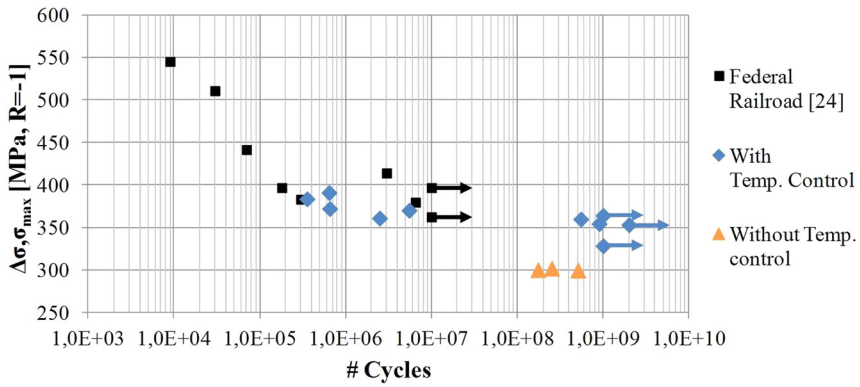
When ultrasonic tests were performed on carbon steel without temperature control, enormous amounts of heat were dissipated at the center of the specimen. With uninterrupted testing conditions, the specimen reached temperatures up to 270°C within just a few seconds. Figure 16 shows the S-N results for carbon steel with temperature control (in the range of 40°C to 60°C) and without temperature control. Results from the literature are also shown [24] for comparison.

With temperature control, tests were performed in the range of 45°C to 50°C for copper and 40°C to 60°C for steel. These ranges were established to be as narrow and low as possible, so that effects due to temperature in the fatigue process could be neglected.

With respect to the use of amplitude control in copper, it was concluded that it did not change the appearance of the S-N plot. This can be explained because temperature control restricts the variation of other control parameters (that depend on temperature themselves, like the amplitude of vibration). Because the temperature

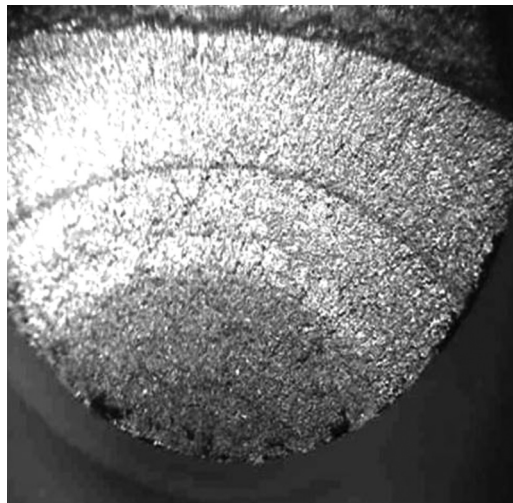
**FIG. 15** Copper S-N curve.



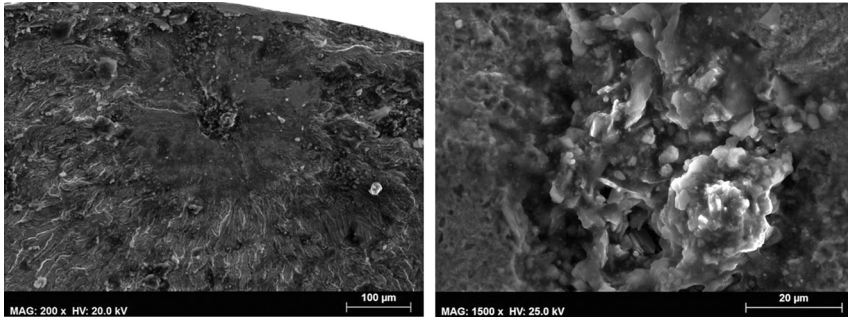
**FIG. 16** Carbon steel S-N curve.

control was set for a very narrow range, the use of amplitude control together with temperature control became redundant.

From the analysis of Fig. 16, it is possible to verify that the experimental results obtained near to  $1E^6$  cycles in the temperature range of  $40^\circ\text{C}$  to  $60^\circ\text{C}$  are similar to those presented in the literature [24]. The material performance up to  $1E^9$  cycles with temperature control was consistent as well.

**FIG. 17** Copper fracture surface ( $94.5\text{ MPa}$ ;  $7.7E^7$  cycles).

**FIG. 18** Carbon steel “fish-eye” fracture surface (360 MPa;  $5.5E^8$  cycles).



Without temperature control, fracture occurred at lower levels of stress (less than 55 MPa, or 15 %) than when temperature control was used. In this case, ultrasonic fatigue tests were performed at 270°C and over.

### FRACTOGRAPHY

In VHCF, fracture may occur due to either internal or external cracks [1]. All fractured specimens were observed with an optical microscope. Sample photographs are shown in Figs. 17 and 18 for copper and steel, respectively.

Figure 17 shows that for copper, the crack initiated and grew from the surface of the specimen. All three stages of fatigue are clear: crack initiation, propagation, and fracture. It is still possible to observe typical “beach marks.”

In contrast, Fig. 18 shows that for carbon steel, the crack initiated in the interior of the specimen. A “fish-eye” pattern, very characteristic of VHCF failures in steel, is clearly observed. The fish-eye fracture is characterized by a “fine granular area” (FGA) in the vicinity of an inclusion. A scanning electron microscope was used to examine the FGA.

## Conclusions

The operation and testing of an ultrasonic fatigue testing machine were presented and discussed.

The exciter’s horn and specimen were designed so that their first longitudinal vibration mode would be tuned with the piezoelectric actuator working frequency (20 kHz).

The instrumentation of the machine allowed monitoring of the specimen’s temperature and displacement amplitude in a closed-loop control fashion. Data acquisition, monitoring, and control were done with a custom-made package developed under the LabVIEW platform.

A method for estimating the hysteretic damping factor evolution during fatigue tests is presented, as well as an indirect way to measure damage in the specimen.

A set of experimental tests using the presented ultrasonic fatigue testing machine were carried out, using two types of controls:

- temperature control, with the temperature measured at the area of maximum stress of the specimen (node at the middle), ensuring that the specimen did not exceed the predefined temperature limits, and
- amplitude control, with the displacement level measured at the bottom of the specimen, ensuring that the stress level was kept constant during the whole test.

S-N curves were obtained for copper and carbon steel, showing typical behaviors for these materials that were in good agreement with the available literature.

## References

- [1] Bathias, C. and Paris, P. C., *Gigacycle Fatigue in Mechanical Practice*, Marcel Dekker, New York, 2005.
- [2] Bathias, C., "Piezoelectric Fatigue Testing Machines and Devices," *Int. J. Fatigue*, Vol. 28, No. 11, 2006, pp. 1438–1445.
- [3] Marines, I., Bin, X., and Bathias, C., "An Understanding of Very High Cycle Fatigue of Metals," *Int. J. Fatigue*, Vol. 25, Nos. 9–11, 2003, pp. 1101–1107.
- [4] Bathias, C., Drouillac, L., and Le François, P., "How and Why the Fatigue S–N Curve Does Not Approach a Horizontal Asymptote," *Int. J. Fatigue*, Vol. 23, No. 1, 2001, pp. 143–151.
- [5] Bathias, C. and Paris, P. C., "Gigacycle Fatigue of Metallic Aircraft Components," *Int. J. Fatigue*, Vol. 32, No. 6, 2010, pp. 894–897.
- [6] Bathias, C., "Influence of the Metallurgical Instability on the Gigacycle Fatigue Regime," *Int. J. Fatigue*, Vol. 32, No. 3, 2010, pp. 535–540.
- [7] Stanzl-Tschegg, S., "Very High Cycle Fatigue Measuring Techniques," *Int. J. Fatigue*, Vol. 60, 2014, pp. 2–17.
- [8] Stanzl-Tschegg, S. and Schönbauer, B., "Near-threshold Fatigue Crack Propagation and Internal Cracks in Steel," *Proc. Eng.*, Vol. 2, No. 1, 2010, pp. 1547–1555.
- [9] Mayer, H., "Ultrasonic Torsion and Tension–Compression Fatigue Testing: Measuring Principles and Investigations on 2024-T351 Aluminium Alloy," *Int. J. Fatigue*, Vol. 28, No. 11, 2006, pp. 1446–1455.
- [10] Mayer, H., Fitzka, M., and Schuller, R., "Constant and Variable Amplitude Ultrasonic Fatigue of 2024-T351 Aluminium Alloy at Different Load Ratios," *Ultrasonics*, Vol. 53, No. 8, 2013, pp. 1425–1432.
- [11] Müller, T. and Sander, M., "On the Use of Ultrasonic Fatigue Testing Technique—Variable Amplitude Loadings and Crack Growth Monitoring," *Ultrasonics*, Vol. 53, No. 8, 2013, pp. 1417–1424.
- [12] Sohar, C. R., Betzwar-Kotas, A., Gierl, C., Weiss, B., and Danninger, H., "Fractographic Evaluation of Gigacycle Fatigue Crack Nucleation and Propagation of a High Cr Alloyed Cold Work Tool Steel," *Int. J. Fatigue*, Vol. 30, No. 12, 2008, pp. 2191–2199.

- [13] Zimmermann, M., Stöcker, C., and Christ, H. J., "On the Effects of Particle Strengthening and Temperature on the VHCF Behaviour at High Frequency," *Int. J. Fatigue*, Vol. 33, No. 1, 2011, pp. 42–48.
- [14] Huang, Z. Y., Wagner, D., Bathias, C., and Chaboche, J. L., "Cumulative Fatigue Damage in Low Cycle Fatigue and Gigacycle Fatigue for Low Carbon-Manganese Steel," *Int. J. Fatigue*, Vol. 33, No. 2, 2011, pp. 115–121.
- [15] Yu, Y., Gu, J. L., Shou, F. L., Xua, L., Bai, B. Z., and Liu, Y. B., "Competition Mechanism between Microstructure Type and Inclusion Level in Determining VHCF Behavior of Bainite/Martensite Dual Phase Steels," *Int. J. Fatigue*, Vol. 33, No. 3, 2011, pp. 500–506.
- [16] Müller-Bollenhagen, C., Zimmermann, M., and Christ, H. J., "Very High Cycle Fatigue Behaviour of Austenitic Stainless Steel and the Effect of Strain-induced Martensite," *Int. J. Fatigue*, Vol. 32, No. 6, 2010, pp. 936–942.
- [17] Furuya, Y., "Specimen Size Effects on Gigacycle Fatigue Properties of High-strength Steel under Ultrasonic Fatigue Testing," *Scr. Mater.*, Vol. 58, No. 11, 2008, pp. 1014–1017.
- [18] Freitas, M., Reis, L., Anes, V., Montalvão, D., Ribeiro, A. M., and Fonte, M., "Design and Assembly of an Ultrasonic Fatigue Testing Machine," *Proceedings of the Anales de Mecânica de la Fractura*, Vol. 28, No. 1, 2011, pp. 335–340.
- [19] Anes, V., Montalvão, D., Ribeiro, A. M., Freitas, M., and Fonte, O., "Design and Instrumentation of an Ultrasonic Fatigue Testing Machine," *Proceedings of the 5th International Conference on Very High Cycle Fatigue*, C. Berger and H.-J. Christ, Eds., DVM, Berlin, Germany, June 28–30, 2011, pp. 421–426.
- [20] Maia, N. M. M. and Silva, J. M. M., *Theoretical and Experimental Modal Analysis*, Research Studies Press LTD, Somerset, UK, 1997.
- [21] Lage, Y., Cachão, H., Reis, L., Fonte, M., Freitas, M., and Ribeiro, A., "A Damage Parameter for HCF and VHCF Based on Hysteretic Damping," *Int. J. Fatigue*, Vol. 62, 2014, pp. 2–9.
- [22] Lage, Y., Freitas, M., Montalvão, D., Ribeiro, A. M. R., and Reis, L., "Ultrasonic Fatigue Analysis on Steel Specimen with Temperature Control: Evaluation of Variable Temperature Effect," *XIII Portuguese Conference on Fracture* J. Ferreira, J. Costa, and L. Borrego, Eds., Univ. Coimbra, Portugal, Feb 2–3, 2012, pp. 59–64.
- [23] Lage, Y., Freitas, M., Reis, L., Ribeiro, A. M. R., and Montalvão, D., "Instrumentation of Ultrasonic High-frequency Machine to Estimate Applied Stress in Middle Section of Specimen," J. F. Silva Gomes and M. A. P. Vaz, Eds., *Proceedings of the 15th International Conference on Experimental Mechanics*, Porto, Portugal, July 22–27, 2012.
- [24] Federal Railroad Administration, *Fatigue Behavior of AAR Class A of Transportation Railroad Wheel Steel at Ambient and Elevated Temperatures*, Federal Railroad Administration Office of Research and Development, Washington, D.C., 2006.

---

STP 1571, 2014 / available online at [www.astm.org](http://www.astm.org) / doi: 10.1520/STP157120130074

Jidong Kang,<sup>1</sup> Guowu Shen,<sup>1</sup> Jie Liang,<sup>1</sup> Kyle Brophy,<sup>1</sup>  
Andrew Mendonca,<sup>1</sup> and James Gianetto<sup>1</sup>

## Evaluation of Fracture Toughness Test Methods for Linepipe Steels<sup>2</sup>

### Reference

Kang, Jidong, Shen, Guowu, Liang, Jie, Brophy, Kyle, Mendonca, Andrew, and Gianetto, James, "Evaluation of Fracture Toughness Test Methods for Linepipe Steels<sup>2</sup>," *Application of Automation Technology in Fatigue and Fracture Testing and Analysis*, STP 1571, Peter C. McKeighan and Arthur A. Braun, Eds., pp. 101-115, doi:10.1520/STP157120130074, ASTM International, West Conshohocken, PA 2014.<sup>3</sup>

### ABSTRACT

Reliable evaluation of fracture toughness resistance curves, including both  $J$ -resistance ( $J$ -R) and crack tip opening displacement- resistance (CTOD-R) curves, is becoming an integral part of pipeline integrity assessment for demanding applications. Using MTS TestSuite Software with Multipurpose Elite, we have successfully realized the automation of fracture toughness test procedures for single-edge bend [SE(B)] test specimens based on ASTM E1820-11 and BSI 7448. The software offers the option to use either load-line displacement (LLD) or crack mouth opening displacement (CMOD) as the control parameter for both shallow- and deep-cracked SE(B) specimens and exports both the  $J$ -R and the CTOD-R curves simultaneously. In order to validate the developed software, we have tested two different pipe steels, namely, X60 and X100 steels. The nominal initial crack lengths  $a/W$  after precracking were equal to 0.2 and 0.5 for the shallow- and deep-cracked specimens, respectively. A 10% deep side groove was machined after the precracking on each side of the specimen. The results show that for  $J$ -R curves, the differences between the LLD and CMOD methods are negligible within the  $J_{\max}$  criteria range. Beyond this

---

Manuscript received May 16, 2013; accepted for publication November 26, 2013; published online April 30, 2014.

<sup>1</sup>CanmetMATERIALS, 183 Longwood Rd. South, Hamilton, ON, Canada, L8P 0A5.

<sup>2</sup>This licence is granted on the condition that clear attribution is given to the author(s) and Natural Resources Canada and, when feasible, that the Crown copyright is acknowledged as follows: © Her Majesty the Queen in Right of Canada, as represented by the Minister of Natural Resources, 2014.

<sup>3</sup>ASTM Sixth Symposium on *Application of Automation Technology in Fatigue and Fracture Testing and Analysis* on May 23, 2013 in Indianapolis, IN.

range, however, some differences were observed. There was no significant effect of work hardening rate on the  $J$ -R curves obtained using either LLD or CMOD for the two pipe steel materials investigated. However, it is worth noting that there were large discrepancies between the ASTM and BSI methods in terms of CTOD-R curve measurements, especially for the shallow-cracked specimens. This was attributed to the fact that the standards use different definitions of CTOD.

### Keywords

fracture toughness testing, automation, single-edge bend specimen, ASTM E1820-11, BSI 7448, pipe steels

## Introduction

Weldment fracture toughness evaluation is an integral part of CAN/CSA-Z662-11 [1], which requires that “crack tip opening displacement (CTOD) tests be carried out as specified in BSI BS 7448 or ASTM E 1290.” In this case, testing is conducted using a single-edge bend [SE(B)] specimen with deep cracks ( $0.45 \leq a/W \leq 0.55$ ) to establish the lower-bound fracture toughness for the weld metal and heat-affected zone regions of pipe welds. For demanding pipeline applications in which a strain-based design is required in order to accommodate secondary loads caused by ground movements, the  $J$ -integral and CTOD resistance curves may be measured by use of testing standards and recommended practices specified in ASTM E1820 [2] and BSI 7448, Part 4 [3]. In the recent versions of ASTM E1820, CTOD results are calculated from  $J$ -integral data. More recently, low-constraint tests appropriate for the assessment of defects such as girth weld imperfections have made use of SE(B) [4] or clamped single-edge tension [SE(T)] specimens [5] with shallow cracks. In the former case, details have been included in ASTM 1820-11 [1] as an appendix. This test method requires continuous measurement of crack mouth opening displacement (CMOD) and load-line displacement (LLD). The elastic compliance method is used for crack-length measurement. It is important to note that the testing procedures described here have not yet been fully implemented in testing control software to allow for the automation of fracture toughness testing procedures in accordance with the latest ASTM standards, especially for cases in which shallowly cracked specimens are used. Therefore, in the present study, we focused our effort on developing testing control software for SE(B) testing, and in the future we will address SE(T) testing based on the recommended procedures developed by CanmetMATERIALS [5].

Among the commercially available testing software packages, MTS TestSuite Software [6] serves as a platform that allows the development and implementation of test control software. A key feature of MTS TestSuite Software is the ability to analyze raw data from testing equipment and to output calculations and graphs while a test is underway. To expand the application of MTS TestSuite Software, we implemented test procedures for measuring  $J$ -resistance ( $J$ -R) and CTOD-resistance (CTOD-R) curves based on ASTM E1820 and BSI 7448 for SE(B) specimens with shallow and deep cracks. Automation of the test procedures has allowed real-time

display along with the export of testing parameters, raw data, and results, while allowing  $J$ -R and CTOD-R curves to be created during and after the test.

To further evaluate and test the developed procedures, we used them to measure  $J$ -R and CTOD-R curves of X60 and X100 pipe steels for SE(B) specimens with shallow ( $a/w = 0.20$ ) and deep ( $a/w = 0.50$ ) cracks. All testing was carried out at room temperature.

## Test Control Software Development

The present version of MTS TestSuite Software comes with a number of default tests and geometries. It includes an SE(B) test and geometry based on ASTM E1820-08 that only supports LLD measurements for the determination of the  $J$ -integral for deeply cracked specimens.

Developing the new test control software allowed all errors in the default tests to be corrected and the equations to be updated so that they complied with ASTM E1820-11. The CTOD calculation based on BSI 7448 was also included to facilitate comparison with the CTOD based on the ASTM standard. The test procedure was also modified to allow shallow-cracked specimens to be tested using both CMOD and LLD for  $J$ -integrals. As the geometry factor  $\eta_{LLD}$  for shallow-cracked specimens using LLD is not given in ASTM E1820-11, the equation developed by Zhu et al. [7] was used as follows:

$$\eta_{LLD} = 1.620 + 0.850(a/w) - 0.651(a/w)^2 \quad (1)$$

For clarity, all equations used in ASTM E1820-11 and BS 7448 are not presented here, and the reader is referred to the standards for these details.

In order to perform a test using the test control software, it is necessary to first create a “specimen” for a given test within the MTS TestSuite Software program Multipurpose Elite. A specimen is simply created based on a chosen geometry file appropriate for the specimen being tested; it must also be given values for dimensions and material properties corresponding to the specimen.

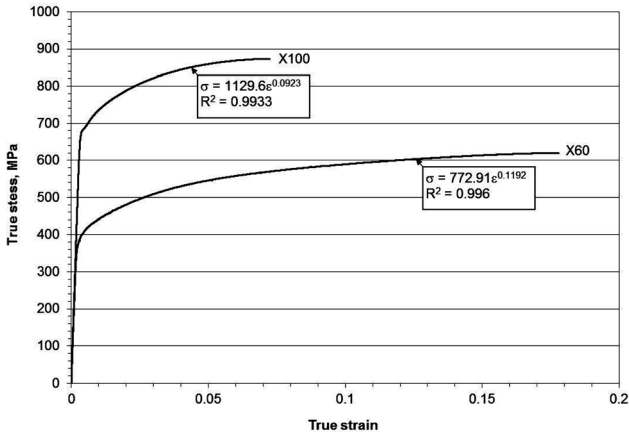
When a user starts a new test run by selecting “New Test Run,” a specimen must be selected so that the test control software will run. The software will create a window with various options for controlling certain aspects of the test. This interface allows various parameters such as  $J_{IC}$  and precrack parameters to be altered, and it performs various tasks, including precracking, crack-size checking, and  $J_{IC}$  testing.

Once the  $J_{IC}$  test is running, Multipurpose Elite will show a run-time display of various tables and graphs of data files that are continuously updated as the specimen is tested. This includes graphs of load versus LLD and CMOD,  $J$ -R curves, and CTOD-R curves. The instructions for using the developed test control software can be found in the Appendix.

## Experimental

SE(B) specimens machined from sections of X60 and X100 steel pipe were used to test the developed test control software. A total of six SE(B) specimens were

**FIG. 1** Tensile stress-strain curves of X60 and X100 pipe steels.



machined from each of the X60 and X100 steel pipes parallel to the pipe axis. For each steel, three shallow-cracked and three deep-cracked specimens were prepared for testing. The final dimensions of the SE(B) specimens were 24 mm in width, 12 mm in thickness, and approximately 120 mm in length. A span of 96 mm was set for all tests. The initial  $a/W$  ratios for the shallow- and deep-cracked specimens were targeted as 0.15 and 0.45, respectively. After precracking, side grooves of 10% on each side (for a total of 20% or 2.4 mm) were machined on the specimens, and this resulted in a net thickness of 9.6 mm. Round bar tensile specimens were machined parallel to the pipe axis and tested at room temperature to determine the tensile properties of the respective pipe steels, including the work hardening coefficient, as shown in Fig. 1. Note that the X60 steel had a higher work hardening rate than the X100 steel.

## Results

The  $J$ - $R$  curves obtained from all the specimens were determined in accordance with ASTM E1820-11 and BSI 7448 with the calculations based on both CMOD and LLD measurements. To keep the presentation simple,  $J$ - $R$  curves using CMOD results are presented first, and the results from LLD are discussed later.

For the X60 specimens, the shallow-cracked specimens had a noticeably greater fracture toughness beyond 0.2-mm crack growth than the deep-cracked specimens (Fig. 2). A slight amount of deviation was noticeable between the  $J$ - $R$  curves obtained from shallow-cracked specimens and was attributed to the delamination that the X60 specimens experienced during testing. For the X100 specimens, the difference between  $J$ - $R$  curves for the shallow- and deep-cracked specimens was marginally less than observed for the X60 tests (Fig. 3).

FIG. 2 J-R curves of X60 SE(B) specimens.

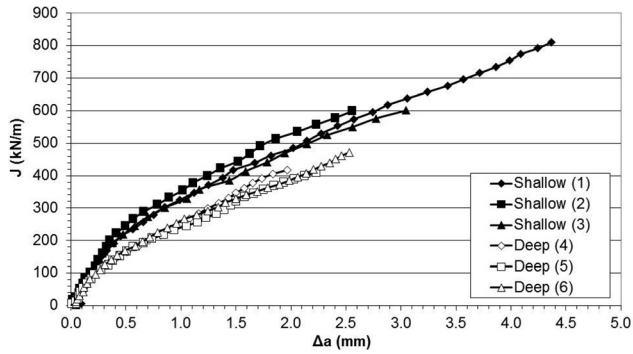


FIG. 3 J-R curves of X100 SE(B) specimens.

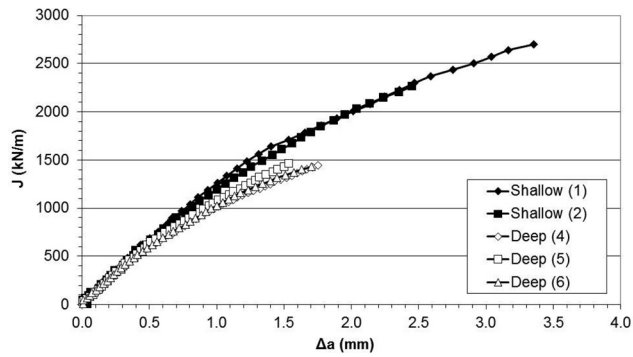


FIG. 4 Comparison of J-R curves for shallow-cracked SE(B) specimens of X60 and X100.

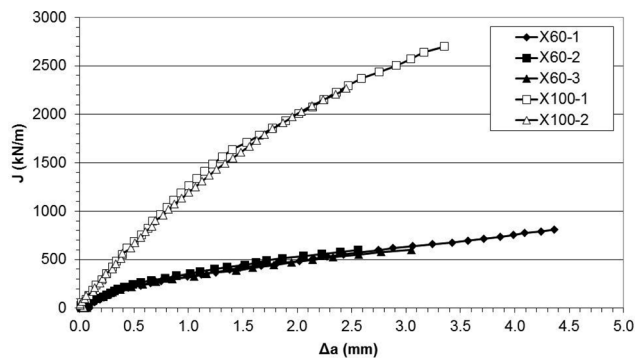


FIG. 5 CTOD-R curves for X60 SE(B) specimens.

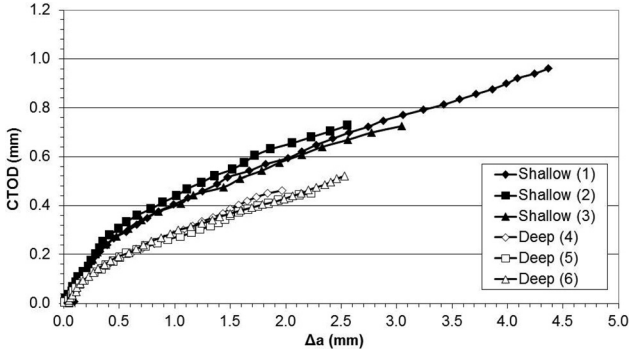


FIG. 6 CTOD-R curves for X100 SE(B) specimens.

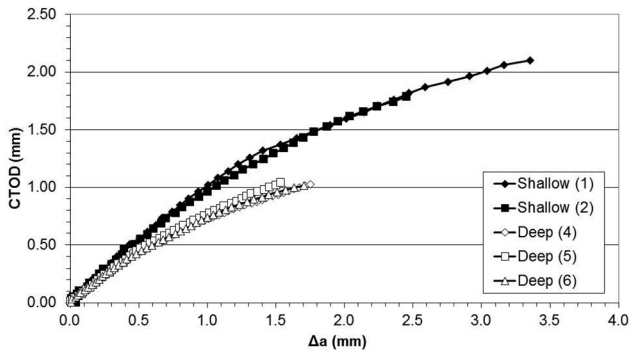
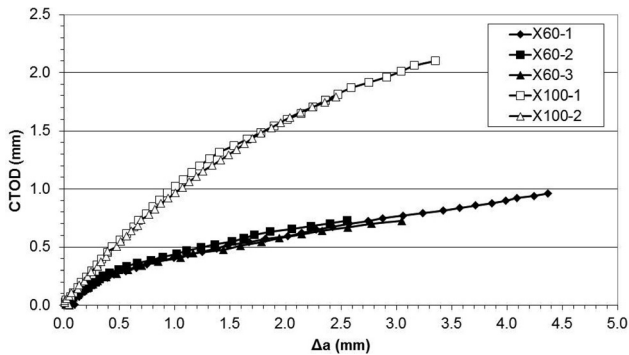


FIG. 7 CTOD-R curves for shallow-cracked SE(B) specimens of X60 and X100.



In comparing the  $J$ - $R$  curves of X60 and X100 specimens with shallow cracks, we noticed that the X100 steel showed much greater fracture toughness than the X60 steel (Fig. 4). A similar trend was observed for the deep-cracked specimens.

CTOD values were also obtained from all specimens using both the ASTM method and the BSI method. Again, for the sake of the simplicity, we first present the results from ASTM E1820-11 and leave the results from BSI 7448 for later discussion. It can be seen in Fig. 5 that for X60, the shallow-cracked specimens consistently had higher CTOD values than the deep-cracked specimens. Similar to the  $J$ - $R$  curves, there was again some deviation among the shallow-cracked specimens that likely was due to the effect of the observed delaminations.

The results for the X100 specimens also show higher CTOD values for the shallow-cracked than for the deep-cracked specimens (Fig. 6). It is worth noting, though, that the difference between shallow- and deep-cracked specimens was less pronounced and more gradual for the X100 steel than for the X60 steel.

A comparison of the results obtained for the X60 and X100 shallow-cracked specimens revealed that the X100 steel had much higher CTOD values than the X60 steel (Fig. 7). A similar trend was found for the deep-cracked specimens.

## Discussion

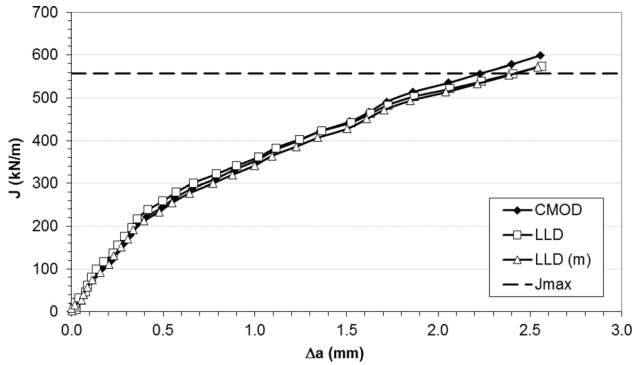
To validate the automatically calculated  $J$ - $R$  and CTOD- $R$  results, an Excel spreadsheet was developed to reanalyze the exported raw data, and all results have been confirmed.

One of the main purposes of the present study was to determine the differences in  $J$ - $R$  curve measurements using CMOD or LLD. There is an inherent complication in using LLD. LLD is by definition the displacement measured between the two load points of the testing machine. The problem with this is that some of the measured displacement is likely from the load train and not the specimen itself. The displacement from the testing machine is referred to or known as machine stiffness. If this factor is not taken into account, the calculated compliance might not be accurate. In the case of SE(B) testing, one needs to remove the influence of machine stiffness in order to obtain the true compliance of the specimen. This may be done by comparing the measured initial LLD compliance with the theoretical one given by Eq A1.10 in ASTM E1820-11 [2].

The CMOD measures displacement right at the crack mouth opening by means of a clip gauge that is attached to the specimen surface directly above the crack. This eliminates the influence of machine stiffness on  $J$ -integral calculations and results in more reliable measurements.

For the two pipe steel materials evaluated in this study, the difference between  $J$ - $R$  curves calculated using CMOD and LLD proved to be very small (Figs. 8 and 9). For the X60 tests, the two curves deviate slightly below the  $J_{\max}$  line specified by ASTM E1820-11 [2]; however, the difference is still fairly negligible beyond the  $J_{\max}$  line (Fig. 8). The CMOD and LLD curves are nearly indistinguishable for X100 steel

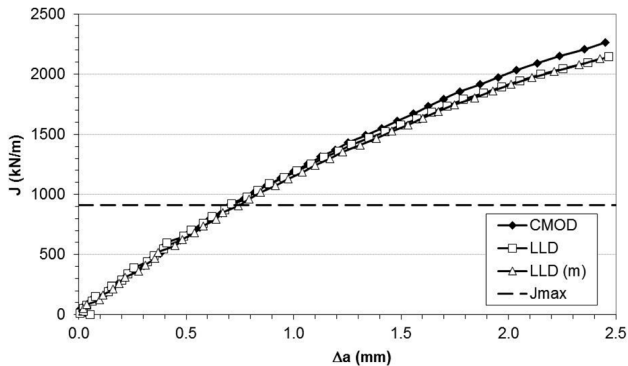
**FIG. 8** Example J-R curves for an X60 SE(B) specimen using CMOD and LLD.

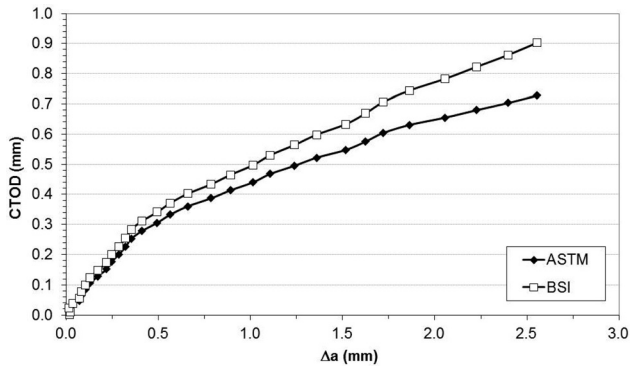


below the  $J_{\max}$  line (the line below which data are valid) and begin to deviate only slightly beyond this point (Fig. 9).

It is also important to take into account the effect of machine stiffness on the LLD calculations. Machine stiffness had a more noticeable effect on the X60 specimens, although it was still very small (Fig. 8). The machine stiffness appeared to have a negligible effect on the J-R curve for the X100 specimens (Fig. 9). With machine compliance removed, the LLD curve even more closely resembled the CMOD curve for the X60 specimens. In Figs. 8 and 9, “LLD (m)” refers to the results with the influence of the machine compliance removed. Overall, the machine stiffness had a very minimal effect on the results obtained in this investigation.

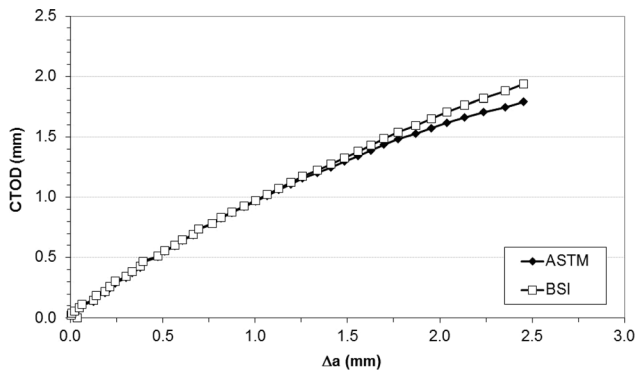
**FIG. 9** Example J-R curves for an X100 SE(B) specimen using CMOD and LLD.



**FIG. 10** CTOD-R curves for an X60 SE(B) specimen using ASTM and BSI methods.

ASTM E1820-11 and BSI 7448 provide different ways of calculating CTOD both in theory and in application. The ASTM method takes into account the fact that the crack tip moves during testing. This method calculates CTOD based directly on the calculated  $J$ -integral value. The BSI method, in contrast, takes the initial position of the crack tip and calculates CTOD based on the plastic hinge model using a rotation factor.

For the X60 specimens tested, there was a fairly large difference between CTOD-R curves calculated using the ASTM method and the BSI method (Fig. 10). It can be seen in Fig. 10 that the two methods produced nearly identical results until a crack extension of roughly 0.25 mm was reached, and beyond that they deviated

**FIG. 11** CTOD-R curves for an X100 SE(B) specimen using ASTM and BSI methods.

more significantly. The difference between the two methods for the X100 specimens was not nearly as large (Fig. 11). From Fig. 11, one can see that the curves for the ASTM and BSI methods are almost identical to a crack extension of 1.25 mm; the curves then gradually start to deviate in a way that is much less pronounced than observed for the X60 test.

It can be seen in Figs. 10 and 11 that the BSI method usually produces CTOD-R curves that are higher than those produced via the ASTM method. This is consistent with the trend observed in the recently published Japanese round-robin tests of 36 types of steels [8]. Clearly, these differences are caused by the definition of CTOD in the two standards. Moreover, the difference between methods can vary greatly depending on the material being tested, mainly as a result of the difference in work hardening rate.

## Conclusions

Using MTS TestSuite Multipurpose Software (Elite version), we have successfully developed test control software that provides automation of fracture toughness ( $J$ -R and CTOD-R curves) testing procedures for single-edge bend [SE(B)] specimens based on ASTM E1820-11 and BSI 7448. The software offers the option of using either LLD or CMOD as the control parameter for both shallow- and deep-cracked test specimens and allows the export of both  $J$ -R and CTOD-R curves simultaneously.

We have used the developed test control software to measure  $J$ -R and CTOD-R curves for SE(B) specimens of X60 and X100 pipe steels with shallowly ( $a/W = 0.20$ ) and deeply ( $a/W = 0.50$ ) cracked specimens. The results show that both  $J$ -R and CTOD-R curves of X100 pipe steel were much higher than those of X60 steel. Although in this investigation both CMOD and LLD produced nearly identical  $J$ -R curves, the CMOD provides fewer complications associated with the need to consider correction to compliance crack length measurements. The results also show that CTOD-R curves from BSI 7448 are generally higher than those from ASTM E1820-11, but this greatly depends on the material being tested, and in particular its work hardening rate.

## Appendix: Use of the Test Control Software

Before any tests can be completed, MTS TestSuite Multipurpose Elite must be started, and the proper test control software must be selected by choosing “New Test” from the “File” menu or by clicking the “New Test” button at the top of the screen. Once this has been done, test runs may be performed by selecting “New Test Run” from the “File” menu or by clicking the “New Test Run” button at the top of the screen. Beginning a new test run will bring up a window with a list of specimens to choose from. If no specimens are shown, then a new specimen must be created. Once a specimen has been selected, the test control software will start

running and a window will appear that allows the user to edit specific variables for the test specimen (Fig. 12).

After this, the main test window will appear (Fig. 13). This window provides test information and access to all the settings and operations of the test control software. The operations that may be performed are crack size checking, precracking, JIC testing, and fatigue testing to fracture. Settings that may be edited are precrack parameters, data storage parameters, JIC test parameters, test termination parameters, precrack data, crack size check parameters (though not directly from this window), and measured crack sizes. Not all of these functions and settings are relevant; only the important ones are covered here.

Of the first four parameters in the menu (precrack, JIC, data storage, and test termination), the JIC parameters are the most important and are generally all that need to be changed from the defaults. Precrack parameters need to be changed only if a specimen is going to be precracked. The data storage and test termination parameters are usually fine with the default settings, but they can be changed if necessary. The “Assign Precrack Values” function allows manual editing of the

FIG. 12 Test window with test variables that can be modified.

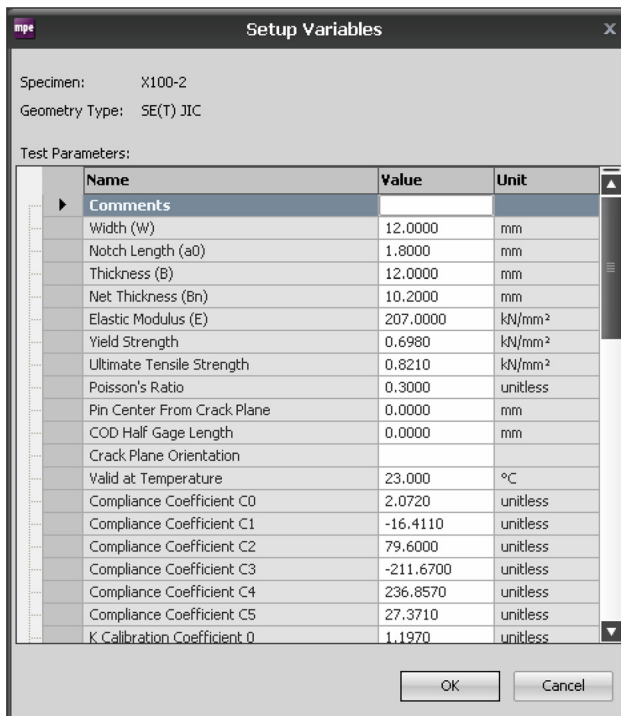
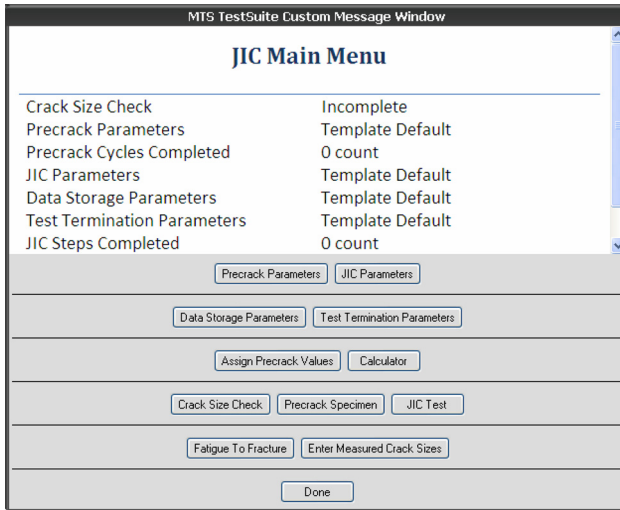
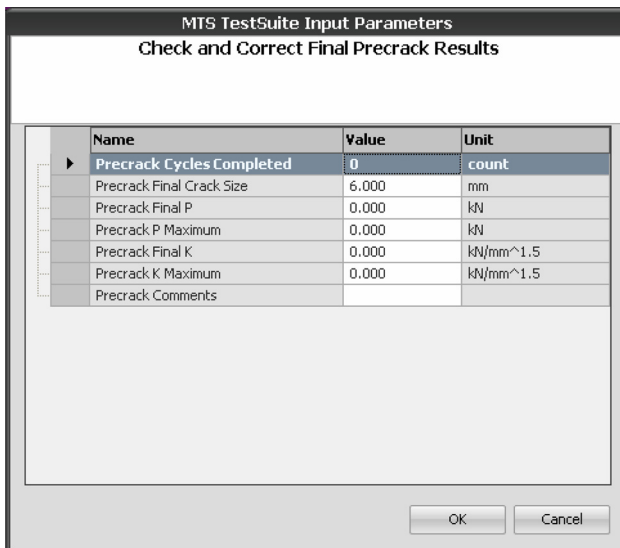


**FIG. 13** Main test window for test control software.



variables associated with precracking (Fig. 14). The precrack values should need to be manually edited only if the specimen is not being precracked in the current test run but was precracked previously.

**FIG. 14** Window for manual editing of precrack variables.



Clicking on “Crack Size Check” will bring up a new window with some new information and options (Fig. 14). The information in this window is specific to the crack size check; some of it is calculated beforehand using existing data and parameters, and the rest is calculated after the crack size check has been run. Clicking on “Change Parameters” in this window will allow editing of the crack size check parameters. When the “Measure Crack Size” button is clicked on, a window requesting the maximum and half-maximum load values will appear (Fig. 15); once these values have been entered, the crack size check will run. When the check is completed, the window in Fig. 16 will reappear. The crack size check can be run as many times as needed, and the load values may be changed each time if necessary. Closing the crack size check window will return the user to the main test window.

Once parameters have been set and the crack size checks have been run, the JIC test can be run by clicking on the “JIC Test” button. The test will run until a condition set in the test termination parameters occurs, the “Stop” button at the top is clicked, or some sort of error occurs. After the test ends or is stopped, the main test window will reappear.

Clicking the “Done” button at the bottom of the window will end the test run permanently, meaning no further testing may be done with that specific test run; the user should do this only if he or she is sure that the test run is completely finished. A better option is to simply click the downward-pointing arrow button at the top of the screen to the right of the “Stop” button. This will let the user exit the test run but allow the run to be reopened for continued testing later on.

FIG. 15 Crack size check window.

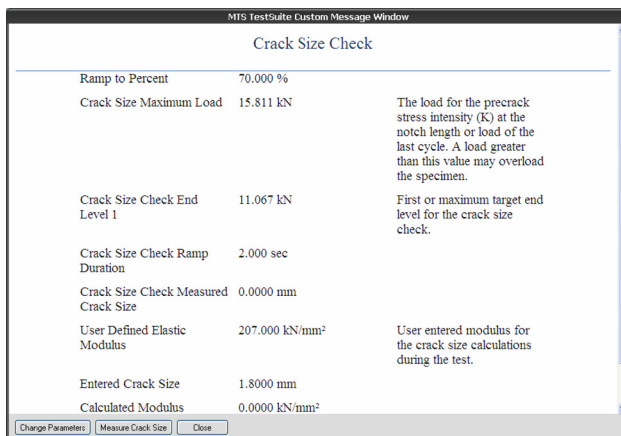
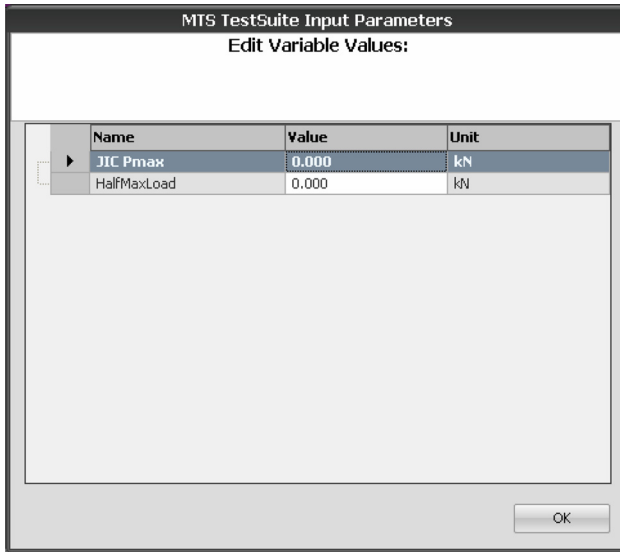


**FIG. 16** Window for entering crack size check load values.



## References

- [1] CAN/CSA-Z662-11, 2011, "Oil and Gas Pipeline Systems. Annex K (Informative): Standards of Acceptability for Circumferential Pipe Butt Welds Based upon Fracture Mechanics Principles," Canadian Standards Association, Mississauga, ON, Canada.
- [2] ASTM 1820-11: Standard Test Method for Measurement of Fracture Toughness, *Annual Book of ASTM Standards*, ASTM International, West Conshohocken, PA, 2011.
- [3] BSI 7448, Part 4, 1991, "Fracture Mechanics Toughness Tests, Part 1, Method for Determination of  $K_{IC}$ , Critical CTOD and Critical J Values of Metallic Materials," British Standards Institution (BSI), London.
- [4] Joyce, J. A., "J Resistance Curve Testing of Short Crack Bend Specimens Using Unloading Compliance," *Fracture Mechanics, Twenty-Second Symposium, Vol. 1, ASTM STP 1131*, ASTM International, West Conshohocken, PA, 1992, pp. 904–926.
- [5] Shen, G., Gianetto, J. A., and Tyson, W. R., "Measurement of J-R Curves Using Single-Specimen Technique on Clamped SE(T) Specimens," *Proceedings of the Nineteenth International Offshore and Polar Engineering Conference*, Osaka, Japan, June 21–26, 2009, International Society of Offshore and Polar Engineers, Cupertino, CA.
- [6] MTS Systems Corporation, *MTS TestSuite Software With Multipurpose Elite Version Testing Software*, MTS Systems Corporation, Eden Prairie, MN, 2010.

- [7] Zhu, X. K., Leis, B. N., and Joyce, J. A., "Experimental Estimation of J-R Curves from Load-CMOD Record for SE(B) Specimens," *J. ASTM Int.*, Vol. 5, 2008, pp. 1-15.
- [8] Tagawa, T., Kayamori, Y., Ohata, M., Handa, T., Kawabata, T., Yamashita, Y., Tsutsumi, K., Yoshinari, H., Aihara, S., and Hagihara, Y., "Comparison of CTOD Standards: BS 7448-Part 1 and Revised ASTM E1290," *Eng. Fract. Mech.*, Vol. 77, No. 2, 2010, pp. 327-336.

---

STP 1571, 2014 / available online at [www.astm.org](http://www.astm.org) / doi: 10.1520/STP157120130117

Peter C. McKeighan<sup>1</sup> and Mark A. James<sup>2</sup>

## Analysis Round Robin Results on the Linearity of Fracture Toughness Test Data

### Reference

McKeighan, Peter C. and James, Mark A., "Analysis Round Robin Results on the Linearity of Fracture Toughness Test Data," *Application of Automation Technology in Fatigue and Fracture Testing and Analysis*, STP 1571, Peter C. McKeighan and Arthur A. Braun, Eds., pp. 116–133, doi:10.1520/STP157120130117, ASTM International, West Conshohocken, PA 2014.<sup>3</sup>

### ABSTRACT

All ASTM standards require precision and bias statements that address the typical variability observed when performing the standard. It is useful to determine the different sources of variability in a given standard so that future efforts can be undertaken to minimize error in the resulting material properties measured by that standard. This analysis round robin was undertaken with nine participants using fifteen different previously measured load-displacement datasets from linear-elastic,  $K_{IC}$  fracture toughness tests fabricated from aluminum, titanium, and steel material. Each round robin participant analyzed the data using their own previously proven methods. A bi-modal trend in  $P_Q$  variation was noted with  $\pm 1\%$  variability capturing 40% of the datasets and  $\pm 4\%$  generally capturing the remaining 60% of the datasets, although there were outliers observed. In summary, the method used to analyze the load-displacement response in a linear-elastic fracture toughness test contributes to between a minimum of one-tenth and on average one-third of the overall uncertainty quoted in the  $K_{IC}$  precision and bias statement. Although the analysis methodology is likely not a primary contributor to the overall variability observed in a fracture toughness test, it is a significant contributor. In two of the nine datasets, linearity analysis methodology accounted for in excess of 10%

---

Manuscript received July 13, 2013; accepted for publication January 21, 2014; published online September 5, 2014.

<sup>1</sup>Exponent, Warrenville, IL 60555.

<sup>2</sup>Alcoa, Alcoa Center, PA 15069.

<sup>3</sup>ASTM Sixth Symposium on *Application of Automation Technology in Fatigue and Fracture Testing and Analysis* on May 23, 2013 in Indianapolis, IN.

error. The observed variability did not definitively appear to be material related although some systematic trends were noted as a function of participant.

### Keywords

fracture toughness, linearity analysis, round robin

## Introduction

The ASTM standards that are routinely used to perform tests were typically developed in the era when data acquisition was of an autographic ( $x$ - $y$  plotter) nature and analysis was performed with a straight edge and a pencil. With the development of high speed digital data recording systems, the autographic methods typically included in the test standards (tensile, fracture, and fatigue) are now routinely converted to automated, yet flexible, algorithmic methods for analyzing the recorded data. This is a fairly straightforward process for the simplest aspects of testing, for instance sorting for absolute minimums or maximums or determining local slope changes in a given transducer signal response. As complexity of a given analysis increases, this typically means that more user input (or qualitative judgment) will be required to perform the task.

As an example, consider the task of determining the slope of a given set of dual channel data, for instance load-displacement ( $P$ - $\delta$ ) data recorded during a linear-elastic fracture toughness test [1] (a similar slope analysis is required during fatigue crack growth testing for determining compliance crack length or during a tensile test when calculating the linear modulus from the initial portion of the load-strain data). Most current computer-based algorithms assume a range for slope determination, or conversely allow a user to select a given range. The test standards provide no guidance regarding how to choose the linear region of the test record. Clearly, the range of the data chosen can have a significant effect on the resulting slope and subsequent data analysis. It is also uncommon for any automated algorithm to provide feedback on the suitability of a given range of data analysis. In practice, the data is only “truly” linear over a small portion of the data with gradual deviations from linearity evident above and below this region.

Automated algorithm development for test data analysis has been addressed in the past, although the citations in the technical literature are few. ASTM Committee E08 has held a series of five Automation Symposia, the first referenced in Ref. [2], where the focus has been development of automated capability for materials testing. In the early days of the series, computers were being introduced primarily to perform the testing although the role of the computer in the test laboratory became greater as local computing power increased dramatically over the years. For instance, McKeighan and Hillberry [3] presented a method in the earlier days of test automation that detailed an approach for automating tensile test data analysis. More recent efforts are underway to automate the process of determining the slope of a given set of dual transducer data by Graham and Adler [4] based on a method presented by Scibatta and Schuurmans [5]. In this approach, slope determination

using analysis of residuals (SDAR), all possible linear fits of a given set of data are analyzed and a minimization of residual error approach is used to optimize the selection of the linear region of the data. The goal of the method is to remove the subjective user input required to fit a given set of data. In fact, this technique is currently the subject of a standardization effort in an ASTM E08 task group.

The variability of a material property emerging from an ASTM test method is a function of the actual test methods applied during the test, the inherent variability in the test material and the techniques used to analyze the data. Intuition suggests that computer automation to both perform and analyze materials testing should decrease variability. However, a recent round robin for fatigue crack growth testing methods [6] showed that variability was essentially the same over a 30 year period, although intra-laboratory variability was somewhat reduced. Ultimately, the desire is to develop standardized approaches that yield reproducible and repeatable test data from lab-to-lab.

In an effort to understand the sources of the variability for fracture toughness testing, a round robin approach is utilized in this work where laboratory recorded load–displacement datasets from a variety of test materials are provided to different test labs for analysis only. Each round robin participant uses their own well-developed and proven methodology for choosing the linear region. This approach then allows assessment of primarily the role of analysis method on the variability of fracture toughness, although different test records will have different “sensitivity” to where this linear region is selected.

It is arguably estimated that over 90 % of the users of the fracture toughness test standards utilize a computer automated analysis methodology<sup>4</sup>. Prior to this round robin, no data existed indicating the pure contribution of only the analysis methodology on the variability of fracture toughness. By identifying the contribution of analysis method, and understanding what aspect of the contribution impacts the overall toughness value obtained, future standardization efforts can then be undertaken to minimize error.

## Round Robin Analysis Methods

It is worth briefly reviewing the method used to analyze a load-displacement response to determine a fracture toughness value from an ASTM E399 [1] test. Given a load–displacement response, the linear region of the data is identified and the slope ( $P/\delta$ ) of that data is determined. A line is then projected from the origin of the test data with a slope reduced 5 %,  $0.95(P/\delta)$ . The intersection between that construction line and the test data defines the conditional load  $P_Q$ , provided no previous load data at lower displacement exceeded the value of  $P_Q$ . Standard fracture mechanics K-solutions are then used with crack length and specimen dimensions to calculate a conditional fracture toughness,  $K_Q$ , that may or may not be  $K_{IC}$ , depending upon a variety of different validity checks.

---

<sup>4</sup> During a recent survey of the ASTM E08.07 subcommittee, only one laboratory indicated that it still uses the graphical method on a regular basis for production work.

## PARTICIPANTS AND METHODS

The round robin participants were drawn from ASTM E08 task groups focused on both fracture test methods as well as automation. The nine participants included Alcoa, FTA, Metcut, USNA, APES Inc, NIST, University of California—Davis, USAF-AFRL, and Exponent. Each participant was labeled with a random arbitrary letter identifier to protect confidentiality of the individual results.

The round robin participants were largely from laboratories in the fatigue and fracture testing community actively performing and routinely analyzing ASTM E399 [1] fracture toughness tests. As such, the tools that each participant utilized had been developed, exercised and proven to some extent of validation with past testing. Using this approach, the tools utilized in the round robin assessment represent those typical of the more experienced segment of the testing community.

As part of the round robin documentation required, each participant supplied detail regarding how their analysis was performed. These details, shown in Table 1, can be summarized as follows: one participant (participant G) used a graphical method (consistent with the spirit and nature of the original codification of ASTM E399 predating digital data acquisition), two participants used fully automated approaches with no user subjectivity (participants F and I) with the six remaining round robin participants using analysis approaches that required some user subjectivity.

However, it should be noted that classifying analysis methods was in some cases difficult; for instance, the analysis employed by participant H utilized a fixed

**TABLE 1** Different methods employed by the round robin participants for linearity analysis.

ID	Linearity Assessment Procedures and Methods
A	Spreadsheet based approach utilizing a reduced-displacement technique to graphically identify and pick-off the linear region.
B	LabVIEW based program where the user changes the min and max of the linear region and minimizes the residue to determine the best fit.
C	Spreadsheet based approach starting with a 10 %-50 % range and adjusted if warranted based on plots (R-curve crack extension approach).
D	Spreadsheet based approach visually observing the load-displacement record to determine the optimum linear region.
E	Spreadsheet based approach, pinning the lower point at 0 % and examining 0 %-60 %, moving the upper point as desired (13 of 15 datasets used 0 %-60 %, remainder 0 %-75 %).
F	Fully automated MathCAD program using a slope determination using analysis of residuals algorithm (limited user latitude and input).
G	Completely graphical approach on an $x$ - $y$ plotter.
H	Computer program (QBASIC) with an assumed 20 %-80 % (removed from closure, plasticity and crack extension effects)
I	Fully automated LabVIEW based program sliding the endpoints of the analysis interval up and down to optimize the selection based on minimum residual.

20 %–80 % linearity assessment, although this range was something that was selected based upon the character of the data and typical data in the past. As such, this method could alternatively be classified as a fully automated approach, albeit with no optimization routine.

## MATERIAL AND TESTING DATASETS

Sample datasets of load-displacement responses were gathered from a variety of different sources. In total, fifteen sets of load-displacement data were provided to round robin participants including the following:

- Seven sets of data from aluminum specimens (unidentified alloys) including six C(T) specimen geometries (AL1, 2, 4, 5, M1, and M2) and one SE(B) specimen geometry (JB4-3),
- Four sets of data from Ti-6Al-4V material, including two C(T) specimen geometries (HCC16 and HCC12) and two SE(B) specimen geometries (HCC2 and HCC4), and,
- Four sets of data from D6AC landing gear steel material, all C(T) specimen geometry (D6AC1, 3, 5 and 6)

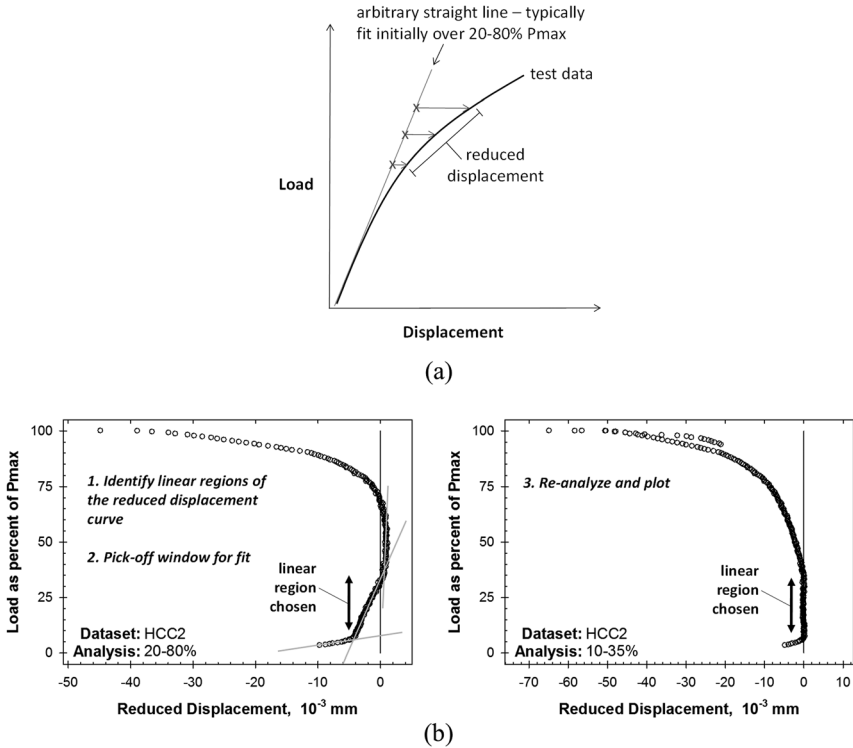
The load-displacement data were supplied to analyze participants in excel format along with the then current ASTM E399-09<sup>e2</sup> standard [1]. Round robin participants were asked to analyze the data sets using their standard methods and supply the conditional  $P_Q$  load along with several other analysis parameters as well as a description of the methods used. The region of the data used for the linearity assessment is identified for all participants in terms of the percentage of peak load; in other words, a set of data analyzed from 20 %–80 % is the portion of the  $P-\delta$  response from 20 % of  $P_{\max}$  to 80 % of  $P_{\max}$  for that data set.

A useful tool for assessing the nonlinearity of a given dataset is the so-called reduced-displacement plot. This method, described in more detail in Appendix X2 of the fatigue crack growth rate standard [7] for analyzing crack closure load, consists of fitting a line to a portion of the response and subtracting the response from that line. The reduced-displacement method, schematically depicted in Fig. 1(a), graphically amplifies nonlinearities and hence provides insight into the localized departure from linearity. As such, it is a useful tool and is used herein to provide additional detail into the nonlinearity observed in the analyzed data.

An application of a reduced-displacement plot for illustrating nonlinearity is shown in Fig. 1(b). To start, an arbitrary range of the data (in this case, the data interval corresponding to 20 %–80 % of the peak load) is selected and the least-squares-fit line for the load-displacement data is calculated. The reduced displacement is defined as the difference between the data and the best-fit line.

Given this reduced-displacement plot, the key then is to identify the linear regions of the data as shown in Figure 1(b). These linear regions of the reduced-displacement plot depict portions of the load-displacement data where linearity is evident. In Fig. 1(a) (left plot), three regions are identified: an initial portion at load levels less than 10 %  $P_{\max}$ , then a linear region spanned by approximately

**FIG. 1** The reduced-displacement method (a) described schematically and (b) utilized to depict the linear region of a set of data.

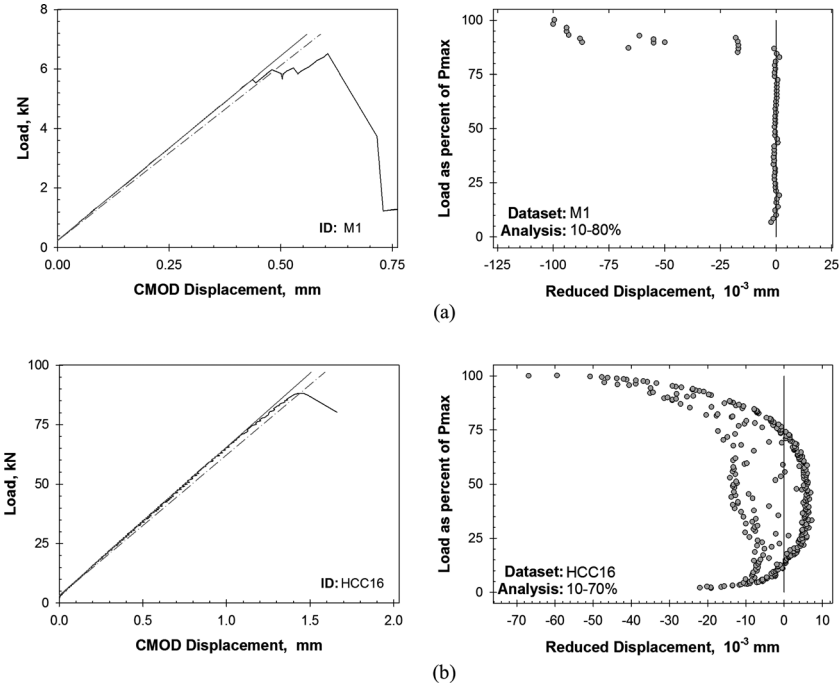


10 %–35 %  $P_{\max}$ , and finally a region from 35 %–60 %  $P_{\max}$ . The reduced-displacement is then recalculated, based on fitting the optimum 10 %–35 %  $P_{\max}$  interval as shown in Fig. 1(b). Using this approach, the reduced-displacement values in the best fit interval can be observed to be minimized in the interval of 10 %–35 %  $P_{\max}$  in Fig. 1(b). Using this approach, the challenge to the user is judging and selecting which of the “more linear regions” represent the true linear material behavior.

The fifteen datasets supplied to each round robin participant were selected to essentially represent the broadest range of behavior typically observed during linear–elastic fracture toughness testing. This is one reason that the datasets included three different materials, with very different resulting fracture toughness values as well as differing degrees of linear–elastic behavior.

For illustration, two typical datasets are shown in Fig. 2; in this case, each is from a C(T) specimen although fabricated from different materials. Both the original load–displacement response as well as the reduced-displacement plots are shown. In the case of the aluminum material, Fig. 2(a), the response is highly linear,

**FIG. 2** Typical P- $\delta$  and reduced displacement plots for (a) a highly linear dataset and (b) a more non-linear dataset.



with a distinct pop-in evident at about 85 % peak load. This is contrasted to the more nonlinear case for the titanium material, Fig. 2(b), where no clearly obvious linear region is identifiable.

In the case of the Ti-6Al-4V in Fig. 2(b), the spurious datapoints to the left of the primary response in the reduced-displacement plot are from unload-reload sequences applied during the fracture test. These unload-reload sequences were edited out of the file for convenience (prior to supplying the data to the round robin participants), although the very initial portion of them remained in the data and are clearly illustrated in the reduced-displacement plot.

### ANALYSIS RESULTS

This round robin effort, undertaken within the auspices of task group E08.03 on Test Automation, is detailed with the motivation and results presented in an extensive report on file with ASTM International [8]. The brief summary herein highlights the primary findings detailed in that report.

The analysis results from the nine different participants in this round robin analysis are included in Table 2. Two characterizations of the data are included in

**TABLE 2** Results from each participant for each dataset indicating  $P_Q/P_{max}$  and load ranged used in the linearity analysis.

Dataset ID No.	Round Robin Participant ID ( $P_Q/P_{max}$ and Percent Load Range Utilized for Analysis)								
	A	B	C	D	E	F	G	H	I
AL1	0.956	0.959	0.954	0.954	0.953	0.955	0.951	0.954	0.955
	15 %-65 %	20 %-78.4 %	10 %-43 %	11 %-64 %	0 %-60 %	7 %-66 %	14 %-56 %	20 %-80 %	15 %-59 %
AL2	0.968	0.971	0.966	0.966	0.928	0.974	0.962	0.966	0.991
	20 %-70 %	20 %-76 %	25 %-48 %	21 %-74 %	0 %-60 %	18 %-73 %	21 %-58 %	20 %-80 %	28 %-61 %
AL4	0.963	0.970	0.970	0.970	0.970	0.970	0.970	0.970	0.970
	5 %-65 %	20 %-79 %	29 %-50 %	18 %-81 %	0 %-60 %	4 %-83 %	11 %-31 %	20 %-80 %	3 %-80 %
AL5	0.989	1.000	1.000	1.000	1.000	1.000	0.998	1.000	1.000
	15 %-65 %	20 %-83 %	15 %-47 %	18 %-80 %	0 %-60 %	15 %-87 %	12 %-53 %	20 %-80 %	11 %-90 %
HCC16	0.999	0.999	1.000	1.000	0.998	1.000	0.999	1.000	1.000
	10 %-70 %	15 %-81 %	20 %-50 %	23 %-68 %	0 %-60 %	5 %-85 %	10 %-38 %	20 %-80 %	4 %-24 %
HCC12	0.995	0.996	0.996	0.994	0.995	0.996	0.961	0.996	0.981
	10 %-70 %	15 %-75 %	20 %-50 %	11 %-57 %	0 %-60 %	5 %-86 %	4 %-18 %	20 %-80 %	5 %-25 %
HCC2	0.973	0.999	0.991	0.999	0.984	0.999	0.940	0.999	0.974
	10 %-35 %	18.5 %-82.5 %	11 %-54 %	24 %-72 %	0 %-60 %	39 %-62 %	9 %-35 %	20 %-80 %	8 %-36 %
HCC4	0.981	0.994	0.991	0.996	0.982	0.991	0.988	0.996	0.992
	10 %-40 %	18.5 %-80.5 %	10 %-50 %	23 %-80 %	0 %-60 %	21 %-57 %	10 %-52 %	20 %-80 %	25 %-60 %
JB4-3	0.959	0.994	0.970	0.996	0.938	0.959	0.930	1.000	0.957
	10 %-45 %	20 %-83 %	10 %-50 %	23 %-70 %	0 %-60 %	11 %-41 %	15 %-31 %	20 %-80 %	12 %-37 %
M1	0.909	0.917	0.917	0.917	0.917	0.917	0.917	0.917	0.917

**TABLE 2** *Continued*

Dataset ID No.	Round Robin Participant ID ( $P_o/P_{max}$ and Percent Load Range Utilized for Analysis)								
	A	B	C	D	E	F	G	H	I
	10 %-80 %	20 %-83 %	10 %-48 %	15 %-77 %	0 %-60 %	37 %-72 %	19 %-77 %	20 %-80 %	24 %-72 %
<b>M2</b>	0.789	0.789	0.764	0.788	0.802	0.785	0.612	0.847	0.660
	15 %-65 %	18.5 %-65 %	10 %-48 %	24 %-58 %	0 %-75 %	9 %-63 %	4 %-29 %	20 %-80 %	4 %-20 %
<b>D6AC1</b>	0.919	0.920	0.941	0.934	0.937	0.911	0.904	0.940	0.966
	25 %-60 %	13.5 %-68 %	1 %-49 %	15 %-74 %	0 %-60 %	29 %-52 %	18 %-51 %	20 %-80 %	1 %-28 %
<b>D6AC3</b>	0.911	0.936	0.912	0.925	0.920	0.901	0.865	0.945	0.901
	5 %-50 %	18 %-75 %	1 %-51 %	12 %-63 %	0 %-60 %	6 %-33 %	4 %-32 %	20 %-80 %	7 %-34 %
<b>D6AC5</b>	0.890	0.907	0.893	0.905	0.916	0.888	0.744	0.933	0.884
	5 %-50 %	20.5 %-70 %	1 %-50 %	11 %-67 %	0 %-75 %	5 %-45 %	4 %-41 %	20 %-80 %	13 %-40 %
<b>D6AC6</b>	0.914	0.921	0.928	0.916	0.917	0.921	0.870	0.954	0.895
	5 %-50 %	18.5 %-59 %	1.5 %-70 %	13 %-51 %	0 %-60 %	19 %-51 %	2 %-41 %	20 %-80 %	3 %-30 %

Table 2: the  $P_{\max}$  normalized  $P_Q$  load as well as the specific range of the data, in terms of %  $P_{\max}$ , used in the linearity assessment. The data in Table 2 are further analyzed in Table 3 providing the average  $P_Q$  value (normalized by  $P_{\max}$ ) as well as the minimum, maximum, and two standard deviations of the mean (all normalized by average  $P_Q$  value). Assuming a normal distribution, the two standard deviations represent the 95 % probability level. Note that Table 3 groups the datasets in terms of different materials and also provides a material-by-material statistical summary of the data.

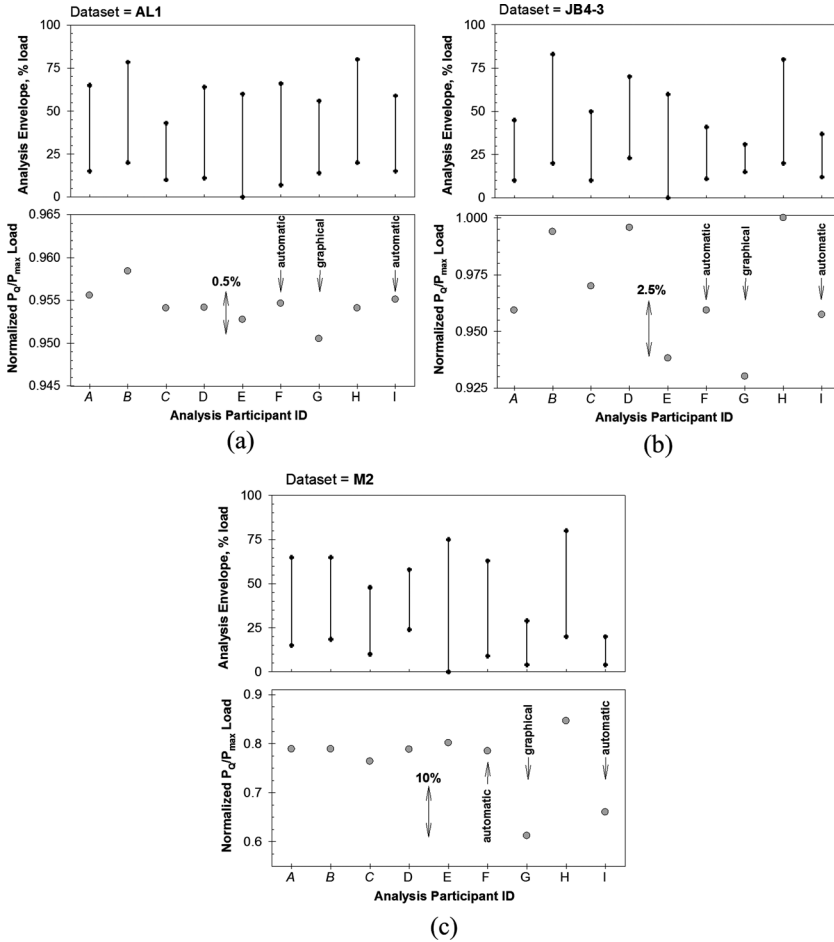
Further insight into the round robin analyses can be gained by observing the results from three different datasets indicated in Fig. 3. These datasets have been chosen to represent a simply scattered case (AL1, Fig. 3(a)), a high variability case (JB4-3, Fig. 3(b)), and the highest observed variability (M2, Fig. 3(c)). Each of these examples are made up of two plots with the upper one illustrating the range of the load data chosen by each participant and the lower one illustrating the corresponding variability in  $P_{\max}$  normalized  $P_Q$  value. Note, too, that annotations to the lower plot indicate an error range (% of  $P_Q/P_{\max}$ ) as well as the participants using the two automatic and one graphical analysis methodology.

What is striking about Fig. 3 is the variability in the range chosen to fit the data. Examining for instance Fig. 3(a), participant C utilized the load range of 10 %–40 % and achieved nearly the same result as participant H who utilized the

**TABLE 3** Statistical analysis of the results from each participant grouped by material.

Test Material	Dataset ID	Average $P_Q/P_{\max}$	Normalized by Average $P_Q$ Value		
			Minimum	Maximum	2 std devs
aluminum	AL1	0.9545	0.9960	1.0042	0.0045
	AL2	0.9659	0.9612	1.0258	0.0339
	AL4	0.9693	0.9934	1.0008	0.0049
	AL5	0.9985	0.9903	1.0016	0.0074
	JB4-3	0.9671	0.9618	1.0340	0.0519
	M1	0.9159	0.9927	1.0009	0.0055
	M2	0.7596	0.8057	1.1145	0.1959
	<i>average</i>	<i>0.9330</i>	<i>0.9573</i>	<i>1.0260</i>	<i>0.0434</i>
titanium	HCC16	0.9993	0.9984	1.0007	0.0017
	HCC12	0.9900	0.9703	1.0063	0.0244
	HCC2	0.9842	0.9553	1.0153	0.0400
	HCC4	0.9900	0.9911	1.0056	0.0108
	<i>average</i>	<i>0.9909</i>	<i>0.9788</i>	<i>1.0070</i>	<i>0.0192</i>
steel	D6AC1	0.9302	0.9722	1.0387	0.0403
	D6AC3	0.9129	0.9478	1.0354	0.0509
	D6AC5	0.8843	0.8410	1.0550	0.1243
	D6AC6	0.9150	0.9513	1.0423	0.0497
	<i>average</i>	<i>0.9106</i>	<i>0.9281</i>	<i>1.0428</i>	<i>0.0663</i>
ALL MATLS	<i>average</i>	<b>0.9424</b>	<b>0.9552</b>	<b>1.0254</b>	<b>0.0431</b>

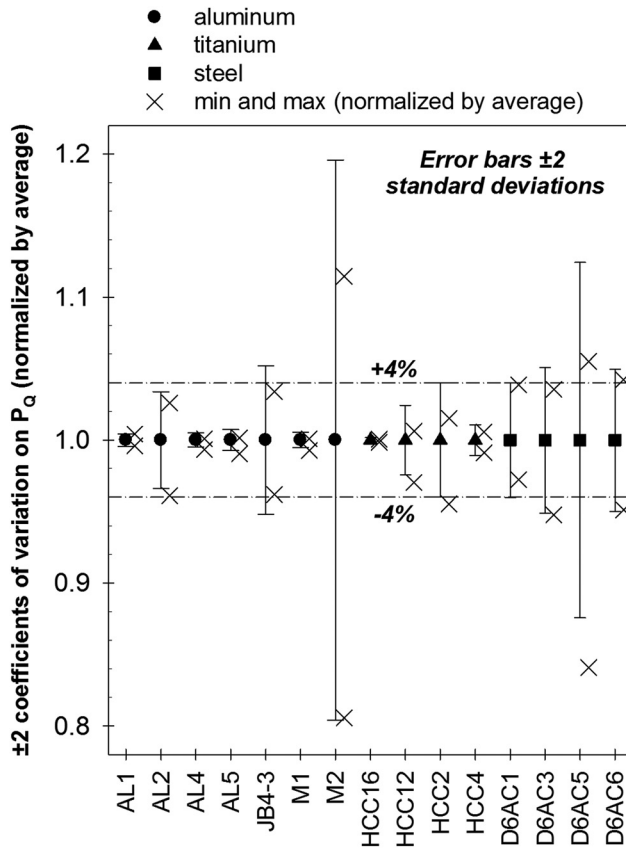
**FIG. 3** Three different dataset analyses indicating (a) simply scattered (AL1), (b) high variability (JB4-3), and (c) the highest variability (M2).



range 20 %–80 %. This is clearly suggestive that dataset AL1 had a fairly linear load–displacement response and exhibited some insensitivity to the analysis range utilized to assess linearity. This is contrasted to the case of M2, Fig. 3(c), where the participants utilizing the smallest range (participants G and I) generated  $P_Q$  results markedly lower than all the other participants.

An overall summary of the statistics in Table 3 is graphically summarized in Fig. 4. Note that all the quantities have been averaged by the mean  $P_Q$  value so as to be able to compare results for the different materials and different sized specimens. The ordinate of Fig. 4 is  $\pm 2$  standard deviations divided by the average value (the coefficient of variation of the  $P_Q$  data). For comparative purposes, the  $\pm 4$  %

FIG. 4 Statistics associated with each analyzed dataset.



horizontal limits are also shown on the plot which is a reasonable level that captures most of the analysis error depicted in Fig. 4. To further interpret the error bars in Fig. 4, the “x” symbols depict the minimum and maximum apparent in the data. Since these symbols fall within (or very near) the error bars for most tests, this indicates that the error bar extrema (error bar extents) is a reasonable descriptor of the range observed in the data.

## Discussion

### TEST-BY-TEST DIFFERENCES

The differences on a test-by-test basis are apparent by examining the data from each test, individually shown in Tables 2 and 3 and Fig. 4. Considering first the tests performed on aluminum material, some tests (AL1, AL4, AL5, and M1) exhibit

little  $P_Q$  variability. In these cases, the  $P_Q$  data are tightly grouped with overall variability less than  $\pm 1\%$ . Higher levels of variability are evident for AL2, JB4-3, and M2. In the case of AL2 and M2, the  $P_Q$  values tend to be grouped (see Table 2), with an outlier or two affecting the overall variability (see, for instance, M2 in Fig. 3(c)). This is contrasted to the case for JB4 (Fig. 3(b)) where the data variability is simply large and quite varied, with no apparent  $P_Q$  grouping.

The titanium material behaved similarly to the aluminum, with essentially a bimodal form of the data with either little variability or larger amounts of variability. This is contrasted to the steel material where all tests exhibited higher levels of analysis variability. In the case of D6AC1 and D6AC3, the data was simply scattered, with no apparent  $P_Q$  grouping. This is contrasted to the other two tests, D6AC5 and D6AC6, where  $P_Q$  grouping is apparent and the variability occurs due to an outlier or two.

In terms of overall variability (see material averages in Table 3), the titanium material tests yielded the lowest amount of error and the steel material tests the highest, with the aluminum material tests in between the two extremes. However, it is not believed that there is sufficient data to make any definitive observations regarding variability as a function material type; these observations are based on the few data contained herein.

**OUTLIERS AS A FUNCTION OF PARTICIPANT**

If all analysis errors were random and all analysis methodologies the same, one would expect no systematic grouping of outliers (minimum or maximum  $P_Q$  values) as a function of participant. Examining the data in this manner is important from the viewpoint of standardization; if there are particular aspects of the analysis in the E399 standard that require modification to ensure consistency, examining the data on the basis of systematic trends is an excellent way to identify these types of ambiguity.

The number of times that each participant was responsible for either the unique maximum or unique minimum  $P_Q$  is shown in Table 4. Given the results in Table 4, there does appear to be some systematic trends since the data are not distributed among all of the round robin participants.

**TABLE 4** Summary of systematic trends observed in the analysis of the round robin data.

Statistical	Round Robin Analysis Participant, Number of Times...									
	A	B	C	D	E	F <sup>a</sup>	G <sup>b</sup>	H	I <sup>a</sup>	other
uniquely minimum $P_Q$	4 <sup>c</sup>	—	—	—	2	—	9	—	—	0 ties
uniquely maximum $P_Q$	—	1	—	—	—	2	—	6 <sup>d</sup>	2	4 ties

<sup>a</sup>Automated analyses.

<sup>b</sup>Graphical analysis.

<sup>c</sup>Three of 4 due to interpolation (versus discretization).

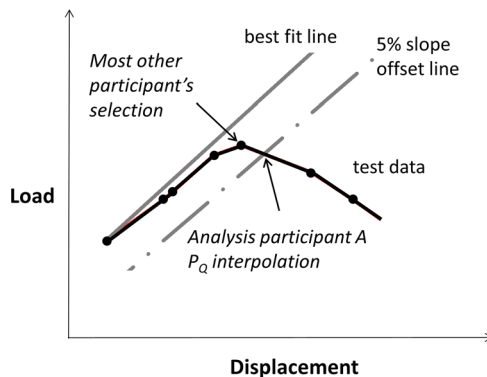
<sup>d</sup>Method assumed a 20-80 % load window.

Participant A's analyses yielded the minimum  $P_Q$  value four times. However, upon further examination of the approach used by Participant A, the reason for this is the way their analysis algorithm works. Participant A utilized an interpolation scheme to determine the  $P_Q$  load (see Fig. 5) identical in form to what would be done with an autographic analysis. However, Participant A failed to note that the ASTM E399 [1] standard states that if a load preceding  $P_Q$  exceeds  $P_Q$  (a Type III response in ASTM E399), then the preceding higher load level is  $P_Q$ . This error was responsible for three of the four minimum extrema noted for Participant A in Table 4. In the strictest sense, three of the four minimums were due to not correctly following the ASTM E399 standard.

As shown in Table 4, for 60 % of the datasets, Participant G yielded the minimum  $P_Q$  value. Recall that Participant G was the sole participant who used a purely graphical approach to analyze the data. The results are clearly suggestive that a graphical technique can yield minimum  $P_Q$  values, although it is unclear (since there were no other graphical-based approaches) whether consistently yielding low values is a consequence of how Participant G implemented their graphical analysis or whether graphical analysis is by its nature conservative (yielding lower  $P_Q$  values).

A less conservative analysis was provided by Participant H who yielded the highest  $P_Q$  value for 40 % (6 of 15) of the datasets. Recall that Participant H used a fixed 20 %–80 % interval for analysis. In five of the six cases where they noted maximum  $P_Q$  values, the lower and upper envelope selection was typically higher than that utilized by the rest of the analysts. After the results of this round robin were published in Ref. [8], Participant H re-evaluated their approach and instead of using a fixed 20 %–80 % interval modified their analysis to utilize the range of 20 %–70 % (coincidentally the default range for that participant's software package). When the data were re-analyzed, instead of yielding the high value six times, the new load envelope yielded the high value only twice.

**FIG. 5** Interpolation difference for analysis utilized by Participant A.



Finally, it is worth noting that the two participants that used an automatic analysis method with no user subjectivity (F and I) yielded the uniquely maximum values four times. However, the statistical significance of this observation is certainly questionable due to the few automated analyses employed (two of nine participants) and the limited number of occurrences.

#### PIVOT METHODOLOGY FOR THE 5 % SLOPE OFFSET LINE

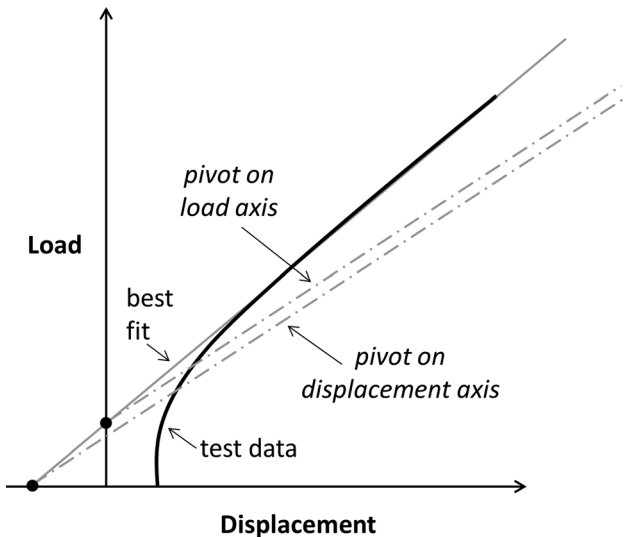
These round robin analyses also highlighted an ambiguity in the ASTM E399 test standard [1]. The standard says to draw the 5 % slope offset line, rotating the line through the “origin” of the data, although the origin is not specifically defined. The ambiguity in this approach is more clearly shown in Fig. 6; an origin could be interpreted for the intersection point with either the load or the displacement axis. Depending upon how the line is fit and the boundary conditions applied, the offset line could be rotated about either the load or the displacement intercept.

This issue was subsequently discussed at an ASTM meeting and a specific clarification was added to the ASTM E399 standard more definitively indicating that the origin of rotation was the displacement axis intercept.

#### ANALYSIS METHODOLOGY CONTRIBUTION TO FRACTURE TOUGHNESS ERROR

Based upon the preceding discussion and the data presented in Tables 2 and 3 and Fig. 4, the global statistics suggest that the  $P_Q$  analyses follow a bimodal

**FIG. 6** One of the ancillary issues related to ASTM E399 analysis that the round robin identified.



form, with either a very low overall impact on  $P_Q$  or a markedly higher level. Quantifying these two levels, the very low corresponds to  $\pm 1\%$  whereas the higher level is on the order of  $\pm 4\%$ . Recall these levels are based on the graphical data in Fig. 4 based on  $\pm 2$  coefficients of variation on the average  $P_Q$  value.

Examining the precision and bias section of the ASTM E399-09 standard [1] (Tables 1 and 2 in the standard) shows that a similar  $\pm 2$  coefficients of variation (regardless of whether precision, repeatability, or reproducibility is examined) suggests about  $\pm 13\%$  uncertainty for aluminum and  $\pm 8\%$  uncertainty for steel. However, it is interesting to note that the steel material testing herein suggested higher levels of variability for steel, although the D6AC material test data analyzed during this current round robin does differ from the alloy steel detailed in the round robin testing in reference [1].

Thus, neglecting the influence, if any, of material suggests an overall  $K_Q$  (or  $P_Q$ ) uncertainty of about  $\pm 10\%$ . Given that range, and the observed average coefficient of variation herein of  $\pm 4.3\%$  (Table 3), this implies that the analysis methodology alone on average account for up to one-third of the overall uncertainty. Conversely, in the case of the low uncertainty ( $\pm 1\%$ ) results, the analysis methodology can accounts for approximately one-tenth of the overall uncertainty. This implies that the analysis methodology is a meaningful contributor, although not likely a primary contributor, to the observed variability in fracture toughness.

#### **FUTURE STANDARDIZATION EFFORTS**

One of the primary purposes of an analysis round robin like this one is to make the testing community aware of how subjective analysis can impact the results from a given standard test. This subjective user input will never be completely removed from the testing process. In part, subjectivity in a standard test method is required to ensure that it applies to the broadest possible range of possible test outcomes. Nevertheless, by providing tools such as the reduced-displacement method described herein as well as techniques such as the previously described SDAR algorithm [4], users of test standards can make better, more-informed choices when having to subjectively influence the analysis process.

Understanding the role of analysis on the variability of a given test result is a key to developing standardization strategies to minimize these types of errors. As test laboratories become more and more digitally based, our test standards need to reflect this trend and accommodate the changing character of testing. However, the challenge for the standards writing community is how to do this effectively while still maintaining flexibility in a test standard. The first step in this process is to raise the awareness by analysis round robins such as this and then subsequently developing the tools to equip the testing community with methods and techniques that can provide insight into how analysis methods influence test results.

## Conclusions

An analysis round robin involving nine participants and fifteen load–displacement datasets from three different materials was undertaken utilizing the linear–elastic analysis methodology in the ASTM E399-09 standard [1]. This analysis round robin showed the following:

1. A bi-modal trend in  $P_Q$  variation was noted with  $\pm 1$  % variability capturing 40 % of the datasets and  $\pm 4$  % variability generally capturing the remaining 60 % of the datasets (although there were datasets beyond this general variability range).
2. The variability did not definitively appear related to material; although for these analyses, the titanium alloy exhibited the least variability and the steel alloy the most variability, with the aluminum alloys in between the two extremes.
3. Some systematic trends were noted as a function of the methods used by the round robin participants. One participant applied an interpolation scheme that resulted in minimum values for a number of the tests. Another participant utilized a purely graphical approach that yielded conservative minimums for 60 % of the tests. Finally, one other participant utilized a fixed interval for analysis (20 %–80 % of load) that yielded non-conservative maximum values for 40 % of the datasets.
4. The method utilized to analyze the load–displacement response in a linear–elastic fracture toughness test contributes to between a minimum of one-tenth and on average one-third of the overall uncertainty observed in more extensive round robins varying all aspects of the test methodology. In two of the nine datasets, linearity analysis methodology accounted for in excess of 10 % error in  $P_Q$  value.
5. Although the analysis methodology is likely not a primary contributor to the overall variability observed in a fracture toughness test, it is a significant contributor. Additional standardization efforts to provide guidance to users of the ASTM E399-90 [1] standard regarding optimally selecting the linear region of the load–displacement response will undoubtedly minimize the error resulting from subjective user input.
6. The round robin highlighted an ambiguity in the ASTM E399-90 [1] standard regarding how the fit line was pivoted. As a consequence, the standard was subsequently modified through the ASTM consensus balloting process to resolve the ambiguity.

### ACKNOWLEDGMENTS

This work was originally motivated by extensive discussions within ASTM subcommittee E08.03 on Test Automation several years ago. Recent efforts within task groups of this subcommittee have yielded valuable tools in the way of analysis method development, standardized datasets for assessing the performance of automated tools, and calibration/sensor issues. Finally, the voluntary effort of all of the participants in this analysis round robin is greatly appreciated.

## References

- [1] ASTM E399-09: Standard Test Method for the Linear-Elastic Plane-Strain Fracture Toughness  $K_{Ic}$  of Metallic Materials, *Annual Book of ASTM Standards*, ASTM International, West Conshohocken, PA, 2012.
- [2] A. A. Braun, N. E. Ashbaugh, and F. M. Smith, Eds., *Applications of Automation Technology to Fatigue and Fracture Testing, STP 1092*, ASTM, Philadelphia, PA, 1990.
- [3] McKeighan, P. C. and Hillberry, B. M., "An Algorithm for Determining the Tensile Properties From Digitally Recorded Tensile Test Data," *Exp. Tech.*, Vol. 15, No. 6, 1991, pp. 27-30.
- [4] Graham, S. M. and Adler, M. A., "Determining the Slope and Quality of Fit for the Linear Part of a Test Record," *J. Test. Eval.*, Vol. 39, No. 2, 2011, pp. 260-268.
- [5] Scibetta, M. and Schurrmans, J., "Development of Qualification of an Algorithm for The Determination of the Initial Linear Portion of a Force Versus Displacement Record," *J. Test. Eval.*, Vol. 32, No. 6, 2004, pp. 500-503.
- [6] McKeighan, P. C., Feiger, J. H., and McKnight, D. H., "Round Robin Test Program and Results for Fatigue Crack Growth Measurement in Support of ASTM Standard E647," *Final Report*, Southwest Research Institute, San Antonio, TX, 2008.
- [7] ASTM E647-11: Standard Test Method for Measurement of Fatigue Crack Growth Rates, *Annual Book of ASTM Standards*, ASTM International, West Conshohocken, PA, 2012.
- [8] McKeighan, P. C., "ASTM Task Group Activity Report: E399 Data Analysis Round Robin Results," ASTM International, West Conshohocken, PA, 2011.

---

STP 1571, 2014 / available online at [www.astm.org](http://www.astm.org) / doi: 10.1520/STP157120130069

Stephen M. Graham<sup>1</sup>

# Uncertainty in Ductile Fracture Initiation Toughness ( $J_{IC}$ ) Resulting From Compliance Measurement

## Reference

Graham M., "Uncertainty in Ductile Fracture Initiation Toughness ( $J_{IC}$ ) Resulting From Compliance Measurement," *Application of Automation Technology in Fatigue and Fracture Testing and Analysis*, STP 1571, Peter C. McKeighan and Arthur A. Braun, Eds., pp. 134-152, doi:10.1520/STP157120130069, ASTM International, West Conshohocken, PA 2014.<sup>2</sup>

## ABSTRACT

ASTM E1820-13 for determining ductile fracture initiation toughness ( $J_{IC}$ ) includes a single-specimen technique where crack length is determined using the compliance measurement from partial unloads. Noise and nonlinearity in the compliance data, together with the method used to select data to perform linear regression, lead to statistical uncertainty in the resulting crack lengths and  $J_{IC}$ . Statistical analysis of linear regression was used to quantify variability in compliance for different selection methods. A Monte Carlo simulation was conducted to propagate that variability to the determination of  $J_{IC}$  and to quantify the resulting uncertainty. Recommendations are made regarding how to select data for linear regression to minimize uncertainty. The simulation shows that a standard error on compliance of less than 0.25 % of the compliance results in a standard deviation in  $J_{IC}$  of less than 4 % of the mean  $J_{IC}$ .

## Keywords

unloading compliance, fracture toughness, uncertainty

---

Manuscript received May 13, 2013; accepted for publication June 27, 2014; published online August 29, 2014.

<sup>1</sup>Department of Mechanical Engineering, United States Naval Academy, 590 Holloway Road, Annapolis, MD 21402.

<sup>2</sup>ASTM Sixth Symposium on *Application of Automation Technology in Fatigue and Fracture Testing and Analysis* on May 23, 2013 in Indianapolis, IN.

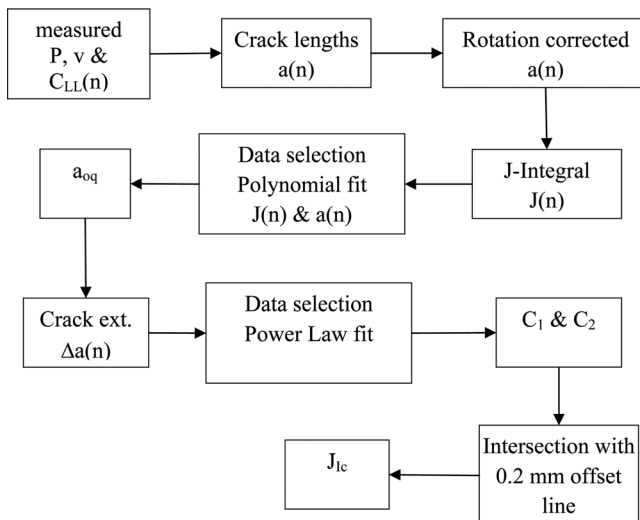
## Introduction

ASTM E1820-13 [1] provides a resistance curve procedure whereby the  $J$ - $R$  curve can be generated using a single specimen by conducting partial unloads periodically during the test and using compliance determined from the unload/reload to calculate crack length. The flow chart in Fig. 1 illustrates the data analysis procedure required to go from compliance data to  $J_{Ic}$  as well as the various parameters involved. Variables in the figure are:  $P$  is force,  $v$  is displacement,  $C_{LL}$  is load line compliance, and  $(n)$  denotes that there is one for each of  $n$  unloads;  $a$  is compliance determined crack length,  $J$  is the  $J$ -integral,  $a_{oq}$  is the analytically determined initial crack length from from a polynomial fit,  $\Delta a$  is crack extension, and  $C_1$  and  $C_2$  are coefficients from the power law fit.

Link conducted an analysis of an analytical round robin where labs were provided data sets and asked to determine  $J_Q$  per ASTM E1820, Annex A9, and check validity criteria [2]. Link found that the variability in  $J_Q$  between labs originated from variability in calculation of crack extension, which is related to both the analytically determined initial crack length,  $a_{oq}$ , and the crack lengths calculated from the partial unloads. This is a case where the quantity of interest is the difference between two quantities that are close in magnitude, and relatively small variability

**FIG. 1** Flow-chart illustrating data analysis procedure to determine  $J_{Ic}$  per E1820.  $(n)$  indicates that there is one value per compliance measurement.

### $J_{Ic}$ Determination per E1820-13 for a C(T) specimen



in each quantity can result in large variability in the difference. He observed that the calculated crack extensions were a strong function of the method used to select data for the linear regression to determine crack length. There are two aspects of the data selection, clipping the data at the start and end of the partial unload, and selection of either unload data, reload data, or both for the linear regression. No specific information was given on how the labs clipped the data to remove the non-linearity at the start and end of the partial unload. Of the 5 labs included in the study, one lab used unload data only, one lab used reload only, and three labs used both. Link concluded that “the uncertainty in fracture toughness could be reduced considerably by the prescription of a specific method for selecting data points used in the compliance estimates.”

There are many steps in the process, and consequently it is difficult to relate the effect of measurement errors and noise on the resulting ductile fracture initiation toughness,  $J_{Ic}$ . Van Der Sluys and Futato [3] conducted a sensitivity study to determine how digital resolution and noise in force ( $P$ ) and displacement ( $v$ ) signals affects uncertainty in crack length determination by unloading compliance. Digital resolution is less of a concern with new 16-bit or higher data acquisition systems. However, they did show that electrical noise in force and displacement signals limits the statistical confidence in crack length measurement. They recommended that there be at least 100 points over the unload/reload, and they recognized the importance of excluding regions of the data that exhibit nonlinearity. They did not extend their analysis to show a relationship between uncertainty in crack length and uncertainty in  $J_{Ic}$ . A later study by Futato et al. [4] expanded the scope by conducting a sensitivity study where they considered nonlinearity in the displacement transducer and how it affects errors in crack length and the corresponding  $J$  values. They also factored in errors in specimen thickness, width, and elastic modulus on the resulting  $J$  values. They noted the important effect of data selection on determination of  $J_{Ic}$ , and looked at the effect of errors in flow stress on  $J_{Ic}$ , but were not able to include all of these effects to arrive at an estimate of uncertainty in  $J_{Ic}$ . They concluded that crack length calculation is relatively insensitive to errors in specimen dimensions and displacement transducer nonlinearity, and that the net effect on  $J_{Ic}$  is small. They also found that  $J_{Ic}$  is insensitive to error in flow stress, but that it is sensitive to the location of  $J-\Delta a$  points used to determine  $J_{Ic}$ . This is consistent with the Link's conclusions and points to the importance of uncertainty in crack lengths from unloading compliance measurements. However, the test method does not give any guidance on how to conduct the compliance determination. It is typically done using linear regression of both unload and reload data. Examination of the data for an unload/reload reveals that they do not always fall right on top of one another. In some cases there is a displacement shift that occurs in transitioning from unloading to reloading, and in other cases there is non-linearity at the ends that results in a hysteresis loop. It is also possible that the noise level in unload and reload may be different. For any of these cases, the choice of whether to fit just unload, just reload, or both can have an effect on the resulting compliance, and consequently on the

determination of  $J_{Ic}$ . The objective of this study was to quantify uncertainty in  $J_{Ic}$  resulting specifically from variability in compliance.

The mechanics of a specimen subjected to a partial unloading indicate that the unload/reload response is predominantly elastic and linear. Consequently, linear regression is an appropriate method for determining the compliance. The most common approach is to use a simple linear regression model that represents the unload/reload as a process whereby displacement is the independent variable and force is the dependent variable. The specimen response consists of a linear relationship between the mean value of force  $E(Y)$  and displacement ( $x$ ) with a superimposed random error in force ( $\varepsilon$ ), as shown in Eq 1. Linear regression is used to determine the slope ( $\beta_1$ ) of the data, which corresponds to  $\Delta P/\Delta v$ .

$$(1) \quad Y = E(Y) + \varepsilon$$

where

$$(2) \quad E(Y) = \beta_0 + \beta_1 x$$

The random error term ( $\varepsilon$ ) is assumed to be normally distributed with zero mean and variance  $\sigma^2$ . Consequently, the response  $Y$  at any value of  $x$  follows a normal distribution with a mean of  $E(Y)$  and a variance of  $\sigma^2$ .

$$(3) \quad \sigma = \sqrt{\frac{1}{n-2} \sum \varepsilon_i^2}$$

where

$$(4) \quad \varepsilon_i = y_i - (\beta_0 + \beta_1 x_i)$$

Estimates of the slope and intercept ( $\hat{\beta}_0, \hat{\beta}_1$ ) are determined by minimizing the sum of the squared residuals.

Data collection during the unload/reload represents sampling of data from the process. If the unload/reload were repeated many times, the resulting slopes would exhibit some variance. When the error is normally distributed, the estimate of slope ( $\hat{\beta}_1$ ) is also normally distributed with mean  $\beta_1$  and standard error:

$$(5) \quad s_{\beta_1} = \sqrt{\frac{\frac{1}{n-2} \sum (y_i - (\hat{\beta}_0 + \hat{\beta}_1 x_i))^2}{\sum (x_i - \bar{x})^2}}$$

where  $\bar{x}$  is the mean of the  $x$ -values. Uncertainty in the slope can be characterized by generating confidence bounds. The Student's-t distribution can be used with the standard error of the slope to generate confidence bounds provided that:

1. There is just one independent variable,  $x$ , and one dependent variable,  $Y$ .
2. For any value of  $x$ , the  $Y$ -values are independent and are normally distributed.

3. For each value of  $x$ , the probability distribution of  $Y$  has the same standard deviation.

The first condition requires that force is only a function of displacement, which is reasonable in the absence of crack growth, creep, or significant temperature variations. The second condition requires that the variation in force be due to random noise, and the third requires that the noise level is independent of displacement. In the absence of non-linear effects that can lead to hysteresis, it is reasonable to conclude that these conditions are satisfied. The confidence interval at confidence level  $(1-\gamma)$  can then be estimated using Eq 6.

$$(6) \quad \beta_1 \in \left[ \hat{\beta}_1 - s_{\beta_1} t_{n-2}^*, \hat{\beta}_1 + s_{\beta_1} t_{n-2}^* \right]$$

where  $t_{n-2}^*$  is the  $100(1 - \gamma/2)$  percentile of the students-t distribution ( $t_{n-2}$ ).

In this study, compliance ( $\Delta v/\Delta P$ ) was determined directly by making force the independent variable and displacement dependent instead of determining the stiffness ( $\Delta P/\Delta v$ ) and taking the inverse. Checking both ways revealed that there is a difference between the resulting compliances for these two approaches. This is likely due to round-off error in the algorithms typically used for linear regression, even when double precision is used. The direct approach was selected here to avoid adding any additional sources of uncertainty.

## Analysis of Uncertainty

In 2011, the task group responsible for developing and maintaining test method ASTM E1820 held an analytical round robin specifically addressing the determination of  $J_{Ic}$ . The data sets supplied to the participants included aluminum and steel alloys that exhibit stable tearing, and included tests with valid and invalid results. This study utilized the round robin data sets for compact tension,  $C(T)$  specimens, shown in Table 1.

Raw data consisting of load and load–line displacement from ASTM E1820 tests with unloading compliance were available for the round robin specimens. The data files did not contain any information indicating where the partial unloads started or ended. Therefore, a replay program was written to extract the unload/reload data for each compliance measurement. The start of an unload was determined using a “box + 5-point” algorithm where the maximum load–line displacement is monitored and as soon as a decrease is detected, a “box” is “drawn” around the point of maximum displacement. An unload is determined to have started when 5 consecutive points fall outside the box. The purpose of this box is to prevent noise in either force or displacement from triggering a false unload. The force and displacement representing the start of the unload correspond to the point of maximum displacement used to establish the “box.” The box dimension for force varied from 10 to 50 lb and for displacement varied from 0.00001 to 0.00002 in. These dimensions were based on observations of noise levels in the data. The extracted

**TABLE 1** Specimens used in ASTM E1820 analytical round robin to determine  $J_{Ic}$ .

	Description	Material	<i>W</i>	<i>B</i>	<i>B<sub>n</sub></i>	<i>B<sub>e</sub></i>	<i>a<sub>o</sub></i>	<i>a<sub>f</sub></i>	<i>E</i>	Yield Strength	UTS
			in.	in.	in.	in.	in.	in.	psi	ksi	ksi
FGN-30	1T C(T)	CS-19 AL	1.992	0.995	0.793	0.954	1.180	1.676	$1.07 \times 10^7$	32.5	60
FGN-74	1/2T C(T)	CS-19 AL	0.997	0.502	0.404	0.483	0.571	0.839	$1.07 \times 10^7$	32.5	60
GJO_12A	1T C(T)	A533B	2.001	1.000	0.800	0.960	1.115	1.275	$2.90 \times 10^7$	65	87.1
FYB_A1	1T C(T)	HY-80	1.998	0.998	0.800	0.959	1.210	1.753	$2.90 \times 10^7$	89	106
Eur-U26	1T C(T)	Euro <sup>a</sup>	1.996	0.998	0.825	0.968	1.191	1.297	$3.00 \times 10^7$	68	89
Eur-U44	1T C(T)	Euro <sup>a</sup>	1.993	0.997	0.821	0.966	1.146	1.253	$3.00 \times 10^7$	68	89

<sup>a</sup>Quenched and tempered pressure vessel steel, DIN 22NiMoCr37, which is similar to ASTM A508 Class 3.

unload/reload data start with the sixth point that falls outside the box and end when the displacement exceeds the displacement of the first point outside the box. This algorithm removes some of the non-linear region that typically occurs at the start of an unload. The point of minimum force in an unload was used to determine the start of the reload.

### **EVALUATION OF DATA SELECTION**

The first part of this study looked at how data selection for compliance determination influences the resulting  $J$ - $R$  curves. Compliance was determined for the unload data only, the reload data only, and for both. The slope determination by analysis of residuals (SDAR) algorithm was used to obtain the best fit to the data [5]. The SDAR algorithm finds the best linear fit using two steps, the first of which finds the optimum region (OR) by performing linear regressions on every possible contiguous sub-set of the compliance data and locates the region with the lowest standard error. This is done by starting with the bottom 20 % of the data, performing the regression to obtain the standard error, then adding one point to the upper end and repeating the process until the full range is fit. The process continues by starting with the point second from the bottom and fitting 20 %, then adding one point to the upper end and repeating the process as before. The last regression dataset consists of the 20 % at the top end. This typically results in thousands of regressions, but can be done pretty quickly using modern computers. The second step uses analysis of residuals to adjust the selected data by eliminating outliers and extending the fit range. The algorithm had to be adjusted when fitting both unload and reload for some data sets because offsets or hysteresis between unload and reload caused the residuals to be relatively large, which created a problem with the second step of the algorithm. The data for each unload/reload was shifted to start from (0,0) and scaled by the maximum force and displacement so that  $x$  and  $Y$  both range from 0 to 1. The resulting fit ranges for all compliance measurements in one particular test specimen are shown in Fig. 2. Each point corresponds to the relative fit limits for one compliance measurement. A point in the upper left corner represents a regression where all of the data was used. The graph presents data for unload only and reload only. When fitting both unload and reload the range had to be extended to include all of the data due to hysteresis in the residuals. For this specimen, the reload was more linear than the unload, as evidenced by clustering of the circles in the upper left corner. For the reloads, the upper fit was about 80 %–100 % of the total range and the lower fit limit was less than 20 % of the range. Although the reload data appeared to be more linear, it was observed to have more noise resulting in larger residuals, which increases the fit range in SDAR. It is not possible to generalize whether unload or reload data are better for compliance determination because many of the round robin specimens were from the same lab, so the difference could be particular to the setup used by that lab. However, it is informative to check the data in this way in order to gain a better understanding of the test system and for quality control purposes.

FIG. 2 Range of fit from SDAR algorithm showing non-linearity in compliance data

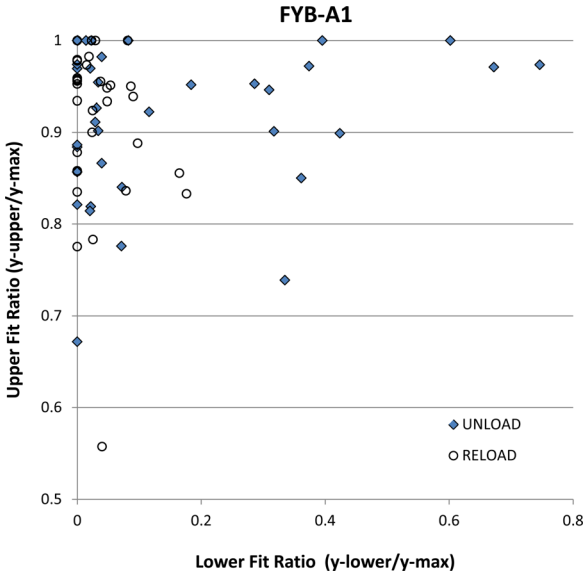
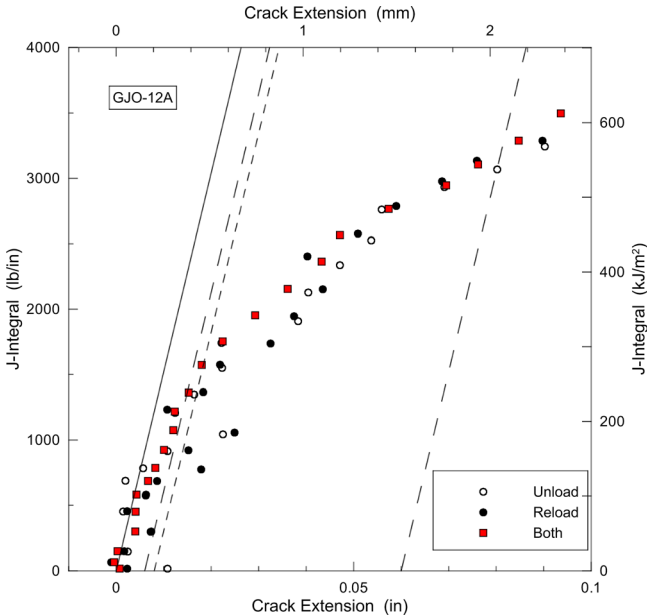


FIG. 3 J-R curves for specimen GJO-12A using different data selection methods and SDAR to fit most linear region.

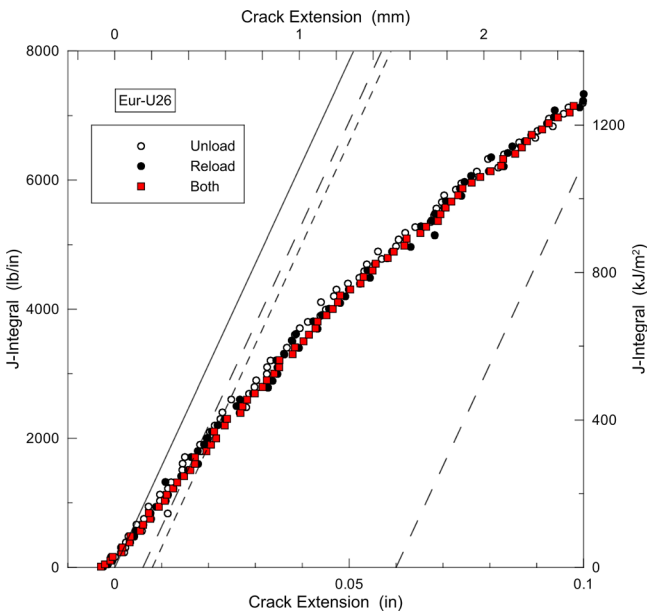


Compliances determined for unload, reload, and both were used to calculate crack length and  $J$  following the procedures in ASTM E1820. The results for selected specimens that represent the full range of behaviors are shown in Figs. 3 and 4. The differences in crack length that result from the different data selection methods are obscured by the determination of  $a_{oq}$  for each, and the subsequent conversion to crack extension. The points for both unload/reload do not necessarily fall between unload only or reload only because of the previously mentioned adjustment made in the SDAR algorithm to account for large residuals. The graph for GJO-12A shows the uncertainty in  $J_{Ic}$  that can result solely from the data selection approach for regression. The graph for Eur-U26 (Fig. 4) shows the opposite extreme where there is not much variability in crack extension; however, the steepness of the tearing resistance curve causes uncertainty in  $J_{Ic}$ .

### QUANTIFYING UNCERTAINTY IN THE J-R CURVE

Most labs using compliance to measure crack length do not have sophisticated algorithms to select the most linear region of the compliance data. With this in mind, the next part of the study used simple linear regression of all data in unload only, and both unload/reload, to generate 95 % confidence limits on compliance from the linear regression using Eq 6. Unload only and both unload/reload were selected for this part because these are the most commonly used approaches. Crack lengths

**FIG. 4** J-R curves for specimen Eur-U26 using different data selection methods and SDAR to fit most linear region.



were then determined for the mean, upper, and lower confidence bound, and  $J$  versus crack length curves were generated as shown in Figs. 5 and 6.  $J$  is plotted versus crack length instead of crack extension because it is difficult to determine what data should be used to find  $a_{oq}$ . For instance, if mean and upper confidence bound slopes are used to find  $a_{oq}$ s and the data is plotted versus  $\Delta a$ , then the mean and upper confidence bound curves are effectively normalized to fall just about on top of one another and the differences in slope are hidden. It is also highly unlikely that all compliance measurements would fall at the upper confidence bound. Using both the unload and reload data to calculate slope tends to increase the confidence interval.

The width of the confidence interval on crack length is a measure of the quality and quantity of data. The confidence interval is a function of the standard error and the number of points (the two parameters in the students-t are the number of points and the confidence level). Standard error increases with increases in unload/reload offset, noise, non-linearity, and with a decrease in the number of data points. These graphs provide an indirect indication of uncertainty in  $J_{Ic}$  that results from noise and nonlinearity in compliance data. It is indirect because it is not statistically correct to determine  $J_{Ic}$  from lower and upper confidence limit curves, and use the difference to quantify uncertainty in  $J_{Ic}$  because the crack extension for any single

**FIG. 5** Confidence bounds on crack length for simple linear regression of all unload data for round robin specimen GJO-12A.

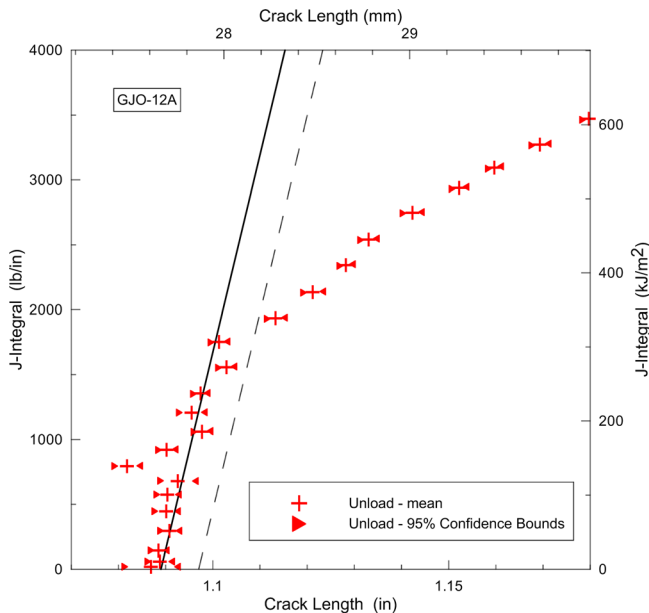
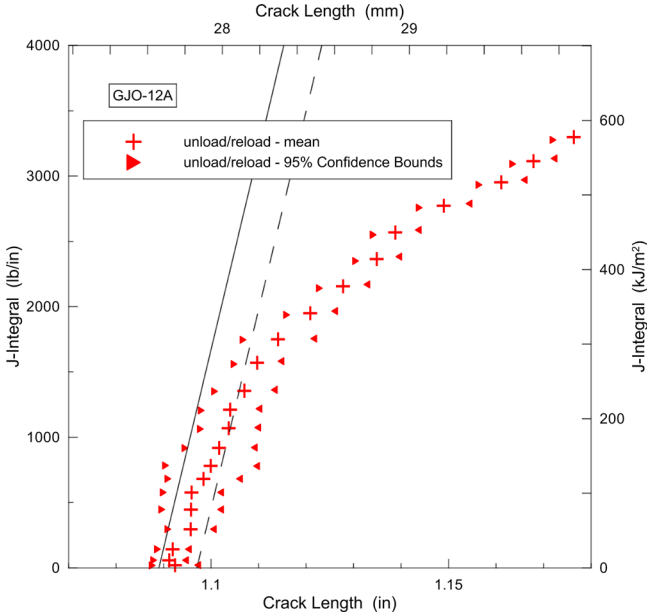


**FIG. 6** Confidence bounds on crack length for simple linear regression of all unload/reload data for round robin specimen GJO-12A.



point can fall anywhere between the limits at 95 % confidence. A more statistically correct approach would be to randomly sample compliance from each measurement point and then generate a  $J-R$  curve from those samples. This is the approach followed in the next part of this study.

This part of the study focused on three data selection approaches. Recognizing the fact that there typically is some non-linearity in compliance data, a modification of the SDAR algorithm was used to find the best region for linear regression. In an effort to simplify the process, the optimum region from step one of the SDAR algorithm for unload only data was used without any further adjustment. The results for this case are referred to as UOR. The second data selection approach was to use all data in the unload only (UA), and the third was to use all data in both unload and reload (BA). For each case, the mean and standard deviation of the compliance were determined for each compliance measurement. A Monte Carlo simulation of the J-test was conducted by randomly sampling compliances for each compliance measurement, and repeating the process 1000 times for each specimen. For each trial, crack lengths were calculated and rotation corrected following the process in ASTM E1820 (Fig. 1). Values of the J-integral were calculated for each point, and a polynomial regression was performed to get  $a_{oq}$ . Crack extensions were then calculated and data was selected for the power law regression to get  $C_1$ ,  $C_2$ , and  $J_{Ic}$ .

The slope of  $J$ - $R$  curve ( $dJ/da$ ) at  $J_{Ic}$  was also calculated for each trial. Results for the 1000 trials were then used to determine means, standard deviations and coefficients of variation ( $cov = \text{standard deviation}/\text{mean}$ ) for parameters  $a_{oq}$ ,  $C_1$ ,  $C_2$ ,  $J_{Ic}$ , and  $dJ/da$ .

For a given specimen, it was observed that the variability in  $a_{oq}$  for all trials is small in spite of relatively large variation in  $\Delta a$  in the early part of the  $J$ - $R$  curve (Fig. 7). The polynomial fitting procedure for  $a_{oq}$  is robust and no manipulation of data used in fitting was required for any of the specimens.

In order to check whether  $J_{Ic}$ s from the Monte Carlo simulation were normally distributed, normal probability plots of  $J_{Ic}$  were generated for each specimen.  $J_{Ic}$  is very sensitive to the data points used for the power law fit. Large variations in  $\Delta a$  early in the  $J$ - $R$  curve can cause points in the blunting region to fall between the exclusion lines. These point(s) pull the power law fit down causing a significant decrease in  $J_{Ic}$ . Normal probability plots revealed large deviation from normality when variance in early  $\Delta a$  causes them to fall inside the exclusion lines, as seen in Fig. 8. The data selection procedure in ASTM E1820 does not include a means to exclude these points. Sometimes these errant points resulted in  $C_2 > 1$ , meaning that the power law fit has increasing slope with increasing  $\Delta a$ . The data selection

**FIG. 7** Variation in  $a_{oq}$  for 1000 trials in Monte Carlo simulation for round robin specimen FYB-A1.

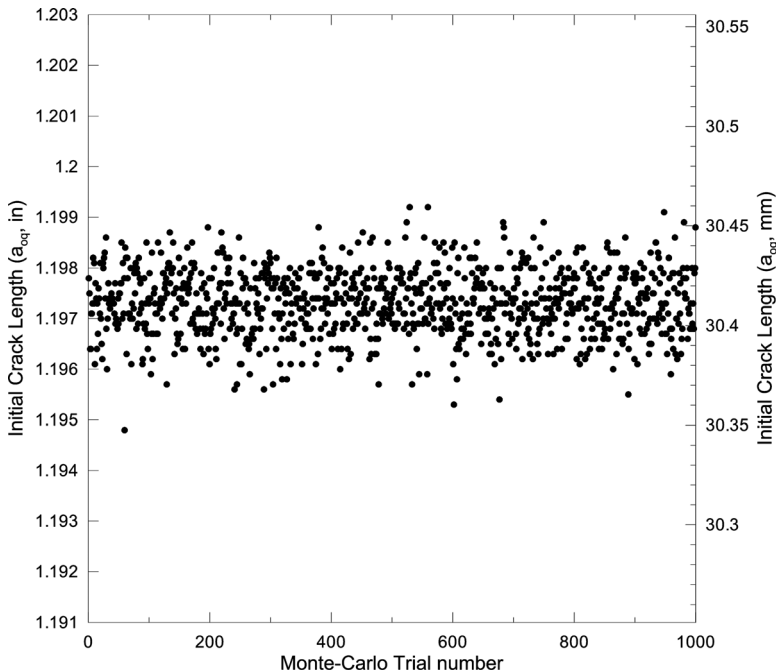
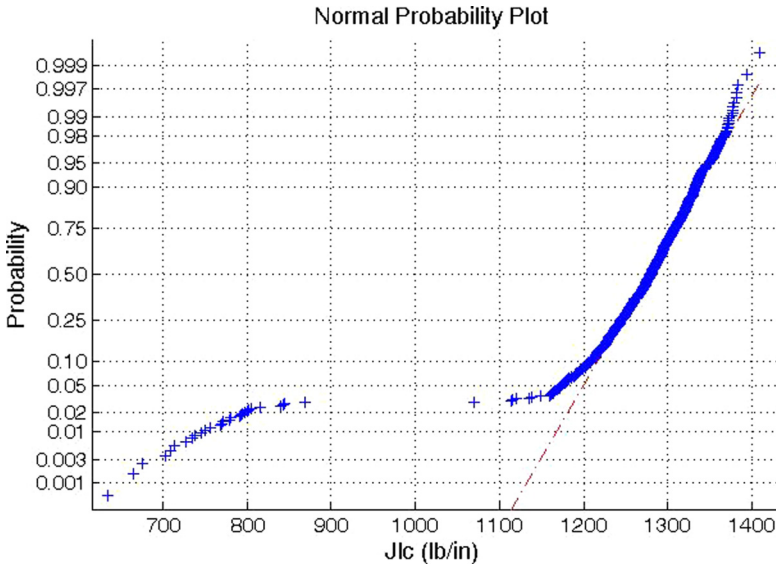


**FIG. 8** Normal probability plot for specimen GJO-12A with no adjustment of points selected for power law fit.



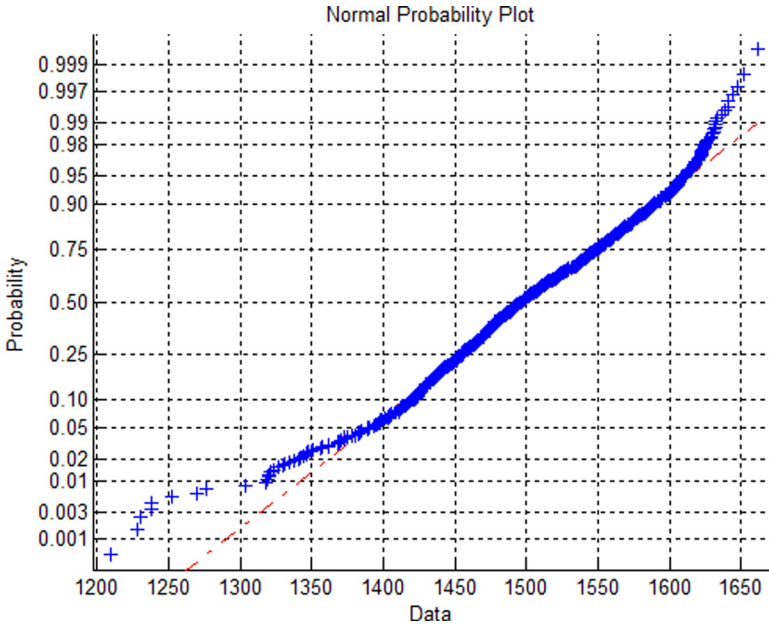
procedure as written in ASTM E1820 requires manual adjustment of the selected data to avoid excessive variance in  $J_{Ic}$ . This problem can be eliminated if the data selected is required to be contiguous starting from last point and moving toward  $J_{Ic}$ . This approach places emphasis on the crack growth region of  $J$ - $R$  curve to determine  $J_{Ic}$  and de-emphasizes the early blunting region up to  $J_{Ic}$ . This approach allowed the analysis to be fully automated, required no manual manipulation in data selection, reduced variance in  $J_{Ic}$ , and retained the normality of the  $J_{Ic}$  distribution, as shown in Fig. 9.

The results from the Monte Carlo simulation were examined in an effort to determine how variation in  $J_{Ic}$  relates to variation in the other parameters involved in the analysis. The cov of  $J_{Ic}$  is plotted versus the cov of load-line compliance ( $C_{LL}$ ) for the three data selection methods in Fig. 10. The abbreviations used in the legends for the following graphs are explained in Table 2.

The mean and standard error for each compliance measurement were the inputs to the Monte Carlo simulation. The standard error does not vary much from one measurement to the next. Therefore, the variability in compliance for a given specimen was characterized by taking the mean of the  $cov(C_{LL})$  only for points used in the power law fit.

The  $cov(C_{LL})$  is largest for FYB-A1 and GJO-12A using the BA approach, and the corresponding  $cov(J_{Ic})$  is also the largest. The UA approach exhibits a smaller range in  $cov(J_{Ic})$ , and the UOR approach exhibits the least. For some specimens

**FIG. 9** Normal probability plot for specimen GJO-12A with only contiguous points selected for power law fit.



(FGN-30, Eur-U26 and -U44), the data selection method for determining  $C_{LL}$  does not have much effect on variation in  $J_{Ic}$  while for others, it can have a large effect. Based on the results from these 6 tests, a mean  $cov(C_{LL})$  for points between exclusion lines of less than 0.0025 results in a  $cov(J_{Ic})$  of less than 0.04. In other words, the

**FIG. 10** Influence on variation in load-line compliance on variation in  $J_{Ic}$ .

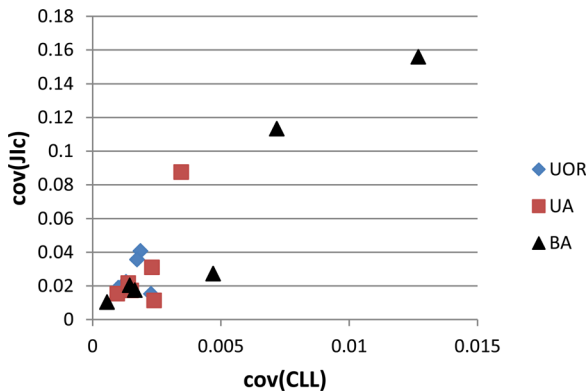


**TABLE 2** Data selection methods used to quantify uncertainty in  $J_{Ic}$ .

Designation	Part of Compliance Measurement Used in Linear Regression	Region of Data Used in Regression
UOR	Unload only	Optimum Region
UA	Unload only	All (no adjustment)
BA	Both unload and reload	All (no adjustment)

standard deviation in  $J_{Ic}$  is less than 4 % of the mean  $J_{Ic}$  when the standard error on compliance for points used in the power law fit is less than 0.25 % of the compliance.

It is also informative to look at how variation in the power law fit parameters correlates with variation in  $J_{Ic}$ . The power law equation is:

$$(7) \quad J = C_1 \left( \frac{\Delta a}{k} \right)^{C_2}$$

where  $k = 1.0$  for  $\Delta a$  in mm and 0.0394 for  $\Delta a$  in inches. The fit parameter  $C_1$  controls the height of the curve while parameter  $C_2$  controls the shape. As shown in Fig. 11,  $cov(J_{Ic})$  is linearly related to  $cov(C_1)$ , which is not surprising since  $J$  is proportional to  $C_1$ . The slope of the correlation is 4.23. Figure 12 shows that  $cov(J_{Ic})$  is also linearly related to  $cov(C_2)$ , but the slope of the correlation is 0.56, which means that variability in  $C_1$  has almost 8 times the effect on variability in  $J_{Ic}$  that  $C_2$  has. This effect is traced back to variation in  $C_{LL}$  in Figs. 13 and 14. Variation in  $C_2$  is more sensitive to variation in  $C_{LL}$  (slope = 22) than variation in  $C_1$  is (slope = 2.8). Therefore, variation in compliance in the crack growth region has a large effect on the shape of the power law  $J$ - $R$  curve, but variation in  $J_{Ic}$  comes from the height,

**FIG. 11** Influence of variation in power law parameter  $C_1$  on variation in  $J_{Ic}$ .

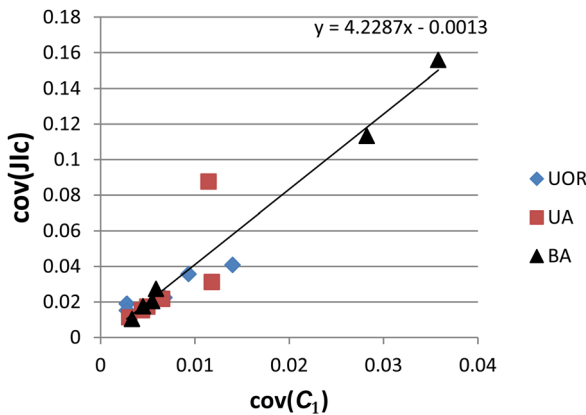


**FIG. 12** Influence of variation in power law parameter  $C_2$  on variation in  $J_{Ic}$ .

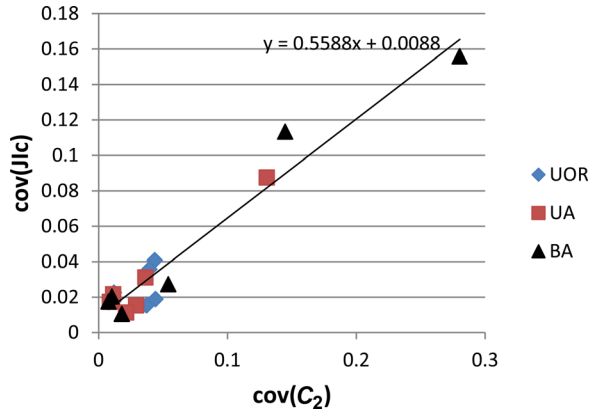
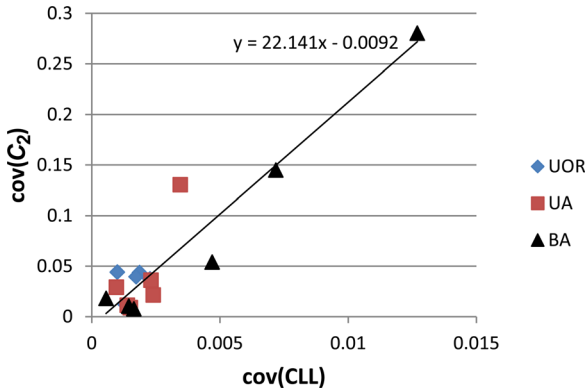
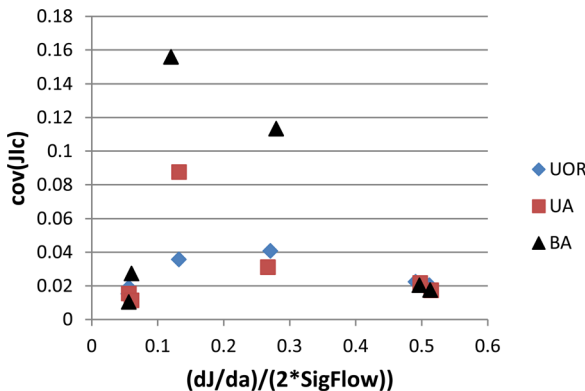


**FIG. 14** Influence of variation in load-line compliance on power law parameter  $C_2$ .



variation needs to be considered in terms of its magnitude relative to  $J_{Ic}$ . In order to investigate this, the  $cov(J_{Ic})$  was plotted versus the slope ratio  $(dJ/da)/(2SigFlow)$ , as shown in Fig. 15. The lack of a correlation for specimens exhibiting a slope ratio of up to about 0.5 indicates that, when considered in relative terms through the cov, variation in  $J_{Ic}$  is not due to the slope of the curve near  $J_{Ic}$ . It should be noted that in this study, the intersection of the construction line and the power law  $J-R$  curve was determined using numerical methods, which removes any subjectivity in finding the intersection. A stronger correlation could be anticipated if a subjective optical method were used.

**FIG. 15** Influence of power law slope at  $J_{Ic}$  on variation in  $J_{Ic}$ .



## Conclusions

1. Variation in  $J_{Ic}$  can be decreased for some tests by using either unload or reload data to determine compliance, but not both. In general, if there are a sufficient number of data points in a compliance measurement, it is recommended that unload only or reload only be used in the regression. The increase in standard error that comes from using less data points is more than offset by the decrease due to the smaller error values. Standard error in compliance can be decreased through careful attention to noise, digital resolution, and sampling rate of the measurement system.
2. Based on comparison of the UOR and UA data selection methods, it can be concluded that it is not necessary to use a sophisticated algorithm to find the optimum linear region in the unload or reload portion of the compliance data. Typically, the data is very linear; however, for some tests, the variation in  $J_{Ic}$  can be decreased somewhat by avoiding the non-linear region when performing linear regression on the compliance data. Data from the very beginning of the unload and the very end of the reload is typically where much of the non-linearity occurs.
3. As part of the linear regression, calculate the standard deviation and cov of the compliance for each compliance measurement. The mean cov for the points used in the power law fit provides a metric for quality of the compliance data. A mean  $\text{cov}(C_{LL})$  for points between exclusion lines of less than 0.0025 results in a  $\text{cov}(J_{Ic})$  of less than 0.04, or the standard deviation in  $J_{Ic}$  is less than 4 % of the mean  $J_{Ic}$ .
4. A less rigorous measure of uncertainty in  $J_{Ic}$  can be obtained by calculating confidence limits on each crack length determination, using  $a_{oq}$  from the mean curve to calculate crack extension, and plotting the confidence intervals along with the mean  $J$ - $R$  curve.
5. The most significant effect of variation in compliance is on data points near the first exclusion line where the standard error can cause them to fall on either side. The presence or absence of these points in the data selected for the power law fit can have a large effect on the resulting fit parameters and  $J_{Ic}$ .
6. The data selected for the power law fit should only include contiguous points that fall between the exclusion lines and less than  $J_{\text{limit}}$ , where this is determined by starting from the second exclusion line and working back toward the first exclusion line. This approach allows automation of the analysis, significantly reduces the chance of getting  $C_2 > 1$ , reduces variation in the fit parameters,  $C_1$  and  $C_2$ , and in  $J_{Ic}$ .

## References

- [1] ASTM E1820-13: Standard Test Method for Measurement of Fracture Toughness, *Annual Book of ASTM Standards*, ASTM International, West Conshohocken, PA, 2010.
- [2] Link, R. E., "Round-Robin Analysis of Standard Data Sets for Fracture Toughness Evaluation in ASTM E1820," *J. Test. Eval.* (accepted).

- [3] Van Der Sluys, W. A. and Futato, R. J., "Computer-Controlled Single-Specimen J-Test," *STP 803, Elastic-Plastic Fracture, Second Symposium*, Vol. 2, J. P. Gudas and C. F. Shih, Eds., ASTM International, Philadelphia, PA, 1983, pp. 464-482.
- [4] Futato, R. J., Aadland, J. D., Van Der Sluys, W. A., and Lowe, A. L., "A Sensitivity Study on the Unloading Compliance Single-Specimen J-Test Technique," *STP 856, Elastic-Plastic Fracture Test Methods: The User's Experience*, E. T. Wessel and F. J. Loss, Eds., ASTM International, Philadelphia, PA, 1985, pp. 84-103.
- [5] Graham, S. M., "Determining the Slope and Quality of Fit for the Linear Part of a Test Record," *J Test. Eval.*, Vol. 39, No. 2, 2011, pp. 260-268.

---

STP 1571, 2014 / available online at [www.astm.org](http://www.astm.org) / doi: 10.1520/STP157120130086

E. A. Schwarzkopf<sup>1</sup>

# Combining Visual and Numeric Data to Enhance Understanding of Fatigue and Fracture Properties and Mechanisms

## Reference

Schwarzkopf, E. A., "Combining Visual and Numeric Data to Enhance Understanding of Fatigue and Fracture Properties and Mechanisms," *Application of Automation Technology in Fatigue and Fracture Testing and Analysis*, STP 1571, Peter C. McKeighan and Arthur A. Braun, Eds., pp. 153–162, doi:10.1520/STP157120130086, ASTM International, West Conshohocken, PA 2014.<sup>2</sup>

## ABSTRACT

Often, it is desirable to combine both visual data with more traditional numeric data during a mechanical test. By definition, numeric values such as force, displacement, and cycle count are quantitative, while visual data is often difficult to use quantitatively. Visual data, however, is extremely useful in a qualitative sense. It can be used to verify deformation mechanisms and to validate test correctness in long-term, unattended automated tests. This paper presents two different methods for embedding visual data (static pictures and dynamic video) in standard mechanical tests. The paper discusses mechanical tests (tensile and fatigue) run using MTS' TestSuite mechanical testing software with commercially available cameras, and screen capture software. In a typical Fatigue Crack Growth test on a metallic alloy, static photos of the crack on one surface of a compact tension specimen are periodically acquired and stored to disk. In a fatigue crack growth test, the visual data can be used to verify other crack length measurement techniques such as compliance or direct current potential drop (DCPD). In a typical tensile test, video of the entire test is stored along with an embedded Picture in Picture of the stress-strain curve.

---

Manuscript received May 29, 2013; accepted for publication January 8, 2014; published online September 17, 2014.

<sup>1</sup>MTS Systems Inc., Eden Prairie, MN 55344.

<sup>2</sup>ASTM Sixth Symposium on *Application of Automation Technology in Fatigue and Fracture Testing and Analysis* on May 23, 2013 in Indianapolis, IN.

This technique can be used to correlate interesting features on the stress strain curve with necking behavior during the test.

### Keywords

video, photos, fatigue crack growth

## Introduction

Some say “a picture is worth a thousand words.” Others, such as scientist and software engineer Fred Brooks, say “show me your flowcharts and conceal your tables, and I shall continue to be mystified. Show me your tables, and I will not usually need your flowcharts; they will be obvious” [1].

Most fatigue and fracture researchers need both pictures and tables. Most researchers need to do more than simply create a model or tell a good story; they need to create and validate quantitative predictions based on their models. However, no matter how accurate a physical model is, if it is not conveyed to other researchers, engineers, and designers, its value is minimal. While ignoring an accurate, valid model is a missed opportunity, misusing a poorly understood model can be disastrous. Combining multiple ways of conveying the same information is necessary in most circumstances to effectively communicate technical results.

Academic, scientific, and technical publications have long used a combination of charts, graphs, technical drawings, and photos along with equations, tables, and prose to convey technical information. Data visualization pioneer, Edward Tufte [2], popularized Charles Joseph Minard’s 150 year old map of Napoleon’s march to Moscow (see Fig. 1). This quantitative chart packs an incredible amount of information into a single, poster-like graphic. The graphic requires little prose to show how devastating the Russian winter was to Napoleon’s army.

With the advent of the Internet as a distribution media, and inexpensive cameras or video capture devices, it is trivial to collect and convey photos or video of our tests along with quantitative information of load, displacement, temperature, etc., to others. With advanced computing hardware and software algorithms, this visual data can be transformed into quantitative data. In addition, quantitative data can be combined with qualitative information to tell a richer, fuller story. Unfortunately, these new tools do not make the researcher Charles Joseph Minard any more than the cell phone camera makes the owner Ansel Adams or Cecil B. DeMille.

## Deformation Mechanisms and Digital Image Correlation

An active area of research is the size effect of fatigue and fracture mechanisms with a goal of creating a unified model for deformation in various material systems. These sophisticated or unified models often treat various mechanisms as coupled



These software and hardware providers generally acquire photos as a function of time, and sometimes as a function of space (allowing three-dimensional analyses.) The solution providers generally have a variety of tools allowing varying degrees of visualization of the changing pixel images.

## Overlays to “Tell a Story”

Sometimes the simplest way to tell a “story” is to combine simple numeric data (in the form of a plot or a graph) overlaid on a simple video of the test specimen. This Picture in Picture information allows the viewer to visually correlate different features of the macroscopic specimen deformation with the numeric information in continuously updating plots. This same technique can provide significant understanding when an instrumented component of a machine or structure is loaded with a realistic duty cycle. Drivers commonly use dash board instruments on automobiles to provide information while driving down the road. Similar, software generated instruments can be overlaid on video from a helmet or roll bar camera for a Nascar or Formula 1 driver to give the design teams a better understanding of the stresses or loads placed on different components on the vehicle. Figure 2 shows the University of Minnesota Formula SAE car instrumented for wheel normal forces, torques, and lateral G forces in addition to steering angle. Figure 3 shows the same car cornering as seen from the roll bar camera with significant steering angle and significant G forces.

## Tensile Test

To illustrate the overlay, a simple tensile test was performed on 1018 cold rolled steel specimen with a round cross section. The specimen dimensions are shown in

---

**FIG. 2** University of Minnesota Formula SAE car instrumented with transducers for data acquisition.

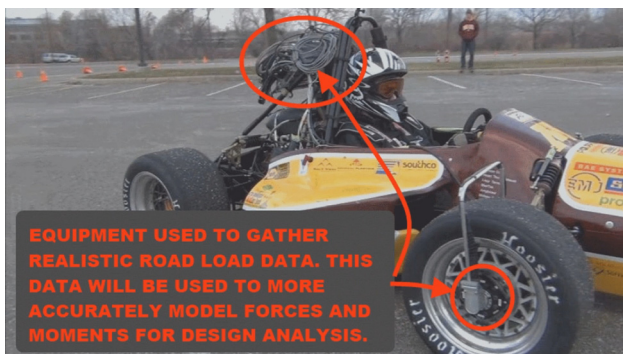
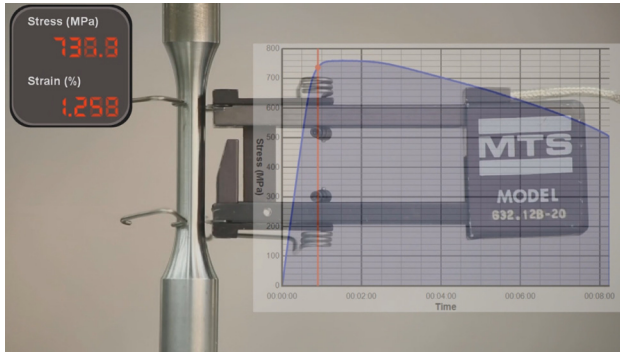




**FIG. 5** Tensile test with numeric and graphical data overlays just prior to yield. Yield is approximately 740 MPa.



The Dashware software allows the plots and meters to have varying degrees of transparency. The numeric data meter is opaque while the stress-time plot is partially transparent.

## Time Elapse Still Photos Follow Trends

Some tests or some systems only vary over longer periods of time. Time lapse photography is useful in understanding mechanisms and processes that change slowly over time. In real life structures, daily loads for rush hour traffic on bridges, or

**FIG. 6** Tensile test with numeric and graphical data overlays just prior to failure. Strain at failure is approximately 30 %. This snapshot taken at a strain of about 25.4 % strain.

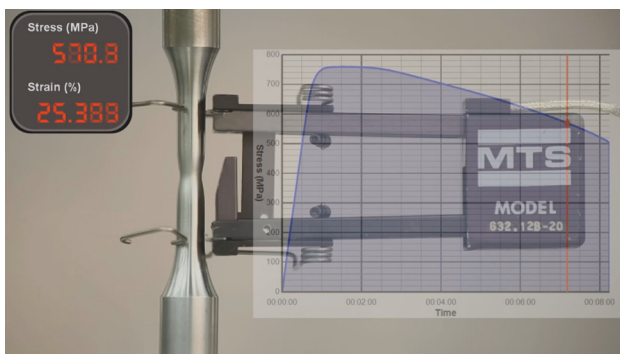


**TABLE 1** Fatigue crack growth test conditions.

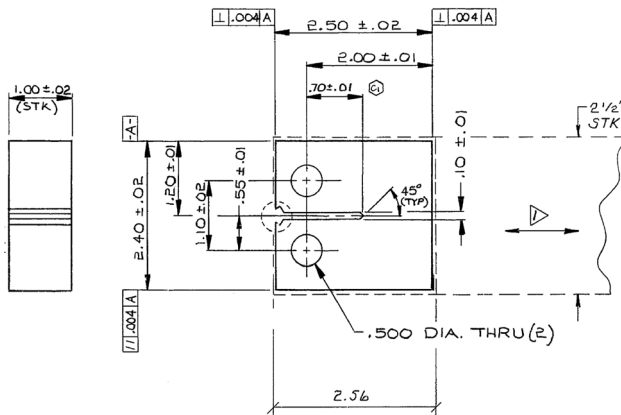
Material	2024 T351 Aluminum
Specimen Type /Dimensions	C(T) W = 50.8 mm, B = 25.4 mm, Notch length 17 mm
Test Hardware	MTS Landmark load frame, MTS FlexTest 40 Controller, MTS model 632.02 clip gage
Test Software	MTS TestSuite, Breezesys PSRemote, Dashware
Test Amplitude	12 Mpa-m 0.5 (load amplitude automatically reduced as crack length increases to keep delta K constant)
Load Ratio R	0.1
Test Frequency	10 Hz
Number of Specimens	2
Master Crack Length Measurement Method	Compliance method using clip gage on specimen front face
Camera Triggering	Increment 0.1 mm or 0.05 mm of crack length measured by compliance
Optical Reference	Steel ruler, clamped to specimen face

seasonal loads for snow on building roofs are simple examples. In material testing, fatigue tests, creep tests, or corrosion tests might require time lapse photography.

## Fatigue Crack Growth Calibration

To illustrate the idea of correlating measurements made from a series of still photos with measurements performed from traditional electronic transducers, a Fatigue Crack Growth test was performed on a standard C(T) specimen using the parameters described in Table 1. The specimen dimensions are shown in Fig. 7. While the

**FIG. 7** Typical 2024-T351 aluminum specimen used for Fracture Toughness and FCG testing. All dimensions are in inches.



test was running, a simple consumer camera (Canon Powershot G10) on a consumer tripod was automatically triggered to take a photo whenever the crack grew by 0.1 mm in one test, and 0.05 mm in a second test. The surface of the specimen was prepared by sanding it in the vertical direction (perpendicular to the crack growth direction) with 320 grit emery cloth. A simple steel ruler was clamped to the specimen to add a length scale to the photos and video (but the steel ruler was not used to determine the crack length in any automated manner from the optical data). The cycling system was not stopped when photos were taken, meaning that some photos were acquired at low loads, and others at high loads. The MTS Test-Suite software was configured to launch a software program created by a company called Breezesys [5] whenever the crack length (as measured by the compliance method) increased by the specified amount (0.05 mm or 0.1 mm). The Breezesys software program, called PSRemote, provides a mechanism to communicate with the camera in an automated manner. The PSRemote software program commanded the Canon camera to take a picture and store it to the computer disk with a file name that was constantly modified to incorporate the crack length (i.e., “cracklength 17.7 mm.jpg”) Two of the photos (with overlay data from the Dashware program) are shown below in Figs. 8 and 9.

From the resulting series of photos, it is easy to correlate the crack length on the surface of the specimen with the crack length calculated via the compliance method from the load cell and clip gage data. The correlation is seen below in Fig. 10 where crack length from the various techniques is plotted as a function of cycles. It is clear that for this limited range of crack lengths on this limited range of alternating stress intensities, the crack length measured from optical information on the surface of the specimen is consistently less than the crack length measured via the compliance method. By breaking the specimen open, after the fatigue crack

**FIG. 8** The Fatigue Crack Growth crack on the surface of the Compact Tension specimen after about 57 000 cycles. The specimen notch is 17 mm and the surface crack is about 27 mm (10 mm from the end of the bnotch) while the compliance measured crack is reading almost 29.1 mm.

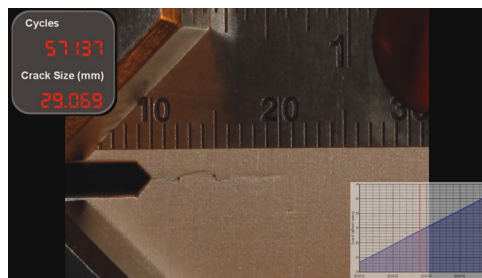


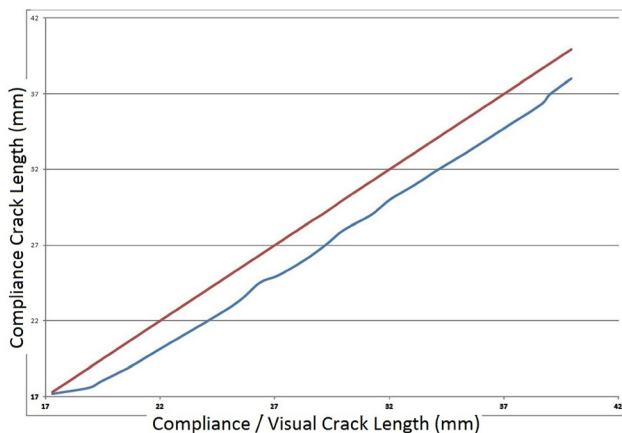
**FIG. 9** The FCG crack on the surface of the CT specimen after about 80 000 cycles. The specimen notch is 17 mm and the surface crack is about 32 mm (about 15 mm from the end of the notch), while the compliance measured crack is reading 34.0 mm.



growth test, it is apparent that this is due to the well-known crack front bowing due to plane strain conditions in the bulk of this specimen.

A time lapse series of photos can easily be turned into a video using a variety of tools. Both QuickTime Pro by Apple and Vegas Movie Studio were used to create a video from a series of appropriate still photos.

**FIG. 10** Crack lengths from compliance method plotted against crack lengths measured visually from photos of specimen surface. If the correlation between the two methods were exact, the two lines would lie on top of each other. Note how the specimen surface measurement is consistently less than the through thickness measurement calculated from compliance.



## Concluding Remarks

The two examples shown here are part of a much wider family of integration of numeric and optical information which deepen our understanding of deformation models and deformation mechanisms. Identifying and codifying these models and mechanisms is only one aspect of engineering failure resistant components and structures. Communicating the models and mechanisms to other researchers and designers is also necessary. Visual data in the form of photos and video when combined with traditional quantitative data in the form of plots and tables can further this communication. With the advent of faster processors and cheaper signal processing, these tools, already common place in laboratories with find further use.

## References

- [1] Brooks, F., *The Mythical Man-Month: Essays on Software Engineering, Anniversary Edition*, 2nd ed., Addison-Wesley, Reading, MA, 1995.
- [2] Tufte, E. R., *The Visual Display of Quantitative Information*, Graphics Press, Cheshire, CT, 1986.
- [3] Sutton, M. A., Orteu, J.-J., and Schreier, H. W., *Image Correlation for Shape, Motion and Deformation Measurements*, Springer, New York, 2009.
- [4] Dashware, 2013, "Dashware.net—Telemetry Data Overlay on Your Videos," <http://www.Dashware.net/> (Last accessed 5 May 2013).
- [5] Breeze, C., 2013, "Breeze Systems—Digital Camera Workflow Software: Browser, Downloader, Canon Remote Capture," <http://www.breezesys.com/> (Last accessed 5 May 2013).

---

STP 1571, 2014 / available online at [www.astm.org](http://www.astm.org) / doi: 10.1520/STP157120130081

Christoph Leser,<sup>1</sup> Frank Kelso,<sup>2</sup> Ali P. Gordon,<sup>3</sup> and Sherri Ohnsted<sup>4</sup>

## Software Tools for a Materials Testing Curriculum

### Reference

Leser, Christoph, Kelso, Frank, Gordon, Ali P., and Ohnsted, Sherri, "Software Tools for a Materials Testing Curriculum," *Application of Automation Technology in Fatigue and Fracture Testing and Analysis*, STP 1571, Peter C. McKeighan and Arthur A. Braun, Eds., pp. 163–172, doi:10.1520/STP157120130081, ASTM International, West Conshohocken, PA 2014.<sup>5</sup>

### ABSTRACT

Instructors of both undergraduate and graduate courses of materials science with a laboratory section employ hands-on sessions to further students' understanding of key materials behavior principles. A typical solid mechanics laboratory session exposes students to topics such as: tensile, torsion, hardness, fatigue, and fracture testing procedures as well as associated properties and the like. Even though observing the different modes of material deformation and rupture response first-hand fosters a better mastery of the course content, limitations in available "face time" with students, course budget, availability of test devices, etc., are obstacles. Integrating software tools that simulate mechanical testing represents an alternative approach that can potentially transform and enhance the students learning outcomes. The identical graphical user interface is used for conducting both virtual and physical testing of materials. The software tools will aid in the classroom, laboratory, and student self-study for the subjects of a material's plastic

---

Manuscript received May 22, 2013; accepted for publication December 23, 2013; published online April 30, 2014.

<sup>1</sup>MTS Systems Corporation, 14000 Technology Drive, Eden Prairie, MN 55344, United States of America, e-mail: [christoph.leser@mts.com](mailto:christoph.leser@mts.com)

<sup>2</sup>Mechanical Engineering Department, Univ. of Minnesota, 111 Church Street Southeast, Minneapolis, MN 55455, United States of America, e-mail: [kelso001@umn.edu](mailto:kelso001@umn.edu)

<sup>3</sup>University of Central Florida, 4000 Central Florida, PO Box 162450, Orlando, FL 32816-2450, United States of America, e-mail: [apg@ucf.edu](mailto:apg@ucf.edu)

<sup>4</sup>MTS Systems Corporation, 14000 Technology Drive, Eden Prairie, MN 55344, United States of America, e-mail: [sherri.ohnsted@mts.com](mailto:sherri.ohnsted@mts.com)

<sup>5</sup>ASTM Sixth Symposium on *Application of Automation Technology in Fatigue and Fracture Testing and Analysis* on May 23, 2013 in Indianapolis, IN.

yielding, stress-strain relationships, fatigue, crack growth, and fracture. These same tools are then used in the laboratory to perform physical testing. This integrated virtual/physical curriculum prepares the student in test setup, execution and data analysis and makes the laboratory experience more efficient. It is also instructive for gaining an understanding of the value and limitations of modeling approaches in describing material behavior.

### **Keywords**

universal testing machine, console emulator, strength of materials, simulated data

## Introduction

Instructional methodologies, especially those employed in the post-secondary educational stage, are constantly evolving to better engage students and to more adequately prepare them for the industrial workplace. A modern engineering curriculum not only combines both theory and practical application of engineering principles, but is also multi-mode to cater to the various learning styles of student audiences [1]. This contemporary mix of content and modes is synergistic with the industrial approach to problem solving (e.g., product development, failure reconstruction, etc.). Engineering workplaces often introduce a layer of simulation between theoretical design and actual prototype building.

Many engineering courses containing a laboratory component are inherently constrained because test devices are not always available to students to either: (1) adequately learn to use the device or (2) conduct a multitude of experiments. For example, students in a typical solid mechanics laboratory course having limited resources may only have a few hours from week-to-week to interact physically with a universal test device, its console, and test specimens. Despite the budget limitations that constrain many institutions, there is a tangible need for allowing engineering students more hands-on exposure to key test devices in their engineering coursework. Computational methods have advanced to the stage where simulations of experiments match real ones [2,3]. Embedding these numerical tools within a graphical user interface (GUI) allows instructors to bring a virtual test lab into the classroom and students to perform virtual tests prior to actually going into the testing laboratory. With regard to experiments concerning the mechanics of materials, all aspects of materials testing from test definition to test execution and data analysis should be performed without requiring actual test equipment or specimen. Others [4] have developed a software environment that included a simulation and visualization of the physical testing environment. The advantages of combining physical and simulated testing were described as giving students essentially unlimited access to experiments and facilitating study of many testing scenarios in a short period of time.

In this paper, we outline efforts to apply this integrated approach to a teaching curriculum for tensile, fatigue, and fracture testing of materials. Each of these three fundamental experiments of mechanics of materials is overviewed in the next

sections with emphasis to instructional materials (i.e., lecture notes, laboratory testing instructions, homework assignments, test program definitions, test report templates and simulation definitions).

## The Tension Test

Force, deflection, stress, and strain are all fundamental principles that engineering students acquire early in their studies and apply throughout their careers. For example, farm machinery such as plows or disks, must deflect under force, but with too much deflection the function of the machine will be lost. Automated packaging equipment must transmit power through rotating shafts and design engineers deficient in their knowledge of stress and strain will have broken parts to show for it. Understanding stress–strain relations is important, and that understanding is empirical in origin.

Experiments by Hooke and Young [5] and others over the past several hundred years established the basis for our modern definition of stress and strain or, in their time, force and extension. These experiments evolved into formal tests for determining material physical properties used by engineers to characterize the behavior of materials subjected to actual service conditions. It makes sense, then, to include a discussion of materials testing in the engineering curriculum.

One of the oldest and most useful material tests is the tension test, that is used to determine stress and strain and predict conditions that will cause failure. For tests to be repeatable, the test procedure must be well-defined. In the United States, the tension test for metals is specified by the ASTM International (American Society for Testing and Materials International) in test standard ASTM E8/8M [6]. The outcomes of this test include such useful properties as modulus of elasticity, yield strength, ultimate strength, and elongation at fracture, to name a few. The specimen is inserted into a tensile testing system capable of applying a uniaxial quasi-static force to the specimen, and equipped with sensors that monitor and record force and deformation from start to finish. As Hooke learned three hundred years ago, many metals have a linear relationship between the amount of force applied to a specimen, and the amount of resulting deflection. If the force is removed before it becomes too high, then the material returns to its original shape. If too high a force is applied, however, the specimen is permanently deformed even after the force is removed. In the latter case, the material *yielded* and the deformation changed from elastic to anelastic. In the elastic region, Hooke's Law, *ut tensio, sic vis* (*As the extension, so the force*), holds for a "linear" deforming material: stress is directly proportional to strain. This constant of proportionality is Young's modulus or the modulus of elasticity.

Students who perform physical tension tests learn the stress–strain relationship *experientially*. Their knowledge of Young's modulus is not just one of a dozen definitions to be memorized and soon forgotten. Engineering students learn about stress and strain the way Hooke and Young learned about stress and strain—

through direct experimentation and observation. Several hundred years of human experience are codified in the tension test, and actually running the test is the most direct means of acquiring an intuitive, as well as a mathematical, understanding of material behavior and its engineering description.

## Tension Test Lecture

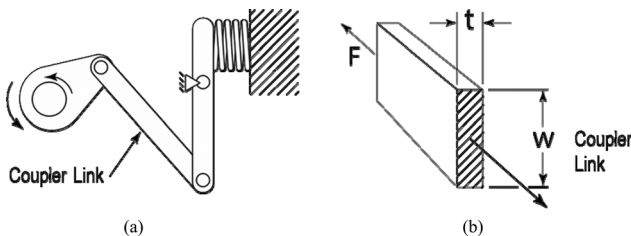
Simple examples and case studies are often effective for motivating students to learn the topic at hand. For a discussion on yield strength; for example, the design of a clutch linkage provides an excellent illustration. The coupler link in the linkage of Fig. 1 is a two-force member experiencing a 4.5 kN tensile force. If the force is too high, then the part will yield; that is considered failure. Students are asked to design the link by choosing an appropriate width  $w$  for a link made with a thickness,  $t$ , of 6 mm steel plate. To complete the design, though, students will need to know the yield strength of the steel plate. The laboratory section of the curriculum will teach the student how to measure the yield strength through measurement of the stress-strain curve and the calculation of the offset yield strength.

## Test Equipment and Simulation

The test lab associated with this class uses an electromechanical Universal Test Machine powered by a DC servomotor and controlled by a digital closed loop controller. Test definition, execution, and communication with the controller are achieved via software running on a PC using Microsoft Windows. This software has a simulation mode that can be connected to a “virtual” test system to run tests on a range of “virtual” samples of different materials. The same software is installed on the lecturer’s computer, the test lab computer, and in a student accessible computer lab. In that way, students can witness the test first virtual test in the classroom, and then perform their own virtual tests in the computer lab and finally perform actual test in the laboratory.

The introduction of simulation technology is beneficial to students as it provides an experiential link between the behavior of materials and physical

**FIG. 1** (a) Coupler link and (b) dimension  $w$  to be determined.



phenomena, and illustrates how they can be described using engineering principles. The use of the Python [7] programming language makes the translation from equation to program easy to follow as the language has little “overhead” or abstraction. The code is written essentially in the same way as a manual calculation would be performed. Furthermore, Python is an open source language, so various samples programs and documentation exist in the open domain.

There are two basic materials supported in the current tension test simulation, steel, and acetal polymer. Upon starting the test, the student is prompted for which material to use for the specimen. The test is then performed in displacement control where a slowly increasing displacement is induced into the specimen until it fails. In simulation mode, the force response is simulated to respond appropriately for the selected material. The force signal is calculated from the displacement signal at the rate at which the data is collected. This is currently set up for 50 Hz, but can be set to any rate up to the controller update rate of 1024 Hz.

The simulation first converts the prescribed displacement signal into a strain signal using the following equation (terms in “quotation marks and Courier font” refer to the label of the term in the Python program example further below):

$$(1) \quad \varepsilon = dl/l_0$$

where:

$\varepsilon$  = unitless measure of engineering strain, “strain”  
 $dl$  = change of length (m), “displacement\_m,” and  
 $l_0$  = gage length (m), “GageLength.”

For steel, the strain signal is divided into 5 regions. Stress is related to strain using a spline curve fit: essentially a set of third order polynomials that relate stress to strain. An appropriate set of polynomial coefficients was determined for each segment of the curve from an actual tension test of mild steel. The acetal polymer curve fit was divided in to 7 regions, and again fit with a spline. As each displacement point is measured, it is compared with the boundaries of the region to determine which set of coefficients to use; stress at each displacement point is calculated using the appropriate set of coefficients.

The stress is then converted to force using the following formula:

$$(2) \quad F_n = \sigma / A, \text{ "stress" * Area}$$

where:

$\sigma$  = normal stress (N/m<sup>2</sup>), “stress,”  
 $F_n$  = normal component force (N), “SimulatedForce\_Steel,” and  
 $A$  = specimen cross section area (m<sup>2</sup>), “Area.”

Two of the five equations relating stress ( $y$ ) to strain ( $x$ ) for simulation purposes for steel are:

$$(3) \quad y = 207x; \text{ from } 0 \text{ to } 0.130 \text{ m/m, region of Hooke's Law}$$

$$(4) \quad y = -0.101343x^3 + 7.90634x^2 - 205.235x + 2221.09; \text{ from } 24.9 \text{ to } 36 \text{ m/m}$$

Below is the Python function that the simulation tool uses for calculating the force response for the simulated steel under elongation.

```
def SimulatedFoad_Steel(displacement_m):
    strainCurve=[ 0.0, 0.130, 0.360, 1.3, 24.9, 36]
    coef1=[ 0.0, 207, 0.0, 0.0]
    coef2=[ 151.433785723072, 1214.621345688630,
-2871.363627044977, 2450.515601295664]
    coef3=[ 239.453661520087, 435.466129855619,
-580.220664014717, 211.658303073500]
    coef4=[ 291.492977403970, -2.337568897015,
0.946004094869, -0.024071351014]
    coef5=[ 2221.091011391235, -205.234635658303,
7.906343158352, -0.101343125448]
    strain=displacement_m/GageLength*100
    if (strain <= strainCurve[ 1 ]):
        stress=Polynomial(strain, coef1)
    if (strainCurve[ 1 ] < strain and strain <= strainCurve[ 2 ]):
        stress=Polynomial(strain, coef2)
    if (strainCurve[ 2 ] < strain and strain <= strainCurve[ 3 ]):
        stress=Polynomial(strain, coef3)
    if (strainCurve[ 3 ] < strain and strain <= strainCurve[ 4 ]):
        stress=Polynomial(strain, coef4)
    if (strainCurve[ 4 ] < strain and strain <= strainCurve[ 5 ]):
        stress=Polynomial(strain, coef5)
    if (strainCurve[ 5 ] < strain):
        stress=0.0
    stress=stress*1000*1000
    return stress*Area.
```

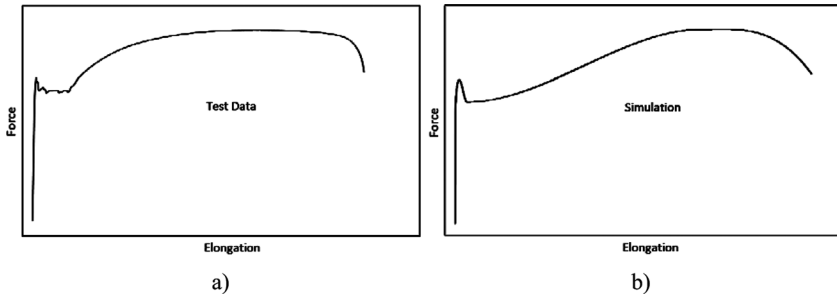
See Fig. 2 for actual test data and the approximation by the simulation via the Python function.

## High Cycle Fatigue Test Lecture

The design for fatigue requires knowledge of a material's fatigue limit, defined as the fatigue strength at a fixed cyclic life. Unlike a tension test, the HCF test will require much more than 30–60 s to complete. If runout, or non-failure, is defined to be  $10 \times 10^6$  cycles, an HCF test that cycles force at 30 Hz will require more than 90 h to complete. Simulation in this case is very useful for condensing the test and presenting the results quickly in the course of a lecture.

The tension test example considered static failure of the connecting link. For HCF, students will consider fatigue failure of the same link. For design

**FIG. 2** (a) Actual test data (for a mild steel) and (b) simulated force–elongation curve.



purposes, the stresses must be compared to the fatigue limit of the steel. The fatigue limit for laboratory specimens has been found to be approximately half the ultimate tensile strength<sup>6</sup>. The fatigue test simulation is run during lecture, demonstrating runout for fully reversed forces that are less than half of the ultimate tensile strength.

It is possible to use the same simulation tool, albeit with different formulas, in the classroom demonstration of an HCF test. Time spent learning the behavior and the user interface can be applied uniformly for all of the materials tests. In an actual laboratory, of course, a servohydraulic load frame would be required. An electro-mechanical system uses motor-driven ballscrews to apply force and displacement to the specimen. This technology works well for quasi-static tests such as tension and fracture toughness where the force and the displacement are increased slowly and uniformly in one direction (the tensile direction, in these tests.) Dynamic tests such as high cycle fatigue require much higher loading rates, as well as high frequency direction reversals, and forces that can alternate between tension and compression. Backlash in ballscrews becomes an issue when switching from tension to compression. Loss of lubricant between ballscrews and bearings will result in heat generation and wear. Servohydraulic systems are far more appropriate for cyclic tests such as the high cycle fatigue test, and this is discussed in the laboratory section of the course.

## Fracture Toughness Test Lecture

The fracture toughness test according to ASTM E399 [8] corresponds to a paradigm shift in design. Traditional engineering design uses a stress analysis approach to guard against overloads. The maximum stresses in a component are determined and in a first design approximation are compared to the yield strength (static

<sup>6</sup> This is true for steels with an ultimate tensile strength less than 1380 MPa (200 ksi). For those steels whose strength is greater, the fatigue limit or fatigue strength at  $10^6$  cycles is approximated as  $[1/2] \times 1380 = 690$  MPa (100 ksi).

failure), or the fatigue limit for cases with cyclic loading. This has been the traditional approach defined by Wöhler in the 1800s, and is still (albeit acknowledged by the authors to be an approximation) taught in engineering curricula today.

Fracture mechanics, on the other hand, is a relatively recent engineering development. Although the theory of linear elastic fracture mechanics was developed in the 1920s, widespread application of the theory had to wait until testing technology was able to provide designers with the corresponding material properties. This occurred in the 1960s, particularly in the aircraft and nuclear industries, and facilitated the development of damage tolerant design.

An important material property in damage tolerant design is the fracture toughness,  $K_{IC}$ . The fracture toughness is the critical value of the stress intensity “ $K$ ” that results in failure by catastrophic fracture, and as such it is given the subscript “ $c$ ” for “critical.” (The Roman numeral “ $I$ ” in  $K_{IC}$  stands for mode one opening displacement.) Instead of comparing the worst-case stresses to the yield strength, the designer compares the stress intensity ( $K$ ) to the fracture toughness ( $K_{IC}$ ). Designers often perform this comparison to determine the critical crack length in the component under design. Like the tension test, the fracture toughness test entails a monotonic, quasi-static ramp. The mode of control is force control, rather than strain or displacement control. The specimen has been pre-cracked prior to the test, so the failure force corresponds to the force that causes an “atomistically sharp” crack to propagate to failure. This failure force is used to calculate the corresponding critical value of the stress intensity ( $K = K_{IC}$ ).

Fracture toughness tests can be performed using either servohydraulic test systems or electro-mechanical test systems. This lecture on fracture toughness incorporates the electro-mechanical system simulation used in the previous two materials tests. The fracture force is determined using the 5 % offset line, and the fracture toughness is calculated from the fracture force in accordance with ASTM E399. The simulation provides a very effective demonstration of the similarity between the tension test and the fracture toughness test: students who understood the tension test can easily grasp the fracture toughness test. This provides an excellent learning path for advancing from the traditional, intuitive understanding of stress and yield strength to the newer concepts of stress intensity and fracture toughness.

## Integration

For mechanics of materials laboratory students, thrusting the task of learning new software on top of their homework, lab report writing, and other responsibilities might be counterproductive by further diluting their focus on mastering core concepts. A more strategic approach to integrating software mastery is needed. In tensile testing, the pre-lab homework could, for example, contain the following tasks:

- With regards to mechanics of materials, define the following terms: (1) necking, (2) proportional limit, (3) elastic limit, (4) fracture stress, (5) % reduction area, etc.

- Acquire the material properties of the candidate material being used (e.g., modulus, yield strength, tensile strength, and Poisson's ratio).
- Develop the dimensions of a test specimen that complies with ASTM E8/8M-11 [6].
- Use the virtual testing software to develop simulated test results for the candidate material. Verify that the simulated data is in agreement with the defined mechanical properties.

It should be noted that the software can include “helper text” to illuminate concepts as the student is running the experiment. One source for terminology used in experiments in mechanics of materials is available via Ref. [9]. This would reduce the number of resources students might have to consult.

In the lab session, the instructor would assume the students have had some level of interaction with the software and would thus show less obvious aspects of the GUI, i.e., displacement control versus force control, data acquisition rates, etc. Actual tensile tests would be performed and students could analyze the specimen and the data. In the corresponding lab report, the student would be tasked with analyzing data generated in the lab session, and possibly generating additional simulated data under conditions that might vary from those used in the lab session. Topics such as rate-dependence, temperature-dependence, and so on, that are not typically covered could be studied in great depth with this virtual testing tool.

Another level of integration between classroom learning and engineering work is reached by exposing students to the use and development of standards. One useful resource that will be integrated into this materials testing curriculum is the ASTM Professor Tool. These are learning materials that ASTM makes available to the public on their website, without license, to teach on the subject of standards use.

## Conclusion

There are a number of advantages to this integration of lecture presentation, simulation, and physical testing. As discussed earlier, students have a direct experience with the material property needed to successfully complete their design exercise. It also provides a direct illustration of material behavior (elastic versus inelastic deformation, ductility, yield failure, fracture failure, energy absorption). These, in turn, can serve as a discussion prompt for more advanced concepts: why does a material yield? What makes a material ductile as opposed to brittle? Define ductility. Why are some materials stronger than others? What if we designed our link out of plastic instead of steel?

Furthermore, students become familiar with test methods, learn testing concepts, procedures, and vocabulary, collect and interpret data and extract property values, and identify where empirical results are used in an engineering analysis. This approach therefore prepares students to perform actual material tests.

Another advantage of giving students access to all tools in a simulation environment is that they can learn at their own pace rather than in a lab setting with limited machine and specimen availability.

Engineering students like to see the connection between what they learn in school and what they do in industry. Design examples requiring knowledge of material properties provide both a context and a motivation for learning, and the empirical nature of our knowledge of material properties makes it important to bring the materials test into the classroom where it belongs.

Simulation plays a growing role in any industrial development process and exposure to its capabilities and limitations should therefore be part of any lecture on design.

It is the authors' belief that the integration of instruction, simulation, and hands-on interaction with a physical specimen ensures better understanding and therefore prepares students best for work in the global engineering market.

## References

- [1] Hawk, T. F. and Shah, A. J., "Using Learning Style Instruments to Enhance Student Learning," *Decis. Sci. J. Innovat. Educ.*, Vol. 5, No. 1, 2007, pp. 1-19.
- [2] Mirone, G. and Corallo, D., "Stress-Strain and Ductile Fracture Characterization of an X100 Anisotropic Steel: Experiments and Modeling," *Eng. Fract. Mech.*, Vol. 102, 2013, pp. 118-145.
- [3] McWilliams, B., Sano, T., Yu, J., Gordon, A. P., and Yen, C., "Influence of Hot Rolling on the Deformation Behavior of Particle Reinforced Aluminum Metal Matrix Composite," *Mater. Sci. Eng. A*, 2013, (accepted).
- [4] Barham, W., Preston, J., and Werner, J., "Using a Virtual Gaming Environment in Strength of Materials Laboratory," *Proceedings of the 2012 ASCE International Workshop on Computing in Civil Engineering*, Clearwater, FL, June 17-20, 2012.
- [5] Timoshenko, S. P., *History of Strength of Materials*, McGraw Hill, New York, 1983.
- [6] ASTM E8/8M-11: Standard Test Methods for Tension Testing of Metallic Materials, *Annual Book of Standards*, ASTM International, West Conshohocken, PA, 2011.
- [7] Python Software Foundation, "Programming Language Reference," <http://docs.python.org/2/reference/>, 1990-2013, (Last accessed 23 Jan 2014).
- [8] ASTM E399-12e1: Standard Test Method for Linear Elastic Plane Strain Fracture Toughness  $K_{Ic}$  of Metallic Materials, *Annual Book of Standards*, ASTM International, West Conshohocken, PA, 2012.
- [9] Gordon, A. P., *Dictionary of Experiments of Mechanics of Materials*, Creative Printing and Publishing, Sanford, FL, 2012.

**ASTM INTERNATIONAL**  
Helping our world work better

ISBN: 978-0-8031-7587-7  
Stock #: STP1571

[www.astm.org](http://www.astm.org)